Title
Fundamentals of Hydrogen Sulfide Removal from Gaseous Streams via Reactive Sorption with Copper Oxide

Author
AZZAM, SARA

Publication Date
2020

Peer reviewed|Thesis/dissertation

UNIVERSITY OF CALIFORNIA

Los Angeles

Fundamentals of Hydrogen Sulfide Removal from Gaseous Streams via Reactive Sorption with Copper Oxide

A dissertation submitted in partial satisfaction of the requirements for the degree Doctor of Philosophy in Chemical Engineering

by

Sara Azzam

2020

ABSTRACT OF THE DISSERTATION

Fundamentals of Hydrogen Sulfide Removal from Gaseous Streams via Reactive Sorption with Copper Oxide

by

Sara Azzam

Doctor of Philosophy in Chemical Engineering

University of California, Los Angeles, 2020

Professor Dante Simonetti, Chair

Hydrocarbon streams derived from natural gas and petroleum processing contain high concentrations of hydrogen sulfide (H_2S) which is corrosive to process equipment, detrimental to product quality, and harmful to human health and the environment. Reaction of trace concentrations (<100 ppm) of sulfur compounds in natural gas streams with copper oxide (CuO) to form environmentally benign copper sulfides is an effective method to purify these streams. Such reactive sorption processes are advantageous because they are thermodynamically more favorable than physisorption, leading to higher purity streams and higher solid phase contaminant capacities. However, the primary drawbacks to reactive sorption systems are incomplete conversion of the copper oxide phase and slow kinetics, which detrimentally impact their industrial use by necessitating continuous process shutdowns to reload the reactors or/and over-sized beds. Moreover, most current predictive models lack the detail to fully capture the important reaction-diffusion phenomena associated with reactive sorption at the molecular level. Thus, the

extrapolation of these models across a broad range of conditions is difficult. Motivated by these considerations, the overall goal of this project is to combine advanced characterization experiments at the atomic level with intrinsic reaction kinetic data at the reactor level to create microkinetic descriptions that relate reaction mechanisms of sulfur-containing molecules to the chemical and structural changes of CuO-based materials. This multi-scale research approach (atoms, crystals, pellets, reactor) exhibits a significant departure from traditional approaches that focus on either iterative materials screening or simplified reactor modeling.

This project has unraveled the following fundamental insights about the CuO-H_2S reactions: i) CuO-based materials with decreasing extents of crystallinity contain high concentration of oxygen vacancies which results in higher extent of conversion due to the slower rates of molecule dissociation and increased diffusivities of sulfur atoms, oxygen atoms, and/or reactant molecules within the solid phases. ii) The $Cu_{2-x}S_x$ products change over the course of the reaction due to changes in the electronic and coordination environments of the interfacial disulfide groups, with products resembling covellite (CuS) as the conversion increases. iii) The introduction of foreign atoms to CuO lattice (Zn and La atoms) enhances CuO sulfidation conversions by disrupting the CuO lattice and forming vacancies for the diffusion of sulfur and oxygen atoms, and by donating electron density to Cu^{2+} centers and consequently weakening the Cu-O bonds and making them more susceptible to rapture and reaction with sulfur moieties. Finally, the project highlights the utility of using fixed bed tests and simple linear driving force models to describe the surface reaction/diffusion phenomena contingent on operating at conditions where bulk and pore diffusion resistances are minimal. These insights, among others, are critical for the rational design of high capacity reactive sorbents and for the optimal operation of the desulfurization processes at conditions that approach their thermodynamic limits.

The dissertation of Sara Azzam is approval by:

Panagiotis D. Christofides

Vasilios Manousiouthakis

Louis Bouchard

Dante A. Simonetti, Committee Chair

University of California, Los Angeles

2020

This dissertation is dedicated to my parents who taught
me kindness, patience, and perseverance and
to my late grandmother, who survived six wars but
never lost faith in love, life, and humanity.

TABLE OF CONTENTS

LIST OF FIGURES

LIST OF TABLES

ACKNOWLEDGEMENTS

I would like to express my gratitude to my advisor, Professor Dante A. Simonetti, for his guidance and support throughout my doctoral work. Professor Simonetti is a great mentor who has continually believed in me and trained me to be the researcher I am today. I was fortunate to be the first student to join his research group and learn from him, firsthand, how to build a catalysis research lab from scratch and how to not (accidentally) set it on fire. In the same respect, I would like to thank Professor Panagiotis D. Christofides, Professor Vasilios Manousiouthakis, and Professor Louis Bouchard for graciously accepting to serve on my doctoral committee.

I would like to thank Dr. Tirso Lopez-Ausens for being an excellent colleague and collaborator in many parts of this project. Tirso inspired me to be more focused, organized and detail-oriented in my approach. I would like to also thank my collaborator from New Mexico University, Griffin Canning, for being generous with his time and knowledge. Griffin helped me tackle some of the most challenging and exciting research questions in my work. I would like to thank my collaborators and advisors at the Stanford Synchrotron Radiation Lightsource (SSRL): Dr. Alexey Boubnov, Dr. Adam Hoffman, and Dr. Simon Bare for their support and supervision throughout countless sleepless nights at the beamline and beyond. Working closely with Dr. Bare's group has been a significant and unparalleled contributor to my doctoral training. Additionally, I would like to thank and acknowledge the following individuals who collaborated with me on this project: Professor Philippe Sautet, Dr. Sergey Prikhodko, Dr. Yijin Liu, Kai Zhang, Faisal Alshafei, Luke Minardi, Richa Ghosh, Brian Ko, Zubin Mishra, Nicole Chiang, and Brook Wander.

I would like to thank Mr. William A. Herrera for empowering me and giving me the opportunity to facilitate the High School Summer Research Program (HSSRP), for three

consecutive years, as it has been one of the most meaningful and rewarding experiences I have had at UCLA. I would like to also thank my labmates and peers for their direct and indirect contributions to my research work and journey at UCLA.

I would like to gratefully acknowledge the funding from the Department of Chemical and Biomolecular Engineering and the Office of Equity, Diversity, and Inclusion at UCLA and to the donors of The American Chemical Society Petroleum Research Fund. I would like to also acknowledge the use of the SSRL, SLAC National Accelerator Laboratory, supported by the U.S. Department of Energy (DOE).

I would like to thank my previous mentors during my undergraduate education who have continued to be influential beyond my time at the American University of Sharjah (AUS). I would like to especially thank Professor Oussama M. El-Kadri, an exceptional mentor and role model who was the reason behind me pursuing a double major in chemistry. This decision prepared me for the research work I did during my doctoral work. I would like to also thank Professor Lucia Pappalardo, Professor Ghaleb Al Husaini, and Professor Yousef Salamin for their invaluable guidance and mentorship.

Finally, and most importantly, I am forever grateful for the special people in my life who supported me emotionally throughout this journey: My parents (Salwa and Abdulmajid), my siblings (Belal and Hajar), my partner (Ayman Al-Abdallah), and my friends (Reem Karmouta, Nour Jabaieh, Tina Al-Attar, Hafsa Shurbaji, Anas Al-Anqar, Hawra Salami, Randa Asaad, and my late dear friend Jason Donovan).

Chapter 2 is a version of: Azzam, S.; Simonetti, D. A.; Alshafei, F.; Lopez-Ausens, T.; Minardi, L. Reactive Sorption of Sulfur on Metal Oxides: Applications, Reactor Engineering Descriptions, and Opportunities to Develop Molecular Understanding. In preparation, **2020**.

Chapter 3 is a version of: Azzam, S.; Simonetti, D. A. Linear Driving Force Approximations as Predictive Models for Reactive Sorption. *Energy Technol.* **2019**, 1900718.

Chapter 4 is a version of: Azzam, S. A.; Alshafei, F. H.; López-Ausens, T.; Ghosh, R.; Biswas, A. N.; Sautet, P.; Prikhodko, S.; Simonetti, D. A. Effects of Morphology and Surface Properties of Copper Oxide on the Removal of Hydrogen Sulfide from Gaseous Streams. *Ind. Eng. Chem. Res.* **2019**, *58* (40), 18836–18847.

Chapter 5 is a version of: Hoffman, A. S.; Azzam, S.; Zhang, K.; Xu, Y.; Liu, Y.; Bare, S. R.; Simonetti, D. A. Direct Observation of the Kinetics of Gas–Solid Reactions Using *in Situ* Kinetic and Spectroscopic Techniques. *React. Chem. Eng.* **2018**, *3* (5), 668–675.

Chapter 6 is a version of: Azzam, S.; Boubnov, A.; Hoffman, A.; López-Ausen, T.; Chiang, N.; Canning, G.; Sautet, P.; Bare, S.; Simonetti, D. A. Insights into Copper Sulfide Formation from Cu and S K-edge XAS and DFT studies. *Inorg. Chem.,* submitted, **2020**.

Chapter 7 is a version of: Azzam, S.; boubnov, A.; Hoffman, A. S.; Cannin, G.; Alshafei, F. H.; Ko, B.; Ghosh, R.; Datye, A.; Bare, S. R.; Simonetti, D. A. Lanthanum Induced Weakening of Lattice Copper-Oxygen Bonds Improves Hydrogen Sulfide Capacities of Copper Oxide Adsorbents. In preparation, **2020**.

VITA

2010–2014	Bachelor of Science, Chemical Engineering Department of Chemical Engineering American University of Sharjah
2011–2014	Bachelor of Science, Chemistry Department of Biology, Chemistry and Environmental Sciences American University of Sharjah
2015	Graduation Distinction
2015–2020	Graduate Student Researcher Department of Chemical and Biomolecular Engineering University of California, Los Angeles
2017–2020	Teaching Assistant Department of Chemical and Biomolecular Engineering University of California, Los Angeles

PUBLICATIONS

1. Saeed, H.; Husseini, G.; Yousef, S.; Saif, J.; Al-Asheh, S.; Fara, A.; Azzam, S.; Khawaga, R.; Aidan, A. Microbial Desalination Cell Technology: A Review and a Case Study. *Desalination* **2015**, *359*.
2. Hoffman, A. S.; Azzam, S.; Zhang, K.; Xu, Y.; Liu, Y.; Bare, S. R.; Simonetti, D. A. Direct Observation of the Kinetics of Gas–Solid Reactions Using *in Situ* Kinetic and Spectroscopic Techniques. *React. Chem. Eng.* **2018**, *3* (5), 668–675.
3. Azzam, S. A.; Alshafei, F. H.; López-Ausens, T.; Ghosh, R.; Biswas, A. N.; Sautet, P.; Prikhodko, S.; Simonetti, D. A. Effects of Morphology and Surface Properties of Copper Oxide on the Removal of Hydrogen Sulfide from Gaseous Streams. *Ind. Eng. Chem. Res.* **2019**, *58* (40), 18836–18847.
4. Azzam, S.; Simonetti, D. A. Linear Driving Force Approximations as Predictive Models for Reactive Sorption. *Energy Technol.* **2019**, 1900718.

5. Azzam, S.; Boubnov, A.; Hoffman, A.; López-Ausen, T.; Chiang, N.; Canning, G.; Sautet, P.; Bare, S.; Simonetti, D. A. Insights into Copper Sulfide Formation from Cu and S K-edge XAS and DFT studies. *Inorg. Chem.*, submitted, **2020**.

Chapter 1 | Overview

This dissertation compiles the author's work on unravelling the fundamentals of the reaction between CuO and trace amounts of H_2S through reactive sorption. Chapter 2 of this dissertation covers a literature review of reaction engineering descriptions, materials development approaches, advanced mechanisms characterization, and an in-depth review of density functional theory (DFT) studies that are relevant to the project.

The dissertation work is then organized in an order of descending length scales. At the macro-scale, Chapter 3, assesses the utilization of linear driving force approximations as predictive models for H_2S removal in fixed beds of commercial CuO-based sorbent at different flow conditions, temperatures, total pressures, and inlet hydrogen sulfide concentrations. This study demonstrates that, in the absence of bulk and pore diffusion resistances, linear driving force approximations that are zero order in bulk gas phase concentration but first order in solid phase capacity effectively model contaminant breakthrough curves. The model-deduced sorption rate parameters reflect, predominantly, the reaction and diffusion at reactive interfaces, rather than bulk or pore diffusion.

Zooming in on the micro-scale, Chapter 4 explores the structure-function relationships governing the CuO-H_2S reaction. The effect of different physiochemical properties (microscopic shape, porosity, crystallinity, and purity) on H_2S removal capacity of CuO sorbents is probed using fixed bed experiments at ambient conditions. The study shows that, despite ostensible differences between the various properties of the tested sorbents, a strong linear relationship was recognized between the sorbents' sulfur removal capacity and crystallite size, independent of changes in the materials' microscopic shape and porosity. In addition, the effect of residual carbon on CuO

surfaces is also probed in this study for the first time, showing that amorphous carbon inherently imparted by the use of a polymer (PVP or PEO) or a surfactant (P123) in the synthesis procedure inhibits reaction and deleteriously impacts the H_2S uptake capacity. First principles atomistic simulations were performed to explain which surface oxygen anions are most reactive and supportive to the observations.

Chapter 5 probes the spatial-temporal chemical and structural changes of copper during the sulfidation reaction using advanced synchrotron-based characterization techniques such as X-ray absorption spectroscopy (XAS), and transmission X-ray microscopy (TXM). This study demonstrates that H_2S removal reaction kinetics show similar trends in fixed bed reactors as in 10-20 μm sized particles. However, reaction fronts proceed through the entire diameter of particles heterogeneously, indicating the presence of pore diffusion resistance even at very small length scales. In addition, the study shows that CuO sorbents of similar characteristics exhibit different sulfidation conversion and reaction rate constants. These differences in reaction kinetics and conversion indicate the critical impact of possible atomic scale differences and the formation of different copper sulfide products.

On the atomic scale, Chapter 6, combines *ex-situ* and *in-situ* XAS at the S and Cu K-edges and other characterization techniques to speciate the CuS products formed at different temperatures and from CuO sorbents with different crystallite sizes. This work identifies, unprecedentedly, the initial formation of a distorted CuS layer at the surface of CuO crystals with disulfide groups that have longer Cu-S bonds and higher delocalization of the positive charge of the Cu center into $(S^{-1})_2$. First principles atomistic simulations confirmed the thermodynamic favorability of the formation of surface $(S^{-1})_2$ on both CuO (111) and $(\bar{1}11)$ surfaces, providing further support for the experimental observations.

Chapter 7 branches out to explore the effects of lanthanum (La) additives on the capacity and kinetics of CuO sorbents for the removal of H_2S. La was selected because of its relatively large cationic radius (R_{La}/R_{Cu} = 1.5) compared to the more commonly studied additives such as Zinc, Nickel and Cobalt (R_x/R_{Cu} = 1.0). The results of the study show that two La-CuO sorbents with nominal La/Cu ratio of 1:2 achieved 64% and 85% conversion respectively, compared to 59% conversion achieved by the best performing CuO sample. Advanced multi-edge XAS tests were performed to identify the structural and chemical changes introduced by La that led to the increase in capacity. X-ray absorption near edge structure (XANES) analysis at Cu K-edge suggested more electron-rich Cu species in La-CuO samples, while X-ray absorption fine structure (EXAFS) modelling showed longer second, third and fourth shell single scattering paths. Together, these changes suggest that La weakened Cu-O bonds thereby lowering their barrier for rupture via reaction with H_2S-derived species.

Finally, Chapter 8 summarizes the findings of the dissertation and suggests avenues for the expansion of this work.

Chapter 2 | Background

Reactive sorption involves employing a selective and high-capacity solid substrate that possess preferential affinity towards a targeted molecule and reacting that solid with the general purpose of removing a gaseous contaminant. One industrially and environmentally relevant application is the removal of sulfur-containing contaminants from hydrocarbon streams derived from natural gas processing[1–4] and petroleum refining.[5,6] This purification application is essential to meet product specifications[5] and emissions regulations[3,5,6] and to protect equipment and catalysts.[1,2] Many regenerable adsorbents can remove these contaminants[7] through adsorptive separation where trace amounts (1-1000 ppm-mol) of sulfur compounds (e.g., mercaptans, H_2S, CS_2, COS)[3,5] and elemental mercury (1-2000 μg/Nm^3 ~ 0.1-200 ppb-mol)[4] are picked up from these streams. However, reactive sorption using metal oxide has proven to be superior due to (i) the favorable thermodynamics compared to physisorption resulting in higher purity effluent streams[5] and (ii) the permanent sequestration of contaminants in an environmentally benign form.[1,8] Figure 2-1 shows how COS and H_2S molecules react with metal oxides via different reaction stoichiometries to form stable metal sulfides.[8–10] Each of these reactions is governed by different kinetics.[11,12] Therefore, fundamental knowledge of these reaction paths and their respective kinetics is critical to the efficient use of reactive sorbents in hydrocarbon purification processes.

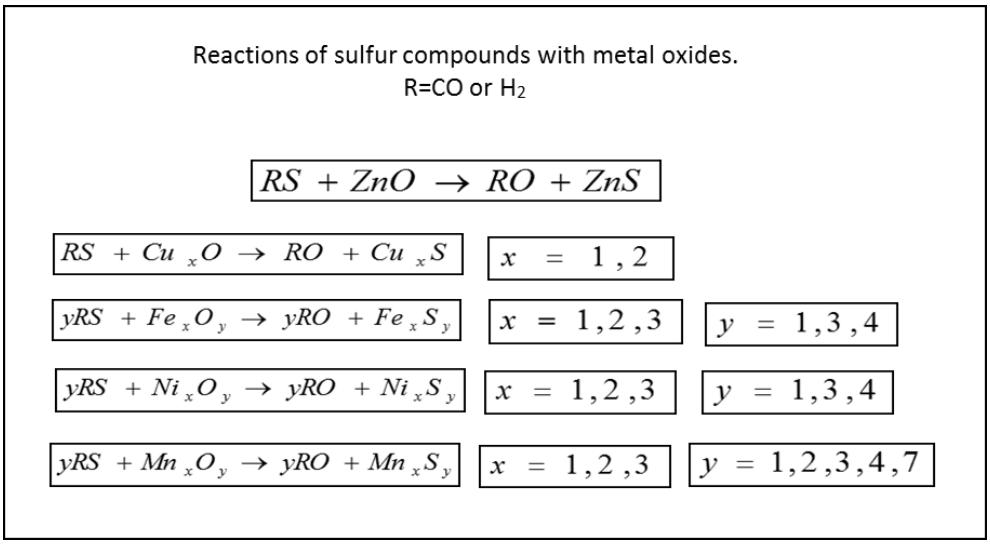

Figure 2-1: Possible reaction stoichiometries for sulfur compounds with different metal oxides.

Several catalyst companies (e.g., UOP, Johnson-Matthey, Axxens, Clariant) sell these materials at very large scale, highlighting the importance of these reactive sorption processes. Nevertheless, despite the maturity of these technologies and the abundance of their applications, these materials still suffer from incomplete conversion of the active phase and high sensitivity to process upsets. This variation in performance between materials is illustrated in the materials development section of this review.

Even though many decades of research have been conducted on these systems, most of the previous work has focused on two areas: reactor engineering models and materials development. In this review, we aim to focus on the work that has been conducted to combine advanced characterization techniques with microkinetic and computational models to probe the fundamentals of these reactions at the molecular level. It is this molecular level of understanding that will be required to advance previous research beyond combinatorial studies of materials and macro-scale reactor engineering models. Indeed, this fundamental knowledge could lead to a

rational framework for designing new materials and to higher-fidelity predictive models for fluid-gas reaction processes that will help overcome reactive adsorption process limitations.

2.1 Reaction Engineering Descriptions

Solid-gas reactions in an industrial setting occur in packed bed reactors where the desired effluent gas is free from sulfur containing compounds. As the solid material becomes saturated the concentration of the sulfur compound increases along the length of the reactor as a function of time until it is measured in the effluent. It is critical to be able to quantify capacity of the solid materials and to predict the breakthrough time.

Two types of experiments are typically run to characterize the solid reactant or sorbent, the first is static thermogravimetric experiments and the second is packed bed breakthrough experiments. The change in mass as a function of time can give insights to the reaction kinetic limited regime and diffusion limited regime. These static experiments can be described with solid models to quantify the kinetic rate constant and diffusivity constant while accounting for structural variations and changes within a material.[13]

Packed bed experiments are modeled with a gas phase transport model, the term for the consumption of the sulfur compound is described by either the aforementioned pellet-scale reaction model[14,15] or the linear driving force model.[16] The pellet-scale model was referred to above and will be discussed in detail below, the linear driving force model is a mass transfer model where the driving force is the difference between the equilibrium and the average adsorbate concentration. In the following sections we will discuss the solid reactant model, the reactor scale model, and finally the coupling of models with experiments and model limitations.

2.1.1 Pellet scale models

The backbone of complex grain reaction models is the sharp interface model where there is a fast surface reaction step and a slower diffusion-controlled reaction step as the reaction progresses to the center of a grain. Some research has used the sharp grain model to describe a very low surface area zinc titante, ~2m^2 g^{-1}, react with H_2S. The sharp grain model used by, Huang et al., accurately captured the zinc titanate conversion as a function of time and observed the expected temperature dependence of the parameter estimate of diffusivity.[17] The sharp interface model can be made more complex by including temperature gradients due to heat of reaction and structural changes due to the solid reaction.

Grain or distributed pore models are more realistic models for many processes where an individual pellet is composed of many grains having a tortuous pore structure. Each individual grain or surface element is treated the same as the sharp interface model where the surface reaction is fast and there is an unreacted core of solid reactant beneath the surface. Pore structure is included in these models, so the sharp interface includes surfaces inside of the pellet that the gas must diffuse to. Precise knowledge of the internal pore structure is typically poorly understood, so models have used different methods to describe them. There are various pore models from single pore,[18] random pore,[19,20] and distributed pore models.[21] Further, both pore and grain models are easily made more complex by allowing for the pore structure change as a function of conversion of the solid material due to changes in the molar volume of the solid[21] or accounting for changes in temperature due to heat of reaction.[13] Due to the more realistic nature of the grain and pore models, they are typically used to describe desulfurization for static experiments.

Assumptions typically made for solid reaction modeling for simplicity include assuming the reaction order,[22] gas-solid mass transfer resistance is negligible,[23] gas concentration at each grain is uniform,[23] and/or no pore creation or clogging[19].

Bhatia and Perlmutter applied the random pore model they developed[19,20] to the reaction of SO_2 with limestone (CaO).[24] Equation 1 and Equation 2 are both dimensionless and they describe the conversion of mass with surface reaction and diffusion.

$$\frac{1}{\eta^2}\frac{\partial}{\partial\eta}\left(D_e^*\eta^2\frac{\partial C^*}{\partial\eta}\right)=\phi^2\frac{dX}{d\tau} \quad (1)$$

$$\frac{dX}{d\tau}=\frac{C^*(1-X)\sqrt{1-\psi ln(1-X)}}{1+\frac{\beta Z}{\psi}[\sqrt{1-\psi ln(1-X)}-1]} \quad (2)$$

A variety of additional equations and material data[24] are necessary to describe the solid surface such as surface area, pore length, pore structure, modified Thiele modulus, etc. Bhatia and Perlmutter used data from Hartman and Coughlin[23] and Borgwardt[25] to model with the random pore model, which resulted in accurate fits to both data sets and resulted in parameter estimates for reaction rate constants and diffusivity from the model fit. Additionally, the parameter estimates for the reaction rate constant and product layer diffusivities fit the expected relationship as a function of temperature.

Experimentally, material information must be characterized with N_2 physisorption either to describe the average grain radius for the grain model or to determine the internal pore structure for the distributed pore model. Equations developed by Sohn and Szekely[26] can be used to estimate the average particle radius for various grain geometries. Equations developed by Bhatia and Perlmutter[19] can be used to estimate structural parameters for the distributed pore model. Most of the other information necessary to use the grain model or random pore model is available based on experimental conditions (i.e. temperature) or a literature review (i.e. change in molar volume).

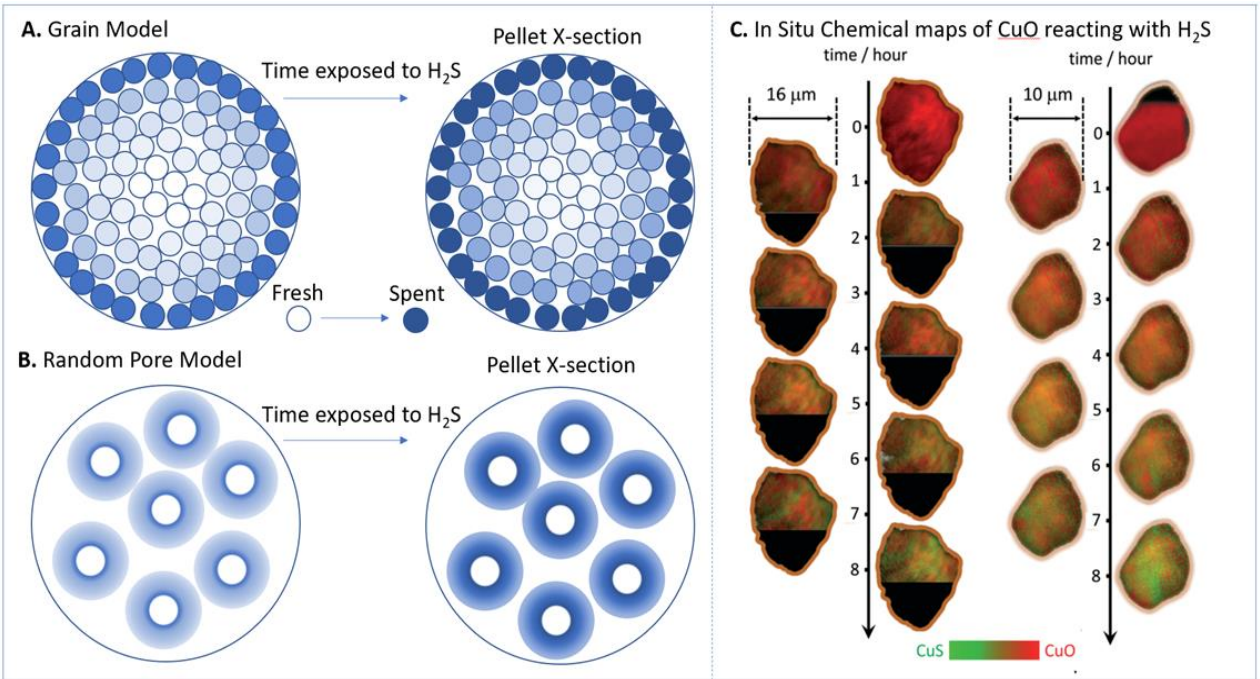

Figure 2-2: Model representations of an individual pellet undergoing sulfidation for A. Grain model and B. Random pore model adapted from Ramachandran et al.[27] and Bhatia et al.[19] compared to C. In situ mapping of CuO particles undergoing sulfidation figure from Hoffman et al..[28]

2.1.2 Reactor models

One of the most common models for packed bed reactors where a contaminant is adsorbed or there is reactive sorption is a 1-D Plug Flow Reactor (PFR) model. Bohart[29], Cooper[30]and Yoshida[31] each developed dimensionless forms of the 1-D PFR model for chlorine contaminant removal, ion exchange columns, and generic adsorption with square breakthrough curves, respectively. Each of these models used a linear driving force to describe contaminant consumption but used different expressions for concentration as a function of time. There are two parameters in these models the maximum capacity of the sorbent material and the sorption rate parameter. The maximum capacity (concentration) of the contaminant on the solid is determined by thermodynamics (adsorption isotherms) or stoichiometry (reactive sorption). Maximum capacity is determined by calculating the total amount adsorbed when the material is fully saturated by a mass balance. The adsorption rate parameter is then related to adsorption resistance to the

bulk diffusion, diffusion in solid pores, and reaction and diffusion on the surface. The method of using a 1-D PFR with LDF was recently applied to H_2S breakthrough experiments with a CuO bed.[16]

The 1-D PFR model can be made more complex by adding an axial dispersion term[32] or using a pellet/grain model if there is a bulk solid reaction. The governing equations of a recent model developed by Parandin and Rashidi, recently studied zinc oxide reacting with H_2S and developed a model that combined a 1-D PFR with axial dispersion model with the grain model.[15]

$$D_d \frac{\delta^2 C_b}{\delta Z_r^2} - U_s \frac{\delta C_b}{\delta Z_r} - k_m a_s \left(C_b - C_p\right) = \varepsilon_p \frac{\delta C_b}{\delta t} \qquad (3)$$

Equation 3 is the mass balance over the bed, where C_b and C_p is the bulk and pellet concentration, respectively. D_d is the axial dispersion coefficient, U_s is the superficial velocity, km is the convective mass transfer coefficient, a_s is the solid surface area per unit volume, and ε_P is the bed porosity. The independent parameters are: Z_r the distance from the start of the bed and t is the time.

Equation 3 is the fundamental equation for each of the 1-D PFR models, with boundary conditions defined as:

$$D_d \frac{\delta C_b}{\delta Z_r} = U_s (C_b - C_{in}), Z_r = 0 \qquad (4)$$

$$\frac{\delta C_b}{\delta Z_r} = 0, Z_r = L_b \qquad (5)$$

where C_{in} is the concentration of the inlet gas and L_b is the length of the bed. The pellet mass balance was based on earlier work by Hartman and Coughlin,[23] defined as follows:

$$\frac{1}{r}\frac{\delta}{\delta r}\left(rD_e\frac{\delta C_p}{\delta r}\right)-\frac{3k_r(1-\varepsilon_p)}{r_g}\left(\frac{r_c}{r_g}\right)^2 C_p=\varepsilon_p\frac{\delta C_b}{\delta t} \qquad (6)$$

where r_c and r_g are the radial position of the unreacted core and the radius of the particles in the pellet. k_r and D_e are the reaction rate and effective diffusion coefficient of the gas through the pellet.

Work by Knox et al.[32] combined the experimental study of water and CO_2 breakthrough curves in a packed bed reactor (Zeolite 5A) with a model of 1-D axially dispersed PFR with LDF mass transfer coefficient. This work found that experimental systems must satisfy the plug flow condition to have accurate adsorbate/adsorbent mass transfer information. The only way to verify that this condition is satisfied is by comparing the breakthrough curves with *in situ* data along that axis center.

2.2 Materials development approach

A variety of adsorbents such as, metal oxides (supported and unsupported),[10,12,33–52] zeolites (aluminosilicates and all-silica),[53–62] metal-organic frameworks (MOFs),[63–70] carbons,[71–76] and composite materials[69,77–81] have been used and reported on in the literature for H_2S capture from gas mixtures containing CH_4, CO, CO_2, N_2, H_2, and/or H_2O. This large body of literature, however, is beyond the scope of this review, and so in this section, we focus on unsupported metal oxide sorbents with emphasis on oxide materials that operate at low to moderate temperatures (25-500 ^oC). Also, to avoid overlap with[34] a recent review which presents on new materials development for various H_2S adsorbents (e.g., ionic liquids, metal oxides, metals, metal-organic frameworks, aluminosilicates, etc.), this section was kept intentionally short, albeit here we try to expand on this subject as well as highlight the need for fundamental understanding for rationale

materials design. Readers interested in metal oxides for high temperature (> 600 ^{o}C) H_2S removal [33–35] or zeolites[34,82] may refer to the cited reviews.

In 1976, Westmoreland and Harrison[12] conducted a pioneering thermodynamics study, screening the high-temperature (400-1200 ^{o}C) desulfurization potential of 28 solids comprising primarily of metal oxides. The authors used a computational free energy minimization method to estimate equilibrium sulfur removal and determine solid compound stability. Eleven candidate solids based upon the metals Fe, Zn, Mo, Mn, V, Ca, Sr, Ba, Co, Cu, and W showed thermodynamic feasibility for high-temperature desulfurization of low-Btu gas (i.e., at least 95% desulfurization and solid stability). Much of the research conducted to date on these metal oxides and others are presumed to remove H_2S according to the general reaction ($M_xO_{y\,(s)} + yH_2S_{\,(g)} \leftrightarrow M_xS_y + yH_2O_{\,(g)}$, where M denotes a suitable metal). Of the metals proposed by Westmoreland and Harrison, Zn, Mg, Cu, Fe, and rare earth sorbents are among the most promising and most extensively investigated. Table A-1 and A-2 show selected results of pure and doped-metal oxides at various experimental conditions. Table A-1 comprises primarily of zinc- and copper oxide-based sorbents, which are the most promising oxides for low- to moderate- temperature H_2S removal,[10,33,34] whereas Table A-2 comprises of other metal oxides that have been less investigated. The majority of the metals in Table A-2 are drawn from a screening study performed at room temperature on simple oxides (Ag, Co, Ni, Ca, Mn, and Sn).[10]

Zinc-based sorbents have been extensively used in the desulfurization of natural gas feedstock typically in the 300 – 400 ^{o}C range. Early work on ZnO dealt with trying to understand the effects of product layer diffusion, pore diffusion, and gas-film diffusion on the sulfidation kinetics.[83] Gibson and Harrison,[83] for instance, attributed the low utilization of ZnO at temperature below 600 ^{o}C to grain diffusion resistance and formation of a dense sulfide layer. Skrzypski et al.[84]

later performed a study on the sulfidation of pure and metal-doped ZnO nanostructure sorbents, focusing in their study on the performance of ZnO sorbents at temperatures between 200 and 350 ^{o}C. The authors reported that the adsorption of H_2S by ZnO is stoichiometric at 350 ^{o}C but falls off rapidly as the temperature is reduced due to slower reaction kinetics. Although ZnO has a high theoretical and experimental H_2S sorption capacity at ~350 ^{o}C when compared to other oxides, ZnO, at elevated temperatures, can be reduced in syngas atmosphere. Therefore, a significant part of research on ZnO as well as on other promising oxides, has gravitated towards doping the desired metal oxide with other inert or active metallic species. In most screening studies, the choice of dopant is rather arbitrary and is based on trial and error, but the goal behind doping is to improve the sorbent's properties in one or more of these areas: sorption capacity and selectivity, sorption kinetics, stability, structural regenerability upon repeated sulfidation-regeneration cycling, chemical (e.g., crystallite size) and mechanical properties (e.g., low attribution).[33–35]

Skrzypski et al.[84] demonstrated that the reactivity of nanostructured ZnO-based sorbents at low temperatures can be further enhanced by doping. Specifically, it was shown that the addition of Fe, Mn, Ni, Co, and/or Cu oxides to ZnO allows an increase in the H_2S breakthrough capacity of the sorbent at room or moderate temperatures.[33,84–89] The authors found a 6-fold increase in capacity at 200 ^{o}C by doping 6 mol% Cu. XPS of the Cu-Zn-O sample showed a Cu $2p_{3/2}$ peak at 933.5 eV, characteristic of Cu^{2+} surrounded by oxygen. After partial sulfidation, this peak shifted to lower energy, indicating the appearance of Cu^{+}. Using in-situ synchrotron XRD and TEM to analyze the sulfidation mechanism, the authors suggested an inward growth mechanism where S^{2-} anions diffuse from the external surface to the internal oxide-sulfide interface and exchange with O^{2-} anions. This change in mechanism was attributed to the presence of sulfur vacancies in the zinc sulfide layer due to the replacement of Zn^{2+} by Cu^{+}.[90]

In spite of the promising properties of some metal-doped oxide nanoparticles, like the one described in the previous paragraph and shown in Table A-1 and A-2, detailed kinetic studies of the sulfidation of those sorbent systems are rarely available in the literature, and as such, the origin of the improvement observed in reactivity is unclear. Often, the justification of improved metal dispersion in the doped solids is invoked to explain a better surface reactivity; however, it's not clear how that translates to an increase in the bulk metal oxide reactivity.

Baird et al.[91] reported on the hydrogen sulfide sorption capacity of series of cobalt-zinc oxides at room temperature. The authors reported a 91% conversion for Co_3O_4, however, Xue et al.[10] reported only a 1% conversion for a similar sorbent. These studies, as well as a few others in Table A-1 and A-2, suggest at the possible effect of synthesis recipe on particle and crystallite size, morphology, as well as surface area, which in turn may affect the H_2S breakthrough capacity. In fact, there are several reports exploring desulfurization using different ZnO morphologies.[92–95] Our group recently reported on the chemical reaction of CuO nanoparticles with hydrogen sulfide to form copper sulfide by investigating the effects of microscopic shape, crystallinity and purity.[37] Specifically, we synthesized materials, which had different morphologies (flowerlike, nanobelt-like, petal-like, spherical, and fiber-like) and physiochemical-chemical properties (crystallite size, surface area, and pore volume), and tested them in fixed-bed experiments at room temperature and 1 atm. Despite ostensible differences between the various properties of the tested sorbents, a strong linear relationship was recognized between the sorbents' sulfur removal capacity and crystallite size, independent of changes in the materials' microscopic shape and porosity. What's ambiguous is why the effect of surface area, for instance, is absent in one study such as in our work but present in another such as, in the work of Baird et al.,[96] where transition metals co-precipitated with ZnO produced mixed oxides of higher surface areas, which performed differently. Moreover, Jiang et

al.[97] studied Cu-Zn and Cu-Zn-Al mixed metal oxides prepared via co-precipitation and multi-precipitation. Better aluminum dispersion resulted in smaller crystallite sizes and higher specific surface areas in the samples that contained higher levels of Al. H_2S breakthrough capacities also improved as a result of reducing the thickness of the sulfide shell by effectively reducing the diffusion path length.

Certainly, quantification of improvements in performance due to physiochemical properties such as, surface area, crystallite size, and pore volume under similar reaction conditions at different temperatures for various dopants would be tremendously useful. While it is hard to draw head-to-head comparisons from the independent studies shown in Table A-1 and A-2 due to differences in feed compositions, reactor type and volume, definitions of breakthrough concentration, and gas velocities, the data in those tables aim to highlight (i) the different knobs that can be turned that may influence H_2S capacity, particularly at low to moderate temperatures, and (ii) promising sorbent materials that require further investigation and characterization.

2.3 Advanced characterization for mechanism and active site identification

In the chemical industry, metal oxide-based materials have been used in the past years for purification of feedstocks at temperatures ranging between 350 and 500°C.[98] However, in some other applications, requiring sulfur removal, moderate temperatures must be used (200-300°C).[9] At these moderate conditions, the reactivity of the sorbents (such as ZnO and CuO) is insufficient. To rationally design and assess metal oxide-based sorbents, the reactive sorption process must be understood clearly.

ZnO is a commonly used sulfur sorbent in the industry, despite the mechanism of the entire process not being fully comprehended. It is accepted that the drop in reactivity of this metal oxide

at moderate and low temperatures is the result of a ZnS layer being formed over the oxide, which passivates the rest of the oxide material and keeps it from reacting further with H_2S due to the diffusional barrier of the sulfide layer. Even though the first stage of the process (the surface reaction) is quick, the second step (bulk reaction) is much slower.[99] In principle, smaller nanoparticles exposing more atoms on the surface should be preferred so that a greater fraction of the material reacts in the first stage, and indeed some improvement has been observed.[100] However, even in small nanoparticles, a relatively large fraction of the oxide remains unreacted, as seen in Figure 2-3, resulting in a much lower conversion than the theoretical stoichiometric capacity.

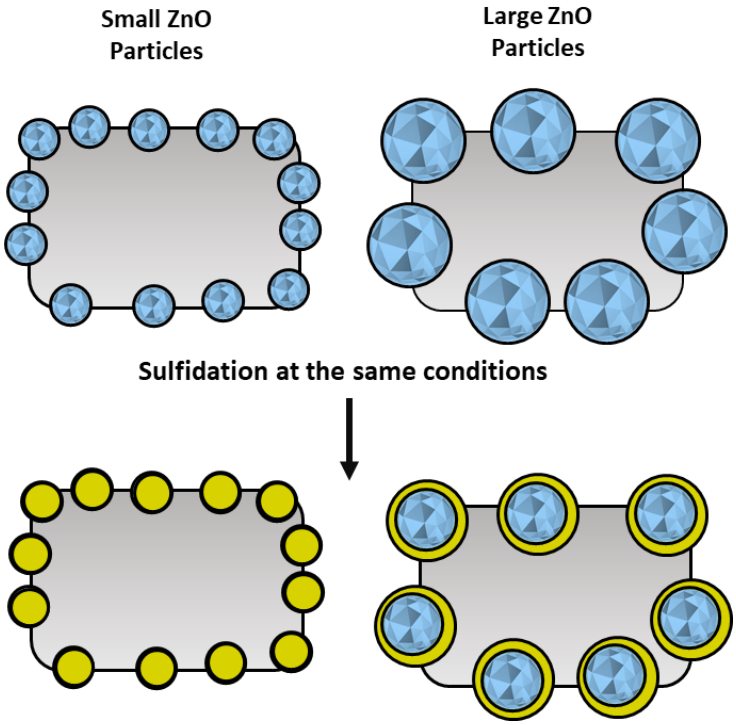

Figure 2-3: Decrease in sulfur removal efficiency due to formation of a ZnS outer layer that impedes access to inner ZnO.

In order to increase the removal capacity of oxide-based materials, one must achieve a complete sulfidation of the bulk material, which means that diffusion through the bulk of the sulfide layer (e.g. ZnS), must be accelerated. This can be done if the process is properly understood

so that rational procedures can be developed to increase the efficiency of the process. To this regard, Bezverkhyy et al.,[90] used advanced characterization in order to shed light on the process of ZnO sulfidation at moderate temperatures. They studied the sulfidation of pure and Cu-doped ZnO nanoparticles at 250-350°C by H_2S, using electron microscopy (TEM) and in-situ X-ray powder diffraction (XRD) to characterize, in detail, the microstructure of the ZnS phase formed after partial and complete sulfidation. The TEM images before and after sulfidation showed ZnO particles with a compact shell of ZnS over them, which was physically separated from the oxide core by voids at the ZnO/ZnS interface. Interestingly, sulfidation at 350°C revealed void formation also, but in this case such voids were of a much lower regularity in shape and size. The formation of voids was attributed to a consequence of the Kirkendall effect,[101] while the differences in them as a function of the temperature was attributed to lower stability of the voids at higher temperatures.

The authors also performed *in situ* XRD on pure and Cu-doped ZnO. They found the absence of a noticeable variation in the crystallite size, attributed to a small width of the reaction front. Also, when comparing the process on these two materials they found that: 1) nearly a pure sphalerite phase (ZnS) was formed in both of them and 2) the width of the Bragg peaks of ZnS decreased sharply with time, indicating that the formed ZnS crystallites grew in size. Specifically, Cu-doped ZnS showed a rapid growth of these ZnS crystallites, showing that the mobility of atoms in both materials is quite different. The in situ XRD spectra thus revealed that in Cu-doped materials the mobility of sulfide anions is much higher than in pure ZnO, which led to a faster growth of ZnS crystallites. Such acceleration of crystallite growth rate was attributed to the presence of anionic vacancies formed through Cu^{1+} charge compensation.[102,103] The authors concluded that the presence of anionic vacancies, probably located at the grain boundaries enabled

a strong acceleration of sulfur diffusion, making the inward growth of ZnS more rapid than the outward one observed for pure ZnO.

Another example of the importance of characterization in shedding light on the identification of active sites and the mechanism at molecular level is the work by Samokhvalov et al.[9] They studied Cu-doped ZnO particles supported on SiO_2 for reactive adsorption of H_2S at room temperature using X-ray diffraction (XRD), Brunauer-Emmett-Teller (BET) surface area analysis, electron spin resonance (ESR), ultraviolet–visible (UV–vis) and diffuse reflectance spectroscopy (DRS), and computational modelling using density functional theory (DFT). Their findings showed that the structural characteristics of ZnO/SiO_2 sorbents did not significantly change when Cu was added as a promoter and yet, sulfur uptake increased significantly.

XRD data showed that at ZnO percentages above 21%, the sorbent exhibits large crystals whose desulfurization behavior corresponded to a 'plateau' in sulfur uptake capacity. XRD data also showed the presence of supported ZnO in a nano-dispersed form with a crystalline size less than ~40Å. No additional lines due to copper compounds were found, indicating a high degree of dispersion of Cu in the sorbent. To further characterize the Cu promoter, they used ESR, a highly sensitive technique which allows the detection and speciation of various localizations and chemical states of the same minor component (Cu) in composite materials. Using this technique, they found that no Cu^0 species existed, and Cu was in the materials as Cu^{2+}. More information about the atomic-level structure of these Cu^{2+} promoter sites was found using UV-vis DRS. This technique showed that Cu^{2+} cations were in an octahedral coordination environment. It also showed a charge transfer occurred between O 2*p* orbitals and Cu 3*d* orbitals. Finally, all these data were combined with a computational DFT study of a model surface of the sorbent, which showed a distorted tetrahedral geometry of Cu^{2+} surface sites, which was consistent with the findings by ESR and

UV-Vis DRS, indicating the presence of surface Cu^{2+} sites featuring a octahedral symmetry with tetragonal distortions, rather than pure tetrahedral sites. This multidisciplinary study concluded that Cu^{2+} acted as promoter by providing surface active sites which showed a higher affinity for H_2S compared to Zn^{2+} sites. Dhage et al. concluded that on a ZnO surface with some Zn^{2+} sites substituted with Cu^{2+}, there can be a displacement of H_2O with H_2S at the Cu^{2+} surface sites which explains the promoter effect of Cu^{2+} sites.

In another work, Samokhvalov et al. performed a multi-characterization study to shed light on the active sites of sulfur sorbent.[8] They studied Ag/TiO_2 sorbents for removal of desulfurization-refractive polycyclic aromatic sulfur heterocycles (PASHs) from liquid hydrocarbon fuels, with the objective of identifying active sites for the process. They found that in this kind of sorbents with this specific synthesis procedure, XPS measurements showed that Ag was present mainly as an Ag oxide, with minor concentrations existing as Ag^{2+} (around 0.1% of total Ag). Furthermore, ESR indicated that the majority of Ag is present in the diamagnetic form Ag^{+1}. These findings were confirmed by XRD and UV-Vis spectroscopy, which found no optical adsorption in the relevant spectral UV-Vis range and no XRD patterns of metallic Ag. Further thermodynamic considerations according to the $Ag\text{-}O_2\text{-}N_2$ phase diagram supported these findings. They also measured surface areas by O_2 chemisorption at 170°C and N_2 adsorption. The Ag specific area they found was 7-14 m^2/g, and 114-58 m^2/g for the total surface area. The data indicated that Ag oxide was highly dispersed on the TiO_2 support, with the average crystallite size being 24-69Å depending on the Ag content. Finally, with all these findings, the authors suggested that based on the oxidation state of the active Ag component of the Ag/Titania sorbent, the adsorption of thiophene and the PASHs at room temperature could proceed via the non-reactive

strong adsorption, without scission of the C–S bond, as what happens with sorbents containing Ni^{2+},[104] and contrary to those with transition and noble metals in metallic state.[40]

2.4 DFT and quantum chemistry utility in describing reactive sorption processes

As already shown in this work, reactive sorption involves contacting a fluid with a solid phase to remove a specific molecule from the fluid via chemical reaction. H_2S reacts with metal oxides to produce a metal sulfide and water. COS and CS_2 can react with a metal oxide to produce a metal sulfide and CO_2 or undergo hydrolysis to H_2S in the presence of H_2O with subsequent scavenging of the H_2S by the metal oxide. Reactive sorption of mercaptans is more complex because these molecules can undergo catalytic reactions to form larger oligomers, desulfurization reactions to form alkenes and H_2S, oxidation reactions to form disulfides, water, and a reduced metal oxide, or chemical reaction to form copper thiolates or copper sulfides. For this reason, most of the scientific literature regarding computational studies on reactive sorption of sulfur contaminants has been restricted to the simple molecule of H_2S, with few exceptions such as SO_2 or thiophene. Such literature, for the most part, have focused on studying the interaction between metal oxide surfaces with the concomitant molecular or dissociative adsorptions. Many of them have studied subsequent steps of dissociative adsorption of H_2S resulting in adsorbed S and OH groups on the surface, while other works have gone further exploring surface reactions of these fragment eventually yielding water or H_2.

Most of the studies use Density Functional Theory (DFT)[105,106] as the computational method of choice, thanks to its accuracy at a reasonable computational cost. It is an ab initio quantum chemical technique nowadays considered as the standard method for calculating energies, determining reaction pathways and modelling geometries of reactive surface sites.[107] This section of the review focuses on the computation work done on metal oxides only, Figure 2-4 and Table

A-3, leaving out the studies involving more complex species such as molecular clusters of metal oxide ions.[108]

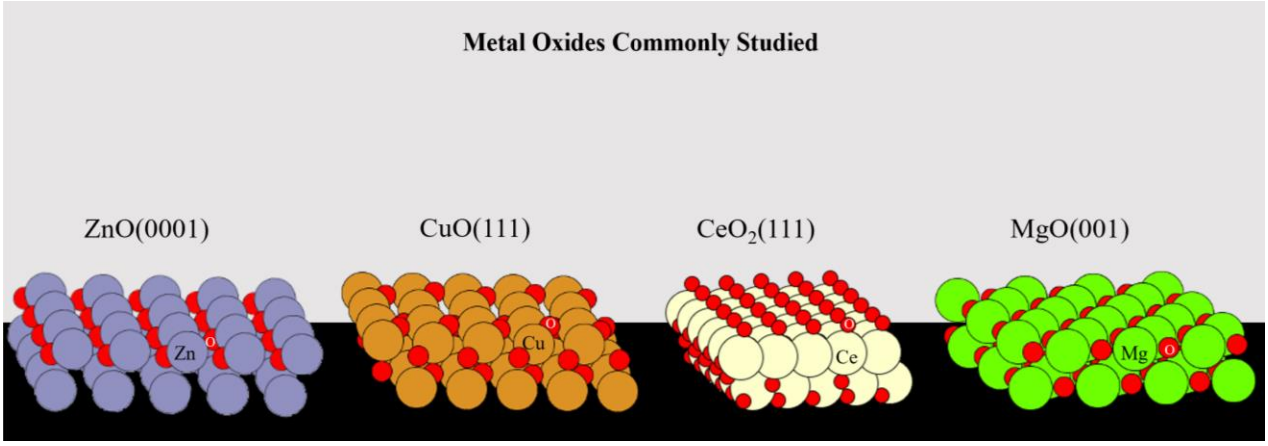

Figure 2-4: Model structure of four metal oxide surfaces commonly studied. They are ZnO(0001), CuO(111), CeO_2 (111), and MgO(001), in order of most to least discussed in this review.

2.4.1 DFT computational studies for the sulfidation of ZnO-based sorbents

As previously stated, ZnO is one of the most widely used materials for removal of sulfur compounds from gaseous streams. Its major advantages are the high sulfur adsorption capacity and the favorable thermodynamics of the sulfurization reaction.[109] Recent interest has focused on low-temperature sulfur adsorbents based in ZnO and operate in the range of 25-100°C,[110] since temporal deactivation of high-temperature desulfurization sorbents occurs partly due to the destruction of their 3D structure. Similar to the wealth of experimental work carried out on ZnO sorbents, most of the computational studies focus on ZnO-based sorbents too.

Early computational studies on ZnO sorbents date back to the late 90s, such as the one carried out by Casarin et al..[111] They conducted a DFT study focused on the chemisorption of H_2S on ZnO (0001) and (10-10) crystallographic surfaces. Using the so-called Local-density Approximation (LDA)[112] coupled with a molecular-cluster approach, they simulated ZnO surfaces using a $Zn_{22}O_{22}$ cluster for the (0001) and a $Zn_{18}O_{18}$ one for the (10-10) surface, onto which they

adsorbed H_2S. They observed that molecular adsorption is favored over dissociative adsorption yielding SH and OH adspecies for the (0001) surface (133 vs 28 kJ/mol). However, they observed the opposite case for the (10-10) which favors the dissociative adsorption (152 vs 248 kJ/mol for molecular vs dissociative adsorption).

Rodriguez et al. also performed DFT studies on (0001) ZnO surfaces.[113] Using the Generalized Gradient Approach (GGA)[114] and periodically repeating slabs to model continuous ZnO surfaces,[115] they investigated the adsorption and decomposition of H_2S molecules. They found that strong bonding occurred between H_2S and S-containing dissociated species and the reactive surface. The bonding energies of the adsorbates followed the sequence: H_2S (-84 kJ/mol) < HS (-152 kJ/mol) < S (-256 kJ/mol). They also tested the influence of surface coverage and found it proportional to the adsorption energies (-256 kJ/mol at 0.25 monolayer vs. -236 kJ/mol at 0.50 monolayer). Additionally, they observed how the smaller degree of ionicity of ZnO compared to other metal oxides such as MgO leads to larger electron densities around Zn atoms which enhances their reactivity towards S-containing molecules.

It should be noted that while some studies focused on the polar Zn-terminated (0001) surface[111,113,116], since it is one of the simplest ZnO surfaces, the (1010) surface is important as well because of its thermodynamic stability and, even more importantly, because it was found experimentally to dominate ZnO nanoparticles and powders.[117] To this regard, Wang et al.[118] studied the (10-10) surface. They modelled not just the dissociative adsorption of H_2S and formation of adspecies, but also further steps involving a proton hopping processes which could yield either molecular H_2 or water. Their calculations were carried out using GGA-DFT with the PW91[119] exchange-correlation function and a double-numeric quality basis set with polarization functions (DNP), being the basis set comparable to that of Gaussian 6-31G**. In a similar way to

the aforementioned work of Rodriguez et al.[113], they found a preferential dissociative adsorption of H_2S. As for adsorbed species, they found that both SH and S adspecies have a tendency towards bridge-like coordination with two Zn atoms, whereas hydrogen atoms prefer one-fold coordinated adsorption on O-top sites. Regarding the reaction pathway yielding a water molecule (coming from the proton hop on one hydroxyl to another), it was found both kinetically and thermodynamically more favorable than the one yielding hydrogen ($E_{activation}$= 319 (H_2O) vs. 421 (H_2) kJ/mol, $E_{reaction}$ = 166 (H_2O) vs. 220 (H_2) kJ/mol).

Goclon et al. also studied the (10-10) ZnO surface at the DFT level using the Perdew-Burke-Ernzerhof (PBE)[120] exchange-correlation functional together with a planewave basis set and Vanderbilt ultrasoft pseudopotentials.[121] In this work they also the so-called Hubbard-U method for a more accurate description of Zn 3*d* electronic states.[122,123] Again, they found a preference for H_2S towards dissociative adsorption. They found essentially no activation barrier for the first S-H bond cleavage (yielding SH and OH groups on the surface), whereas they observed an activation energy of 48 kJ/mol for the second one (yielding adsorbed S and two OH groups). They also found preference of bridge-mode adsorption for surface species. However, upon increased surface coverage, SH groups shifted to single-coordinated environments due to stronger repulsion between neighboring molecules.

Another ZnO-related study was carried by Dhage et al. .[109] In a multidisciplinary work involving characterization techniques and DFT studies, they investigated the H_2S adsorption mechanism of Cu-promoted ZnO nanoparticles supported on SiO_2. They employed the hybrid DFT method B3LYP[124,125] together with the LANL1MB basis set for geometry optimization and the 6-31G(d) for refined energies. They used quantum mechanical slab models consisting of $Zn_{37}O_{37}$ $CuZn_{37}O_{37}$ to simulate ZnO/SiO_2 desulfurization sorbents and investigated the dissociative

adsorption of H_2S and S-H bond cleavages on the surface to yield an adsorbed S atom and two hydroxyl groups. In the $CuZn_{37}O_{37}$ model they tested the Cu atom as the active site for adsorption of a H_2S molecule and then compared it with adsorption on a Zn center on the $Zn_{37}O_{37}$ to account for the effect of Cu. They found that the activation barrier for the first S-H bond cleavage ($H_2S \rightarrow SH + H$) is similar on both pure and Cu-promoted ZnO models. However, the barrier for the second S-H bond cleavage was found to be notably lower (140 kJ/mol difference) for Cu-promoted ZnO. The easier reduction of $Cu^{2+} \rightarrow Cu^{+}$ compared to $Zn^{2+} \rightarrow Zn^{+}$ facilitates the migration. They concluded that when a copper atom replaces a zinc atom on the ZnO surface, the reaction is driven to complete dehydrogenation of H_2S by the high stability of the Cu-S bond.

Finally, in the case of ZnO, it is worth mentioning the computational work by Wang et al., in which he studied the regeneration process of ZnS back to ZnO.[118] This is paramount because a good desulfurizer must exhibit not only high affinity towards sulfur but also must be able to be converted back from the sulfide to the oxide form for subsequent sequestration cycles.[129] Following the regeneration reaction with molecular oxygen: $ZnS + 3/2\ O_2 \rightarrow ZnO + SO_2$, Wang's group studied via DFT GGA level and the PW91 exchange-correlation functional the reaction of S adatoms on the surface with O_2, producing SO_2. They found that the process had two elementary steps (adsorption of S and O_2, and bonds rearrangements to form adsorbed SO_2 on the surface) and that the activation energy for the rate limiting step was just 36.79 kJ/mol, meaning that sulfide ZnO surfaces could be regenerated relatively easily. They tested as well reduced (10-10) surfaces and found they were regenerable as well, with an activation energy of 29.43 kJ/mol.

2.4.2 DFT computational studies for the sulfidation of CuO-based sorbents

CuO sorbents, which are the focus of this dissertation work, are known for their high efficiency in sulfur removal.[130,131] Thermodynamics suggest that lower equilibrium levels of H_2S can be achieved with CuO compared to Fe_2O_3 and CaO at temperatures below 800°C.[132] Indeed, experimental results by Jiang et al.[133] on mixed Cu-Zn and Cu-Zn-Al materials showed that Cu-rich sorbents are more suitable than Zn-rich ones, mainly because of the faster sulfidation rate of CuO compared to ZnO.

Computational studies on sulfur removal using CuO have focused on the (111) surface as it is the most stable one, i.e. lower surface free energy,[134] and because it is found experimentally.[37] To this regard, recent studies such as those Sun et al.[135] and Zhang et al.[136] investigated the dissociative adsorption of H_2S on this surface. For the former, they investigated the sequential abstraction of hydrogen atoms from H_2S until the transformation to elemental sulfur bonded to surface copper atoms, similar to the computational work on other metal oxides. Sun et al. used the GGA approach within DFT with the PW91 exchange-correlation functional together with double numerical basis with polarization functions (DNP) and effective core potentials for the inner electrons of Cu.[137] Since DFT computations do not take formal van der Waals dispersion forces into account, they used a DFT-D correction to account for them. A 3x2 supercell slab was used to model the CuO (111) surface. There, they found that upon dissociative adsorption of H_2S the most stable configurations for SH and S adspecies is a bridge mode with two 4-fold coordinated Cu atoms (labelled as Cu_{sub}), with H atoms from H_2S adsorbing preferentially on surface O atoms with a 3-fold coordination. In addition, they observed that the activation energies for the dehydrogenation process of H_2S exhibited 2.42 and 23.10 kJ/mol for the first ($H_2S \rightarrow SH$) and second ($SH \rightarrow S$) dehydrogenation steps respectively, which indicates that the dissociative

adsorption of H_2S is most likely to occur on low-coordinated O atoms. Figure 2-5 illustrates the 6-step sulfidation mechanism.

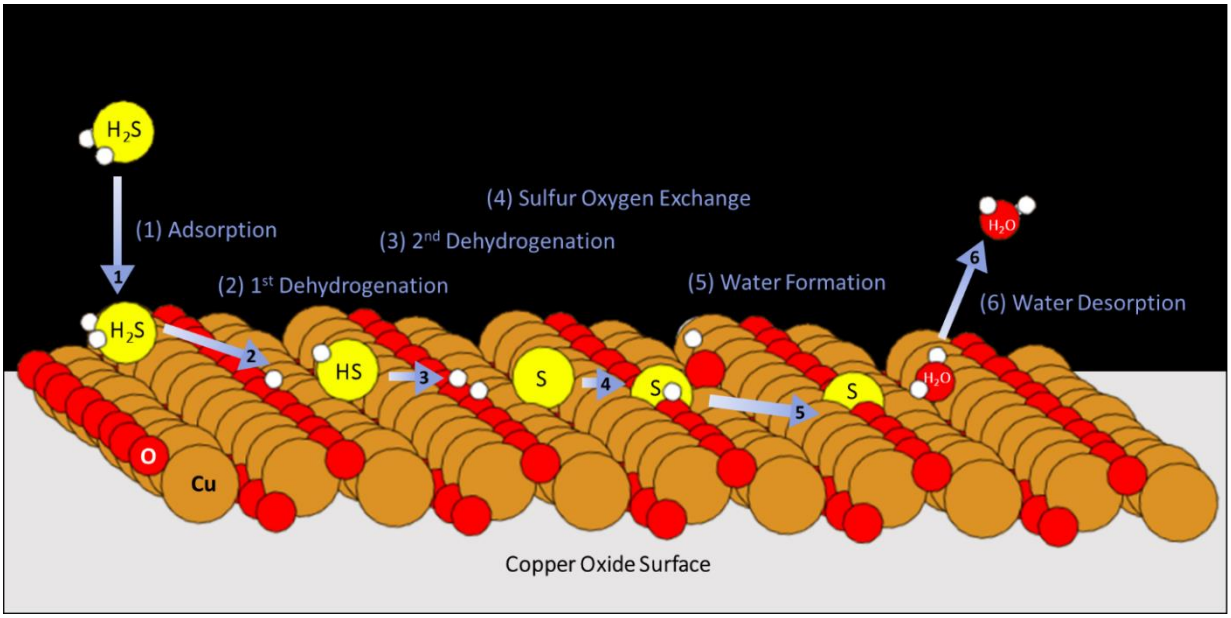

Figure 2-5: Illustration for the reaction mechanism of H_2S molecules on CuO surfaces referenced in the computational studies in literature.[134–136]

Zhang et al.[136] carried out a study on CuO (111) and H_2S with a similar computational methodology but with an expansion of the scope accounting for reduced and slightly-sulfided surfaces. The reduced surface was modelled by creating an oxygen vacancy upon removal of a surface O atom, whereas the slightly-sulfided surface was modelled by adding one S atom to the stoichiometric surface. Sun et al.[135] also found the dissociative adsorption of H_2S to be exothermic on reduced and slightly-sulfide surfaces, although the activation energy for the first dehydrogenation step was higher compared to the stoichiometric surface. Nevertheless, the overall dissociation process was most exothermic on the reduced surface (-169 vs -34 kJ/mol).

However, it should be noted at this point that for metal oxides such as CuO, which exhibit a strongly correlated electronic nature, there is a strong interelectronic interaction and, thus, the

dynamics of electrons are greatly influenced by the rest of the electrons. In these systems, the exchange-correlation functional approximations of standard DFT fall short of properly capturing quantum exchange and correlation effects, giving rise to difficulties in accounting for electron localization.[138] One solution is the so-called Hubbard U approach, in which an additional parameter, namely the Hubbard U, is introduced for electrons to properly describe the on-site Coulomb interaction .[139] The on-site Coulomb correction potential U is introduced as an energy penalty on the delocalization of electrons, thus restricting the amount of delocalization done by standard DFT methods. Its easy implementation coupled with marginal additional computational cost makes it a good choice compared to other higher level functionals and a good choice for studying surface reactivity of highly correlated metal oxides. This approach has been used for adsorption studies on CuO (111).[140–142] It should be noted that the aforementioned studies on CuO did not take into account this fact and therefore did not include any correction of this type. In addition, these studies only reached the dehydrogenation processes of a single molecule of H_2S leading to adsorbed S and OH groups, which does not give any insight about the process on further stages beyond the initial step. These facts led our group to perform a new computational study on this matter.

In a study performed by the authors of this work, we investigated the complete reaction between H_2S and CuO to form H_2O and CuS. After two dehydrogenation steps of the H_2S molecule to give rise to adsorbed S and two OH groups, there is a proton hop between the latter groups, which gives rise to an adsorbed water molecule. The vacancy left by the water molecule is healed by the S atom. Therefore, the process results in an exchange of one O atom from the CuO lattice by a S atom, together with removing H_2S and forming water. In order to account for later stages

of the reaction, we studied also the process in a highly-sulfided surface with most of the O surface atoms already exchanged by S atoms.

We used GGA+U approach of DFT with the PBE exchange-correlation functional and a planewave basis set, modelling the CuO (111) surface with a 2x1 supercell slab. It should be noted that we carried out the same study on the (-111) surface, which is the second most stable CuO surface and we found similar results as in the (111). We found the whole process of forming CuS ($CuO_{1-x}S_x$ more specifically) and H_2O from CuO and H_2S to be thermodynamically favorable ($\Delta G_{T=298K}$ = -106 kJ/mol). The elementary steps that comprise it can be organized into two different groups: Proton hopping processes in which one proton gets transferred from one group to another, and migration of heavier groups. As for the second type of elementary steps, migrations of heavier atoms, we found that migration of hydroxyl species from the lattice position is energetically costly in most cases. Indeed, we found that it was one of the most energetically demanding steps of all the mechanism, together with the initial molecular adsorption of H_2S that is inhibited by the entropy loss. On the other hand, the healing of an oxygen vacancy by a sulfur atom was found to be favorable.

In agreement with the other studies on the (111) surface, we found a greater reactivity on lower coordinated O atoms: $\Delta G_{T=298K}$ = -106 kJ/mol on O atoms with coordination number (CN) 3, whereas $\Delta G_{T=298K}$ = -52 kJ/mol for O atom with CN=4. This is in agreement with experimental data that shows how smaller CuO particles have a greater sulfur removal capacity: As the particle size decreases, the population of low-coordinated O atoms increases due to an increase in defects, dislocations and edges, which in turn increase the reactivity of the particle.

In addition to improved surface reactivity, low-coordinated O atoms may facilitate the diffusion of O atoms through the bulk of the metal oxide by enhancing the creation of oxygen

vacancies. This is important from the mechanistic point of view because solid diffusion of atoms plays a fundamental role in the overall process of reactive sorption in metal oxide materials. A previous work by Elliott et al. studied the formation of oxygen vacancies on (111) CuO surfaces via vacuum annealing and H_2 reduction.[140] They observed that formation of oxygen vacancies is more favorable for O_{3c} than for O_{4c} atoms (265 vs. 314 kJ/mol): A vacancy formed via displacement of lattice O by formation of a OH group is thermodynamically favorable for O_{3c} atoms but unfavorable for O_{4c} ones. All of this, points towards the fact that oxygen vacancies may be formed to a greater extent when the population of low-coordinated O atoms increases (smaller particle size) which may also enhance solid diffusion across the bulk of the material needed to complete the reactive sorption process at later stages.

Finally, two more findings worth noting were related to the later stages of the reaction, namely the process on highly-sulfided CuO surfaces. Reaction with O_{4c} atoms in a bare CuO surface results in $\Delta G_{T=298K}$ = -52 kJ/mol, whereas $\Delta G_{T=298K}$ = -101 kJ/mol is observed for partially-sulfided surfaces in which the outer O_{3c} atoms have been replaced by S atoms. The reactivity of the O_{4c} atoms increases because S atoms disrupt the Cu-O bonding states inducing lattice strain. Additionally, it was also found that sulfur exhibits a tendency towards forming covalent bonds with itself. Results on the (111) surface showed a thermodynamically favorable process for the formation of S_2 dimers from sulfur adatoms present on the surface, with a calculated Gibbs free energy of reaction of $\Delta G_{T=298K}$=-47 kJ/mol. This kind of dimers are present in the CuS phase experimentally formed, namely Covellite, providing a hint for the mechanism to complete sulfidation of CuO.

Another copper which has found its use in reactive sorption processes is Cu_2O. Wang et al. performed computational studies on the (111) surface of Cu_2O (the most stable Cu_2O surface)[144]

analogue to the studies described above for CuO.[145] Wang et al. made use of DFT with the Becke-Lee-Yang-Parr (BLYP) exchange-correlation functional,[146] double-numerical basis with polarization functions for valence electrons, and basis effective core potentials for inner electrons. A 2x2 supercell slab was used as Cu_2O model. They probed both the molecular and dissociative adsorption of H_2S and found that dissociative adsorption occurred predominantly on reduced surfaces with oxygen vacancies present. Similar to the studies on CuO, the dissociative pathway for Cu_2O was found to be exothermic on both the stoichiometric and reduced surfaces (E=-95 kJ/mol and -148 kJ/mol respectively), again with lower-coordinated O atoms being the most reactive ones. From the kinetic point of view, dehydrogenations show activation barriers at around 50 kJ/mol, which are in agreement with experimental findings that showed sulfur present on Cu_2O (111) surfaces via variable-energy photoelectron spectroscopy.[147]

Stenlid et al. used a different approach to study the interaction between sulfur and Cu_2O.[148] In this computational study they investigated early stages of the sulfidation of Cu_2O (111) and (100) surfaces by sequentially exchanging O atoms of Cu_2O by S atoms. Through this approach, they were able to test the thermodynamic stability of the overall process as reaction cycles went on in which H_2S was consumed and water formed (together with the process $Cu_2O \rightarrow Cu_2O_{1-x}S_x$). Using GGA+U DFT level of theory and D3 for dispersion corrections, they found that the replacement of O atoms with S atoms is thermodynamically favorable for all stoichiometries ($Cu_2O_{1-x}S_x$) up to pure Cu_2S for both (111) and (100) surfaces ($\Delta G_{T=298K}$=-683 and – 852 kJ/mol respectively). They also observed that it is more thermodynamically favorable to completely sulfide the first layer rather than the next sublayer partially, indicating that the sulfidation process of the sorbent may proceed on a layer-per-layer fashion.

2.4.3 DFT computational studies for sulfidation of less common metal oxide sorbents

Ceria (CeO_2), a well-known metal oxide in catalysis and other technical application has been subject to several computational studies as well. For example, both Chen et al.[149] and Yildiz et al.[150] used GGA+U and the PW91 functional to study the dissociative adsorption of H_2S on the (111) surface of CeO_2, testing different pathways from H_2S dissociating leading to H_2O, H_2 and SO_2 as products. However, the latter group, whose results were closer to experimental findings, found that none of such pathways were energetically favorable, with activation barriers greater than 182 kJ/mol and reaction energies of around 96 kJ/mol. Only when the surface was previously reduced containing oxygen vacancies the pathways were energetically favorable.

Mixed oxides of Ceria-Lanthanide were studied as well by DFT (GGA+U). Janik et al.[151] investigated dissociative adsorption of H_2S over $Ce_{16}O_{32}$, $La_2Ce_{14}O_{31}$ and $Tb_2Ce_{14}O_{31}$ model slabs, and found that the dissociation for the first S-H bond ($H_2S \rightarrow SH$) was the rate limiting step with barriers greater than 211 kJ/mol on all three cases. However, the apparent activation energy for dissociative H_2S adsorption was much larger in pure Ceria compared to mixed La and Tb oxides, suggesting that the larger sulfur uptake capacity experimentally observed for Ceria-Lanthana is due to faster surface kinetics.

Finally, other sulfur-containing molecules rather H_2S were computationally studied on Ceria-based materials. For instance, the reduction of SO_2 to S by CeO_2 (111) and (110) surfaces was studied using GGA+U by Hermansonn et al. .[152] They observed that, under reducing conditions, sulfide species were the most stable species on the (111) surface whereas sulfate species were predominant on the (110) surface. However, under oxidizing conditions sulfates dominated both of them. They also found that the reduction process followed a Mars-van Krevelen mechanism, for which the activation barrier was relatively low (less than 100 kJ/mol). Similarly,

the same group found that when adsorbing sulfur rather than SO_2, it was likely to be found within the lattice replacing when present in the (111) surface, but on the lattice as SO_2^{2-} when interacting with the (110) surface.

MgO can be also found as the matter of several computational studies regarding adsorption of sulfur-containing compounds. For example, Bagheri et al. used DFT (B3LYP) to study the adsorption and dissociation of H_2S over MgO nanotubes.[153] They found a barrierless process for the non-dissociative molecular adsorption, whereas the dissociative adsorption consisting of $H_2S \rightarrow SH$ showed an activation barrier of 16 kJ/mol respectively and an adsorption energy of -104 kJ/mol, with these low values found on low-coordinated Mg centers.

Since MgO surfaces were not found to be as active for sulfur uptake as other metal oxides, like ZnO, some authors like Rodriguez et al. explored other altered MgO-based materials such as Ni-doped MgO and mixed $Cr_xMg_{1-x}O$.[113,154] For the former, when Mg centers are replaced by Ni, new electronic states are created above the occupied O 2*p* + Mg 3*s* band. In these systems there is a large electron density around Ni centers, which provides strong bonding for S and SH species adsorbed on the surface. Indeed, the H_2S adsorption energy increase from 36 kJ/mol in pure MgO to 68 kJ/mol. Similarly, an enhanced sulfur removal activity is found for mixed $Cr_xMg_{1-x}O$. In this case Cr atoms have a lower oxidation state than the atoms in Cr_2O_3 and exhibit occupied 3*d* levels that are less stable than the valence bands of MgO. Both properties favor strong interactions with the orbitals of S-containing molecules.

The current studies in the literature have mainly dealt with H_2S interaction on selected metal oxides, most of which strongly bind to H_2S and normally dissociate it into elemental sulfur

and OH groups, going beyond simple molecular adsorption. Strong adsorption energies of several kJ/mol are often obtained via computational modelling. Several theoretical studies point out how modification in the type of mixed oxides or doping may induce even more affinity towards sulfur contaminants. Sulfur species in the form of SH or S atoms are found to form strong metal-sulfur bonds with metal surface centers whereas protons from H_2S are transferred to surface O atoms resulting in hydroxylated surfaces. However, reactive sorption is a complex phenomenon which goes beyond dissociative adsorption of sulfur-containing molecules, especially in the later stages of the reaction. Understanding both the transformation of the bulk of a metal oxide into a metal sulfide and other phenomena such as solid diffusion across the oxide and sulfide phases are equally important to fully explain the reactive sorption at the atomic level.[143]

Chapter 3 | Linear Driving Force Approximations as Predictive Models for Reactive Sorption

3.1 Introduction

To optimize the use of CuO-based materials in an industrial setting, modeling the reactor in which the reactive sorption process takes place becomes an important task. In this process, the contact between contaminant molecules and solid phase can be studied at three scales: the bed scale, the pellet scale and the grain scale as demonstrated in Figure 3-1.[171] The contaminated gas flows through a packed bed of granular medium whose properties change in space and time upon the progression of the process. The contaminant travels from the bulk of the flowing gas to the pellet surface and diffuses through layers of product phase and pores of fresh materials to reach the crystallite surfaces available for reaction.[172] At the surface of the grain, H_2S gas reacts heterogeneously with solid CuO forming Copper (II) sulfide (CuS) and water.

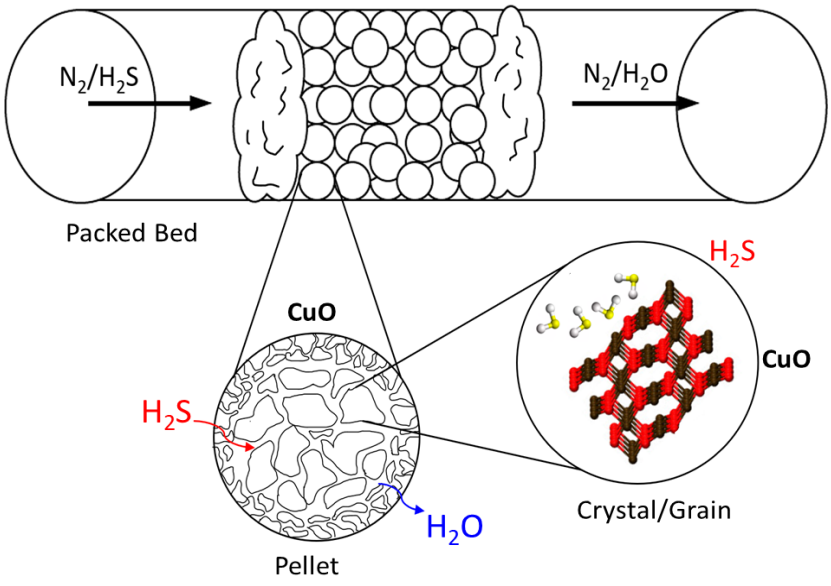

Figure 3-1: Demonstration of the three levels of the process of H_2S removal in a bed of a CuO-based sorbent: Packed bed, pellet and grain levels.

The complexity of this multi-scale process and its dependency on the sorbent and contaminant's properties led to the development of various models such as the single pore model,[173] random pore model,[174] volume reaction model,[175,176] nucleation model,[177,178] grain model,[179,180] and incremental model.[1,12] In this work, we apply mathematically simple linear driving force models to describe the system in terms of the sorbent removal capacity (q_s, g H_2S/ 100 g sorbent) and the sorption rate parameter. These models provide quantitative approximation for adsorptive systems when the equilibrium constant is sufficiently large[181] as is the case for reactive sorption of hydrogen sulfide using CuO (>10^{20}).

The concentration-time profiles of H_2S contaminant in the reactor effluent were analyzed using two linear driving force models: a solid film-based model derived initially by Cooper[182] and a quasi-chemical model derived by Bohart and Adams.[183] A range of process conditions (sorbent pellet size, contact time, temperature, pressure and contaminant concentration) were varied to probe their effects on the parameters if the models as well as to determine apparent rates of reaction/diffusion occurring at the molecular scale.

3.2 Experimental Methods

3.2.1 Materials and characterization

A CuO-ZnO-based sorbent was purchased from Alfa Aesar (HiFUEL W230; 63.5 wt. % CuO, 25 wt. % ZnO and 10 wt. % Al_2O_3; lot number: L04Y006). The sorbent is received as 5.5 mm x 3.65 mm cylindrical pellets which were crushed and sieved to obtain agglomerates with various size distributions within a range of 75-1000 microns.

Scanning electron microscopy (SEM) images were collected on a Nova Nano 230. An ETD detector and 10 kV accelerating voltage settings were used for all the scans with magnifications

ranging from 100x to 15000x. The system was used simultaneously to obtain energy dispersive X-ray spectra (EDS) of the material before and after sulfidation to provide qualitative and quantitative evidence of elemental composition for the surface layers. X-ray diffraction patterns in the range of 0°-100° $2\theta^{\circ}$ (at the rate of $20^{\circ}min^{-1}$) were obtained on JEOL JDX-3530 and Philips X-Pert diffractometers with Cu Kα radiation. The Brunauer-Emmett-Teller (BET) method was used to evaluate surface area and total pore volume of fresh and spent samples from N_2 physisorption isotherms collected on a Micrometrics ASAP 2020 Plus unit. Prior to N_2 adsorption, the sample was degased at 120 $^{\circ}$C for 12 hours under controlled pressure of 10 microns of mercury

3.2.2 Fixed-bed experiments

Reactive sorption of H_2S was studied in an apparatus with plug-flow hydrodynamics shown schematically in Figure 3-2. Flow rates of gaseous H_2S and N_2 were introduced via mass flow controllers (MKS GE50A and GM50A). Feeds to the reactors consisted of H_2S in N_2 (900-2200 ppm-vol) and were produced by diluting a 1.01% H_2S (Praxair UHP) in N_2 mixture with UHP N_2. Sorbent samples (150-500 mg) were fixed between plugs of quartz wool in 0.25-inch, outer diameter, tubular stainless-steel reactors. All gas transfer lines, and the interior of the reactor were treated with an inert coating (SilcoNert 2000) to mitigate H_2S adsorption onto tubing walls. A resistively heated jacket with a PID temperature controller (TEMPCO EPC-100) were used to regulate reactor temperature (21-200 $^{\circ}$C). Downstream back pressure regulator is used to control and adjust total pressure (1-2 atm). Compositions of feed and effluents were determined using online gas chromatography (Agilent 7890B) with a sulfur chemiluminescence detector (SCD; Agilent 755) and continuous gas phase FTIR spectroscopy (MKS Multigas).

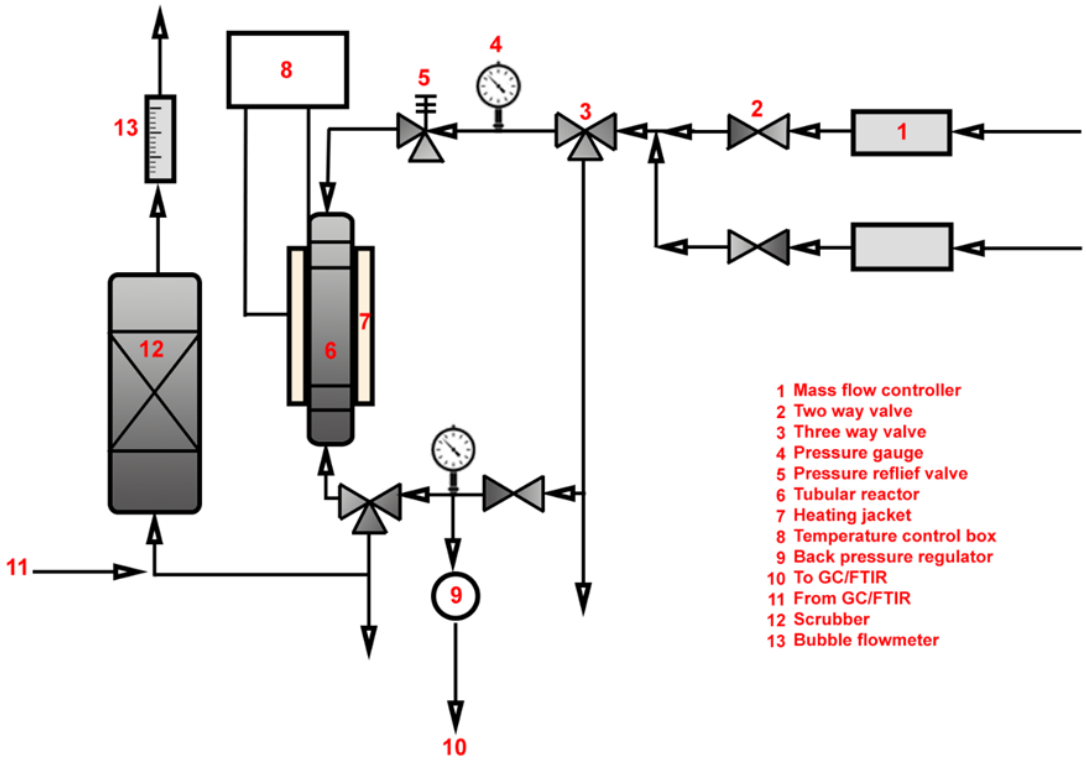

Figure 3-2: Schematic of fixed-bed reactive sorption testing apparatus

3.2.3 Cooper and Bohart-Adams models development

Reactive sorption of hydrogen sulfide from a gaseous stream can be described by the mass balance across a differential element of the bed as follows:[184]

$$v\left(\frac{\delta C}{\delta Z}\right)_t + \left(\frac{\delta C}{\delta t}\right)_z + \frac{1-\varepsilon}{\varepsilon}\cdot\left(\frac{\delta q}{\delta t}\right)_z = 0 \qquad (7)$$

where v is the axial interstitial velocity of fluid, z is the axial distance coordinate in the direction of the flow, C is the concentration of the contaminant in the bulk fluid, t is time, ε is bed void fraction (obtained from Ergun equation) and q is the average concentration of contaminant in the solid phase.

This equation is derived based on several assumptions about the system. The first assumption is that the dispersive terms are negligible which is justified by the system's large axial aspect ratio, $L/d_p > 50$,[185] where L is the bed depth and d_p is the pellet diameter. Since axial dispersion can be neglected, it's reasonable to assume a plug flow and a constant velocity in the axial direction. Moreover, the velocity and concentration are assumed to be invariant in the radial direction because of the plug flow assumption. The high D/d_p ratio, where D is reactor diameter, guarantees minimal channeling effects and constant interstitial velocity (>20 in this study).[186] Finally, the system is assumed to be isothermal as it's well isolated and the temperature is controlled along the length of the bed. To solve Equation 7 for the contaminant concentration, Bohart-Adams model proposes a quasi-chemical law that describes the overall sorption rate $\left(\frac{\delta q}{\delta t}\right)$ as follows:[184]

$$\frac{\delta q}{\delta t} = k_a C(q_s - q) \quad (8)$$

where k_a is the sorption rate constant and q_s is the maximum saturation capacity achieved at equilibrium. The main assumption for this model is that the capacity of the sorbent is fixed at q_s and is independent of the concentration of contaminant in the gas phase (rectangular isotherm).[187] The resulting concentration profile becomes:

$$\frac{C}{C_0} = \frac{e^{\tau}}{e^{\tau} + e^{\mathcal{Z}} - 1} \quad (9)$$

where $\tau = k_a C_0 \left[t - L/v\right]$, $\mathcal{Z} = (k_a q_s L/v)((1-\varepsilon)/\varepsilon)$, and C_0 is the contaminant concentration in the inlet stream. Cooper applied a different linear driving force equation where the overall sorption rate is described as follows:[182]

$$\frac{\delta q}{\delta t} = k(q_s - q) \quad (10)$$

where *k* is the adsorption rate parameter. The analytical solution of the coupled PDE-ODE system (Equations 7 and 10) is a piece-wise equation:

$$\frac{C}{C_0} = 1 - \xi e^{-\tau}, \ \xi \leq 1 \quad (11)$$

$$\frac{C}{C_0} = 1 - e^{\xi-\tau-1}, 1 \leq \xi \leq 1+\tau \quad (12)$$

$$\frac{C}{C_0} = 0, \xi \geq 1+\tau \quad (13)$$

where $\tau = k\left[t - {}^{L}/_{v}\right]$ and $\xi = (kq_sL/C_0v)((1-\varepsilon)/\varepsilon)$. These models relate the properties of the material and the experimental conditions to the concentration-time profile (breakthrough curve) of the contaminant in the effluent of the reactor. The two parameters (the sorption rate parameter (*k*) and the maximum saturation capacity (q_s)) are regressed from breakthrough curve data using Excel's GRG nonlinear least squares solver. Alternatively, the saturation capacity can be determined by integrating the breakthrough curve after the effluent concentration reaches the inlet concentration. In these instances, the linear driving force models reduce to single parameter models (the sorption rate parameter).

The rate parameter (*k*) consists of contributions to the overall sorption rate from (i) diffusion in the bulk fluid, (ii) diffusion in the pores of the solid, and (iii) diffusion through product phase/ reaction occurring at the surface of the reactive phase according to Equation 14:[7]

$$\frac{1}{kK} = \frac{d_p}{3k_f} + \frac{d_p^2}{15\varepsilon_p D_p} + \frac{1}{k_{rxn}} \quad (14)$$

$$= R_b + R_p + R_{rxn} \quad (15)$$

where d_p is the radius of the pellets of the solid phase (derived from particle size distribution measurements), D_p is the effective diffusivity of the contaminant within the pores of the pellet, k_f is the fluid film mass transfer coefficient, and $\mathcal{E}_p$ is the porosity of the solid pellets obtained from N_2 physisorption. The distribution parameter (K) is the ratio of the contaminant in the solid phase to that in the fluid phase at equilibrium (q_s/C_0). The lumped rate parameter (k_{rxn}) contains contributions from both the rate of reaction at the grain surfaces and diffusion of molecules through solid reactant/product phases.

The value of k_f can be determined using the equation for the Sherwood number as follows:

$$\boldsymbol{k_f = \frac{D_M Sh}{2d_p}, \qquad Sh = 2 + 1.1 Sc^{\frac{1}{3}} Re^{0.6}} \tag{16}$$

where Sc is the Schmidt number, Re is the Reynolds number[2,188] and D_M is the molecular diffusivity of the contaminant molecule in the bulk gas phase which is calculated as follows:[189]

$$\boldsymbol{D_M = \frac{0.00266 T^{\frac{3}{2}}}{P M_{AB}^{\frac{1}{2}} \sigma_{AB}^2 \Omega_D}} \tag{17}$$

where T is the absolute temperature (K), M_{AB} is the average molar mass (g/mol), P is the pressure (atm), σ_{AB} is the average collision diameter (Å) and Ω_D is a temperature-dependent collision integral.

The contribution from pore diffusion can be determined by calculating the value for D_p from the sum of diffusion in the macro- and mesopores of the solid according to:

$$\boldsymbol{D_p = \frac{D_t}{\tau}, \qquad \frac{1}{D_t} = \frac{1}{D_M} + \frac{1}{D_K}} \tag{18}$$

Finally, the Knudsen diffusivity is given by:

$$\boldsymbol{D_K = 9700r\left(\frac{T}{M_{AB}}\right)^{\frac{1}{2}}} \quad (\mathbf{19})$$

where r is the pore radius and τ is the tortuosity (assumed to be 3 for spherical pellets).[190]

3.3 Results and Discussion

3.3.1 Identification of reaction products and effects of sulfidation on sorbent morphology

During reaction with H_2S, bulk conversion of CuO occurs in which crystalline CuO forms smaller crystallites of CuS leading to pore structure changes within the solid.[28] SEM and EDS analyses and N_2 physisorption were conducted on the sorbent materials before and after reaction with H_2S to identify solid phase reaction products and to probe the effects of reaction on solid morphology.

The SEM micrograph in Figure 3-3 shows fresh CuO sorbent agglomerates between 75-125 microns at 100x magnification. Individual agglomerates consist of various shapes from crushing and sieving of the initially cylindrical pellets to achieve the desired size range. The particle distribution analysis (Figure 3-3) shows that the mean agglomerate size is 78.4 μm with a mode of 74.0 μm. The mean agglomerate size was used as the agglomerate diameter when calculating uptake resistances from pore and bulk diffusion according to Equation 14. Moreover, the pellet size distribution analysis suggests that the average difference between particles' minimum and maximum diameters is 8 microns (10.5% of the average pellet size), thus, spherical-shaped particles are assumed for these calculations.

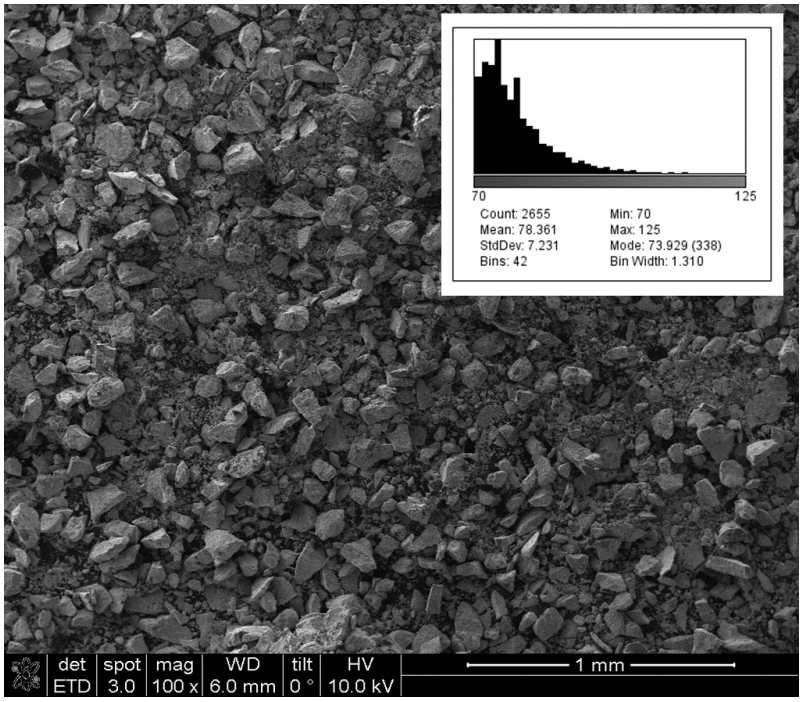

Figure 3-3: SEM image of the CuO-based sorbent (75-125-micron pellets; 120-200-mesh) at 100x and a particle size distribution analysis of the sorbent generated by ImageJ software.

Figure 3-4 shows SEM micrographs at 10,000x and 15,000x magnification before and after reaction with 110 cm^3(STP) min^{-1} of 930 ppm H_2S/N_2 at ambient temperature (294 K) and pressure (1.1 atm). The initial material in Figure 3-4A and 1B exhibited a textured surface with macro-voids which diminished after sulfidation (Figure 3-4C and 1D). This apparent decrease in the volume of voids is also reflected in changes in surface area (via the BET method; Table 3-1) which decreased from 67.3 to 17.6 $m^2 \cdot g^{-1}$ after sulfidation at room temperature.

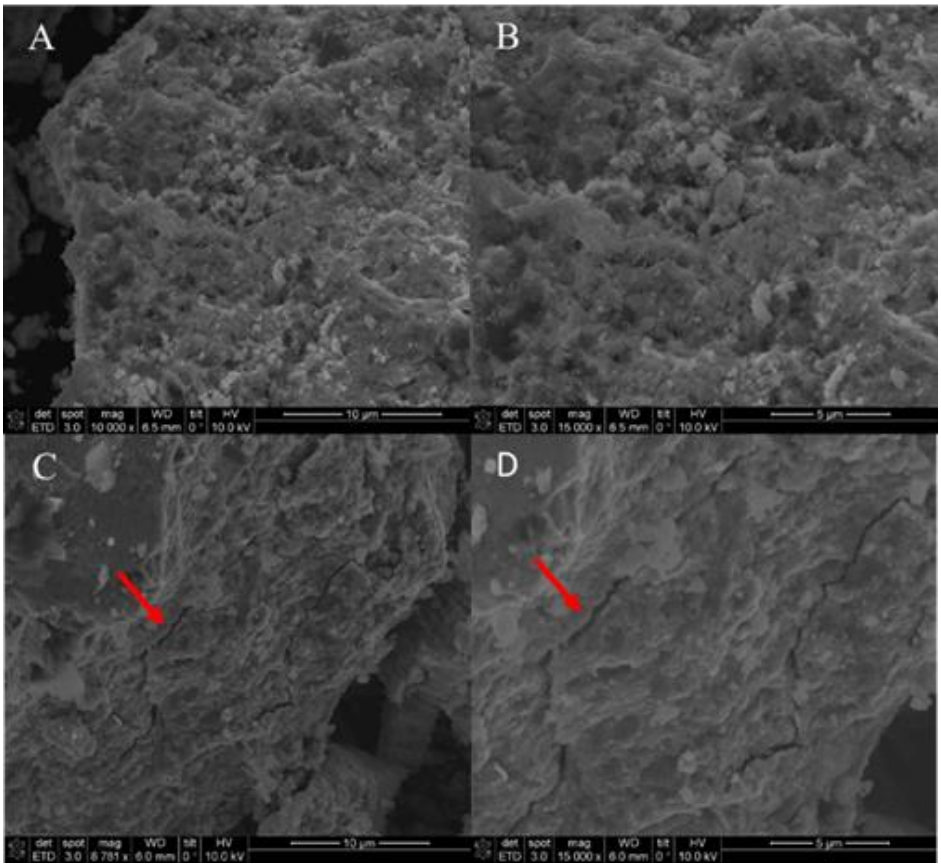

Figure 3-4: SEM images of fresh CuO-based sorbent (75-125-micron pellets; 120-200-mesh) at 10000 x magnification in A and C and 15,000 x magnification in B and D. A-B scans are of fresh materials while C-D set are taken after sulfidation with 110 cm^3(STP) min^{-1} of 930 ppm-vol H_2S/N_2 stream at temperature of 294 K and 1.0 atm pressure. Arrows point to cracks in the particles that form after sulfidation.

Figure 3-4 also shows an appearance of cracks on the agglomerates' surface after reaction (arrows in Figure 3-4C and 1D). These fractures may be the result of the volume expansion accompanying the conversion of CuO (Crystal density of 6.32 $g \cdot cm^{-3}$) to CuS (4.76 $g \cdot cm^{-3}$) which is the predominant product identified by XRD and EDS as discussed below. Despite these changes in volume and texture, the SEM images of the sulfided agglomerates indicate that they retained their initial sizes/shapes without a complete fracturing of 75-125 micron agglomerates into a distribution of smaller particles. The retention of the initial overall shape may be the result of ZnO and Al_2O_3 phases that are unreactive at these conditions and thus serve as a binder for the CuO.[28]

Finally, the surface area of adsorption and total pore volumes obtained from BET measurements for fresh sample and selected spent samples are summarized in Table 3-1. The measurements show a 3.8-fold decrease in surface area and a 2.7-fold decrease in pore volume upon sulfidation of the sorbent at room temperature with 1000 ppm-vol H_2S/N_2. This drastic decrease of porosity resulted in an increase in diffusion resistance which explains the incomplete sulfidation of sorbent at room temperature and pressure. The table also shows a slight but consistent increase in pore volume with temperature increase, from to 0.051 cm^3g^{-1} at 294 K to 0.083 $cm^3 \cdot g^{-1}$ at 383 K. It also shows an increase in surface area from 17.6 to 29.8 $m^2 \cdot g^{-1}$ as temperature increased from 294 K to 383 K. This increase in porosity with temperature aligns with the observed enhancement in conversion.

Table 3-1: Summary of pore volume and BET surface area of N_2 adsorption at 77 K for fresh and sulfided CuO-based sorbent at 1000 ppm-vol H_2S/N_2, ambient temperature (294 K) and ambient pressure (1.0 atm).

Sorbent	Pore volume [$cm^3 \cdot g^{-1}$]	Surface area [$m^2 \cdot g^{-1}$]
Fresh sorbent	0.139	67.3
Spent at 294 K	0.051	17.6
Spent at 323 K	0.066	20.8
Spent at 383 K	0.083	29.8

To probe the chemical changes of the agglomerates after sulfidation, EDS scans of the fresh and sulfided particles were collected. Figure 3-5 shows the elemental maps of copper, zinc, aluminum and oxygen for a fresh 120-micron agglomerate up to 2-micron penetration depth. The quantitative results from the EDS scan demonstrate higher surface sulfur weight percentage (16.3 wt.%) than the bulk removal capacity obtained from mass balance across the reactor (12.5 wt.%) suggesting that surface layers (up to 2 microns) sulfide more readily than deeper layers because of diffusion resistance to molecules and atoms through solid sulfide product layers.

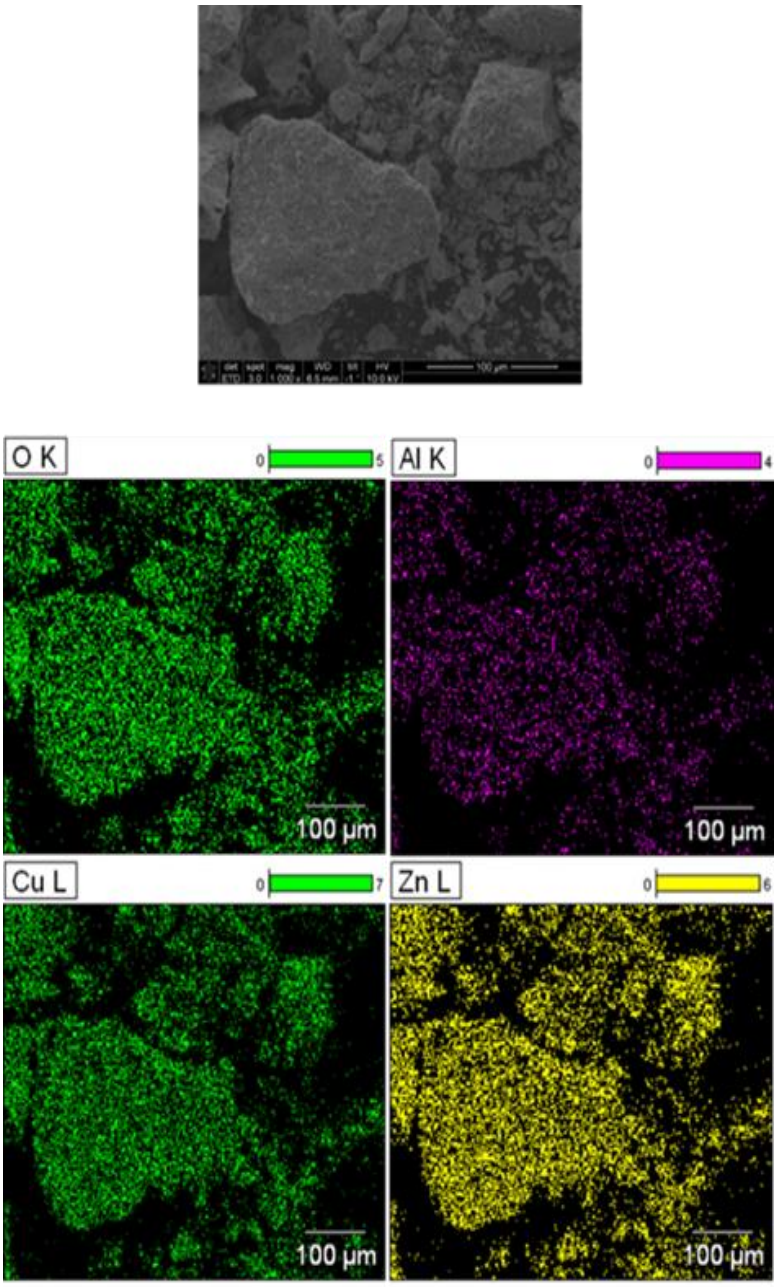

Figure 3-5: Energy Dispersive Spectroscopy (EDS) elemental maps (oxygen, aluminium, copper, and zinc) for a 120-micron pellet of the CuO-based sorbent based on an SEM scan at 1000 x magnification (top panel).

Figure 3-6 shows the X-ray diffraction patterns for the fresh and sulfided sorbents at various temperatures (294-383 K) which resulted in increasing extents of conversion (46 to 100% at 294 K and 383 K, respectively). The peaks at $2\theta = 35.8°$ and 38.9° in the fresh sorbent pattern

correspond to (111) and ($\bar{1}$11) planes of *CuO*, respectively. The diffraction patterns of the sulfided samples at different temperatures show broadening and decreasing intensity of the CuO characteristic peaks with the increase in temperature.

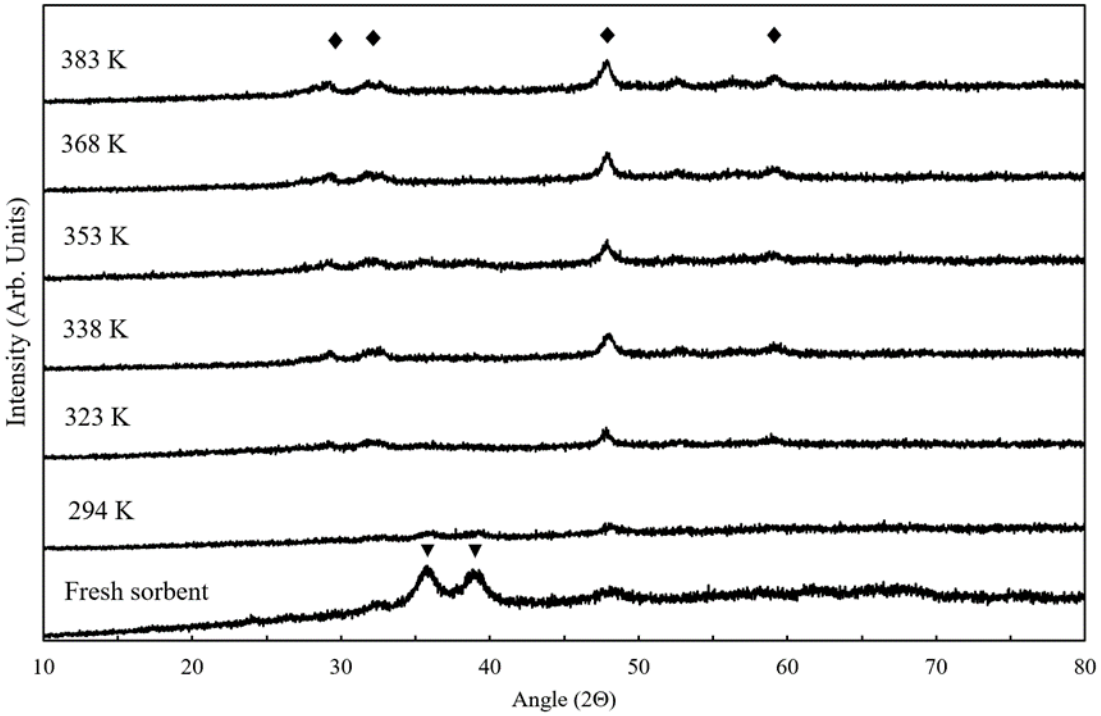

Figure 3-6: Diffraction patterns of fresh CuO-based sorbent and spent samples at 294, 323, 338, 353, 368, 383 K after sulfidation with 110 cm^3(STP) min^{-1} of 970-1016 ppm-vol H_2S/N_2 at ambient temperature (294 K) and pressure (1.0 atm). The triangles correspond to characteristic CuO peaks and the diamonds correspond to characteristic sulfur peaks.

The CuO crystallite size (estimated by Debye–Scherrer formula using $2\theta = 35.8°$) decreased from 3.1 nm for fresh sample to 1.8 nm for the sample sulfided at 294 K. CuO diffraction peaks are absent for samples sulfide at temperatures higher than 323 K. The diffraction patterns also show rising of peaks at 2θ = 29.1°, 32.1°, 48. 3° and 59.5° which correspond to (102), (103), (110) and (116) planes of hexagonal CuS phase, respectively. The emergence of CuS peaks and disappearance of CuO peaks confirm the reaction of CuO to CuS. Furthermore, the change in CuO crystallite size with increasing extents of sulfidation suggests that the reaction disrupts the

crystallite structure of CuO leading to less crystalline (or possible amorphous) CuO, consistent with the textural changes identified via SEM and N_2 physisorption.

3.3.2 Effects of reactor contact time and sorbent agglomerate size on capacity and rate

In this study, the effect of varying contact time, t_c, defined as the ratio of bed volume to volumetric flow rate, was investigated for a range of pellet sizes to explore possible dependency of models' parameters (k and q_s) on flow conditions. A tracer experiment was run using a fixed bed of inert alumina to assure that the delay time is of negligible effect. The delay time, Figure 3-7, was 1.2 minutes compared to ≥ 5 hours breakthrough time for all runs.

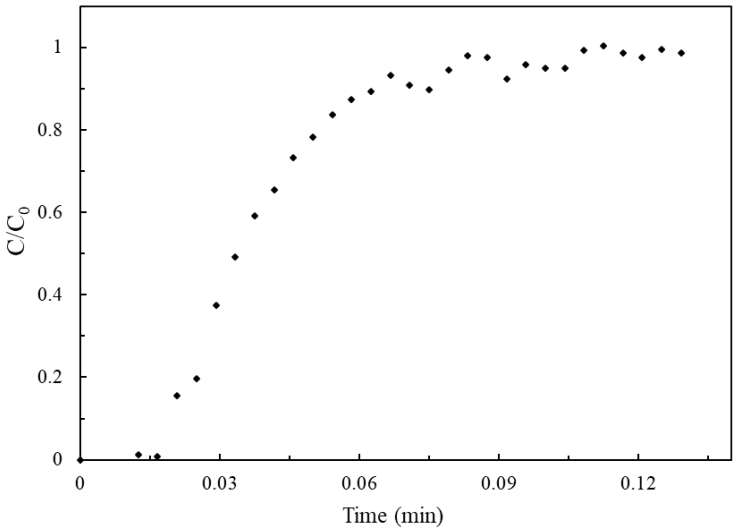

Figure 3-7: Tracer experiment to verify short delay time for the sulfidation tests. 150 mg of inert alumina (Al_2O_3) bed and a feed of 1000 ppm-vol H_2S/N_2 were used at a flowrate of 100 sccm.

Sulfidation experiments were carried for fixed-beds of the CuO-based sorbent with pellet sizes ranging from 125 µm to 1000 µm at ambient temperature (294 K) and pressure (1.0 atm) and inlet concentration of 1000 ppm-vol H_2S/N_2. Figure 3-8 shows that varying contact time within 0.31-1.40 s range had no effect on the saturation capacity for a given pellet size. It shows, though,

that increasing pellet size from 125 to 1000 µm decreased the average saturation capacity from 12.8 wt. % to 9.5 wt. % (g H_2S/ 100 g sorbent) which will be further discussed.

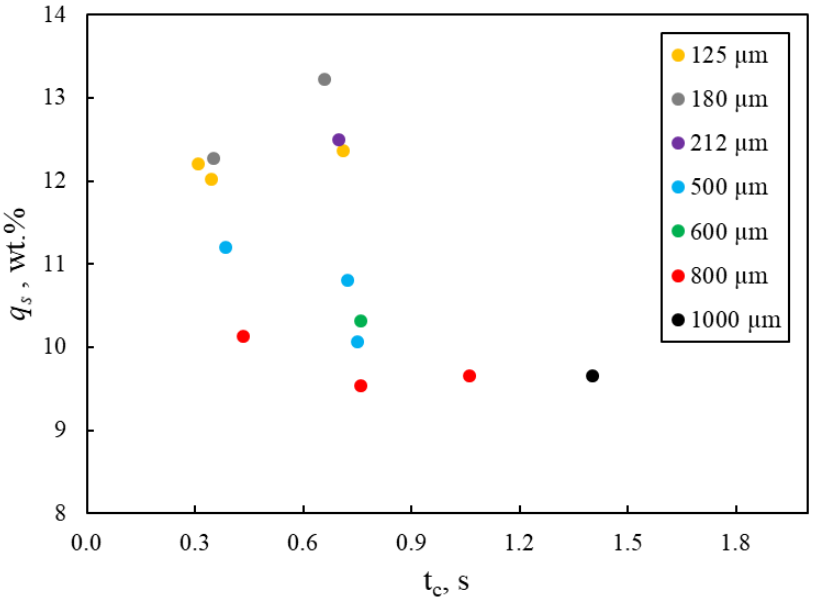

Figure 3-8: Effect of varying contact time on maximum saturation capacity, q_s, for fixed beds of CuO-based sorbent at 1000 ppm-vol H_2S/N_2, 294 K and 1.0 atm. Different color codes are assigned to different pellet sizes.

Figure 3-9 presents selected breakthrough curves where contaminant concentration is normalized for inlet feed concentration and the time on stream is normalized for weight of sorbent and flowrate. The breakthrough curves show a positive shift in breakthrough time with pellet size decrease which correlates to an increase in saturation capacity. It also shows that the shape of the breakthrough curve changed from sickle shape for smaller pellet size (characteristic of Cooper model) to sigmoidal shape (characteristic of Bohart-Adams model) for larger pellet size. Cooper model provided better fit for the breakthrough curves of 125-212 µm runs compared to Bohart-Adams model which tend to underestimate the initial breakthrough rate and over estimate it at later periods. Bohart-Adams model provided better fit for the shape of the larger pellet sizes' breakthrough curves, 800 and 1000 µm, and for the initial part of the medium pellet sizes, 600 and

500 µm, breakthrough curves. Nevertheless, both models provided comparable predictions of the maximum saturation capacity with slightly higher accuracy of Bohart-Adams' estimates as pellet size increases. Summary of all runs' conditions along with regressed parameters and estimated errors are listed in Table B-1.

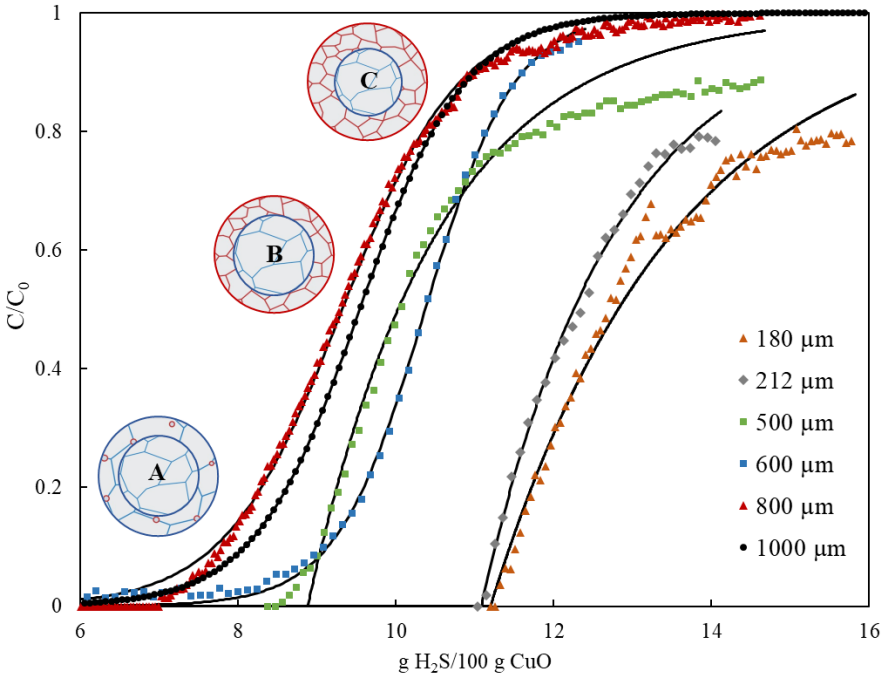

Figure 3-9: Breakthrough curves of normalized effluent H_2S concentration (right) collected for fixed beds of the CuO-based sorbent at 1000 ppm-vol H_2S/N_2, 294 K and 1.0 atm. Solid black lines represent fitted linear driving force models (Cooper model for 120, 180, 212, 500 µm and Bohart-Adams model for 800 and 1000 µm). Inset schematics show representations of the propagation of reaction front through the volume of the pellet for large pellet size (not to scale)

To explain both changes in saturation capacity and model fit with pellet size, the sulfidation process at the pellet and grain scales must be deconvoluted. The sorbent pellet (hundreds of microns) is a porous agglomerate comprised of packed nonporous grains. For larger pellets (≥ 500 µm), the outer surface of the pellet reacts instantaneously with sulfur contaminant but the propagation of the reaction front through the pellet is limited by the high pore-diffusion resistance, R_p, which is proportional to the square of pellet's diameter (Equation 14). The propagation of

reaction follows a nucleation process where the rate increases as nuclei connect (region A, Figure 3-9). Afterwards, significant CuS product layer accumulates which results in (i) restriction of access to unreacted core of grains due to the high solid-diffusion resistance and (ii) decrease in the porosity of the pellet due to the difference in molar volume between products and reactants (factor of 1.6 for CuS/CuO) which causes pore collapsing/clogging. The first effect explains incomplete conversion of individual grains while the other explains incomplete conversion through pellet volume. The combined effects of CuS formation results in switching from nucleation/pore-diffusion-controlled regime (region A, Figure 3-9) to solid-diffusion-controlled regime (Region C, Figure 3-9) which manifests as an inflection in the breakthrough curves (800 and 1000 μm).[190] This inflection is better captured by Bohart-Adams model under these conditions.

On the other hand, for smaller pellet sizes (≤ 212 μm) where pore-diffusion resistance is negligible, no concentration gradient is established across the pellet and access to fresh grain surfaces throughout the volume of the pellet is instantaneous. At the surfaces of the grains, CuS layers are formed and the process is slowed down by solid-diffusion resistance immediately. This explains why Cooper model, which is derived under the assumption of solid-diffusion control,[182] provides better fit for smaller pellet sizes. The change in porosity is less important for smaller pellet sizes as the reaction propagates through the volume of the pellet before the effect of pore clogging can impede access to the pellet core. This explains the enhanced saturation capacity with pellet size decrease.

Explaining the effect of pellet size on rate parameter requires quantification of the contributing resistances using theoretical correlations (Equations 14-19). Figure 3-10 demonstrates how the estimated contributing rate parameters varied with pellet size change. For all pellet sizes, bulk diffusion resistance had a negligible contribution to the rate parameter as discussed earlier.

At small pellet sizes (125-212 µm) both pore and bulk diffusion resistances were negligible and, thus, the rate parameter was dominated by the rate of reaction at CuO/CuS interface and diffusion through solid products, k_{rxn}. In the intermediate range of pellet sizes (500-600 µm) the contributions of solid diffusion and pore diffusion resistances were comparable with an increase in pore diffusion contribution as pellet size increased. For significantly larger pellets (≥ 800 µm), regressed rate parameter equated to the estimated pore-diffusion rate (Equation 14). This can be extrapolated to larger pellet sizes given that flow conditions and axial and radial aspect ratios remain large enough for channeling effects and axial dispersion to be negligible.

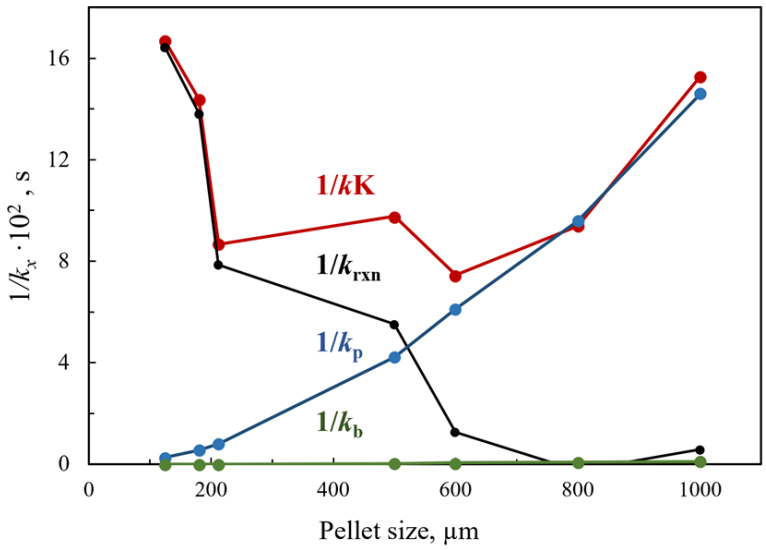

Figure 3-10: Contributions of pore diffusion resistance, $1/k_p$, bulk diffusion resistance, $1/k_b$, and solid diffusion/surface reaction resistance, $1/k_{rxn}$ to the overall rate resistance, $1/kK$, at various agglomerate sizes (125-1000 µm). The resistances were deconvoluted from Cooper's regressed rate parameter for runs at 1000 ppm-vol H_2S/N_2, 294 K and 1.0 atm.

3.3.3 Effects of temperature, concentration, and pressure

To assess the utility of using linear driving force models as a predictive tool when operating under temperatures higher than room temperature, runs were conducted using 212 µm pellets for a range of temperatures (294-423 K). Plots of temperature effect on the regressed rate parameter, kK, and saturation capacity, q_s, are presented in Figure 3-11. Figure 3-11A shows that the value of

maximum capacity increased consistently from 12.5 wt. % at 294 K to 39.2 wt. % at 423 K. The stoichiometric conversion of the CuO phase was achieved at 26.7 wt. % (highlighted by the dotted red line). The saturation capacities that are beyond stoichiometric conversion were a result of reaction of ZnO phase at higher temperatures. Table B-1 summarizes the values of saturation capacity estimated by Cooper and Bohart-Adams models and shows that Bohart-Adams model provided, overall, better fits for the saturation capacity.

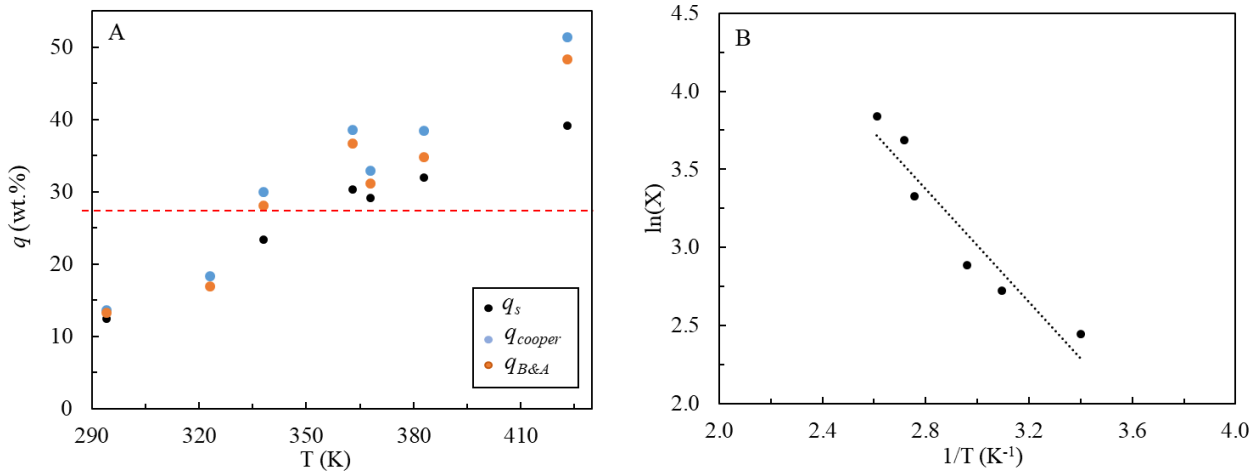

Figure 3-11: A) represents the effect of varying temperature on the maximum saturation capacity at given conditions. B) represents an Arrhenius plot of the rate parameter regressed from Cooper's model fit for runs at 294, 323, 343, 363, 393, and 423 K. The runs were collected for 212 µm agglomerates at 970-1016 ppm-vol H_2S/N_2 and a pressure of 1.0 atm.

In addition to the better estimations of capacity by Bohart-Adams, the model captured the behavior of the breakthrough curves at higher temperatures as demonstrated in Figure 3-12. To explain this change in breakthrough behavior, we must revisit the sulfidation process for small pellets which was discussed earlier. The immediate access to internal grains due to low pore diffusion resistance makes surface reaction on grains throughout the pellet volume fast enough for it not to contribute to the overall resistance. At room temperature, after initial CuS layers are formed, the propagation of reaction through grains is slowed down and the process is dominated by the rate of diffusion through solid product phase.

For higher temperatures, the enhanced diffusivity through solid phase (and porosity as demonstrated in BET measurements) allows for the formation of product nuclei throughout the volume of the grain. The initial increase in the rate of sulfidation is a result of formation and connection of these nuclei (region A).[190] As product layers accumulate, the diffusion resistance increases until the rate of diffusion to fresh grain core is slower than the rate of nuclei formation and connection. At this critical point, the rate shifts from domination by nucleation/connection through grain volume to diffusion through thick product layer. This shift point explains the inflection in the breakthrough curve which resembles the shape of Bohart-Adams model. Although the shape of breakthrough is better captured by Bohart-Adams model, both models deviated from mass-balance-estimated capacity with temperature increase as demonstrated in Table B-1.

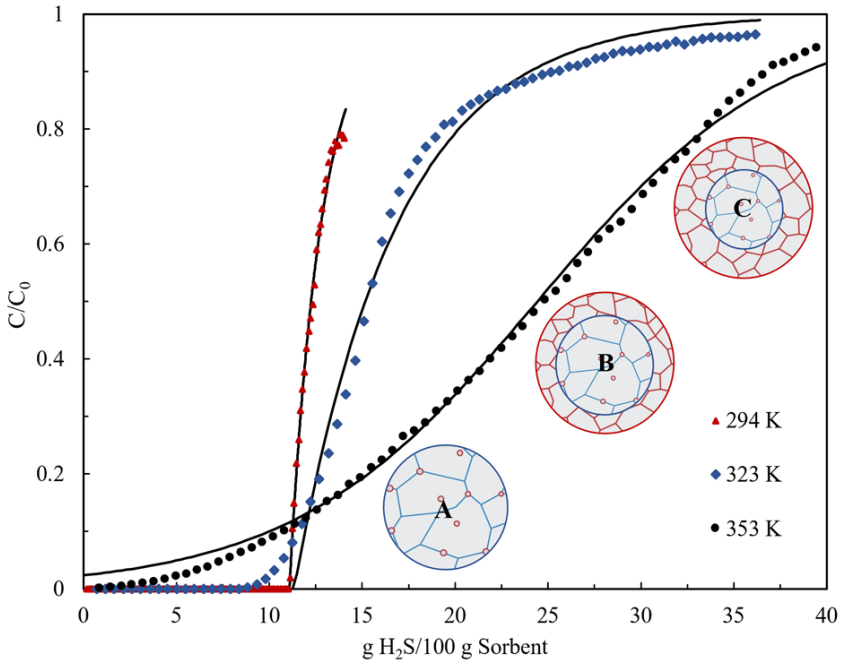

Figure 3-12: Breakthrough curves of normalized effluent H_2S concentration (right) collected for fixed beds of the CuO-based sorbent at 1000 ppm-vol H_2S/N_2 and 1.0 atm for temperatures of 294, 323, 353 K. Solid black lines represent fitted linear driving force models (Cooper model for 294 and 323 K and Bohart-Adams model for 353 K). Inset schematics show a representation of the propagation of reaction front at two temperatures

Figure 3-11 B shows an Arrhenius plot of the log of the regressed rate parameter, *k*K, as a function of the reciprocal of temperature. Since pellets of small size were used in these runs, 212 µm, k_{rxn} and *k*K were expected to be close in value (Table B-1). Based on earlier discussion, for 125-212 µm pellet size range, the dominant resistance is the resistance to diffusion through the solid product phase rather than the surface reaction, pore diffusion or bulk diffusion. Although the increase in temperature enhances diffusivity, the increase in conversion with temperature results in a thicker products layer which poses higher diffusion resistance. These two factors counter one another and have different contributions to the rate of solid diffusion which can't be easily deconvoluted. This explains why the dependency deviates slightly from the predicted Arrhenius law for diffusivity dependence on temperature. Nevertheless, since these processes go hand in hand in chemisorption, the regressed rate parameters can be used to describe the combined effects for a given reactive system given that the pellet size is small enough.

Furthermore, to investigate the effect of varying inlet concentration of hydrogen sulfide on Cooper model's regressed parameters, experiments were conducted at inlet contaminant concentration levels of 980, 1380 and 2200 ppm-vol. The experiments were run at room temperature and pressure using 125 µm pellets of the CuO-based sorbent. Figure 3-13 shows the breakthrough curves collected for the runs along with the Cooper model fits. Varying concentration, for small pellet size, didn't affect the behavior of the breakthrough curve which followed Cooper model for the three concentration levels. The regressed rate parameter, *k*K, increased slightly from 5.0 s^{-1} at 980 ppm to 7.7 s^{-1} at 1380 ppm-vol then dropped down to 6.4 s^{-1} at 2200 ppm-vol. This suggests that changing concentration of feed has no effect on rate parameter which aligns with that the rate of diffusion through solid products, rate determining at this pellet size, has no contributions from elementary reaction steps. Moreover, the removal capacity stayed

constant at around 12.5 wt. % and both Cooper and Bohart-Adams estimates were within 10.4 % of the mass balance estimate, q_s.

Finally, to investigate the effect of varying the total pressure of the reactor on regressed parameters, experiments were conducted at total pressure of 1.0, 1.4, 1.6 and 2.0 atm. The experiments were run at room temperature and an inlet concentration of 1000 ppm-vol using 500 μm pellets of the sorbent. This pellet size was picked to allow for studying the effect of pressure on the two contributions of rate parameter that are relevant at this pellet size: pore diffusion and solid diffusion through products. Figure 3-13B shows that the breakthrough curves followed the Bohart-Adams breakthrough fit for all pressure levels which is expected for this pellet size. Table B-1 shows that no trend was observed in the effect of increasing pressure on rate parameter. The rate parameter consists, at this pellet size, of two contributions: rate of pore diffusion and rate of diffusion through products. For pore diffusion, the molecular diffusivity, D_M, which contributes to effective diffusivity, D_p, is inversely proportional to pressure (Equation 17). Nevertheless, this contribution constitutes only 2-5% of D_p at these tested conditions which explains the lack of dependency. On the other hand, diffusion through product layer is only dependent on the thickness of the product layer and temperature as previously discussed. The tabulated values in Table B-1 also show that no change in sulfidation capacity was observed as pressure increased and both models provided estimates of removal capacity within 11.0% of mass balance estimates.

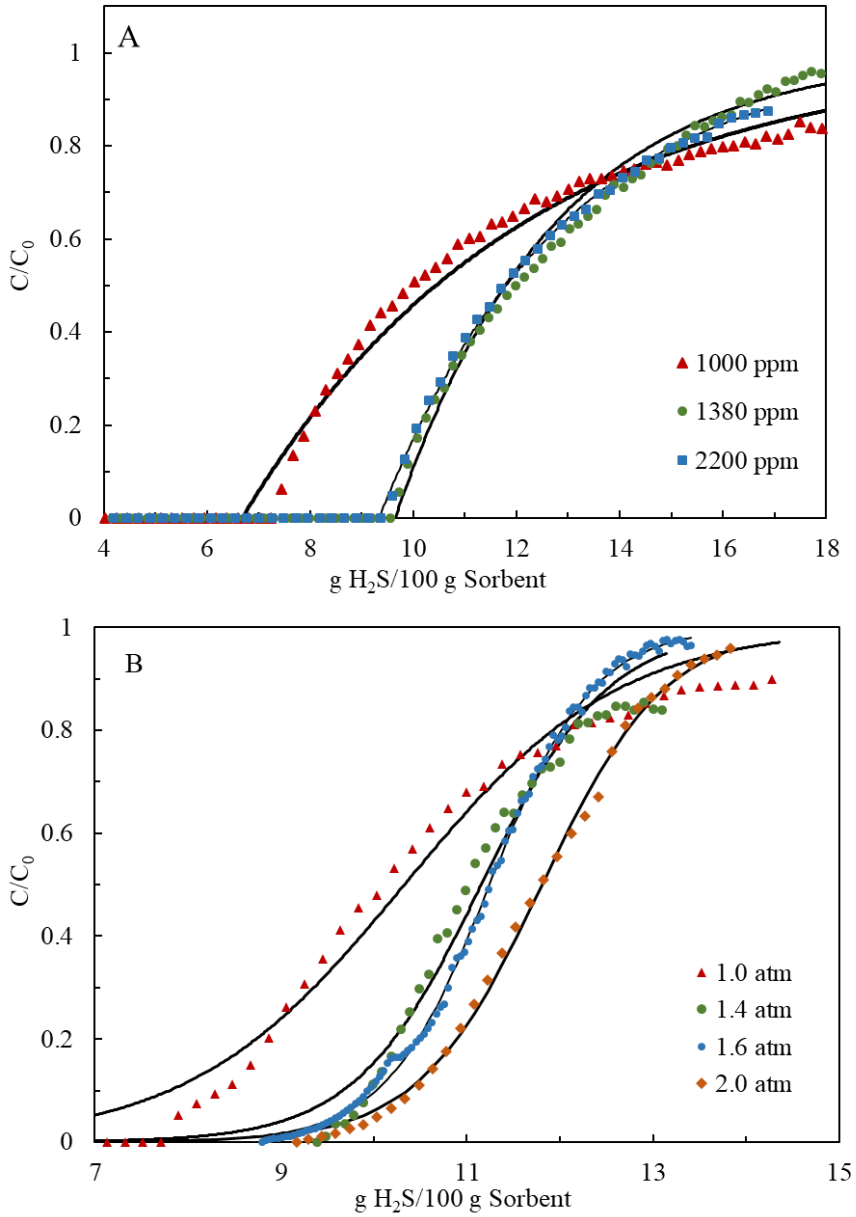

Figure 3-13: Breakthrough curves of normalized outlet hydrogen sulfide concentrations collected for fixed beds of the CuO-based sorbent at A) 1000, 1380 and 2200 ppm-vol H_2S/N_2 (125 µm) and B) 1.0 atm, 1.4, 1.6 and 2.0 atm (500 µm) both at a temperature of 294 K .

3.4 Study Conclusions

In this study, linear driving force models were used to fit breakthrough profiles of H_2S contaminant obtained from fixed beds of CuO-based sorbent for a wide range of conditions. The experiments resulted in deep desulfurization of the feed stream from 1000-2200 ppm to 0-50 ppm.

For runs at room temperature, an average of 42 % of the maximum saturation capacity was achieved (12.5 wt. %) with negligible effects of changing inlet concentration, total pressure or contact time. Cooper model provided good fit for the breakthrough behavior for runs where pore and bulk diffusion resistances weren't dominant (125-212 μm pellet size) at room temperature, while Bohart-Adams captured the shape of the breakthrough curves for the larger pellets' runs (≤ 800 μm) and higher temperatures. Both models provided predictions for removal capacity within 11% of the mass balance estimated capacity at room temperature.

The reproducibility of the models' predictions was demonstrated by varying contact time (changing flowrate and/or bed depth) which proved to have no significant effect on the models' regressed parameters. Cooper's regressed rate parameter was used to predict the reaction/diffusion through products rate parameter, k_{rxn}, (5.8 s^{-1}) at room temperature and pressure for small pellets where the estimated pore and bulk diffusion resistances are negligible. At larger pellet sizes (800-1000 μm), the estimated pore diffusion resistance dominated which makes implementing Bohart-and-Adam model in an industrial setting a feasible option since the pellets' sizes are an order of magnitude larger than the tested pellet sizes. Cooper model predicted, reasonably, the changes in k_{rxn} with temperature (298-423 K) which followed an Arrhenius equation. Finally, variations in total (1.0-2.0 atm) and partial pressure (1000-2200 ppm-vol) of H_2S contaminant had no significant effect on the apparent rate parameter which is expected since the surface reaction is highly irreversibly and, thus, k_{rxn} provides insight into the dominating CuO/CuS interface diffusion resistance rather than the surface reaction kinetics. The ability of the model to elucidate the diffusivity at the CuO/CuS interface, within the established limits of the model, can be used to compare sorbents' microkinetic performance of similar chemical composition but varying structure and morphology.

Chapter 4 | Effects of Morphology and Surface Properties of Copper Oxide on the Removal of Hydrogen Sulfide from Gaseous Streams

4.1 Introduction

Because of the chemical affinity of H_2S for metallic cations, chemical reaction with a solid metal oxide is a frequently used technique to purify natural gas from trace levels of sulfide constituents that often remain even after amine scrubbing. Such reactive sorption processes are advantageous because they are thermodynamically more favorable than physisorption leading to higher purity streams and higher solid phase contaminant capacities. Zn, Fe, Ca, Mn, and V metal oxides have been studied rather extensively in the literature as adsorbents for H_2S removal at elevated temperatures (>573 K).[191–198] Despite possessing favorable thermodynamics ($\Delta G_{T=298}$ = 126 kJ mol^{-1}, -76 kJ mol^{-1}, -74 kJ mol^{-1} and -136 kJ mol^{-1} for CuO, ZnO, Fe_2O_3, and NiO, respectively)[17] these oxides when reacted with H_2S at room temperature suffer from low removal capacities due to (1) slow ion migrations to and from the lattice structure, (2) sintering,[199] (3) mechanical disintegration,[199] (4) diffusional resistance,[200,201] and/or (4) limitations in the number of adsorption sites.

Of the previously reported oxides that can remove H_2S at low temperatures, CuO has garnered interest because of the favored sulfidation thermodynamics of Cu^{2+} and Cu^{+1} at room temperature. The high equilibrium constant of CuO sulfidation ($K_s = 6.8 \times 10^{20}$ at 298 K)[202] enables CuO to reduce H_2S from several thousand ppm down to sub-ppm levels. Realizing this advantage, current research efforts have focused on (1) synthesizing small CuO nanoparticles and supporting them on mesoporous materials (e.g., activated carbon, SiO_2, Al_2O_3, clay, and modified zeolites),[199,203–205] or (2) combining other metal oxides (e.g., Zn, Fe, Al, V, and Mo-based) with

CuO,[200,206,207] to create materials with improved thermodynamic stability and/or kinetics. However, because most of the literature deals with such supported or mixed oxide materials as well as high-temperature H_2S removal processes to avoid kinetic limitations imposed by ambient conditions, little work has been done on unsupported, pure CuO at these milder ambient conditions. Knowledge about several parameters such as the influence of synthesis procedures and crystallite size at low temperatures on reactivity is therefore critical to the use of reactive sorbents in purification processes.

In this work, pure CuO sorbents with varying properties (crystallite sizes, surfaces areas, pore volumes, and purities) and morphologies were synthesized via sol-gel, co-precipitation, hydrothermal treatment, hydrolysis, and electrospinning, and reacted with 1000 ppm-vol H_2S/N_2 in a fixed bed reactor at room temperature and pressure. The sulfur removal capacity, q_s (g H_2S/100 g sorbent), was estimated by a sulfur mass balance across the reactor. The overall rate parameter, k, was evaluated by analysis of the collected breakthrough curves using Cooper[182,208] linear driving force model. Sol-gel, co-precipitation, hydrothermal treatment in the presence of a polymer, and hydrolysis were used to fabricate CuO nanoparticles with appropriate properties (i.e., small crystallite sizes) for this reaction as the literature indicates that high surface areas, porous structures, and nano-sized particles with small cluster sizes are advantageous for metal oxide desulfurization.[209] Electrospinning, which is a simple, easy-to-use electrostatic fabrication technique, was used to generate one-dimensional Cu-containing nanofibers with varying fiber diameters, which were later thermally treated to remove the polymer matrix and form CuO nanofibers. Different polymers (PVP, PEO and P123) and treatment temperatures (353-823 K) were used to probe the effect of purity (i.e., residual carbon remaining on the surface of the sorbent) on CuO activity.

4.2 Experimental Methods

4.2.1 Materials and synthesis methods

4.2.1.1 Sol-gel synthesis of CuO nanoparticles

Polyvinylpyrrolidone (PVP) (M.W. 1,300,000, Sigma-Aldrich), PVP (M.W. 40,000, Sigma Aldrich), polyethylene oxide (PEO) (M.W. 300,000, Alfa Aesar), copper (II) nitrate trihydrate (Sigma Aldrich, 99%), copper (II) acetate monohydrate (Sigma Aldrich, 99%), poly(ethylene glycol)-*block*-poly(propylene glycol)-*block*-poly(ethylene glycol) (P123; Sigma Aldrich, M_n ~ 5,800), methyl alcohol anhydrous (Sigma-Aldrich, 99.8%), sodium hydroxide (BDH, 97%), glacial acetic acid (VWR, ACS grade) and ethyl alcohol (Sigma-Aldrich, 100%) were purchased and used without subsequent purification.

4.2.1.2 Sol-gel synthesis of CuO nanoparticles

CuO nanoparticles were prepared using an acid-catalyzed sol-gel process.[210] 1.0 cm^3 of glacial acetic acid was added to 300 cm^3 of 0.02 M copper (II) nitrate or copper (II) acetate solution under vigorous stirring and heating. At boiling point, 0.8 g of sodium hydroxide was added to the solution with continuous stirring. The solution was then allowed to cool to room temperature while a black precipitate continued to form and settle in the bottom of the beaker. The precipitate was then vacuum filtered or centrifuged for 10 minutes (JA-14 rotor) at 293 K and 6000 RPM. The supernatant was then poured off and the precipitate was washed with deionized water and ethanol. The washed precipitate was dried in a furnace for 8 h at 313 K and then samples were either collected or thermally treated a second time at higher temperatures to achieve particles of various crystallite sizes. Thermal treatment was performed by heating samples at a ramping rate of 1 K h^{-1} and holding the furnace temperature at 623 K, 823 K or 1023 K for 4 h. The samples prepared

via this technique are denoted as NP-X, where X is the sample number (NP-1 to NP-6). Table shows the specific synthesis conditions for making the sorbents prepared in this work.

4.2.1.3 Co-precipitation of CuO nanoparticles

CuO nanoparticles were prepared by a drop-wise addition of aqueous 0.1 M sodium hydroxide solution to aqueous 0.1 M copper (II) nitrate trihydrate solution under continuous mixing. The obtained material, copper (II) hydroxide, was then vacuum filtered with distilled water and ethanol, dried in air at 353 K for 14 h, and then thermally treated in air at 773 K for 4 h at a ramping rate of 1 K h^{-1}. The sample prepared via this technique is denoted as NP-7.

4.2.1.4 Co-precipitation of CuO nanobelts

CuO particles with belt-like shapes were prepared by dropwise adding 5 M sodium hydroxide solution to aqueous 0.6 M copper (II) nitrate trihydrate solution under continuous mixing. The solution was then aged for 3 days and precipitates were then vacuum filtered and washed using ethanol and deionized water. The washed precipitates were dried overnight at 333 K and then thermally treated in air at 623 K for 4 hours. This material is denoted as NB-1.

4.2.1.5 Hydrolysis and precipitation of CuO flowerlike nanostructures

CuO flowerlike nanostructures were synthesized using a facile route by hydrolyzing a copper acetate solution.[211] In a typical synthesis, 100 cm^3 of 0.02 M copper acetate solution was dissolved in deionized water in a beaker, and heated from room temperature to 373 K for 45 minutes. After hydrolysis and crystallization, the black precipitate formed in the solution was centrifuged and washed with DI water and ethanol and dried overnight in air at 353 K. The nanostructures prepared via this technique are denoted as FP-1.

4.2.1.6 Co-precipitation of CuO nanoflake-based flowerlike hierarchical nanostructures

Nanoflake-based flowerlike CuO nanostructures were synthesized via thermally decomposing a $[Cu(NH_3)_4]^+$ solution, without the aid of any surfactants.[212] In a typical synthesis, 0.5 or 2.0 g of copper nitrate was dissolved in 50 or 30 cm^3 of deionized water in a sealed bottle. Ammonia (~ 1-3 cm^3) is then added dropwise until a change of color is observed (darker blue). The bottle is then sealed tightly and heated to 353 K for 8 h or 376 K for 24 h, while stirring. After that, the black precipitate that formed in the bottle was washed with distilled water and ethanol to remove impurities and then centrifuged. The centrifuged solid was dried in a drying oven (353 K) overnight. The solids collected from this synthesis technique are denoted as FP-2 (353 K) and FP-3 (376 K).

4.2.1.7 Hydrothermal synthesis of CuO nanoparticles

A porous CuO sample was synthesized according to the method of surfactant-assisted hydrothermal interaction using CuO powder as starting material.[213,214] The polymer-containing solution was prepared by dissolving either 0.65 g of P123 or 0.65 g, 0.52 g, 0.26 g or 0.13 g of PVP (M.W.=1,300,000) in 15 cm^3 of water while stirring for 2 h. After that, 0.65 g of CuO (NP-7) was added to the beaker and the solution was left to stir at 800 rpm for 48 hours. The solution was then ultrasonically treated for 1 h and transferred to a glass tube reactor (cylindrical pressure vessel) for hydrothermal treatment at 383 K for 24 h. The black solid substance was centrifuged and washed with DI water and ethanol for the removal of the majority of the P123 surfactant or PVP polymer. The solid was then dried overnight in a drying oven at 353 K. The as-obtained material was subsequently thermally treated in air from room temperature to 823 K for 4 h at ramping rate of 2 K min^{-1} for the generation of CuO. These materials are denoted as NPC-1 (P123), NPC-2 (0.65 g PVP), NPC-3 (0.52 g PVP), NPC-4 (0.26 g PVP) and NPC-5 (0.13 g PVP).

4.2.1.8 Electrospinning of PVP-$Cu(NO_3)_2$/PEO-$Cu(NO_3)_2$ and CuO nanofibers

Polymer solutions were prepared by dissolving PVP M.W.=1,300,000 (1.30-1.75 g), PVP M.W.=40,000 (10.5 g) or PEO M.W.=300,000 (2.7 g) in solvent (methanol or ethanol; 22-25 cm^3). The polymer solution was then vortexed (Fisher Scientific Digital Vortex Mixer) at 3000 rpm for 1 h until the polymer was completely dissolved. The solution was left to settle for 10 minutes, transferred to a beaker, and stirred for 0.5 h. The metal containing solution was prepared by dissolving copper (II) nitrate (0.15-4.0 g) in 5-10 cm^3 of DI water and stirring the solution for 0.5 h. The copper containing solution was then added dropwise to the polymer containing solution. The solution was stirred for 0.25 h, and then vortexed for 0.5 h at 3000 rpm.

The electrospinning solution was placed in a 10 mL syringe (BD 10 mL syringe with Luer Lok™ tip) with a hypodermic needle (Monoject™ Standard 30G x ¾"). The distance between the tip of the needle and a stainless-steel collecting plate, which was covered with aluminum foil, was 6-22 inches. A Gamma High Voltage Research ES75 power supply was used to apply 20-35 kV on the polymer jet while the polymer solution was extruded through the needle at a rate controlled by a syringe pump (1.0-5.0 $cm^3\ h^{-1}$; Kent Scientific Genie Plus). Dry air was circulated inside a 3 m^3 chamber at 6 $cm^3\ min^{-1}$ to control the relative humidity at 19.5 ± 2%. All electrospinning was carried out at ambient conditions, temperature (294 ± 3 K) and pressure (101 kPa). The collected fibers were thermally treated in air at 773-898 K for 2-10 h at a ramping rate of 0.4-2.0 $K\ min^{-1}$ to remove the majority of PVP/PEO and form CuO. The CuO nanofibers are denoted as NF-X (NF-1 to NF-6) in Table C-1.

4.2.2 Characterization

The synthesized CuO sorbents prepared via sol-gel, co-precipitation, hydrothermal treatment, hydrolysis, and electrospinning, as described in Section 3.2.2 were characterized using a variety of techniques. Powder X-ray diffraction patterns were obtained on an X-ray diffractometer (JEOL JDX-3530 and Philips X-Pert) using Cu Kα radiation of 1.5410 Å to identify the CuO phases. The average crystallite sizes were found using Scherrer's formula. Nitrogen adsorption-desorption isotherms were measured at 77 K with a Micrometrics ASAP 2020 Plus system. Before measurements, the samples were degassed at 1×10^{-3} Torr and 573 K. The Brunauer-Emmett-Teller (BET) surface areas were calculated from the isotherms by using the BET equation. The pore size distribution was derived from the adsorption branches of the isotherms using the Barrett-Joyner-Halenda (BJH) model.

Scanning electron microscopy (NOVA 230 Nano SEM) was used to determine the morphology of the sorbents. The mean diameter and size distribution (standard deviation) of the electrospun nanofibers were calculated from the SEM micrographs using ImageJ software (n = 250; where, n is the number of fibers that were measured and averaged). Microstructure of the particles was imaged using scanning transmission electron microscope (STEM) Titan (Thermo Fisher Scientific) operating at 300 kV and equipped with the X-MaxN 100TLE (Oxford) detector for energy dispersive spectroscopy (EDS) analysis. Windowless EDS detector was used with high counts rate to optimize the detection of light elements. Samples were prepared by direct deposition of the dry powder onto the carbon film supported TEM grids. EDS spectral maps of individual particles were acquired with the pixel size 2.5 nm in continues mode. Maps were stopped after satisfying elemental images were attained with full map acquisition time varied between 10-20 min. Line scan profile results of individual particles were generated from acquired spectral images.

Thermogravimetric analysis was conducted in a Perkin Elmer TGA. Alumina crucibles were used to hold the samples. Gas flowrates were set to 200 standard cm^3 min^{-1} to minimize external diffusion from the bulk gas to the sample interface. Heating/reaction occurred in air (Matheson UHP Argon, 99.999% purity) at a ramping rate of 10 K min^{-1}. XPS was conducted with PHI 3057 spectrometer using Mg Kα X-rays source at 1286.6 eV. All binding energy values presented in this paper were charge corrected to C 1s at 284.8 eV. For the interpretation of the spectra, the literature positions were applied.[215]

4.2.3 Fixed-bed experiments

Reactive adsorption of H_2S was studied in an apparatus with plug-flow hydrodynamics shown schematically in Figure 3-2. Copper (II) oxide samples (120-200 mg) were sieved to 75-155 μm agglomerate diameter and packed between plugs of quartz wool in a 0.25-inch outer diameter tubular, stainless steel reactor. Flow rates of gaseous H_2S and N_2 (65 sccm) were introduced to the packed reactor via mass flow controllers (MKS GE50A and GM50A). Feeds to the reactors consisted of 1000 ppmv H_2S in N_2 and were produced by diluting a 1.0% H_2S (Praxair UHP) in N_2 mixture with UHP N_2. All the sulfidation tests were carried at ambient temperature and pressure. The compositions of feed and effluents were monitored using online gas chromatography (Agilent 7890B) with a sulfur chemiluminescence detector (SCD; Agilent 755) and continuous gas phase FTIR spectroscopy (MKS Multigas). All gas transfer lines and the interior of the reactor were treated with an inert coating (SilcoNert 2000) to mitigate H_2S adsorption onto tubing walls.

4.2.4 Computational study

Section 4.3.2 of this work features a computational study using Density Functional Theory (DFT) for the reaction mechanism of the dissociative adsorption of H_2S molecules on CuO {111} surfaces. This surface was picked because it is the most stable surface[134] found experimentally.

The dissociative adsorption of H_2S on a CuO surface involves several elementary steps, i.e., the molecular adsorption of H_2S on the surface, with subsequent dissociative steps, rearrangement of adsorbed species and formation of water, which overall corresponds to the stoichiometric reaction:

$$\boldsymbol{CuO + H_2S \rightarrow CuO_{1-x}S_x + H_2O} \qquad (\mathbf{20})$$

The net balance of the process is the exchange of one oxygen atom of the CuO surface by one sulfur atom provided by H_2S. The reaction mechanism was studied by determining the relevant stationary points for all the elementary steps, along with the potential energy surface (PES), using DFT together with a planewave basis set as implemented in the VASP code.[216–219] Exchange and correlation effects were treated within the generalized gradient approximation (GGA), using the Perdew–Burke–Ernzerhof (PBE) functional along with projector augmented-wave pseudopotentials.[120] Potential van der Waals interactions were considered by using the dDsC correction as implemented in VASP.[220] The planewave basis set cutoff was set to 450 eV. A Monkhorst-Pack scheme was used for sampling the Brillouin zone.

Due to the failure of conventional DFT functionals to properly account for the strong correlation effects among the partially filled Cu 3*d* states in CuO.[221] The Hubbard parameter, U, was introduced for the Cu 3*d* electrons to describe the on-site Coulomb interaction (GGA+U). Specifically, the values of U=7 eV and J=0 eV were adopted from the literature.[222] Upon

optimization of a bulk CuO unit cell to agree with experimental lattice parameters and the proper anti-ferromagnetic character, a CuO {111} model surface featuring a 2x1 CuO {111} supercell was built using the slab approach. The dimensions of the supercell were 11.6 Å x 6.1 Å, with a slab thickness of 7 Å and a vacuum region in the Z axis of 19 Å to avoid spurious electrostatic interactions between supercell instances. The model used can be seen in Figure 4-12.

4.3 Results and Discussion

4.3.1 Physio-chemical properties of CuO materials

XRD was used to identify the crystalline phases and average crystal sizes of the nineteen CuO sorbents prepared in this work, using the synthesis techniques described in Section 3.2.1. As shown in Figure 4-1 and Figure 4-2, all the XRD patterns collected show diffraction peaks which are characteristic of the planes of a single-phase monoclinic CuO. The average crystal domain size of the CuO sorbents calculated using Scherrer's formula based on the 38.8^{o} peak were in the range of 5 to 74 nm, with the majority of the sorbents having crystallite sizes less than 25 nm (Table C-1 and Table C-2). The XRD results show that, in general, sorbents that did not undergo thermal treatment in air at elevated temperatures (T > 773 K) as part of their preparation technique had significantly smaller crystallite sizes (< 20 nm). This effect is important to highlight because it was observed in this work that crystallite size influences the H_2S removal capacity of pure CuO sorbents, irrespective of other properties (such as, surface area, pore size, and pore volume) generated by the synthesis technique (discussed in detail in Section 4.2.1). Furthermore, the d-spacing obtained from the XRD data for all sorbents was in the range of 2.29-2.30 Å for the (200) plane, which is consistent with the literature[223], and indicative of phase pure monoclinic CuO.

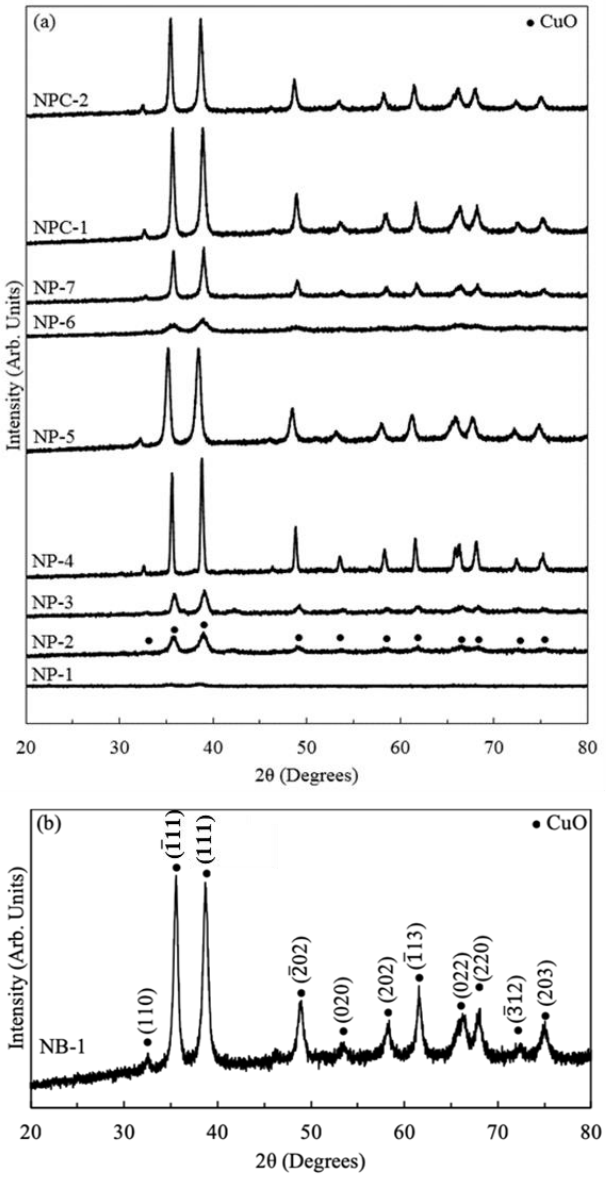

Figure 4-1: X-ray diffraction patterns of CuO sorbents. (a) Nanoparticles via sol-gel, co-precipitation, and hydrothermal treatment (NP and NPC) and (b) nanobelts via co-precipitation.

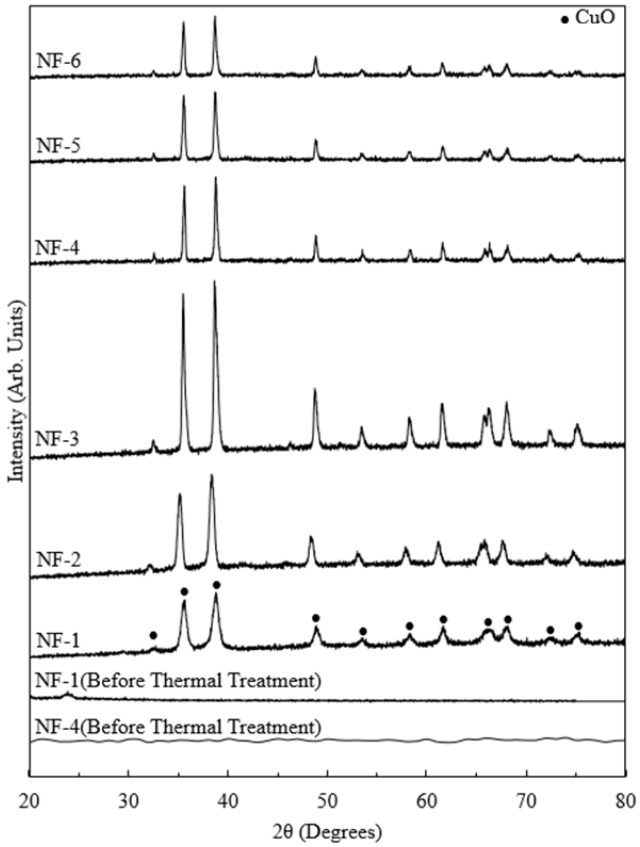

Figure 4-2: X-ray diffraction patterns of CuO nanofibers synthesized via electrospinning (NF) before and after thermal treatment.

Figure 4-2 also shows the XRD patterns of the as-synthesized NF-1 (PEO-$Cu(NO_3)_2$) and NF-4 (PVP-$Cu(NO_3)_2$) prior to any thermal treatment. Well defined diffraction peaks are absent from the XRD pattern of the pre-thermally treated NF-4 fibers, which indicates that these materials consist of amorphous PVP phases and copper species that are too small to diffract X-rays. Moreover, the XRD patterns of NF-1 (prior to thermal treatment) contains several small peaks consistent with PEO as well as copper nitrate peaks reported previously in the literature.[224,225] These results indicate that thermal treatment in air is required for the formation of CuO from the copper-species that exist in PEO or PVP nanofibers after electrospinning.

N_2-physiosorption was performed on one sample from each of the morphologically distinct groups (NP-4, NP-7, NB-1, FP-2, NPC-2 and NF-6) to determine the effect of synthesis method

on surface area and porosity. Table C-2 presents the structural parameters calculated from nitrogen adsorption. Analysis of structural parameters along with the degree of micro- and meso-porosity reveals differences in surface area and porosity among the sorbents. Specifically, sorbents that were prepared via precipitation (NP-7 = 58.8 $m^2 g^{-1}$ and FP-3 = 59.1 $m^2 g^{-1}$) possessed larger BET surface areas than those prepared from sol-gel (NP-1 = 14.5 $m^2 g^{-1}$), hydrothermal treatment (NPC-2 = 17.4 $m^2 g^{-1}$), and electrospinning (NF-6 = 2.79 $m^2 g^{-1}$). CuO nanobelts appear to be an exception to this observation with a surface of area 6.18 $m^2 g^{-1}$ which can be attributed to the long aging step (72 hours) in the synthesis procedure which can lead to micropore and mesopore closure. Additionally, NP-7 (precipitation) had pore volumes of 0.181 $cm^3 g^{-1}$ which is more than double that of FP-3 (0.079 $cm^3 g^{-1}$) despite their comparable surface area. These differences in total pore volume are the result of different pore size distributions. NP-7 consists of a larger concentration of pores in the 15 to 150 nm pore size range compared to FP-3, which has higher pore volume within the lower pore size range > 15 nm. In general, changes in pore volumes followed the same trend as for the surface area (i.e., samples with smaller pore volumes also exhibited lower surface area). The significantly lower surface area and low meso-porosity of the electrospun materials result from the formation of single CuO fibers with large intra-fiber interstices as determined by SEM (Figure 4-3(h)).

SEM was used to investigate the effect of preparation technique on the morphology of the synthesized materials. Figure 4-3 shows the SEM images (20,000 times magnification) of the representative CuO materials synthesized in this work—Nanoparticle samples: NP-1, NP-5, NP-7; Nanoparticles synthesized with polymer: NPC-1; Nanobelts: NB-1; Flower-shaped particles: FP-2, FP-3; and Nanofibers: NF-4. These SEM images reveal that various CuO morphologies and dimensionalities can be obtained by simply varying the preparation technique. Figure 4-3(a-b)

shows that nanostructures prepared via sol-gel (NP-1, NP-5) were found to have irregular particle shapes with varying domain sizes depending on the copper precursor (average domain size of 4.5 ± 1.47 µm for copper (II) acetate in Figure 1(a**)** and 1.3 ± 0.4 µm for copper (II) nitrate NP-5).

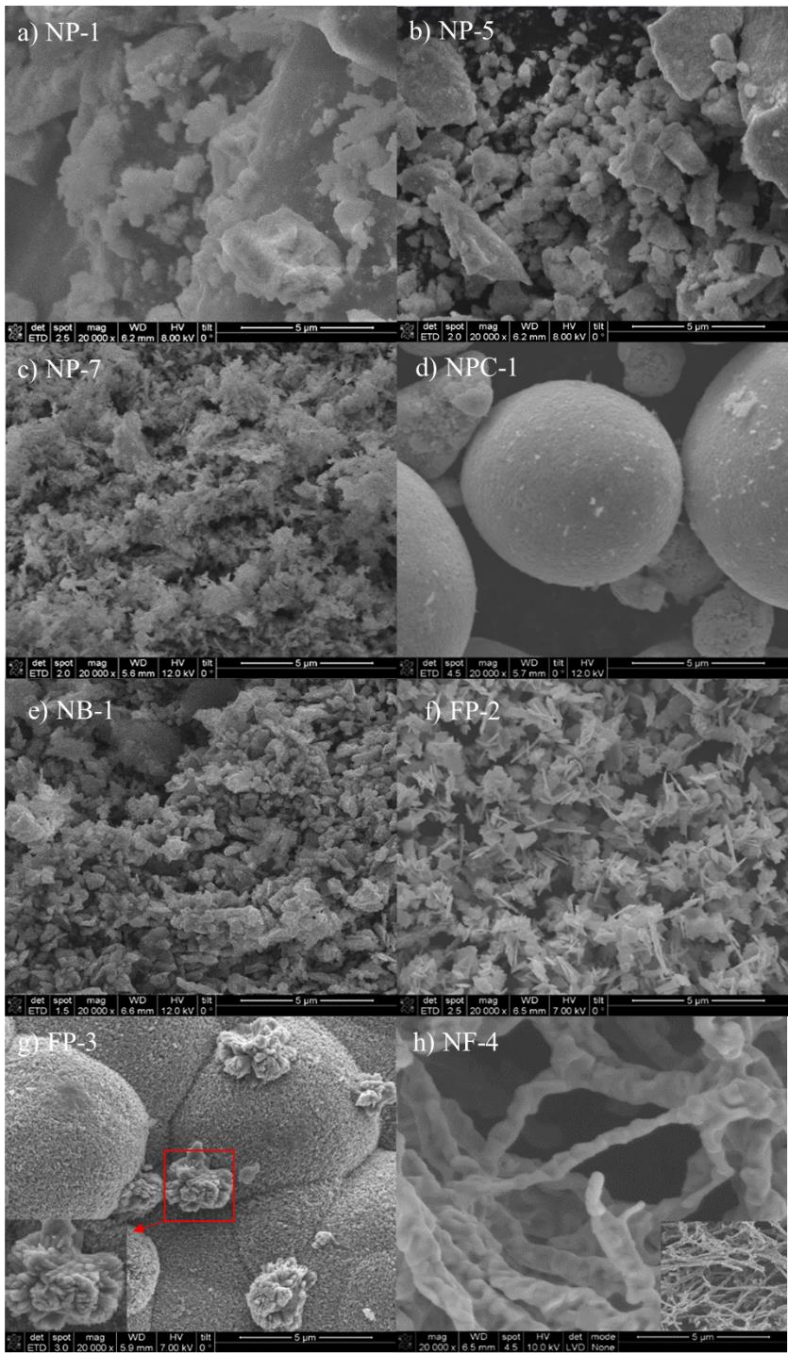

Figure 4-3: SEM images at 20,000 times magnification of a select group of CuO sorbents with different morphological features prepared via various synthesis techniques (e.g., sol-gel, precipitation , hydrothermal treatment with the aid of a polymer, hydrolysis, and electrospinning).

Unlike sol-gel, which yielded materials that were irregular in shape, precipitation, hydrothermal treatment and electrospinning, yielded materials with regular, defined shapes and structures. For instance, by hydrothermally treating NP-7 (Figure 4-3(c)) in the presence of P123 (NPC-1), closely aggregated and distinctly spherical CuO particles were formed, with sizes ranging from 5 to 9 μm as seen in Figure 4-3(d). Properly aging a precipitated CuO sample (NP-7) lead to nanobelt-like materials as shown in Figure 4-3(e). The effect of reaction time and metal concentration on precipitation of flowerlike particles (FP-2 and FP-3) can also be observed in Figure 4-3(f-g). As the reaction time and copper precursor concentration were increased, flowerlike structures formed (Figure 4-3(g)), with an average size of 2.7 ± 0.9 μm. At low concentrations and temperatures, however, instead of forming these micron-sized flowerlike structures, petal-like structures are formed (0.5-2 μm) (Figure 4-3(f)).[226] Lastly, Figure 4-3(h) shows how electrospinning can result in the fabrication of a highly porous, fibrous structure, with significant macro-porosity (NF-4). The fibers formed via electrospinning (NF-4) after undergoing thermal treatment had an average diameter size of 629 ± 194 nm (measured using ImageJ, n=250). The SEM images, indeed, confirm that different synthesis techniques yield nanomaterials with markedly different morphological features while also shedding light on the growth mechanism of CuO nanostructures as a function of synthesis condition.

TGA experiments were conducted on pure PEO (M.W.=300,000), pure PVP (M.W.=1,300,000), and NF-4 (prior to thermal treatment; PVP-$Cu(NO_3)_2$) to quantify the extent of polymer removal during thermal treatment (i.e., quantity of residual carbon left after treatment) and provide evidence of the conversion of copper nitrate to CuO. Figure 4-4 shows the TGA curves of pure PEO, pure PVP, and NF-4. All three samples were decomposed under air at a heating rate of 10 K min^{-1}. The nanofibers synthesized using pure PEO (M.W.=300,000)

decomposed under air in a single step, with a total weight loss of approximately 99%. The TGA results prove that at the 823 K, the majority of the PEO polymer is removed. The nanofibers synthesized using pure PVP (M.W.=1,300,000), on the other hand, decomposed under air in two steps, with a total weight loss of approximately 93.7% at 773 K, 94.2% at 823 K, and 94.7% at 897 K, which is a slightly lower weight loss percentage than PEO (Figure 4-4).

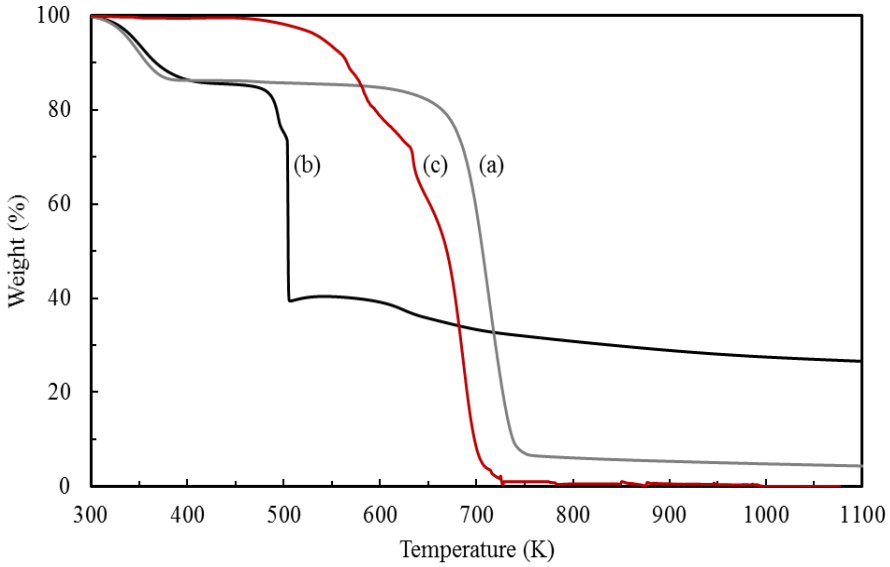

Figure 4-4: Weight loss profiles as a function of temperature from thermogravimetric analysis (TGA) of (a) pure PVP (M.W.=1,300,000), (b) NF-4 prior to thermal treatment (PVP-Cu(NO3)2), and (c) pure PEO (M.W.=300,000) nanofibers.

In the case of PVP, the first step weight loss of 16% occurred between ambient temperature and 622 K and was attributed to the evaporation of volatile solvents. The second step weight loss of 78% from 623 K to 773 K was attributed to the thermal degradation of the PVP chains. It is clear from the TGA curve that the majority of the PVP matrix (much like in the case PEO) is removed at temperatures higher than 773 K and only a small amount of carbon residue is left, albeit this amount of carbon residue is slightly higher in the case of PVP (due to the presence of more carbon atoms in the PVP monomer than in PEO). The work of Borodko

et al. further supports the presence of residual carbon after the thermal treatment of PVP at elevated temperatures.[227] Using spectroscopic techniques, the authors studied the degradation of PVP and showed that in an oxygen atmosphere, the PVP forms a polyamide-polyene-like material at temperatures above 523 K. At temperature above 573 K, these materials transform into amorphous carbon. Lastly, NF-4, an electrospun nanofiber sample consisting of PVP (M.W.=1,300,000) and $Cu(NO_3)_2$, decomposed under air in two steps, with a total weight loss of approximately 84% (Figure 4-4). These total weight losses in air are consistent with the complete conversion of copper nitrate to CuO. Thus, the first step weight loss can be attributed to the evaporation of volatile solvents, and the second can be attributed to the decomposition of the PVP chains and the conversion of copper nitrate to CuO. Figure 4-4 also reveals that the decomposition of NF-4 (475 K) occurs at a much lower temperature than pure PVP (640 K) indicating the effect of copper nitrate, which weakens the bonds within the PVP chains, and of the nitrate anions, which act as an oxidant to combust the polymer. These TGA results are in agreement with the results from the other characterization techniques described in this section, as they provide quantitative evidence of the removal of the majority of the polymer (PEO or PVP), decomposition of the copper nitrate, and formation of CuO during the thermal treatment of electrospun nanofibers (e.g., NF-4) in air while also hinting at the presence of small amounts of amorphous carbon remaining in the sorbent after thermal treatment of the as-synthesized fibers.

To further probe the presence of carbon and quantify its amount on the surface of the oxide sorbents, X-ray photoelectron spectroscopy (XPS) experiments were performed. Figure 4-5 shows the overall XPS spectra as well as the spectra of the C 1s core level for a select group of sorbents (NP-7, NPC-2, and NF-4).

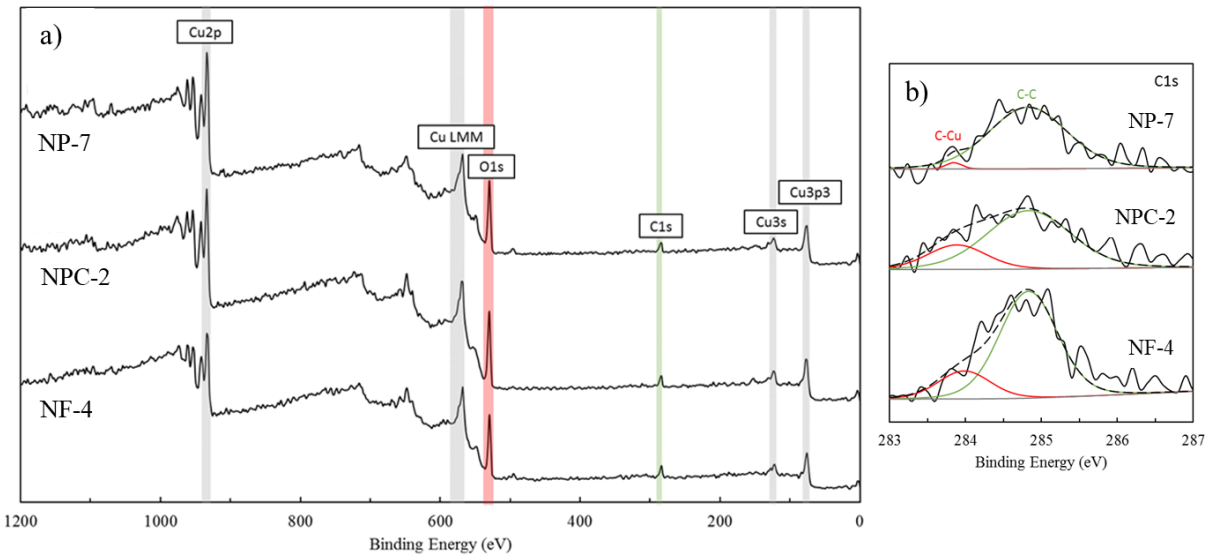

Figure 4-5: XPS spectrum of CuO nanomaterials (NP-7, NPC-2, and NF-4) prepared via precipitation (no polymer), hydrothermal treatment in the presence of PVP (M.W.=1,3000,000), and electrospinning, using PVP (M.W.=1,300,000) as a template, respectively. (a) Wide spectra of the copper oxide sorbents, (b) high-resolution spectra of C 1s, with peak fittings corresponding to C-C and C-Cu.

As mentioned in Section 4.2.1 and Table C-1, NP-7 was a CuO sorbent that was prepared via precipitation , NPC-2 was a CuO sorbent that was prepared by hydrothermally treating NP-7 in the presence of PVP (M.W.=1,300,000), and NF-4 was a CuO nanofibrous sample that was synthesized using electrospinning from a copper nitrate precursor in the presence of PVP. In the case of both NPC-2 and NF-4, the weight ratio of PVP to Cu added during synthesis was 1:1 whereas no polymer was added in the case of NP-7. The XPS results reveal the presence of CuO nanocrystals, as shown by the Cu 2p3/2 peaks in Figure 4-5, for all three sorbents. The binding energy of the Cu 2p3/2 peaks was found to be 933.6 eV, which is in agreement with the literature.[228,229] Additionally, the intensities of the Cu 2p shake-up peaks obtained from the CuO sorbents is close to the ratio characteristics of reference CuO.[215] Figure 4-5(b) shows the C 1s spectra for three selected CuO sorbents. In Figure 4-5(b), the C 1s peak has the highest intensity, demonstrating the presence of carbon. The main carbon peak at 284.8 eV corresponds to the C-C bonding (all three sorbents contain this C-C bond) while the shoulder

at 283.3 eV corresponds to the C-Cu bonding energy, which is mainly due to the carbon residue remaining on the surface of the sorbent after thermal treatment. Fitting results of the C 1s high-resolution XPS spectra were used to quantify the amount of C-Cu present in each sorbent. The fittings reveal that NPC-2 and NF-4 contained 22% and 19% C-Cu, respectively, whereas NP-7 contained less than 2% C-Cu. XPS results for other samples, summarized in Figure 4-6, show a variation in surface C-Cu percentage ranging from 19% to 50%. The XPS results discussed in this section signify the impact of synthesis (i.e., the utilization of a polymer or a surfactant) on the amount of residual carbon (C-Cu) present in the sorbent which is important for the evaluation of sulfur removal performance.

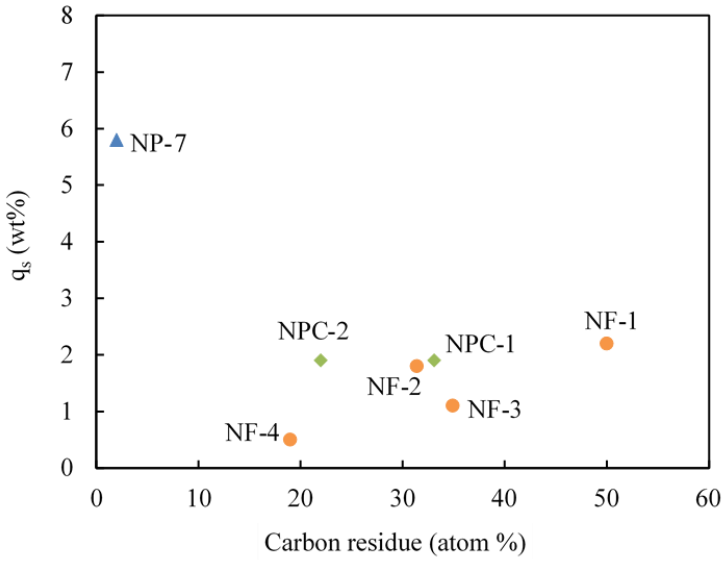

Figure 4-6: Effect of carbon residue on carrying capacities of CuO nanofibers and nanoparticles via hydrothermal treatment. X-ray photoelectron spectroscopy (XPS) was used to determine carbon residue on the samples.

4.3.2 Effect of crystallite size on H_2S removal

To probe the effect of morphology and crystallite size on H_2S removal performance, the capacities of the sorbents synthesized in this work for H_2S removal were measured during fixed bed experiments. The capacities are defined as g H_2S per 100 g of sorbent (wt%) where

complete sulfidation of CuO corresponds to 42 wt%. Capacities were determined by introducing a feed with a nominal concentration of 1000 ppm-vol H_2S in N_2 and monitoring the H_2S concentration in the reactor effluent (as described in Section 4.2.3). Experiments were terminated after the concentration of the effluent was equal to the inlet concentration, and H_2S capacities were calculated from the mass differential between the inlet and outlet of the reactor over the course of the experiment.

The capacities were plotted as a function of surface area, total pore volume and microscopic domain size, Figure 4-7(a-c), but no apparent correlation was observed between capacity and any of these parameters. In contrast, Figure 4-8 shows that H_2S capacity is inversely proportional to crystallite size (from a range of 5-26 nm) regardless of synthesis procedure and thus, regardless of morphology, surface area, and pore structure. Samples with crystallites >26 nm exhibited similarly low capacities (0.4-0.5 wt%) across a broad range of sizes (26-75 nm). These results indicate CuO crystallite size is the critical parameter that influences H_2S removal performance and that a critical crystallite size exists at ~26 nm.

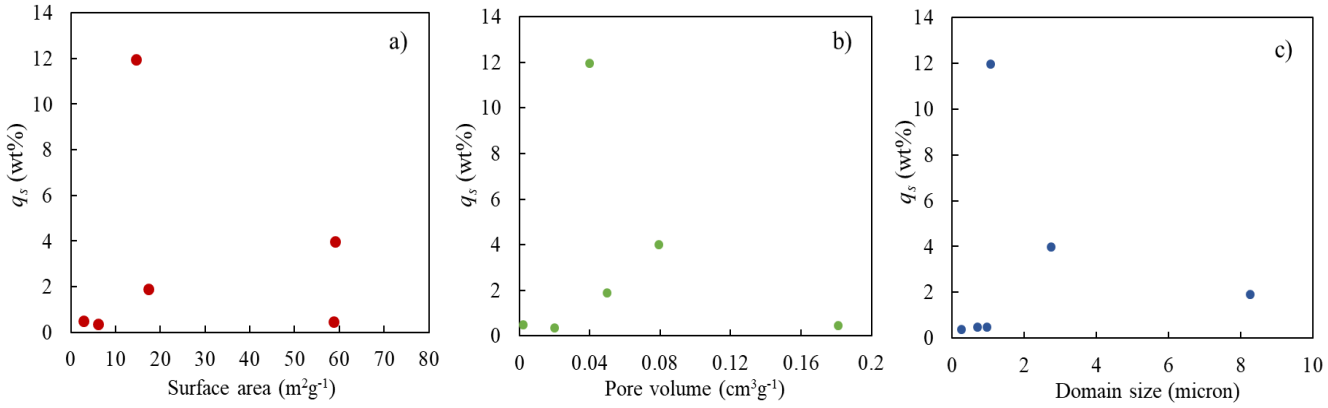

Figure 4-7: Effect of (a) surface area, (b) pore volume and (c) domain size on the carrying capacity. Brunauer-Emmett-Teller analysis was used to determine surface area, pore volume and domain size.

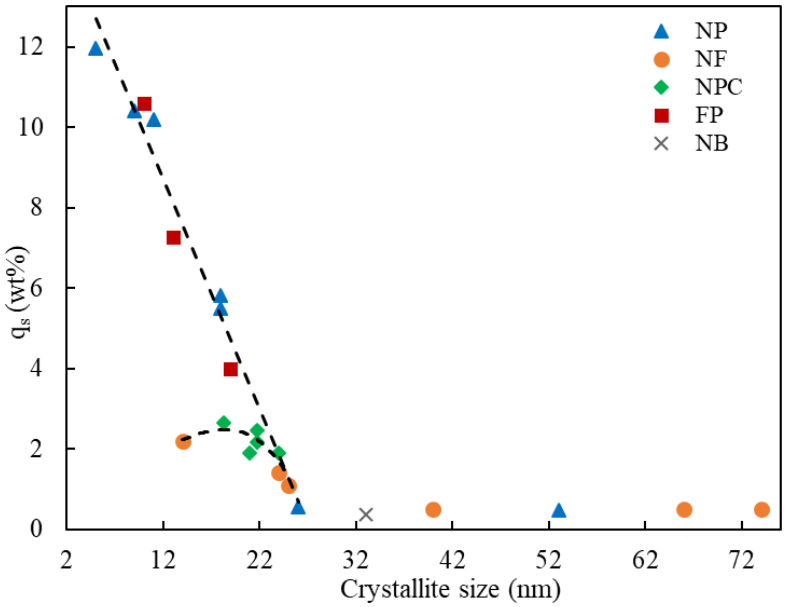

Figure 4-8: Effect of crystallite size of CuO sorbents prepared via various synthesis techniques as described in Table C-1 and Table C-2 on H_2S removal capacity at 1000 ppm-vol H_2S/N_2, 294 K and 1 atm.

TEM images and EDS elemental maps for sulfided NP-1 (5 nm crystals; 12 wt% capacity) and FP-3 (19 nm crystals; 4 wt% capacity) were collected to further probe the length scale that limits H_2S removal capacity. Figure 4-9(a) presents TEM scan of two NP-1 65-75 µm particles after sulfidation at 1000 ppm-vol at 298 K and 1 atm. The scans show nearly spherical particles with some microstructure details in particle 1. The dark areas in particle 1 correspond to unevenly distributed mesopores, and the absence of copper and sulfur in these regions confirms that these areas correspond to voids rather than topographical features. Figure 4-9(b-c) show the corresponding elemental maps for Cu K and S K series derived from EDS spectra. Figure 4-9(d) shows a cross-sectional elemental composition across the indicated line in the TEM image of particle 2. Again, sulfur appears to follow the same concentration trend as copper throughout the cross section.

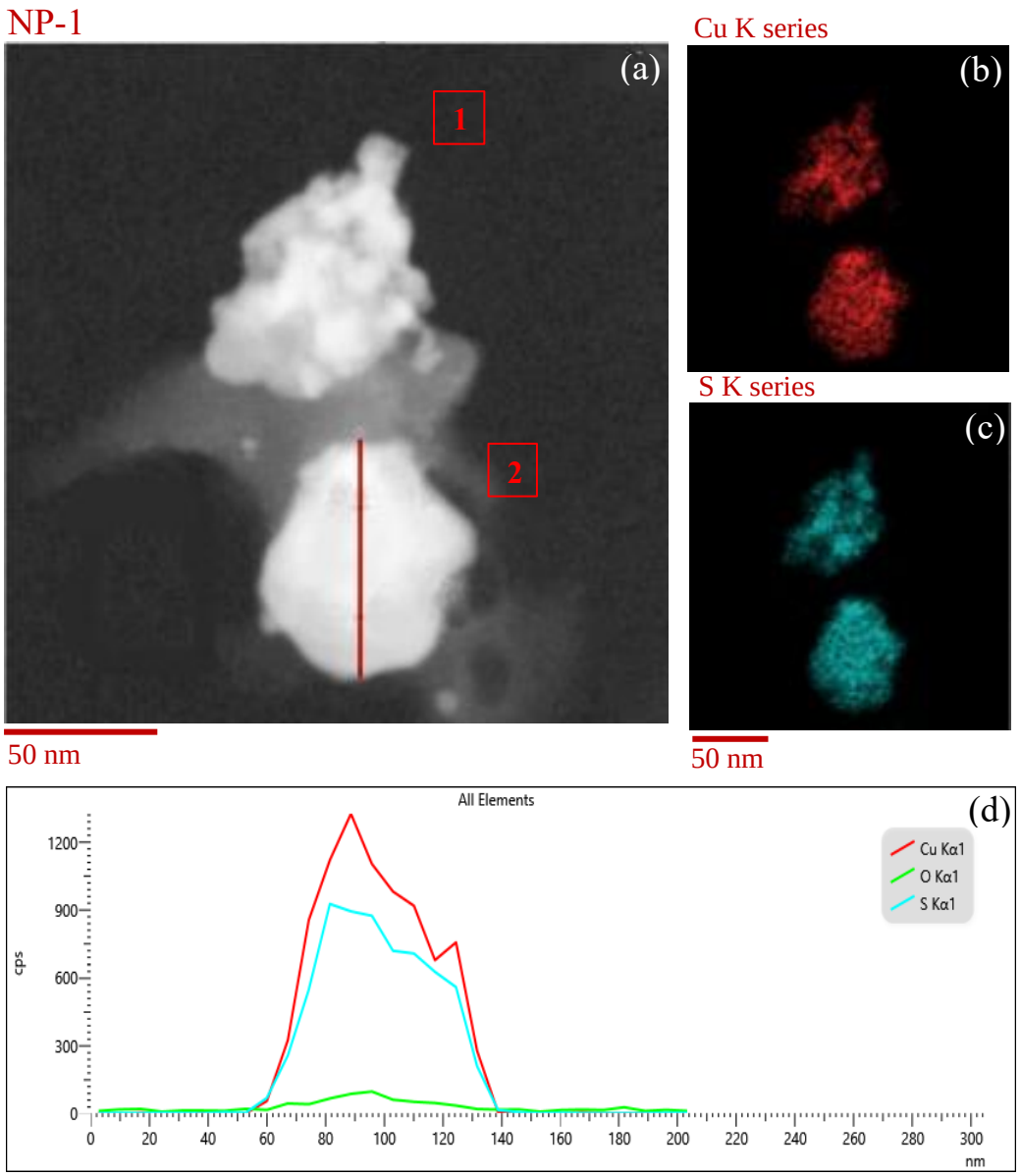

Figure 4-9: a) TEM image for two 65-75 nm particles of NP-1 sorbent after sulfidation at 1000 ppm-vol H_2S/N_2, 294 K and 1 atm. b) Cu K and c) S K elemental maps for the NP-1 sulfidated particles based on EDS spectra. d) Cross-sectional atomic composition of Cu, S and O K spectra across the length of the particle, indicated by a red line in the TEM scan.

For larger particles of NP-1 (Figure 4-10), the elemental maps and TEM images reveal slight heterogeneity. The TEM image in Figure 4-10(a) features 545-620 nm particles, and the Cu K and S K elemental map (Figure 4-10(b-c)) and EDS analysis across the center of the particle (Figure 4-10(d)) shows that the portion of the particle on the right side of the image is

less dense than that on the left side. This density difference may be caused by uneven packing of crystallites within regions of this larger particle, which in turn, leads to the slightly uneven distribution of the elements throughout the volume of the particle as highlighted in Figure 4-10. Despite these intra-particle heterogeneities, intra-particle regions with similar density exhibited constant Cu and S chemical profiles.

Furthermore, Cu K and S K series EDS elemental maps for 55-70 nm particles of sulfided FP-3 (Figure 4-11) also exhibit uniform distributions of Cu and S within the same intra-particle regions, despite the lower ratio of S to Cu in this particle (compared to NP-1). The overlapping and homogeneous spatial distributions of copper and sulfur in these particles suggests a homogenous propagation of reaction front throughout particles (>50 nm diameter) that could consist of on the order of $10^{2\text{-}6}$ individual CuO crystallites (of 5-19 nm diameter). These results confirm the most significant influence of H_2S removal in these studies is at the crystallite level (rather than meso-porosity, macro-porosity and/or microscopic morphology), and thus sulfur gradients (implied by the lower than stoichiometric capacities in Figure 4-8) must exist at the CuO crystallite level.

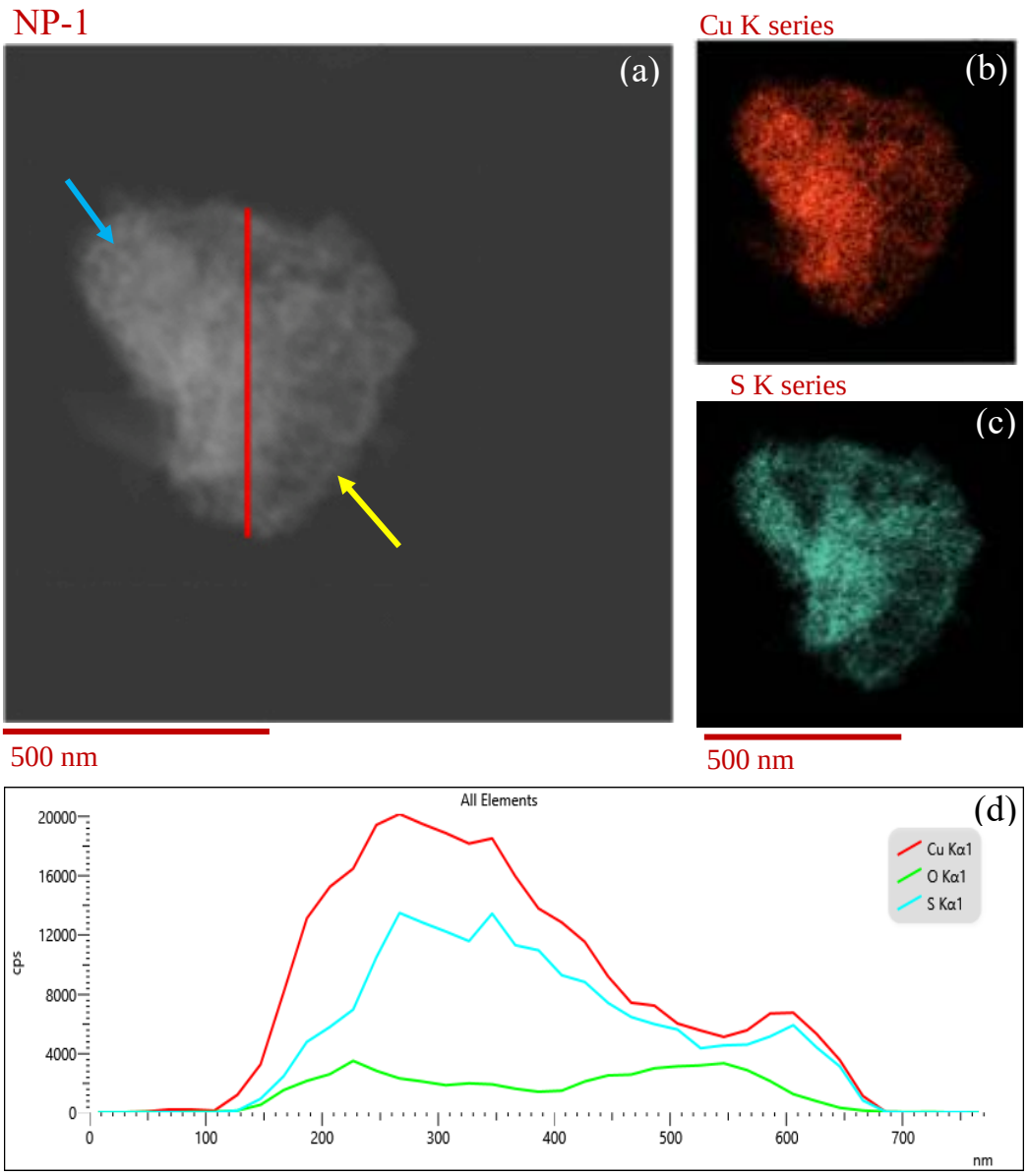

Figure 4-10: a) TEM image for 545-620 nm particles of NP-1 sorbent after sulfidation at 1000 ppm-vol H_2S/N_2, 294 K and 1 atm. b) Cu K and c) S K elemental maps for the NP-1 sulfidated particles based on EDS spectra. d) Cross-sectional atomic composition of Cu, S and O K spectra across the length of the particle, indicated by a red line in the TEM scan.

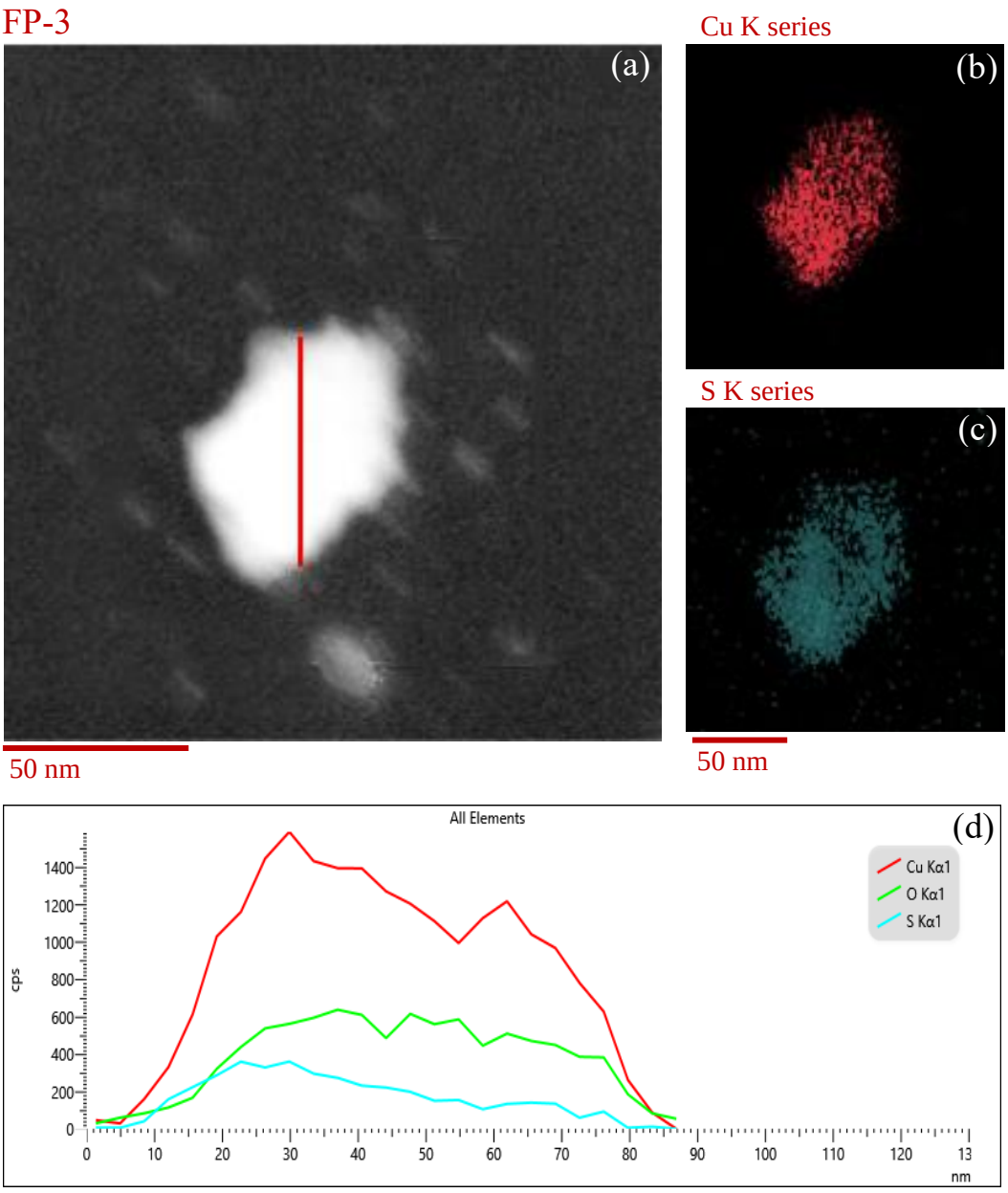

Figure 4-11: a) TEM image for a 55-70 nm particle of FP-3 after sulfidation at 1000 ppm-vol H_2S/N_2, 294 K and 1 atm. b) Cu K and c) S K elemental maps for the NP-1 sulfidated particles based on EDS spectra. d) Cross-sectional atomic composition of Cu, S and O K spectra across the length of the particle, indicated by a red line in the TEM scan.

The apparently much stronger influence of crystallite size on sorption capacity (compared to morphology, surface area, and pore structure) may be the result of enhanced constraints for the solid diffusion of atoms across the crystallite as size increases. Previous

studies of the sulfidation of ZnO[143] proposed a reaction mechanism consisting of the following general steps:

(1) The dissociative adsorption of H_2S on the particle surface

(2) Nucleation of ZnS on the ZnO surface

(3) Outward diffusion steps of Zn and O vacancies and of O atoms

(4) Vacancy annihilation and water desorption

We propose a similar mechanism for CuO sulfidation in which oxygen and/or copper atoms from the bulk CuO crystal phase diffuse to the reaction interface (step 3 above) after reaction of H_2S molecules with the surface oxygen atoms (step 2 above). The increased crystallite size may hinder this diffusion phenomenon, which is necessary for CuO to fully transform into copper sulfide (CuS), in two ways: (i) via the formation of thicker CuS layers which lead to a decrease in effective diffusivity values and (ii) via the formation/presence of surface features that are less reactive toward H_2S and its dissociation products.

Sick et al.[230] reported the formation of dense onion-like sulfide layers during CuO sulfidation which dramatically increase solid diffusion resistance by lower values of effective solid phase diffusivities. Increasing crystallite size would require the formation of a thicker outer sulfide layer to achieve the same conversion as a smaller sized crystallite. Indeed, the thickness of this sulfide layer increases with increasing initial CuO crystallite size between 5-20 nm (and up to 4.0 wt% H_2S capacity). These thicker sulfide layers (compared to smaller crystallites) may inhibit the diffusional processes needed for the reaction to proceed to completion.

If sulfide layer thickness was the only phenomenon impeding complete conversion at the crystallite scale, then calculated thickness should be the same for all samples, and the capacity should have a relationship to initial radius that is approximately R^{-1} (see SI). Since the data in Figure 4-8 follow a linear trend with R, an additional phenomenon must also impede conversion. As mentioned above, changing crystallite size could also impact the surface features of the reaction interface (e.g., CuO facets) which could change the reaction rates of H_2S molecules and surface species with O and Cu atoms. To probe this molecular explanation for the effect of crystallite size on surface reactivity, our group performed a computational study using Density Functional Theory (DFT) for the reaction between H_2S and CuO surfaces, specifically for the dissociative adsorption of H_2S molecules on a CuO {111} surface. This crystallographic surface is the most stable and common facet of CuO and is the predominant peak in the XRD patterns of the materials tested in this work (see Figure 4-1). CuO {111} surfaces feature two types of surface O atoms: 3-fold (O_{3c}) and 4-fold (O_{4c}) coordinated. Figure 4-12 shows the structure of a CuO {111} surface with these types of atoms.

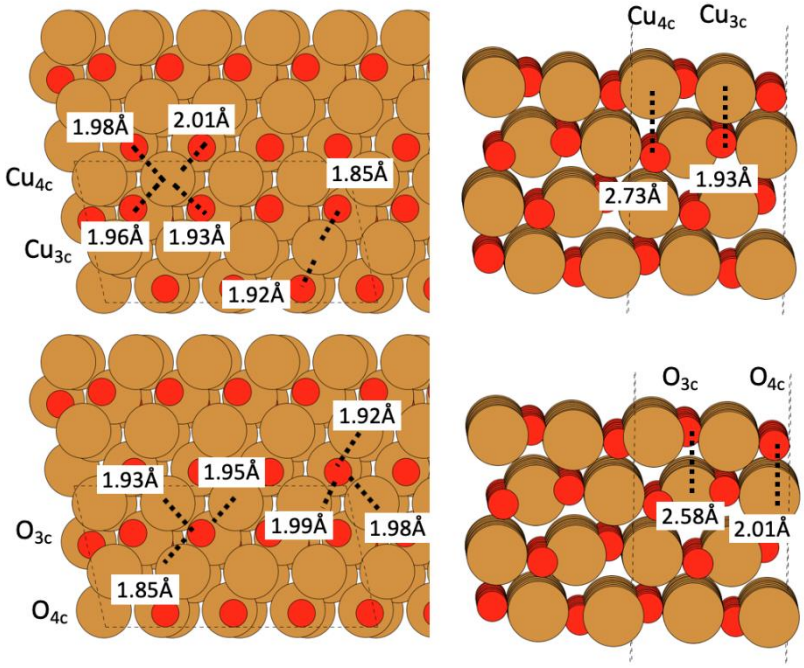

Figure 4-12: Model of a CuO {111} surface used in this study, showing the different types of surface atoms depending on their condition: O_{3c}/O_{4c} and Cu_{3c}/Cu_{4c} atoms.

These computations revealed that low-coordinated O atoms such as O_{3c} atoms are present to a greater extent for smaller crystallite sizes and that these O_{3c} atoms are more reactive toward adsorbed H_2S: They result in $\Delta G_{T=298K}$ = -106 kJ/mol for the stoichiometric reaction $CuO + x\ H_2S \rightarrow CuO_{1-x}S_x + x\ H_2O$ versus $\Delta G_{T=298K}$ = -52 kJ/mol for O_{4c} atoms. Thus, the higher capacity of CuO materials consisting of smaller crystallites may result from a higher concentration of more reactive O atoms.

In addition to improved reactivity, low coordinated atoms may facilitate diffusion of O atoms via more facile vacancy formation (step 2 above). Previous work by Nolan et al.[140] used DFT to study the formation of oxygen vacancies on CuO {111} surfaces via vacuum annealing and H_2 reduction. This study observed that formation of vacancies via vacuum annealing from O_{3c} atoms is more favorable than in O_{4c} atoms (E_{vac}=2.77 eV for O_{3c} vs. E_{vac}=3.27 eV for O_{4c}, computed with the hybrid HSE06 functional). The DFT studies in this work also revealed that

forming O vacancies by formation of water via H_2 adsorption is favorable ($\Delta E_{ads,T=0K}$= -0.82 eV) for O_{3c} atoms but is unfavorable for O_{4c} atoms ($\Delta E_{ads,T=0K}$= 0.02 eV). This is in agreement with what we found in our computational study, in which the formation of O vacancies via displacement of oxygen atoms by formation of hydroxyl groups proceeds at $\Delta G < 0$ for O_{3c} atoms whereas it does at $\Delta G > 0$ for O_{4c} atoms. Thus, O vacancies may be formed to a much greater extent when the population of low-coordinated O atoms increases (i.e., when crystallite size decreases) which would in turn enhance diffusional processes needed for complete sulfidation. Furthermore, DFT studies showed that upon reaction of the O_{3c} atoms (i.e., replacement with S atoms), the reactivity of the O_{4c} atoms increases because S atoms disrupt the Cu-O bonding states inducing lattice strain: Reaction with O_{4c} atoms in a bare CuO surface results in $\Delta G_{T=298K}$ = -52 kJ/mol, whereas they show $\Delta G_{T=298K}$ = -101 kJ/mol in a partially-sulfided surface in which the outer O_{3c} atoms have been replaced by S atoms. This result implies that as the active O_{3c} atoms in small crystallites react (i.e., leave the lattice), the overall reactivity of the particle is maintained because less reactive O_{4c} atoms become activated for vacancy formation and H_2S reaction. Taken together, these DFT results support a molecular interpretation for the increasing capacity of CuO with decreasing crystallite size that extends beyond a simple diffusion length explanation. Specifically, reaction of low coordinated oxygen (which are predominant on small CuO crystallites) rapidly react with adsorbed H_2S to produce a partially-sulfided surface while also increasing the reactivity of more highly coordinated oxygen atoms. Thus, rates of elementary reaction and molecular diffusion steps (steps 2 and 3 above) occur more rapidly and to a greater extent on smaller CuO crystallites.

4.3.3 Influence of carbon-based residues on H_2S removal

Figure 4-8 also shows a group of samples that deviate from the linear trend of increasing capacity with decreasing crystallite size in the range from 14-24 nm. Namely, decreasing the size of NPC and NF samples, both which involved the use of polymer/surfactant in synthesis, didn't result in an enhancement in the removal capacity compared to other samples in the same crystallite range. The deviation appears to be more pronounced for a nanofiber sample, NF-1, which had a crystallite size of 14 nm which fell well below the trend line, as the removal capacity of this material was merely 2.2 ± 0.1 wt% (compared to 7 wt% for other samples with similar crystallite sizes). As explained in Section 2.2, the synthesis of electrospun nanofibers requires the use of a polymer (PVP or PEO), which upon thermal treatment leaves carbon-based residues on the surface of the material, as discussed in Section 3.1. Thus, this residual carbon, which is undetectable by TGA but apparent on the surface from XPS, influences the reaction in such a manner as to decrease capacity when the crystallite size is less than 20 nm. To further probe the effect of residual C, NF-2 and NF-3 samples were prepared using PVP of different molecular weight, M.W.=1,300,000 and 40,000, respectively. XPS results in Figure 4-6 show that the variation in molecular weight didn't affect the amount of residual carbon retained on the surface with 32% C-Cu ratio in NF-2 and 34.9% in NF-3 and it impacted the capacity in the same way.

To further investigate the source of poor removal capacity of carbon contaminated samples, NPC-1, NPC-3, NPC-4 and NPC-5 samples were prepared using PVP (M.W.=1,300,000) and a varying polymer to salt ratio (50%, 40%, 20% and 10%). It appears, as shown in Figure 4-8, that the performance of the sorbent fluctuated between 1.9 and 2.4 wt% regardless of the polymer to salt ratio, and the change in crystallite size in 24-14 nm crystallite

size range. Figure 4-8 also confirms the same conclusion by showing that the presence of any carbon residue (quantified by XPS results as C-Cu atom%) between (19% and 50%) dampened the performance of the sorbent significantly, in the same way. A plausible explanation for why the presence of any carbon-based residues affects the sorption capacity is due to them blocking the active sites of the reaction, namely the surface oxygen atoms acting as Brønsted basic centers that react with the hydrogen atoms of H_2S molecules and/or the surface copper atoms acting as Lewis acid centers that bond to sulfur atoms. Since the sulfidation process is diffusion-limited (with most of the reaction taking place on grain surfaces) as demonstrated in previous sections, the blocking of any surface-active sites will adversely affect the extent of reaction.

The significance of this observation stems from its relevance to the recent interest in applications of nanofibers in catalytic and chemisorptive processes. Most of the synthesis procedures for nanofibers in literature necessitate the use of polymers in the electrospinning process. Our work shows that the thermal treatment at temperatures as high as 898 K, couldn't get rid of all carbon residue. Increasing the temperature of calcination beyond this point, causes crystal growth which will compromise the performance as well.

4.4 Conclusions

Several CuO-based nanomaterials were prepared and tested for their performance as low-temperature desulfurizing sorbents by performing fixed-bed sulfidation experiments at ambient temperature and pressure. These materials were prepared via various synthesis techniques, including sol-gel, precipitation, hydrothermal treatment in the presence of a polymer (PVP or PEO) or surfactant (P123), hydrolysis, and electrospinning. A linear driving force model was used to analyze the collected breakthrough curves, to evaluate the removal

capacity, qs, and overall rate parameter, k, for the nineteen sorbents synthesized in this work and glean information about the properties that affect the sorption capacity of unsupported CuO-based sorbents.

Despite differences between the various properties of the tested CuO sorbents as well as their morphologies, a strong linear relationship was recognized between the sorbents' sulfur removal capacity and crystallite size, particularly when the crystallite size of CuO was below 26 nm. It was also observed that CuO materials with crystallite sizes larger than 26 nm had negligible sulfur uptake capacities (~0.5 wt%). The effect of residual carbon was also investigated, and it was found that carbon residues resulting from the use of a polymer (PVP or PEO) or a surfactant (P123) in the synthesis procedure remained on the surface of the sorbent after thermal treatment and detrimentally effected its H_2S uptake capacity. The results in this paper demonstrate the strong influence of crystallite size of unsupported CuO sorbents and their purity on H_2S removal capacity at ambient conditions, irrespective of morphology and other physiochemical properties, such as surface area, pore size, and pore volume. An atomic scale explanation of the strong influence of crystallite size is proposed from model DFT calculations, explaining how elementary reaction and molecular diffusion steps occur more rapidly and to a greater extent on smaller CuO crystallites.

Chapter 5 | Fundamentals of the Remediation of Sulfur from Gaseous Streams using Copper Oxide

5.1 Introduction

The primary drawbacks with current reactive sorption materials are incomplete conversion and mass-transfer limited rates.[8,231–233] These limitations can result from either morphology (e.g., decreasing porosity) and/or chemical structure changes (i.e., changes at the product-reactant interface) that occur during reaction.[27,174]

Indeed, the technologies that remove sulfur contaminants from natural gas need to be very well understood so that existing and future gas conversion technologies can be deployed successfully. Developing fundamental insight for these gas-solid reactions requires characterization at the molecular/atomistic level while also collecting reaction kinetic data to use in microkinetic models that enable reaction model parameters to be related to chemical and structural changes.[234] These fundamental models have parameters with distinct physical meanings and can be used across a wide range of conditions and materials. Only a few recent studies have used both advanced characterization and intrinsic kinetic studies to develop such molecular descriptions of gas-solid reaction systems,[8,231,235,236] and very few previous studies have attempted to probe, in real time, the spatial and chemical conversion of solid phases during reaction with gaseous species.[8,231]

Herein, we report results from the use of synchrotron-based X-ray techniques to elucidate quantitatively how the fundamental kinetics relates to the evolution of chemical heterogeneity of two different copper oxide sorbent materials during reaction with hydrogen sulfide to form copper sulfide. X-ray absorption spectroscopy (XAS) tracked changes in the

average chemical environment of Cu atoms during sulfidation, and allowed determination of CuO conversion with time, providing direct determination of the bulk sulfidation kinetics. These data were complemented using transmission X-ray microscopy (TXM) within individual micrometer sized CuO particles to quantify chemical and structural changes on a length scale of tens of nm. Our primary discoveries show that H_2S removal reaction kinetics exhibit similar trends in fixed bed reactors and in individual μm-sized particles. However, reaction fronts proceed through the diameter of the these particles heterogeneously. Furthermore, we quantitatively identify, for the first time, H_2S concentration gradients within particles as small as 10 μm, which indicate pore diffusion even at very small length scales. We also show that copper oxide sorbent samples with similar physical characteristics exhibit ~3 times different sulfidation conversion with reaction rate constants that differ by a factor of 1.5. We conclude that differences at the crystallite level must be taken into account with differences in pore structure and/or grain size of CuO even at tens of μm length scales to completely describe the observed differences in sulfidation reactivity. Furthermore, we suggest that the formation of different copper sulfide products also influence the capacity and rate differences between similar copper oxide materials. These results represent an advancement toward the fundamental molecular understanding of gas-solid reactions by simultaneously collecting kinetic data and characterizing the real-time chemical and structural changes of the solid phase.

5.2 Experimental Methods

5.2.1 Materials and synthesis methods

Copper (II) oxide particles were prepared by a dropwise addition of aqueous 0.1 M sodium hydroxide solution (BDH, 97% minimum assay) to aqueous 0.1 M copper (II) nitrate

trihydrate (Sigma Aldrich, 99.0%) solution under continuous mixing. The copper (II) hydroxide precipitate was then vacuum filtered and dried in air at 353 K for 14 hours. The precipitate was treated in air at 823 K (0.7 K min^{-1}) for 4 h. This sample is denoted as CuO-2. A commercially produced copper-based material (HiFUEL W230; lot number L04Y006; 63.5 wt% CuO, 25 wt% ZnO, and 10 wt% Al_2O_3) was purchased from Alfa Aesar. This sample is denoted as CuO-1.

5.2.2 Fixed-bed experiments

Reactive adsorption of H_2S was studied in an apparatus with plug-flow hydrodynamics. Flow rates of gaseous H_2S and N_2 were introduced via mass flow controllers (MKS GE50A and GM50A). Feed to the reactors consisted of H_2S in N_2 (900-1000 ppm-vol) and was produced by diluting a 1.0% H_2S (Praxair UHP) in N_2 mixture with UHP N_2. Powder adsorbent samples (155-260 mg) were sieved (+200-100 US mesh; 75-125 μm agglomerate diameter) and fixed between plugs of quartz wool in a 0.25-inch outer diameter tubular, stainless steel reactor. All gas transfer lines and the interior of the reactor were treated with an inert coating (SilcoNert 2000) to mitigate H_2S adsorption onto tubing walls. Compositions of feed and effluents were determined using online gas chromatography (Agilent 7890B) with a sulfur chemiluminescence detector (SCD; Agilent 755) and continuous gas phase FTIR spectroscopy (MKS Multigas).

5.2.3 Non-synchrotron characterization techniques

Scanning Electron Microscopy (SEM) images of the CuO materials were taken before and after sulfidation using a Nova Nano 230 in the Materials Science and Engineering Department at UCLA. X-ray diffractograms were collected using a Panalytical X'pert Pro Powder X-Ray diffractometer in the UCLA Molecular Instrumentation Center. N_2

physisorption isotherms were collected at 77 K on a Micromeritics ASAP 2020 Plus. Prior to adsorption, the samples were treated at 423 K (10 K min^{-1}) under flowing N_2 for 8 h. Surface areas were calculated using the Brunauer–Emmett–Teller (BET) method, and pore volumes were calculated using the Barrett-Joyner-Halenda (BJH) method.

5.2.4 Synchrotron-based X-ray characterization

XAS and TXM measurements (shown schematically in Figure 1, collected at beamlines 2-2 and 6-2[237] at the Stanford Synchrotron Radiation Lightsource) were performed in order to establish a comprehensive understanding of the reaction kinetics. Bulk XAS data provide spectra with good signal to noise and are sensitive to subtle chemical changes in the chemical state of the copper atoms. However, bulk measurements miss the reaction front propagation within individual particles. Two and three dimensional X-ray spectro-microscopy, with spatial resolution down to 30 nm has the ability to map chemical variations across µm-sized [238–240] and can identify reaction fronts as they proceed through particles. In this work, we designed, constructed, and implemented two different gas phase reaction cells (Figure 5-1) that are compatible with the experimental criteria of TXM and XAS, respectively.

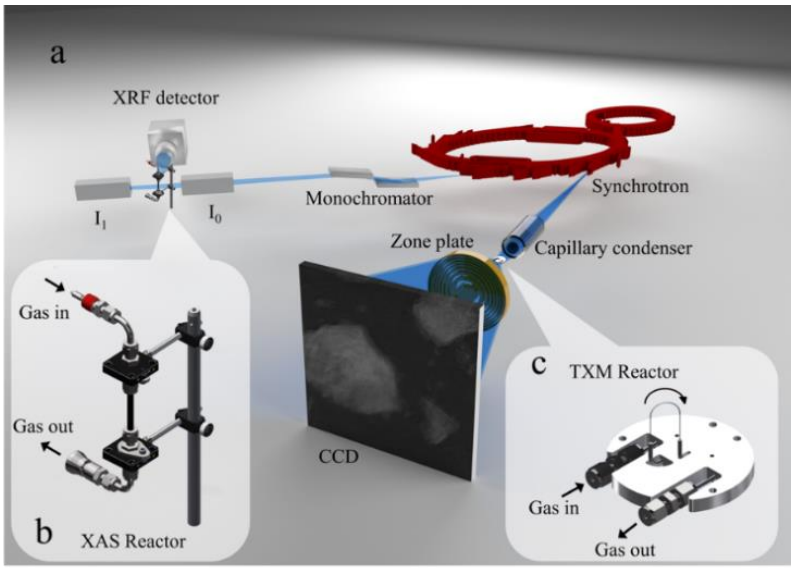

Figure 5-1: a) Schematic of experimental setup for sulfidation of CuO samples at the XAS and TXM beam lines. b) XAS cell schematic used for the room temperature sulfidation of CuO. c) TXM cell schematic featuring 0.5 mm quartz capillary used for the room temperature sulfidation of CuO.

Transmission X-ray images were collected using the full-field TXM at beam line 6-2 of the Stanford Synchrontron Radiation Lightsource, SSRL. The X-rays from a 56 pole 0.9 Tesla wiggler pass through several mirrors and are then focused to a spot size of a few hundred micrometers, which acts as the virtual source for the microscope. The monochromator installed at beam line 6-2 is a liquid nitrogen cooled double-Si(111) crystal system. The monochromator selects a narrow band pass from the incident X-ray, providing quasi-monochromatic illumination over a 2.1– 17.0 keV range for the optics downstream. A mirror pitch feedback system is installed to monitor the micrometer-level beam movements and adjust the toroidal mirror for stabilizing the beam. The TXM, designed to work over an energy range of ~5–14 keV, utilizes a capillary condenser to focus the beam to a spot with size down to a few tens of μm. A Fresnel zone plate with 200-μm diameter and 30-nm outermost zone width is employed to achieve a magnification of around 50 (depending on the energy configuration of the incident X-rays), which is further increased by a factor of 10 using the optical objective lens downstream

of the scintillator crystal. A 2048 by 2048 pixel CCD optically coupled with the scintillator crystal is used to collect the projection images. The nominal spatial resolution of this system is ~30 nm confirmed by a Siemens calibration standard and modulation transfer function.

In our experiments, the energy scan was coupled with the full-field imaging. Transmission images were recorded at over 100 energy points. Over the near edge region, we chose energy step of 1 eV to achieve the necessary energy resolution. The energy step outside of the near edge region is set to be 10 eV for covering a relatively large energy window, which is necessary for normalization or the spectra. The reduction of the spectro-microsocpic data is performed using an in-house developed software package known as TXM-Wizard.[237]

For in-situ, TXM measurements, copper oxide samples were ground into a fine powder. Less than 1 mg of the sample was loaded into a 0.1 mm OD quartz capillary with a 0.01 mm wall thickness that had been previously heat treated into a U shape. X-ray imaging was conducted around the Cu K-edge (~8979 eV), which is sufficient to penetrate through the capillary cell and sample. Both ends of the capillary were cut off to create a U shaped tube. The U shaped capillary was glued into a sample holder using 5 minute epoxy. The gas delivery system at beamline 6-2C of SSRL allows easy switch of different gas environments.

Cu K-edge, 8979 eV, XAS spectra were collected in transmission mode on the bending magnet beamline 2-2 at SSRL. The incident beam energy was selected using a water-cooled Si (220) phi = 0 monochromator with a beam size of 1 mm vertically x 3 mm horizontally. The ion chambers were filled with nitrogen gas. X-ray absorption near edge spectra, XANES, scans were collected every 7 minutes. Extended X-ray absorption fine structure, EXAFS, scans were collected every 15 minutes. A copper foil was scanned simultaneously for energy calibration.

For in-situ XAS experiments, copper oxide samples were ground into a fine powder. Approximately 12 mg of CuO-1 was diluted with 48 mg of boron nitride (Sigma Aldrich) to achieve between 2-3 absorption lengths given the geometry of the experimental cell. In a similar manner, 10 mg of CuO-2 was diluted 100 mg of γ-alumina and 100 mg boron nitride to give a similar absorption length. The addition of the γ-alumina in the copper oxide nanoparticle sample was to prevent the sample bed from packing under gas flow. The samples were packed into a 10 cm long 6 mm OD glassy carbon tube (HTW Hochtemperatur-Werkstoffe GmbH) and stabilized with glass wool to prevent sample movement under gas flow. The glassy carbon tube was mounted into a flow through cell that acts as a plug flow reactor. The cell was purged with flowing helium prior to data collection.

Gases used during the in-situ XAS and TXM sulfidation experiments were helium (99.95%, Airgas) and 1000 ppm H_2S in helium (Airgas).The gas flow rates and pressures for the XANES and TXM measurements were 10 mL(STP)/min and 1 atm, and 2 mL(STP)/min and 1 atm, respectively. Samples were exposed to flowing helium while spectra, EXAFS and energy resolved TXM images, were collected to determine the initial state of the copper in each sample. Maintaining the same flowrates as above, the helium was replaced with the 1000 ppm H_2S/He blend while XANES scans or energy resolved TXM images were collected. The copper oxide samples were exposed to sulfidation conditions for approximately 10 hours during the in-situ XAS and TXM measurements. The samples were purged with flowing helium at the end of the sulfidation process.

5.2.5 XAFS data processing and analysis

The Demeter package[241] was used to process and analyze the XAS data. Athena was used to calibrate, align, and normalize all XAS spectra, to average XAS scans, and to extract the $\chi(k)$ data used in the EXAFS modeling. Artemis was used for the EXAFS modeling. The X-ray energy of each XAS spectrum was calibrated to the first inflection point of the Cu K-edge of the Cu foil, 8979.0 eV, collected simultaneously. The pre-edge was approximated as a second-order polynomial, and the background was approximated with a cubic-spline. Data were normalized by subtracting a pre-edge and normalizing to an edge-jump of 1.

Athena was used for the linear combination fitting of the XANES spectra characterizing the sulfidation of the copper oxide. XANES spectra were fit using normalized spectra over a range from -30 eV to 50 eV above the edge energy. The contributions of all standards were forced such that the weight of each contribution was restricted to a value between 0 and 1. XANES spectra of CuO and CuS were used as standards in the linear combination fitting.

FEFF 6 was used to determine the scattering paths in the EXAFS analysis based upon CIF files (from the Inorganic Crystal Structure Database (ICSD)[242]) of bulk copper compounds (*fcc*-Cu metal (ICSD 53247), and CuO (ICSD 16025)). The amplitude reduction factor, S_0^2, was determined to be 0.81 by modeling of bulk Cu. Due to the complexity and large number of scattering paths in CuO, the models were simplified using the following assumptions: (i) only single-scattering paths; (ii) coordination numbers, N, scale linearly by a factor α; (iii) "like" scattering paths have the same σ^2 values.

The TXM data reduction was conducted using an in-house developed software package known as TXM-Wizard.[237] We first used the difference between the images acquired above and

below the Cu absorption edge to generate an "edge jump map", which is then used to reject pixels with insufficient absorption signal. After that, the spectra over every individual pixel are normalized separately using a well-established method.[243] We performed linear combination fitting of all the pixel XANES using the standard spectra of CuO and CuS. Two dimensional chemical maps are generated based on the fitting results. The chemical maps in Figure 5-6 are color coded to the local chemical compositions based on the similarities of the local Cu XANES spectra that associate with each of the pixels at ~35×35 nm^2 to the standard spectra of the known end chemical compositions. The sample slightly drifted during the measurement. As a result, we did not capture the entire particle throughout the experiment. However, the common area in the chemical maps covers a significant portion of the larger particle (Particle B) in Figure 5-6 and the entire particle (Particle A) in Figure 5-6 (except for the map of the initial state, which is known to be pure CuO (purely red)) and is, therefore, sufficient for further quantification in this work.

5.2.6 Random pore model development

The Random Pore Model (RPM) was used to analyze the conversion versus time data collected from the in-situ XAS studies.[174] Briefly, the model assumes that the pores are cylindrical and are not created nor destroyed, an expression encompassing both the kinetically controlled and the diffusion-controlled regimes can be written as follows:

$$\frac{dX}{dt} = \frac{k_{RPM} S_0 C_b (1-X)\sqrt{1-\Psi ln\,(1-X)}}{(1-\varepsilon_0)[1+\beta Z/\Psi(\sqrt{1-\Psi ln\,(1-X)}-1]} \qquad (21)$$

The Z term is the ratio of the molar volume of the product to the molar volume of the reactants (0.63 for CuS and CuO). The β term represents a modified Biot number that

encompasses the rate constant and the effective product layer diffusivity of the system at hand. For a stoichiometrically balanced equation, such as the sulfidation of CuO, this Biot number can be expressed as

$$\boldsymbol{\beta = \frac{2k_{RPM}(1-\varepsilon_0)}{V_{CuO}D_{RPM}S_0}} \qquad (22)$$

The parameter Ψ is a function of three structural parameters that can be calculated from a pore size distribution of the material[189] obtained by mercury porosimetry. These parameters are the initial surface area of reaction (S_0), the initial total length of pore structure (L_0), and the initial porosity (ε_0). Ψ can be calculated as follows:

$$\boldsymbol{\Psi = \frac{4\pi L_0(1-\varepsilon_0)}{S_0^2}} \qquad (23)$$

In the kinetic region, the modified Biot number tends to 0, and in the diffusion region, the modified Biot number tends to infinity. Applying this to Equation 21, and then integrating and simplifying the resulting equation allows for the creation of two distinct functions relating conversion and time:

$$\boldsymbol{\frac{1}{\Psi}[\sqrt{1-\Psi \ln(1-X)}-1] = \frac{k_{RPM}S_0(C_b-C_e)t}{2(1-\varepsilon_0)}} \qquad (24)$$

$$\boldsymbol{\frac{1}{\Psi}[\sqrt{1-\Psi \ln(1-X)}-1] = \frac{S_0}{1-\varepsilon_0}\sqrt{\frac{D_{RPM}M_{CuO}C_b t}{2\rho_{CuO}Z}}} \qquad (25)$$

The left-hand sides of Equations 24-25 represent a modified conversion which is a simple algebraic relation to the parameters k_{RPM} and D_{RPM}. In the kinetically controlled region, the modified conversion is linearly proportional to time, while in the diffusion limited case, modified conversion has a square root of time dependence. Equations 24 and 25 were used to

regress the experimental data and determine the kinetic rate constants and diffusivities of the copper oxide samples.

5.3 Results and Discussion

5.3.1 Non-synchrotron characterization

Both CuO samples were characterized to identify their initial chemical composition, crystalline phases, and pore structure. XRD patterns for the two samples show only characteristic peaks for hexagonal CuO. Analysis of the peak at $2\theta=37°$, CuO (1 1 1), indicates that the CuO exists as crystallites of 28.3 nm and 2.8 nm in CuO-2 and CuO-1, respectively. No characteristic ZnO peaks were observed for CuO-1, suggesting that the zinc oxide is either amorphous or has crystallites below the detection limit of XRD. SEM images (Figure 5-2 and Figure 5-3) reveal particles that are 1-5 μm in diameter consisting of agglomerates of smaller (<1 μm) particles (CuO-2) and 5-15 μm sized particles, also consisting of agglomerates of smaller (~1 μm) particles (CuO-1). The best-fit model of the Cu K-edge EXAFS data characterizing both CuO-1 and CuO-2 contained only scattering paths matching hexagonal CuO (see Table D-1). However, the coordination numbers for all paths are lower than those of bulk CuO, and for CuO-1 are smaller than CuO-2, consistent with the XRD that the CuO-1 contains smaller CuO crystallites than CuO-2. We note that there were no detectable scattering paths from Cu-Zn or Cu-Al contributions in CuO-1. However, while the Cu K-edge XANES spectrum of CuO-2 contains spectral features that match those of monoclinic CuO, the XANES of CuO-1 appear to be slightly modified. This may be a result of the small crystallite size[244] or from an interaction of the CuO with the ZnO or Al_2O_3 as observed in other mixed oxide

samples.[245,246] Analysis of the pore structures of these materials from N_2 physisorption data reveal similar pore volumes and surface areas for the two samples (Table 5-1). In summary, these characterization data indicate that the two samples studied herein are chemically and structurally similar, with the only measurable difference being the CuO crystallite and particle size.

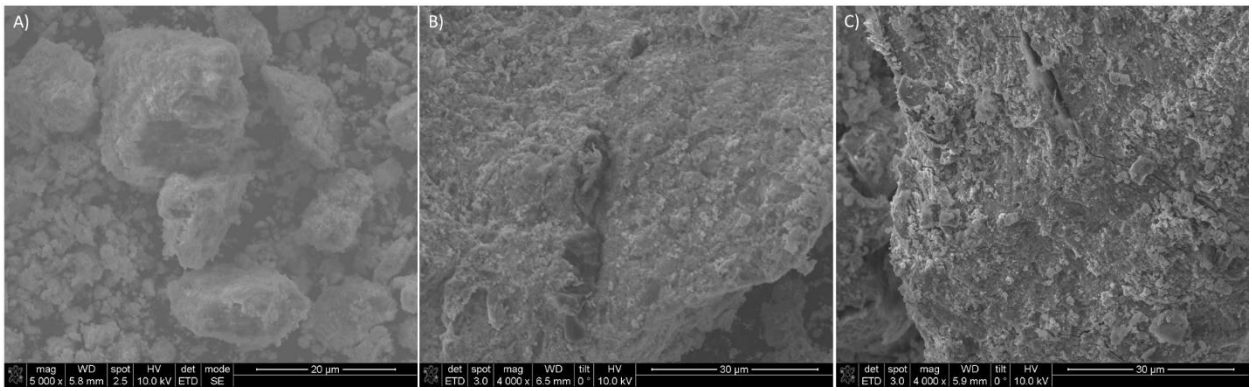

Figure 5-2: SEM images of HiFuel W230, CuO-1, A) -270 mesh (>53 μm) particles before sulfidation, B) +200-100 mesh (75-125 μm particles) before sulfidation, and B) +200-100 mesh (75-125 μm particles) after reaction with 110 cm^3(STP) min^{-1} of 930 ppm H_2S/N_2 at ambient temperature (294 K) and pressure (1.1 atm).

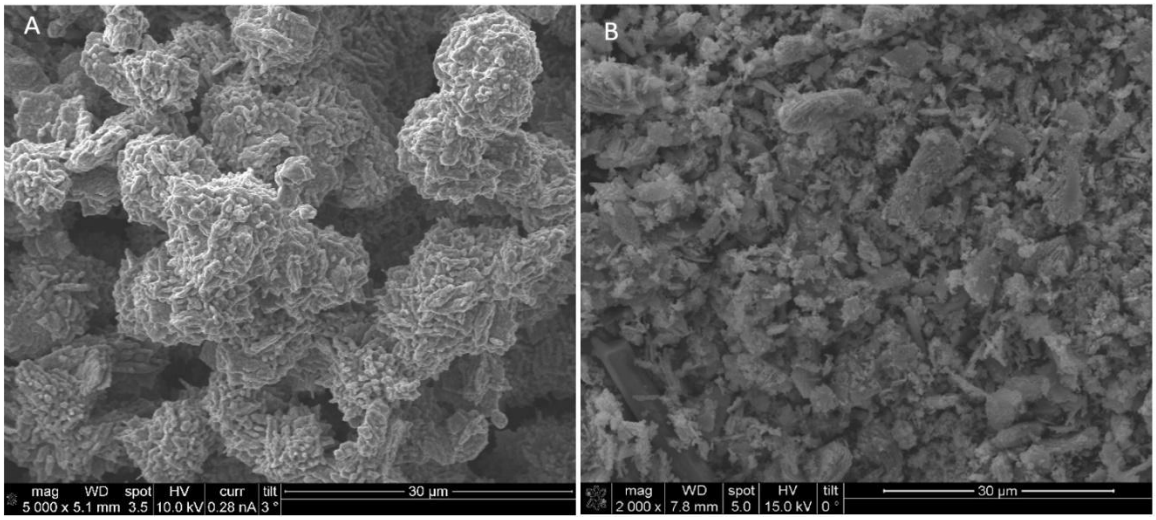

Figure 5-3: SEM images of copper (II) oxide nanoparticles prepared by precipitation from copper (II) nitrate trihydrate precursor, CuO-2, A) before sulfidation and B) after reaction with 84 cm^3(STP) min^{-1} of 1000 ppm H_2S/N_2 at ambient temperature (294 K) and pressure (1.1 atm).

Table 5-1: Pore volumes and BET surface areas of fresh and sulfided CuO-based sorbents.

Adsorbent	Fresh pore volume (cm^3/g)	Fresh surface area (m^2/g)	Spent pore volume (cm^3/g)	Spent surface area (m^2/g)
HiFuel W230 (CuO-1)	0.139	67.3	0.051	17.6
CuO (CuO-2)	0.181	58.8	0.112	87.1

5.3.2 Fixed bed sorption experiments

The sulfidation kinetics of the two samples (at ambient temperature and pressure) were measured in fixed bed sorption experiments to determine the saturation capacities and sorption rate parameters from the breakthrough curves (Figure 5-4). In these breakthrough curves, the time on stream is normalized against the weight-hourly space velocity (mass flowrate of H_2S divided mass of adsorbent). This normalization procedure accounts for any small variation in inlet H_2S flowrate and adsorbent bed size and allows for the direct comparison of breakthrough curves.

The breakthrough data for CuO-1 (red in Figure 5-4) and CuO-2 (blue in Figure 5-4) both exhibit a sickle shape which are best modeled by the linear driving force model derived by Cooper[182,247,248] (black lines in Figure 5-4). CuO-1 exhibited a higher H_2S capacity (12 wt%; 44% conversion) compared to CuO-2 (6.0 wt%; 14% conversion). Reaction rate parameters (k) were determined from linear least square regression of the data using the Cooper model. The values for the bulk and pore diffusion terms were calculated from known engineering correlations (Refer to Section 2.2.3). The calculated values for the bulk diffusion (22,000 s^{-1} and 7400 s^{-1} for CuO-1 and CuO-2, respectively) and pore diffusion (260 s^{-1} and 90 s^{-1} for CuO-1 and CuO-2, respectively) terms are more than an order of magnitude larger than the experimental reaction parameters (5.2 s^{-1} and 6.1 s^{-1} for CuO-1 and CuO-2, respectively) for each sample. Thus, bulk and pore diffusion resistances have negligible impact on the measured

rate of H_2S removal under the conditions of these experiments, and the experimentally determined reaction rate parameter represents the rate of chemical reaction and diffusion phenomena at the interface of CuO-CuS. The rate parameter for CuO-2 was a factor of 10 larger than for CuO-1 ($4.3x10^{-4}$ s^{-1} vs. $4.0x10^{-5}$ s^{-1}). These results suggest that the lower conversion of the CuO-2 sample (compared to CuO-1) results from rapid CuS formation that covers surfaces and fills particle pores, eventually impeding transport of H_2S to CuO surfaces.

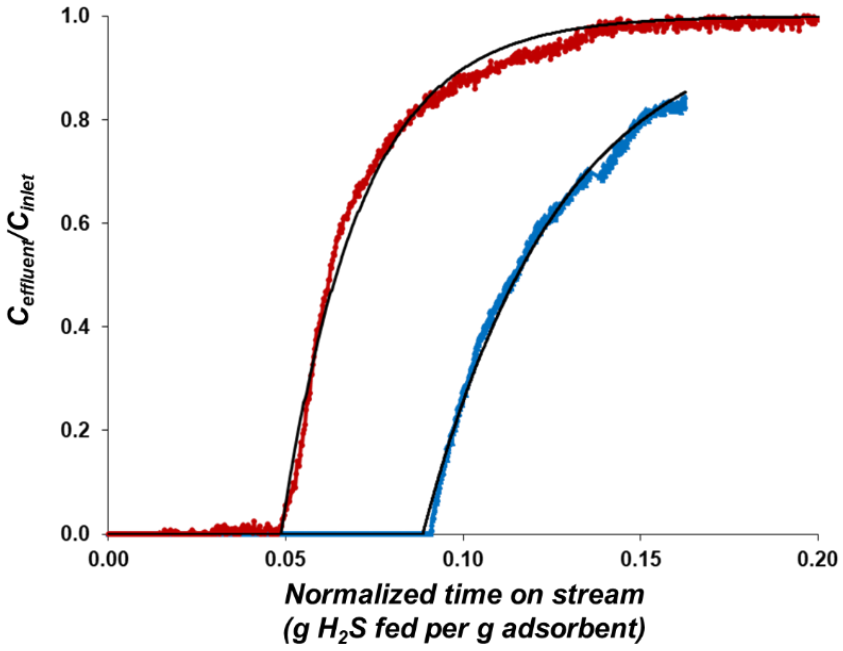

Figure 5-4: Normalized concentration-time profiles for CuO-1 (red circles) and CuO-2 (blue triangles). Normalized time is calculated by multiplying the time on stream with the mass flowrate of H_2S and dividing by the mass of adsorbent. Solid lines are predictions from the linear driving force model derived by Cooper.[12]

5.3.3 Sulfidation kinetics from bulk XAS measurements

Direct determination of the bulk sulfidation kinetics of CuO-1 and CuO-2 were determined using in-situ XAS. The Cu K-edge spectra show changes concomitant with a change from CuO-like features to those of CuS. Linear combination fitting (LCF) of the spectra was used to determine the extent of CuO conversion as a function of reaction time (Figure 5-5).

Conversion rapidly increases with time for both samples during the first 10-30 minutes, but the rate slows thereafter. After ~10 h time on stream, the reaction appears to stop (conversion approaches a constant value with increasing time). The initial region lasted 3 times longer for CuO-1 (30 min) then CuO-2 (10 min), and the total conversion to CuS was ~3-fold higher for CuO-1 than CuO-2 (38% vs 13%), similar to the results of the fixed bed experiments. The LCF XAFS data were analyzed using the random pore model[174] (RPM); a reaction rate controlled regime that evolves into a diffusion controlled regime as conversion increases, and values for reaction rate constants and effective diffusivities were regressed. The rate constant for CuO-2 (8.3×10^{-3} cm^4 mol^{-1} s^{-1}) was higher than that for CuO-1 (5.6×10^{-3} cm^4 mol^{-1} s^{-1}), indicating that rapid reaction rates lead to CuS products that fill pores/cover surfaces and ultimately to the early onset of slower, diffusion controlled reactions. The effective diffusivity in the diffusion-controlled regime was higher for CuO-2 than CuO-1 (2.0×10^{-12} vs 1.1×10^{-12} cm^2 s^{-1}) suggesting that restriction of H_2S to CuO surfaces is more severe in CuO-1 than CuO-2 during their respective diffusion controlled reaction regimes because of higher product content within CuO-1 than CuO-2. While the access to reactive surfaces is apparently more facile in CuO-2 (than CuO-1) during the diffusion-controlled regime, the much earlier onset of this regime mitigates this apparent advantage. Indeed, these data reveal that slower reaction rates are beneficial to extending reaction-controlled sorption rates to achieve maximum conversions.

Previous studies on H_2S reactions with ZnO and ZnO doped with Cu or Ni[8,231–233] attributed improvements in reaction rate and conversion to dopants (e.g., Cu) that can facilitate the oxidation of the sulfur in an adsorbed HS^- species from S^{2-} to S^- because they are more easily reduced than Zn. This oxidation of S leads to a lower energy barrier for H-S dissociation with the final reaction steps being re-reduction of S^- to S^{2-} (with oxidation of Cu^+ to Cu^{2+}) and

formation of ZnS.[8,231] However, both samples in this study are comprised of crystalline CuO, and there is no evidence for significant interaction between the Zn and Cu at the atomic scale (as evidenced by EXAFS) for CuO-1. Furthermore, both samples have similar pore volume and surface area (Table 5-1). Therefore, the differences in reaction rate constant and final conversion in our studies are unexpected and must result from differences in the initial copper oxide surface (e.g., preferentially exposed planes and/or defects) or from differences in the evolution of the reactant-product interface (e.g., different products formed). On predominantly Zn-based materials, the final redox step (S^- to S^{2-}) is likely to occur for all H_2S molecules converted because ZnS is the only product that can form with Zn^{2+}. In contrast, a variety of copper sulfide products can form (Cu_xS_y with $1 \leq x/y \leq 2$) because of the multiple oxidation states of Cu and S (S^{2-} and $(S^-)_2$). Thus, we hypothesize that the differences in the intrinsic reaction rate constants measured in this work suggests that the single reaction assumption (i.e., formation of only CuS) for both materials is insufficient, and therefore, additional studies are necessary to characterize sulfide products and construct a more detailed atomistic-level mechanism that includes the formation of all relevant copper sulfide products.

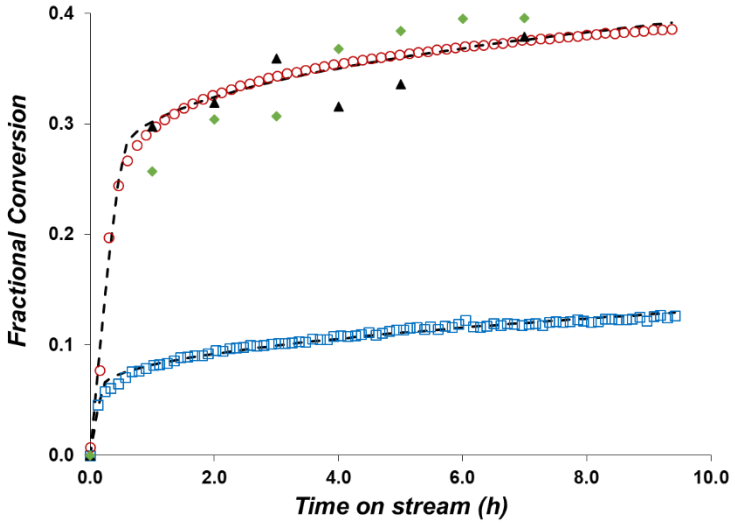

Figure 5-5: Conversion of CuO to CuS as a function of time determined by the LCF of bulk XAS experiments, CuO-1 (red circles) and CuO-2 (blue squares); and LCF of the TXM spectro-microscopy images of individual particles of ~10 µm (particle A in Figure **5-6**; black triangles) and ~20 µm (particle B in Figure **5-6**; green diamonds) of CuO-1. Black lines are model fits to the bulk XAS data.

5.3.4 Sulfidation kinetics of individual particles via TXM

As mentioned previously, both porosity and chemical structure influence the average rate of reaction in particles of metal oxides.[27,174,232,233] Thus, heterogeneity at the particle or sub-particle scale can critically affect the performance of the solid phase, and it is of fundamental interest and practical importance to visualize the evolution of this chemical heterogeneity at fine length scales. Thus, we performed 2-dimensional XANES mapping on particles of the CuO samples (using TXM). Figure 5-6 shows chemical maps, determined by LCF, of a ~10 µm and a ~20 µm particle of CuO-1 during the course of exposure to 1000 ppm H_2S for 8 hours. Direct observation of the chemical maps in Figure 5-6 suggests that the evolution of the chemical heterogeneity follows a complex pathway, highlighting the importance of studying the particles using a chemical sensitive probe with good spatial resolution.

For quantification of the XANES imaging data, we first average the chemical signatures of the entire particle A and the common areas in particle B, respectively. The amounts of remaining CuO in both particles change over time and, follow the same trend as the data from the bulk XAS measurement (Figure 5-5). The matching trends of both the bulk XAS and averaged TXM XANES results not only confirms the reliability of our measurements but also suggests that the critical length scale of the chemical heterogeneity is at the mesoscale (sub-single particle) level. For a better visualization of the dynamic evolution of the chemical distribution at sub-particle level, we segment out the reaction front based on the local chemical composition of particle A. The pixels associated with local CuO/CuS ratio at 1:1 (indicating 50% conversion of CuO to CuS) are labeled in white in Figure 5-6, and are defined as the reaction front. The sulfidation front clearly initiates within the outer portions of the particle (at distances that are >90% of the radius) and propagates towards the center of the particle after being exposed to the H_2S stream for ~5-6 hours. The morphology of the reaction front also changes from isolated pockets into a complex interconnected network upon progression of the reaction. At the beginning of the reaction, the nucleation events dominate the system leading to relatively fast conversion of CuO to CuS. After the first few hours, the propagation of reaction front in the solid phase becomes the dominating event and the system becomes diffusion limited, slowing down the overall conversion efficiency.

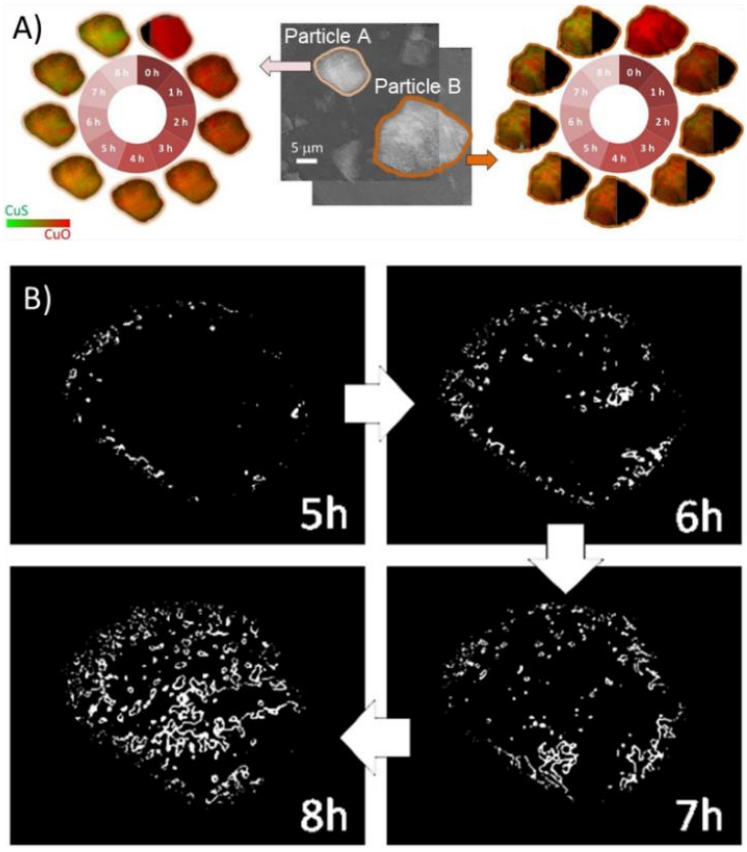

Figure 5-6: A) *In-situ* Chemical maps of CuO particles during sulfidation reaction. 3B) Development of the reaction front (defined by the voxels with a chemical composition of 50% CuO and 50% CuS)

Analysis of the entire volume of both particles reveals similar kinetics as those measured in a reactor (containing multiple particles), indicating that analysis of reaction of mg amounts of powders can produce kinetic expressions suitable for reactor scale design and operation. However, the different dynamic conversion profiles measured at different radial positions within individual particle indicates that H_2S concentration gradients (and thus, pore diffusion) exist even at very small length scales and cannot be detected by analyzing the kinetics in fixed beds of particles. The conversion versus time data at various radial positions within Particle A were analyzed using the RPM to quantitatively determine any kinetic differences with radial position. The RPM predicted the conversion versus time data with good agreement to the experiment data (Figure 5-7A). However, the rate parameters exhibited a sharp decrease at

positions less than 90% of the radius (Figure 5-7B). Furthermore, the diffusivity exhibited a linearly increasing trend with radial distance into the particle (Figure 5-7B). These conversion profiles measured from TXM suggest that H_2S concentrations are higher within the outer regions of the particle, leading to higher initial reaction rates, faster buildup of product layers, and more rapid pore structure change. Conversely, lower concentrations within the particle interior would lead to slower reaction that allows diffusion to occur more rapidly as product layers form more slowly. This explanation is supported by the increasing values of the effective diffusivity with increasing proximity to the particle interior. Furthermore, the abrupt decrease in reaction rate constant (followed by a more gradual decrease of rate constant) indicates that this value is dependent upon H_2S concentration. Thus, this reaction rate constant is an apparent rate constant and not an intrinsic rate constant as has been suggested by previous work.[27,174] This conclusion further supports the need for identification of fundamental mechanism for the reaction between CuO and H_2S that can describe this reaction across a wide range of conditions.

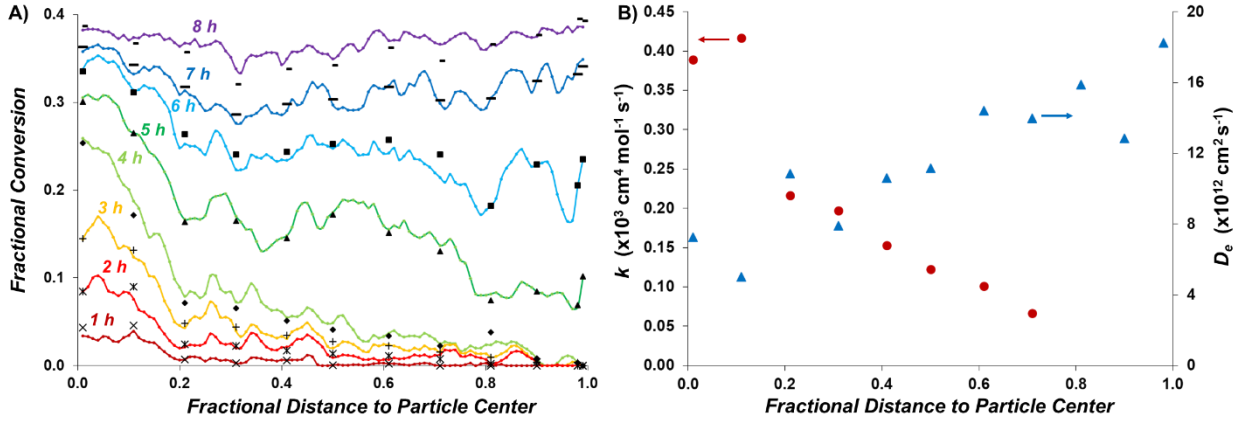

Figure 5-7: A) Conversion (lines are data; symbols are model predictions) of CuO to CuS at various radial distances and at various times on stream. B) RPM rate constants (k) and effective diffusivities (D_e) as a function of radial distance. The value of zero is the particle surface and the value of 1 is the particle center.

5.4 Conclusion

The observations from the in-situ XAS and TXM are consistent with the conventional kinetic studies that evaluate the role of the porosity and chemical structure in affecting the bulk performance of CuO for H_2S removal. These phenomena were quantitatively probed via TXM of individual particles to show average kinetics within single particles mirror the reaction kinetics measured from fixed bed of sorbents. Similarly, analysis of data from XAS of a gradientless reactor reveals the same kinetic differences between the two CuO samples as analysis of breakthrough curves in a fixed bed experiment with sharp axial concentration gradients. However, the growth of reaction fronts proceed heterogeneously within solid phase particles and pore diffusion persists even for particles less than 10 μm in size. This combined characterization-kinetic analysis ultimately revealed that chemically and structurally similar CuO can exhibit different kinetics upon reaction with H_2S and that explaining these differences must include more detailed reaction stoichiometry and analysis of specific surface properties of the reactant and product phase.

Chapter 6 | Insights into Copper Sulfide Formation from Cu and S K-edge XAS and DFT Studies

6.1 Introduction

Earlier work has demonstrated the critical role of crystallite size and micro-porosity in predicting the performance of CuO sorbents at both fixed bed and individual micrometer-sized particle scales.[249] The synchrotron-based techniques of X-ray absorption spectroscopy (XAS) and transmission X-ray microscopy (TXM) have been successfully used to quantify the kinetics of the sulfidation process and to observe the chemical and structural changes that are associated with it in real time. These studies confirmed the presence of pore diffusion resistance within individual particles (< 10 μm) and hinted at the potential formation of different copper sulfide products.[28] Additionally, fixed bed experiments and Density Functional Theory (DFT) calculations showed that reducing crystallite size leads to an improvement in the removal capacity of CuO sorbents.[249] This work uncovered a difference in reactivity of oxygen atoms based on their coordination environment, with three-fold coordinated atoms, more abundant in smaller crystals, being more reactive towards sulfur than four-fold coordinated oxygen. Furthermore, these three-fold coordinated oxygen atoms form oxygen vacancies more readily, which could indicate more facile diffusion of atoms through the bulk of the solid phase in smaller crystals. These studies introduced new questions pertaining the reaction of CuO with H_2S, such as what the type of copper sulfide species are formed, do these phases depend on the structure of the starting material or/and the conditions of the sulfidation process, and how does the phase formation impact the final conversion (and thus, performance) of the material.

The conventional stoichiometry used for the CuO sulfidation reaction assumes the formation of covellite (CuS), however, new emerging evidence has challenged this long-held belief of the formation of a single product species/phase.[28] Indeed, copper sulfide systems are highly complex, featuring a range of species with $Cu_{2-x}S$ stoichiometries ($0 \leq x \leq 1$), diverse crystal phases, and varying bonding arrangements and electronic structures (see Figure 6-9).[250–252] The crystallographic characterization of these intermediate $Cu_{2-x}S$ species (between Cu_2S and CuS) is difficult due to the ill-defined positions of the copper atoms within the close-packed sublattice of S atoms. Despite their simple chemical formulae, the two end members (i.e., x = 0 or 1) of the $Cu_{2-x}S$ family, Cu_2S (chalcocite) and CuS (covellite), also have complex crystalline structures. Covellite features a hexagonal crystalline structure, with two thirds of the Cu atoms in tetrahedral coordination and the other third has a trigonal planar symmetry; the oxidation states of Cu in these centers are +1 and +2, respectively. On the other hand, one-third of S atoms are monosulfides (S^{2-}) in trigonal bi-pyramidal coordination, and two thirds are in disulfide (S^{1-}-S^{-1}) arrangement. These atoms are arranged in alternating S_2 and CuS_3-CuS_3 layers as shown in Figure 6-1. Chalcocite (Cu_2S) is known for its instability and its inclination to degrade to copper deficient species at ambient conditions. The oxidation state of Cu in the 96-atom monoclinic unit of chalcocite is mostly +1 with evidence of mobile Cu (0) centers.[253] Successful elucidation of copper sulfide species that form (and evolve) during reactions between CuO and H_2S will fill a gap in the efforts towards fundamental understanding of this reaction, and the evident complexity of copper sulfides calls for the use of advanced characterization techniques that can probe the oxidation states, local geometry, bond lengths and coordination numbers of both Cu and S in order to achieve accurate speciation.

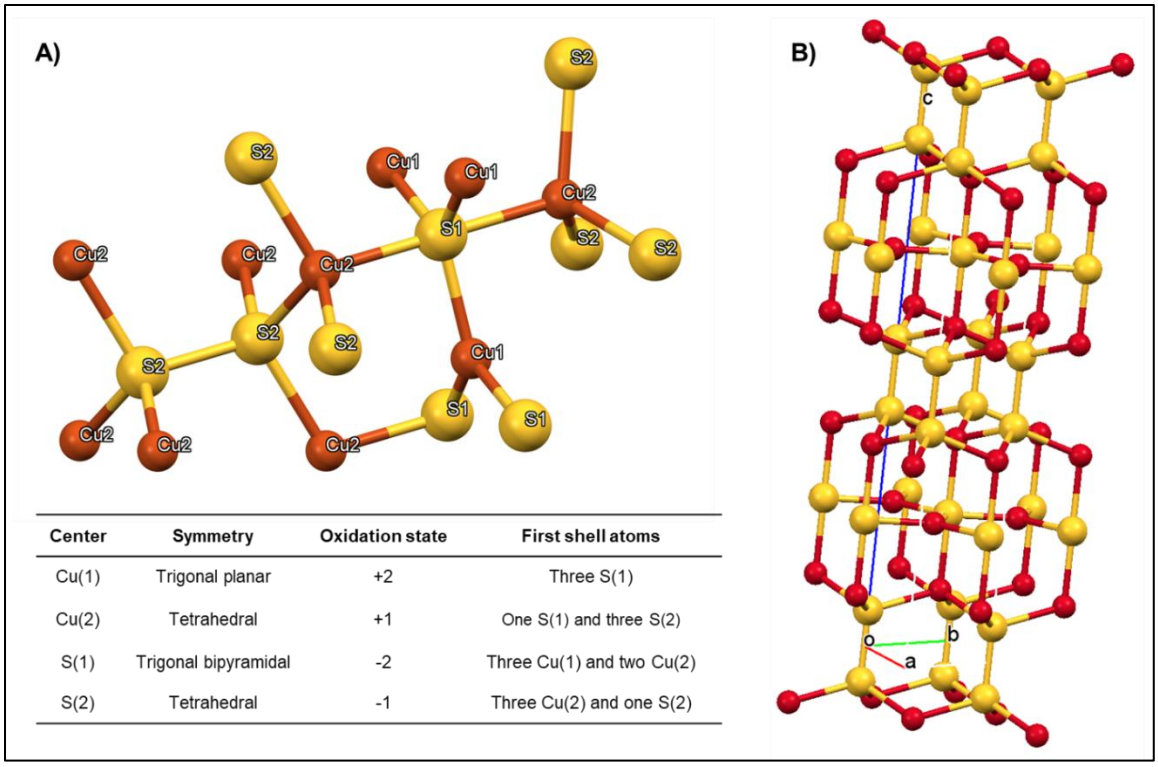

Center	Symmetry	Oxidation state	First shell atoms
Cu(1)	Trigonal planar	+2	Three S(1)
Cu(2)	Tetrahedral	+1	One S(1) and three S(2)
S(1)	Trigonal bipyramidal	-2	Three Cu(1) and two Cu(2)
S(2)	Tetrahedral	-1	Three Cu(2) and one S(2)

Figure 6-1: A) Presents covellite[251] molecular structure and a summary of symmetry, oxidation states, and coordination for the different Cu and S centers. B) Illustrates covellite crystal packing. Both structures are produced using Mercury 3.8 structural visualization application.[254]

XAS is a powerful technique that can provide valuable information in this regard, by both *ex-situ* analysis of fresh and spent samples and *in-situ* study of the evolved species throughout the course of the reaction.[255,256] The extended X-ray absorption fine structure (EXAFS) can be used to determine local structural information about the target atom, and the near-edge spectrum (XANES) can provide information about the oxidation state of an atom and its coordination symmetry.[255,256] Nevertheless, probing a heterogenous mixture of species, such as a partially sulfided CuO sample, is a challenging task because of the numerous local environments of Cu within one phase (CuS) and across the two phases (CuO and CuS). In this work, we probe the reaction of CuO with dilute H_2S gas streams (1000 ppm-vol in N_2) using *in-situ* and *ex-situ* XAS at both the S K- and Cu K-edges. We verify that *in-situ* XAS experiments accurately represent this reaction by comparison with the capacities and kinetics from fixed bed absorption studies at the same conditions. These

experimental techniques (and the resulting data) are also used to probe the influence of CuO crystallite sizes (across a range of 2 – 40 nm) and reaction temperature (298-383 K) on $Cu_{2-x}S$ formation. The results of our work suggest the formation of a distorted CuS layer at the surface of the CuO crystals, with disulfide groups of longer Cu-S bonds and higher delocalization of the positive charge of Cu center into $(S^{-1})_2$ at the initial stages of the reaction. Our findings also suggest the dominance of these species at lower temperatures (298-323 K) compared to higher temperatures (353-383 K) and where the CuS products more closely resemble pure covellite. DFT calculations for the sulfidation of CuO (111) and ($\bar{1}$11) surfaces also support our hypothesis of the formation and dominance of disulfides at the initial stages of CuO sulfidation.

6.2 Experimental Methods

6.2.1 Materials and synthesis methods

A commercial CuO-based sorbent (HiFUEL W230; denoted as CuO-1) was purchased from Alfa Aesar and tested without subsequent treatment. This sorbent is composed of 63.5 wt% CuO, 25 wt% ZnO, and 10 wt% Al_2O_3. For the synthesis of all other CuO sorbents, copper (II) nitrate trihydrate (Sigma Aldrich, 99%), copper (II) acetate monohydrate (Sigma Aldrich, 99%), sodium hydroxide (BDH, 97%) and glacial acetic acid (VWR, ACS grade) were used in the preparation.

CuO nanoparticles (denoted as CuO-2 and CuO-3) were prepared using an acid-catalyzed sol-gel process.[210] For CuO-2, 1.0 cm^3 of glacial acetic acid was added to 300 cm^3 of 0.02 M copper (II) acetate solution under vigorous stirring and heating. Upon boiling, 0.8 g of sodium hydroxide was added to the solution under continuous stirring. The solution was then allowed to cool to room temperature while a black solid continuously precipitated out of solution. The solid

precipitate was recovered via centrifugation of the solution for 10 minutes (JA-14 rotor) at 293 K and 6000 RPM followed by decanting the supernatant liquid. The precipitate was then washed with deionized water and ethanol. The washed precipitate was dried in a furnace for 8 h at 313 K. Sample CuO-3 was prepared by additional thermal treatment of sample CuO-2 in air at 623 K for 4 hours to achieve larger crystallite size (as evidenced by X-ray diffraction patterns). Additional CuO nanoparticles (denoted as CuO-4) were prepared by a drop-wise addition of aqueous 0.1 M sodium hydroxide solution to aqueous 0.1 M copper (II) nitrate trihydrate solution under continuous mixing. The obtained material, copper (II) hydroxide, was then vacuum filtered and washed with distilled water and ethanol, dried in air at 353 K for 14 h, and then thermally treated in air at 773 K for 4 h at a ramping rate of 1 K h^{-1}.

CuO nanofibers (denoted as CuO-5) were synthesized through electrospinning. Polymer solutions were prepared by dissolving 1.30 g of PVP M.W. 1,300,000 in ethanol solvent (23 cm^3). The polymer solution was then vortexed (Fisher Scientific Digital Vortex Mixer) at 3000 rpm for 1 h until the polymer was completely dissolved. The solution was left to settle for 10 minutes, transferred to a beaker, and stirred for 0.5 h. The metal containing solution was prepared by dissolving copper (II) nitrate (1.3 g) in 10 cm^3 of DI water and stirring the solution for 0.5 h. The copper containing solution was then added dropwise to the polymer containing solution. The solution was stirred for 0.25 h, and then vortexed for 0.5 h at 3000 rpm. The electrospinning solution was placed in a 10 mL syringe (BD 10 mL syringe with Luer Lok™ tip) with a hypodermic needle (Monoject™ Standard 30G x ¾"). The distance between the tip of the needle and a stainless-steel collecting plate, which was covered with aluminum foil, was 22 inches. A Gamma High Voltage Research ES75 power supply was used to apply 30 kV on the polymer jet while the polymer solution was extruded through the needle at a rate controlled by a syringe pump

(1.0 cm^3 h^{-1}; Kent Scientific Genie Plus). Dry air was circulated inside a 3 m^3 chamber at 6 cm^3 min^{-1} to control the relative humidity at 19.5 ± 2%. The collected fibers were thermally treated in air at 823 K for 4 h at a ramping rate of 2.0 K min^{-1} to remove the majority of PVP and form CuO.

6.2.2 Non-synchrotron characterization techniques

All CuO sorbents were characterized using a variety oftechniques. Powder X-ray diffraction patterns were obtained on an X-ray diffractometer (JEOL JDX-3530 and Philips X-Pert) using Cu Kα radiation of 1.5410 Å wavelength and used to identify the crystalline copper-containing phases. The average crystallite size of each sample was determined using Scherrer's formula. Nitrogen adsorption-desorption isotherms were measured at 77 K with a Micrometrics ASAP 2020 Plus system. Before measurements, the samples were degassed at 1×10^{-3} Torr and 573 K. The Brunauer-Emmett-Teller (BET) surface areas were calculated from the isotherms. The pore size distribution was derived from the adsorption branches of the isotherms using the Barrett-Joyner-Halenda (BJH) model. Scanning electron microscopy (NOVA 230 Nano SEM) was used to visualize the morphology of the materials. The diameters of the agglomerate sizes of the sorbents were measured from the SEM images using ImageJ software.

6.2.3 Fixed bed sulfidation tests

Fixed-bed sorption breakthrough experiments were carried out in the apparatus outlined in Figure 3-2. A tubular stainless-steel reactor with 0.25-inch outer diameter was packed with 100-180 mg of sorbents with average agglomerate sizes of 75 μm (i.e., particles sieved through +200-100 mesh screens). The packed beds were 1.5 cm in height and were fixed between two plugs of quartz wool. The temperature of the reactor (298-383 K) was regulated using a resistively heated jacket with a PID temperature controller (TEMPCO EPC-100). Reactant feed streams consisted of

1000 ppm-vol H_2S in N_2 and were produced by diluting 1.0% H_2S/N_2 (Praxair) in UHP N_2. The total inlet flowrate of 90 cm^3(STP) min^{-1} was controlled using MKS GE50A and GM50A flow controllers. Online gas chromatography (Agilent 7890B) with a sulfur chemiluminescence detector (SCD; Agilent 755) was used to measure the concentration of H_2S in inlet and outlet streams. The interior of the reactor and all the gas transfer lines were treated by an inert coating (SilcoNert 2000) to mitigate adsorption of sulfur onto the walls of the apparatus tubing.

6.2.4 XAS acquisition and analysis

S K- and Cu K-edge X-ray absorption spectra were recorded at Stanford Synchrotron Radiation Lightsource (SSRL, California, USA) at wiggler beamline 4-3 using a Si (111) double-crystal monochromator. The storage ring was operated at 3 GeV with a ring current of 494-500 mA in top-up mode. The beam cross-section was 1 mm x 3 mm. X-ray absorption near-edge structure (XANES) spectra were recorded at the S K-edge (2472.0 eV) in fluorescence mode using a 7-element silicon-drift detector (Canberra). Energy calibration was achieved using sodium thiosulfate ($Na_2S_2O_3.5H_2O$) where the first peak of the spectrum was fixed at 2472.0 eV. Full extended X-ray absorption fine structure (EXAFS) spectra were recorded at the Cu K-edge (8979.0 eV) in transmission mode. A Cu foil, situated between two ionization chambers after the sample, was scanned simultaneously for energy calibration purposes.

The XAS samples comprised a wafer (36 mg of CuO-based sample mixed with 14 mg of boron nitride (BN) (Sigma Aldrich)) for the S K-edge, and 2.4 mg of sample diluted with 47.6 mg BN for the Cu K-edge. The wafer was placed at 45° to the incident beam on a heated stage inside a 100 cm^3 cell, as described previously and as shown in Figure 6-2.[257]

For in-situ XAS sulfidation experiments, 1000 ppm H_2S in Helium (Airgas) and Helium (99.95%, Airgas) gases were used. XAS scans were initially taken under Helium flow, then the temperature was ramped up to the desired set point (298, 323, 353, or 383 K) at a rate of 5 K min^{-1} and under a 20 cm^3(STP) min^{-1} flow of Helium. Once temperature stabilized, XAS scans were taken again to obtain initial spectra at the reaction temperature. After collection of initial spectra, a stream of 1000 ppm H_2S/He was introduced into the reaction cell, and XAS scans were collected continuously (every 6.25 minutes for Cu K-edge and every 5-11 minutes at S K-edge) until saturation was reached. The cell was then purged with Helium at 20 cm^3(STP) min^{-1} and allowed to cool to room temperature before XAS scans of spent samples were obtained. For the S K-edge, additional XAS scans were obtained for an inert BN sample under H_2S gas flow, in order to allow subtraction of the gas phase H_2S signal contribution from the overall *in-situ* XANES scans.

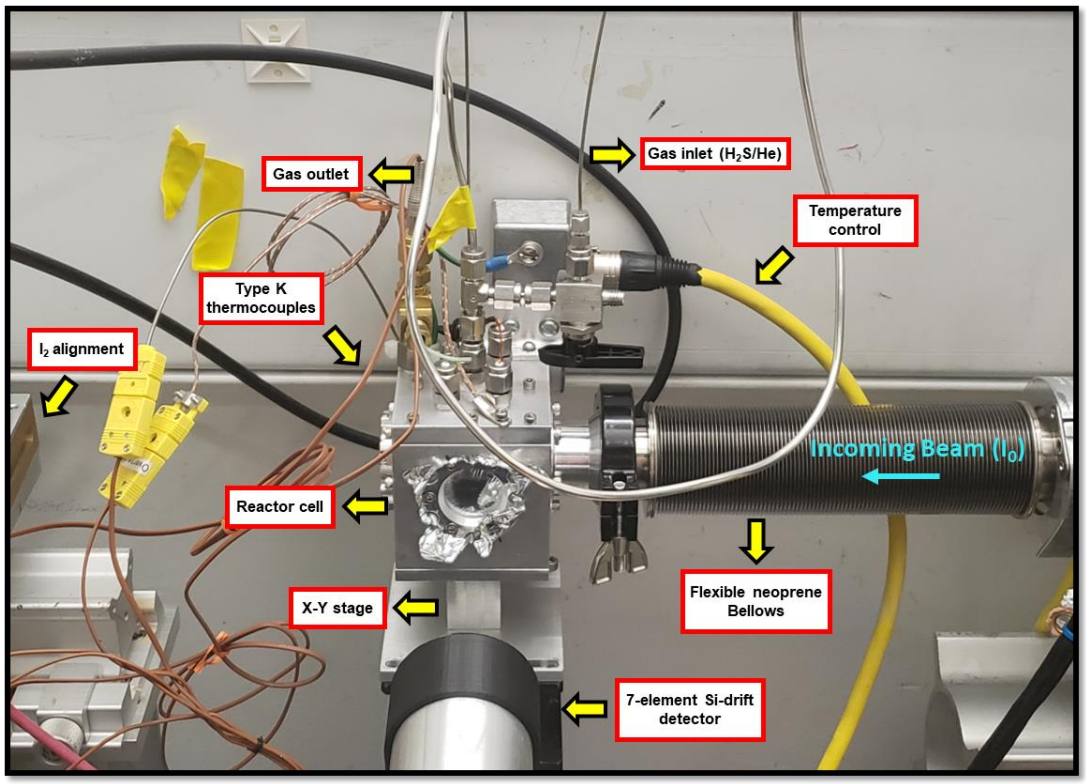

Figure 6-2: Experimental setup for sulfidation of CuO-based samples at beamline 4-3 at the Stanford Synchrotron Radiation Lightsource (SSRL)

XAS data were analysed using ATHENA and ARTEMIS from the Demeter package software.[241] The Cu K-edge EXAFS data was extracted from 3.0-11.3 $Å^{-1}$ in *k*-space, and the Fourier transformed data was analyzed in the range of 1.0-2.4 Å for partially sulfided materials and 1.0-3.4 Å for fresh and reference materials. Experimental data were fitted with theoretical back-scattering paths calculated using FEFF6, based upon CIF files from the Inorganic Crystal Structure Database (ICSD).[242] The fits were performed based on k^1, k^2, and k^3 weighting. The amplitude reduction factor, S_0^2, was determined by fitting a reference copper foil, from each beamline visit, with tabulated coordination numbers of bulk copper (*fcc*-Cu metal: ICSD 53247).[242] This S_0^2 value was 0.86, 0.91, and 0.96 for the three beamline visits at which the data were collected.

Intensity and phase of scattering paths of the oxide materials were calculated using FEFF6 based on crystallographic data from the tenorite CuO structure (ICSD 16025).[242] To simplify the models, only single scattering paths were included and the coordination numbers, N, were scaled by a factor α. The term, α, was introduced in order to account for the size effect on the EXAFS scattering path intensity. This term is a scaling factor for all the scattering paths associated with a spectrum that is consistent across samples of a given crystallite size.

The intensity and phase of the scattering paths in the sulfided material were also calculated using FEFF6 based on a modified CuS covellite CIF file (ICSD 32105).[242] This modified structure averages the two Cu centers (tetrahedral Cu^{1+}, and trigonal planar Cu^{2+}) sites in covellite. Figure 6-3 presents a stick plot of the averaged coordination numbers and distances for Cu in the modified structure. For a reliable quantification of each of the phases, the fitting model of partially sulfided materials was simplified to take into account only the most significant scattering paths. Because the focus of the EXAFS investigation of these materials was the determination of the types of

sulfur species formed, only the first Cu-O and Cu-S shells were fit. In these fits, we assumed that the unreacted CuO material was not significantly modified by the sulfidation reaction. This allowed us to fix the Cu-O path length and associated mean squared displacement term (σ^2) at the values obtained for the starting material, while scaling the coordination number down from the initial value by multiplying with the molar fraction of unreacted material, X_{CuO}. The X_{CuO} term is defined as 1- X_{CuS} where X_{CuS} is the conversion determined by linear combination fitting of the XANES region of sulfided samples. Thus, the CuO component of the final material has fixed EXAFS parameters while the EXAFS parameters of the CuS portion were allowed to vary. These parameters were Cu-S coordination number, *N*, scattering path length, *R*, and its associated mean squared displacement term, σ^2. In all of the fits, ΔE_0 was allowed to vary.

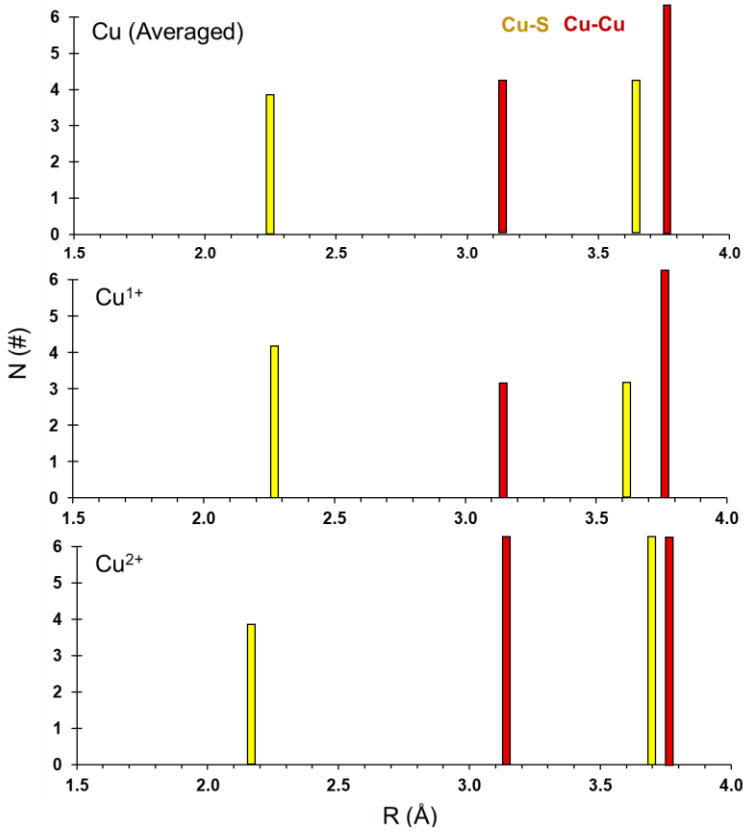

Figure 6-3: Stick-plot representation of the radial distribution of atoms around Cu^{1+} and Cu^{2+} in CuS (covellite) and averaged Cu center in the simplified CuS model used in EXAFS fitting of Cu K-edge spectra.

6.2.5 DFT computational study

First principles atomic simulations were conducted using density function theory (software package VASP) with plane wave basis set, PAW pseudopotentials, and GGA XC functional PBE. A Hubbard U correction of +7 eV was used to account for the strongly correlated d-electrons. This value is found to most accurately reproduce experimental values for properties such as lattice parameters.[141] A 2x1 slab was used to model the CuO (111) and ($\bar{1}$11) surfaces. The local minima on the potential energy hypersurface were found using the conjugate gradient method. The optimized structure of a proposed elementary step is used to calculate the change in free energy using energy differences between connecting elementary steps under realistic conditions of room temperature (298 K) and ambient pressure (1 atm).

6.3 Results and Discussion

6.3.1 Structural characterization of fresh CuO sorbents

Table 6-1 summarizes the key physical characteristics of the five samples, CuO-1 – CuO-5. The diffraction patterns for all samples, Figure 6-4, show characteristic peaks of single-phase monoclinic CuO. (XRD patterns of sulfided CuO are shown in Figure 6-10 and will be discussed in subsequent sections.) The crystallite sizes of the CuO sorbents were determined using Scherrer's formula based on 2θ=38.8°, CuO (111), and are summarized in Table 6-1. The crystallite sizes range from 2.8 nm for CuO-1 to 40 nm for the lab-synthesized nanofibrous sample (CuO-5). The estimated d-spacing for the (200) plane for all samples (2.29-2.30 Å) match literature[223] and confirm the formation of pure monoclinic CuO. The results of N_2-physiosorption experiments are summarized in Table 6-1, and they reveal comparable surface areas (44.5 to 67.3 $m^2\ g^{-1}$) and pore volumes (0.079 to 0.181 $cm^3 g^{-1}$) for all the samples except CuO-5. The notably low surface area

and void volume for the nanofiber sample is due to the electrospinning process which produces samples that consist of fibrous networks (nanofibers with diameters between 160-600 nm) with low meso-porosity, as shown in the SEM images in Figure 6-5. On the other hand, SEM images of the lab-synthesized CuO nanoparticles and CuO-1 sample reveal highly textured micrometer-sized particles consisting of finer agglomerates (<100 nm).

Table 6-1: Physiochemical properties of the CuO sorbents. [a]Based on XRD peak at 2θ=38.8°. [b]First shell oxygen coordination number based on EXAFS fits of Cu K-edge (See Supporting Information). [c]BET method. [d]BJH method. [e]Fixed bed experiments at 298 K with 90 cm^3(STP) min^{-1} of 1000 vol-ppm H_2S/N_2 at 1 atm total pressure.

Sample ID	Morphology	Crystallite size (nm)[a]	N (Cu-O)[b]	Surface area (m^2g^{-1})[c]	Void volume (cm^3g^{-1})[d]	Conversion (%)[e]
CuO-1	Nanoparticles	2.8	3.0 ± 1.0	67.3	0.139	44
CuO-2	Nanoparticles	7.0	2.5 ± 1.1	59.1	0.079	28
CuO-3	Nanoparticles	11	3.2 ± 0.4	44.5	0.102	24
CuO-4	Nanoparticles	23	4.0 ± 0.6	58.8	0.181	14
CuO-5	Nanofibers	40	5.4 ± 0.5	7.23	0.006	3

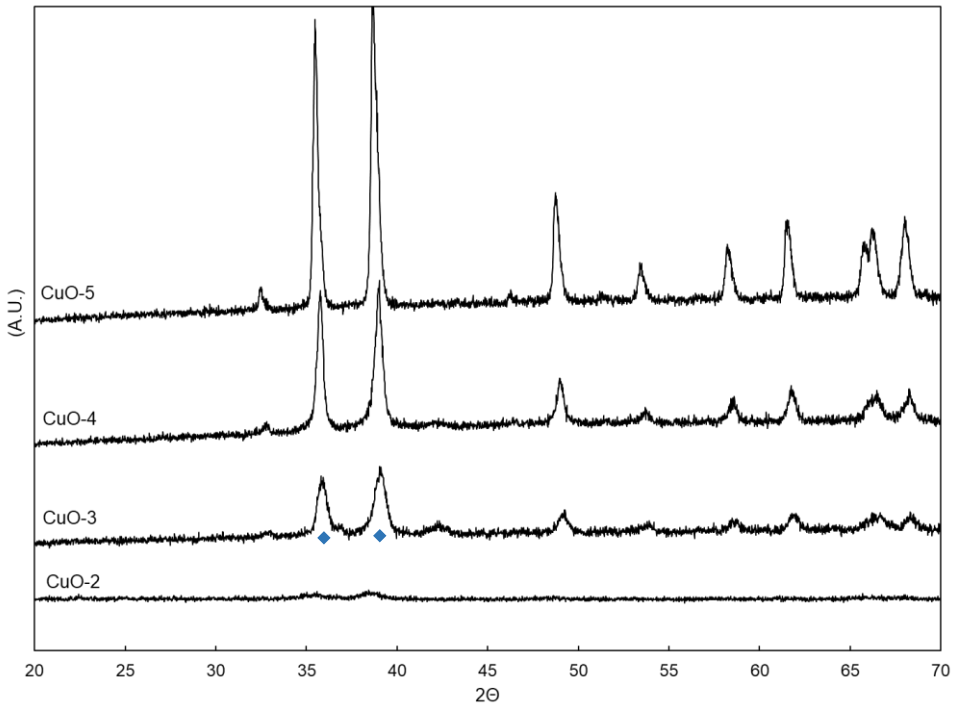

Figure 6-4: X-ray diffraction patterns of CuO sorbents. Blue diamonds indicate characteristic CuO peaks.

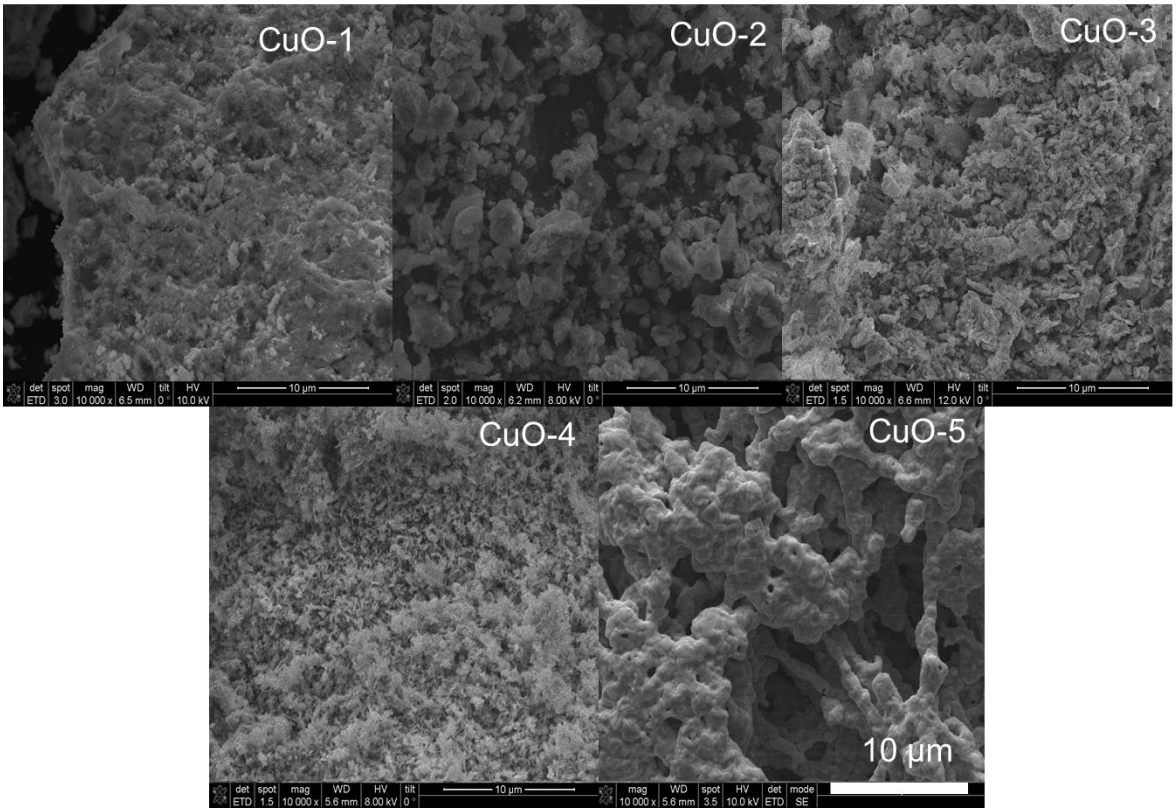

Figure 6-5: SEM images of fresh CuO sorbents at 10,000 X magnification.

Figure 6-6 shows the Cu K-edge XANES spectra for the five CuO sorbents. The spectral features for all samples agree qualitatively with a recent XAFS exploration of copper oxide materials.[258] The small pre-edge feature at 8979 eV results from a Cu 1s → $3d^9$ dipole forbidden transition that is completely absent in compounds with the Cu^+ oxidation state due to its fully occupied d shell. This suggests a 2+ oxidation state of Cu in these samples, which is consistent with the electronic structure of Cu in CuO. Moreover, the best-fit model of the Cu K-edge EXAFS data for all the samples, contain only scattering paths matching monoclinic CuO (see Table E-1) for a summary of best fit parameters the fresh materials. The spectra and fits are displayed in Figures E1- E-5.

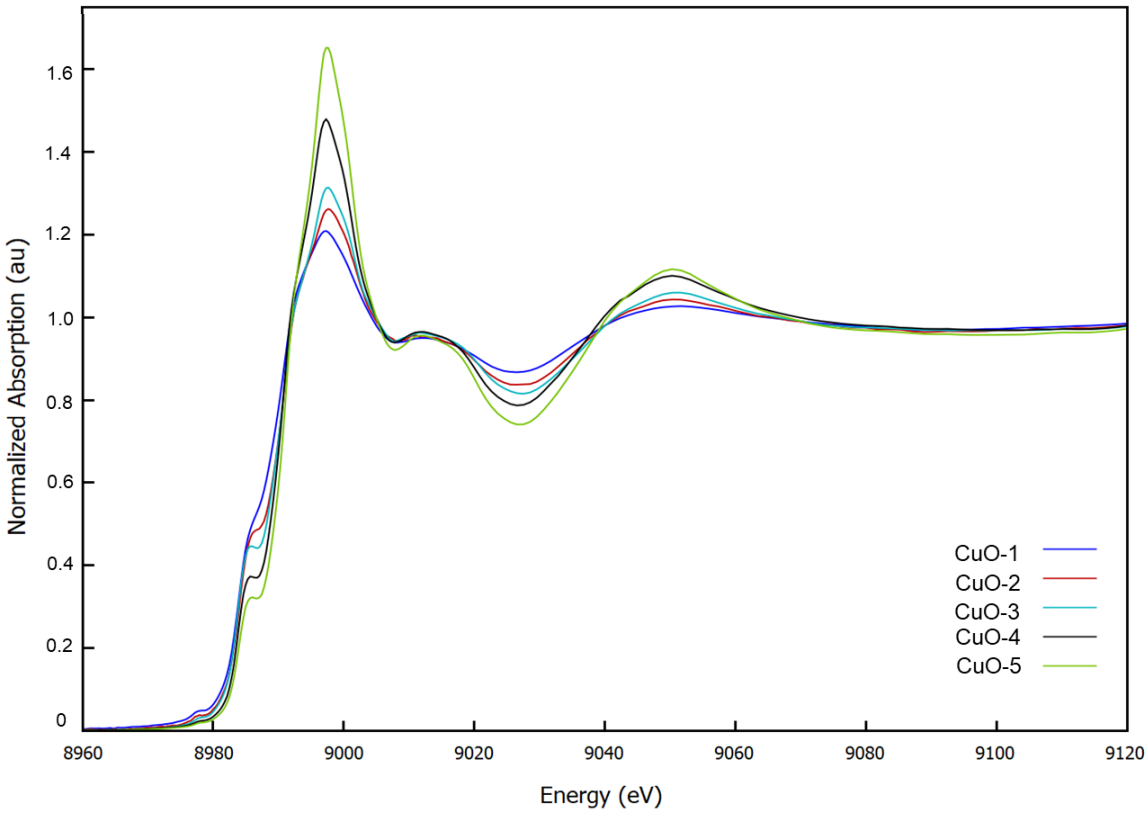

Figure 6-6: Normalized Cu K-edge XANES spectra for CuO sorbents of different average crystallite sizes: CuO-1 (2.8 nm), CuO-2 (7nm), CuO-3 (11 nm), CuO-4 (23 nm) and CuO-5 (40 nm).

The change in the height of white line in the XANES is consistent with literature, where, in the absence of any chemical change to the material, the height of the white line correlates positively with crystallite size of transition metal oxide systems such as CuO.[259] This amplitude change is also accompanied by a change in the magnitude of the oscillations found in the post edge region of the spectra, i.e. the EXAFS signal. As a result of this change in magnitude, the coordination numbers of each of the constituent scattering paths derived from fitting the EXAFS signal also change. Table 6-1 summarizes the coordination numbers of the first shell Cu-O single scattering path as determined by the best-fit model for Cu K-edge EXAFS of the samples. The model-estimated coordination number decreased as crystallite size decreased, with the lowest estimate of 2.5 ± 1.1 in CuO-2 (7 nm) as compared to 5.4 ± 0.5 in CuO-5 (40 nm). Estimating the

coordination numbers in fresh samples proved to be essential for fitting the partially sulfided materials. The Cu-S paths were fit to characterize the formed sulfides, while the Cu-O path lengths were fixed to their fresh materials' counterparts, with the necessary conversion adjustment (See section 6.2.4).

6.3.2 Determination of sorption capacities and kinetics from various techniques

Fixed bed sorption and *in-situ* XAS experiments at Cu and S K-edges were performed to study the sulfidation kinetics of the sample that exhibited the highest conversion, CuO-1, at different temperatures (323 K, 353 K, and 383 K). The effect of crystallite size has been explored in earlier work showing that a decrease in size leads to an increase in the removal capacity and a decrease in the sorption rate parameter.[249] It was demonstrated that the lower sorption rates in smaller crystals leads to extended kinetic regimes allowing for higher conversion.[28] These previous studies also demonstrated that the average kinetics and capacities determined from a small number of particles using synchrotron-based techniques (i.e., 1 mm x 3 mm beam window for in-situ bulk XAS and 10-20 μm diameter particles for transmission X-ray microscopy[28]) are similar to those deduced from the breakthrough curves of a 0.3 mL fixed beds. In this work, we focused on the effect of temperature on kinetics and conversion to further study the relationship between determining capacities and kinetics using various techniques (i.e., fixed beds and in-situ XAS at the Cu and S K-edges).

The fixed bed sorption experiments yielded H_2S concentration breakthrough curves (as shown in Figure 6-7) from which the sorption capacities and linear driving force rate parameters can be estimated. A linear driving force model that is zero order in H_2S concentration (Equation 4) describes the breakthrough curves at 323 K,[182] however, at 353 and 383 K, a model that is first

order in H_2S concentration (Equation 2) describes the curves.[184] The values of rate parameter and conversion of CuO are summarized in Table 6-2. The results show a consistent increase in conversion with an increase in temperature, with complete conversion achieved at 383 K. Moreover, the sorption rate parameter increased following an Arrhenius law relationship with an apparent activation energy of 23.5 kJ mol^{-1}. In our previous study,[260] we demonstrated that bulk mass transfer and macropore diffusion are negligible for pellet sizes of ~75 μm and flowrates of 90 cm^3(STP) min^{-1}. Under these conditions, reaction rate parameters account for reaction-diffusion phenomena in particles with less than ~10 μm diameters (as identified by Transmission X-ray Microscopy).[260] Thus, temperature effects on both reaction and diffusion are likely reflected in this measured activation energy, however, determining the rate of growth of the product layers is required to quantify the relative contributions of diffusion and reaction to the sorption rate, a task that is beyond the scope of the experiments presented herein. Nonetheless, the rate parameters and activation energy can be useful for semi-quantitative comparison with *in-situ* XAS results.

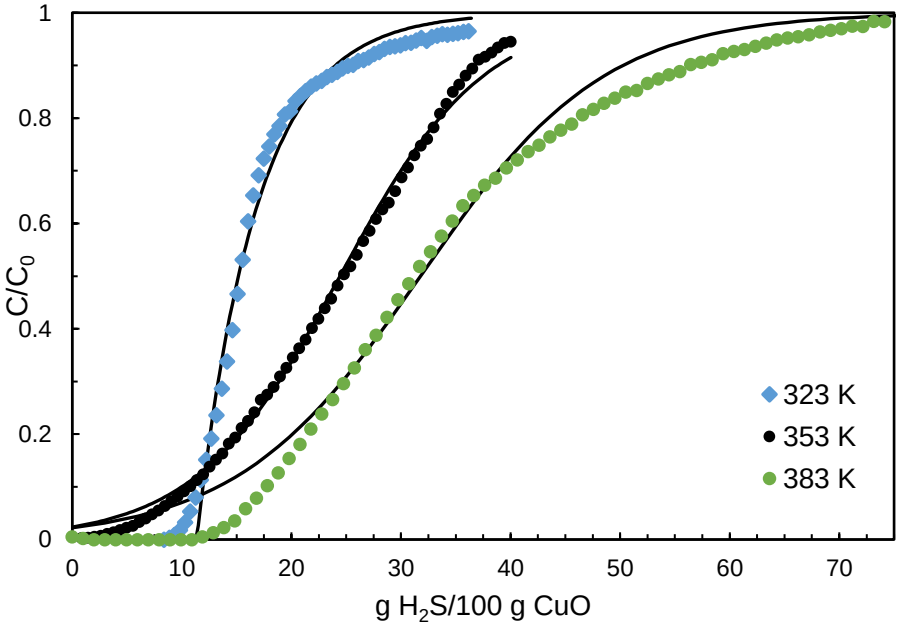

Figure 6-7: Breakthrough curves of normalized effluent H_2S concentration collected for fixed beds of the CuO-based sorbent at 1000 ppm-vol H_2S/N and 1.0 atm for temperatures of 323 K, 353 K, and 383 K. Solid

black lines represent fitted linear driving force models (Cooper model[182] for 294 and 323 K and Bohart-Adams[184] model for 353 K).

Table 6-2: Summary of conversion and kinetic and diffusivity parameters deduced from RPM model for *in-situ* S K-edge and Cu K-edge tests and, Cooper model for fixed bed tests. Conversion data were obtained through linear combination fitting for the XANES region using CuO and CuS references for Cu K-edge tests and using the edge step of fully converted 383 K test as a reference for S K-edge runs. All runs are carried at ambient pressure and a feed concentration of 1000 ppm-vol H_2S.

T (K)	XAS Cu K-edge			XAS S K-edge			Fixed bed	
	(%)	k x 10^3 (cm^4 mol^{-1} s^{-1})	D x 10^{12} (cm^2 s^{-1})	(%)	k x 10^3 (cm^4 mol^{-1} s^{-1})	D x 10^{12} (cm^2 s^{-1})	(%)	k (s^{-1})
323	45	1.3 ± 0.2	4.9 ± 0.7	45	6.0 ± 1.4	4.9 ± 0.3	54	17 ± 2.3
353	89	4.6 ± 1.5	23 ± 4.1	78	41 ± 6.0	29 ± 3.8	88	35 ± 3.9
383	100	45 ± 9.2	50 ± 9.7	100	93 ± 17	31 ± 3.5	100	68 ± 5.9
E_a (kJ mol^{-1})		60.6	40.2		47.3	32.0		23.5

These *in-situ* XAS experiments were performed for the same sample (CuO-1) and conditions (1000 ppm-vol H_2S/He at 323, 353 and 383 K) as the fixed bed experiments. At the Cu K-edge, linear combination fitting (LCF) was used to determine the CuO/CuS ratio at every scan-time point, where the spectra of CuS and fresh CuO-1 were used as fitting references. At S K-edge, the edge steps of the spectra were correlated to the extent of conversion, where the saturation edge step for 383 K (complete conversion) was used as a scaling factor. The contribution of H_2S gas was subtracted from spectra for accurate CuS quantification. Figure 6-8 presents the conversion curves for these runs, which were analyzed using the random pore model (RPM).[174] Similar to the fixed bed experiments, conversion increased with temperature, and complete conversion was achieved at 383 K. Conversion estimates based on Cu and S K-edge XAS data were similar to conversions measured from fixed beds after similar time of exposure to H_2S on stream (Table 6-2).

The rate parameters and effective diffusivities determined from Cu and S K-edge experiments are summarized in Table 6-2. The 95% confidence intervals for the rate parameters are larger (>20% of the parameter value) than those for the diffusivities (less than 10% of the

parameter value), which results from shorter kinetic regimes (i.e., few data points) compared to diffusion-controlled regimes. Comparisons of the effective diffusivity values are within the same order of magnitude for both edges, and the activation energies determined from the two experiments conducted at the two edges are within 25% agreement (and less than a factor of 2 larger than the activation energy determined from the fixed bed studies). Thus, we conclude (similar to our previous work) that the kinetic information derived from our *in-situ* XAS experiments is representative of the kinetics derived from analysis of fixed bed breakthrough curves and is suitable for interpretation of the phenomena that occurs during reaction H_2S sorption.

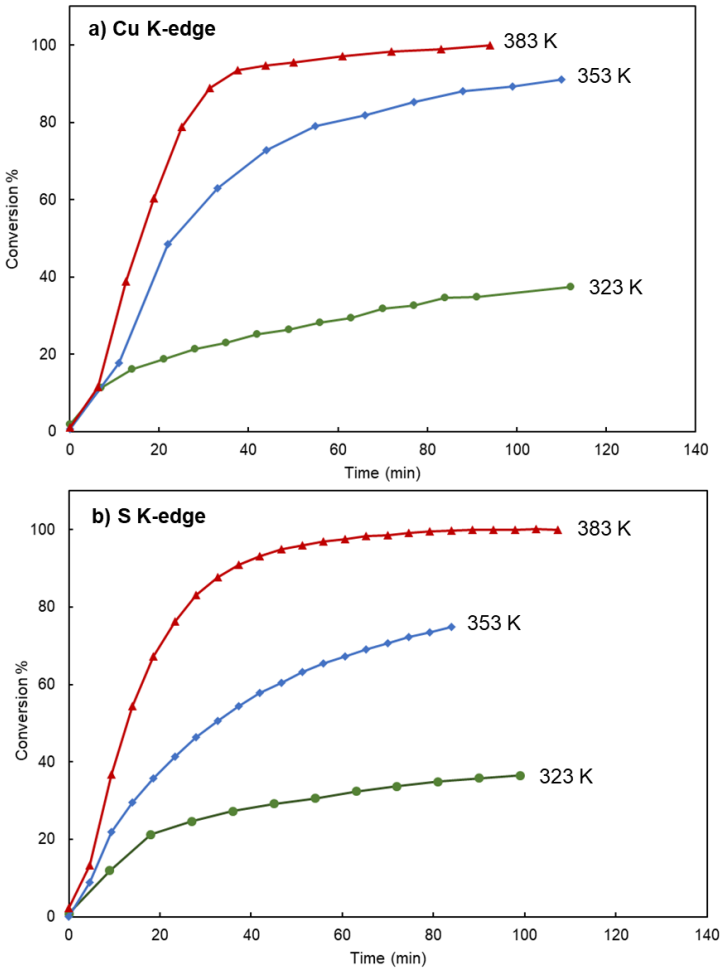

Figure 6-8: Conversion of CuO to CuS as a function of time as determined by the LCF of bulk XAS experiments at Cu K-edge and S K-edge. The experiments were conducted at 323, 353, and 383 K for CuO-1 sample under a flow of 1000 ppm H_2S/He at 1 atm.

6.3.3 Speciation of sulfidation products

The conversion of CuO to CuS is incomplete for all of the sorbents at 1000 ppm-vol H_2S and 298 K (see Table 6-1**)**. The conversion ranges from a high of 44% for CuO-1 to a low of 3% for CuO-5. This makes the speciation of the sulfidation products somewhat challenging as there is a mixture of species present. However, using a combination of S K-edge XANES, Cu K-edge XANES and EXAFS, and XRD on these spent samples, it is possible to identify the sulfide copper species that are formed. These experiments focused on exploring the effect of crystallite size of the CuO starting material and the effect of temperature on the formed copper sulfide species.

Figure 6-10 presents the XRD patterns of the five CuO sorbents after reaction in fixed bed experiments at 1000 ppm-vol H_2S 298 K, and 1 atm. For all samples, a peak at $2\theta = 48°$ is observed in the pattern of the spent samples, which corresponds to the (110) plane of hexagonal copper (II) sulfide (ICSD 16025). Nevertheless, the low conversion (3-28% as summarized in Table 6-1) along with the overlap of XRD patterns of most sulfides (Figure 6-9) suggests that XRD alone is insufficient in determining the speciation of the formed sulfides. Furthermore, Figure 6-11 shows the XRD patterns of spent CuO-1 samples following sulfidation at 323 K, 353 K and 383 K. The patterns show significant broadening of the monoclinic CuO peaks and a consistent increase in the intensity of the $2\theta = 48°$ peak with temperature increase. This is consistent with the increase in conversion with temperature observed in the fixed bed experiments (54-100% for 323-383 K). We note that the conversion of CuO-1 at 383 K is 100% (see Table 6-2 and discussion in Section 3.2). While the XRD results for both sets of samples suggest the formation of CuS (covellite), they are insufficient to conclusively identify the specifications of the CuS phase and whether any distortions are present.

Mineral name	Composition	Crystal System	Cu oxidation states	S oxidation states
Low-chalcocite	Cu_2S	Monoclinic	0, 1	-2
High-chalcocite	Cu_2S	Hexagonal	0, 1	-2
Djurleite	$Cu_{1.94}S$	Monoclinic	1.03	-2
Anilite	$Cu_{1.75}S$	Orthorhombic	0, 1	-2, 0
Geerite	$Cu_{1.6}S$	Cubic	1.25	-2
Roxbyite	$Cu_{1.81}S$	Triclinic	1	-2
Covellite	CuS	Orthorhombic	1, 2	-1, -2

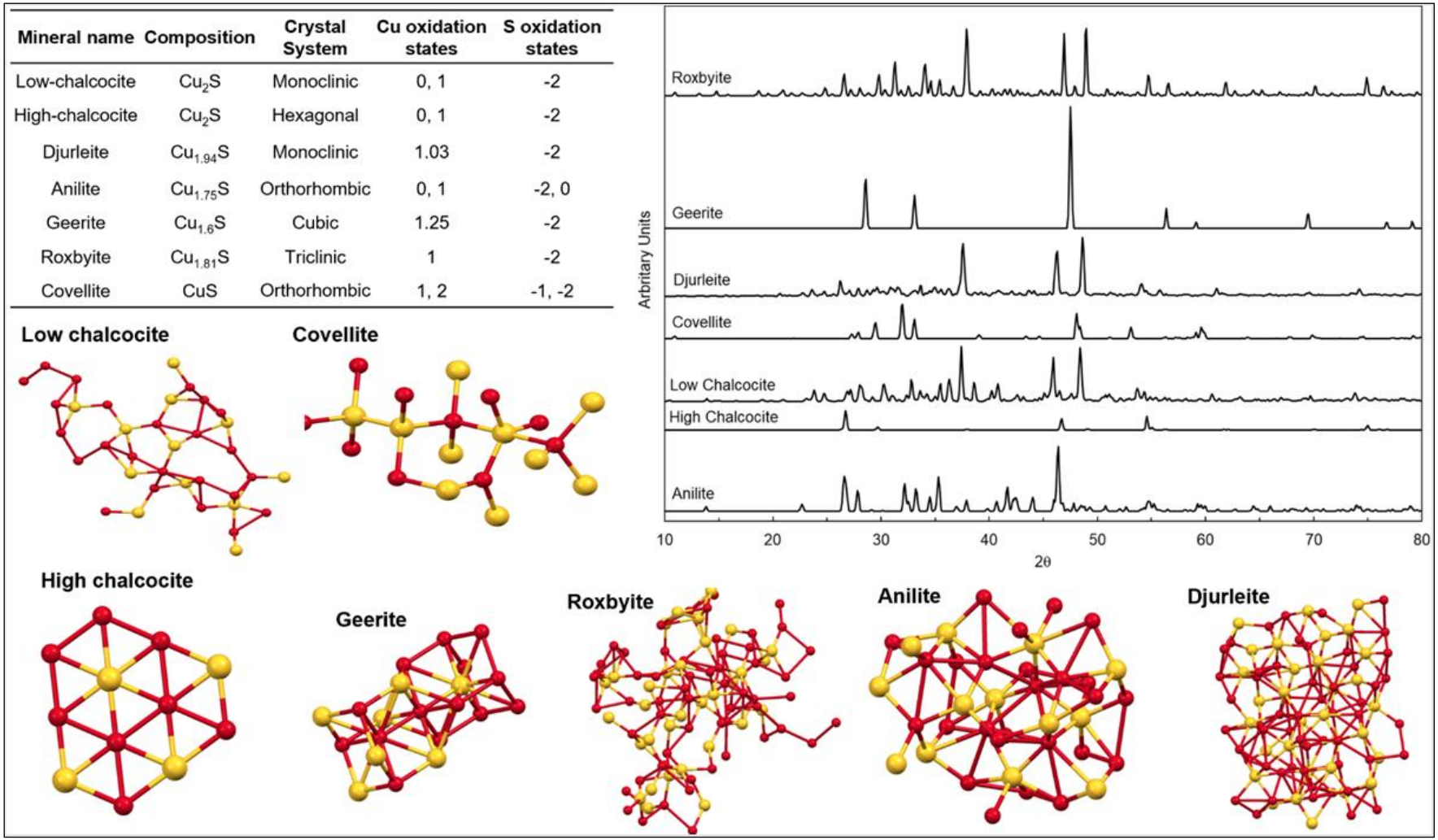

Figure 6-9: Crystal structures, compositions, oxidation states of Cu and S, and X-ray diffraction patterns for low-chalcocite, high-chalcocite, Djurleite,[261] Anilite,[262] Geerite,[263] Roxbyite,[264] and Covellite.[251] Red spheres represent Cu while yellow spheres represent S. The structures are produced using Mercury 3.8 structural visualization application.[254]

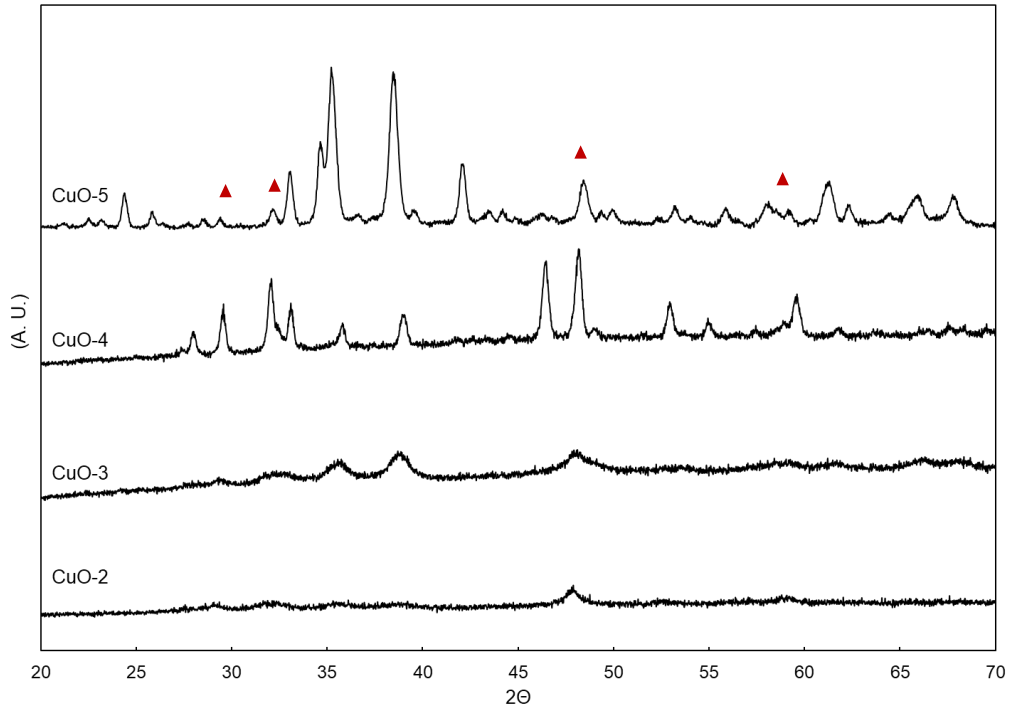

Figure 6-10: X-ray diffraction patterns of spent CuO sorbents. The sulfidation tests are run at 298 K and 1 atm with 1000 ppm-vol H_2S/N_2. Red rectangles identify characteristic covellite peaks.

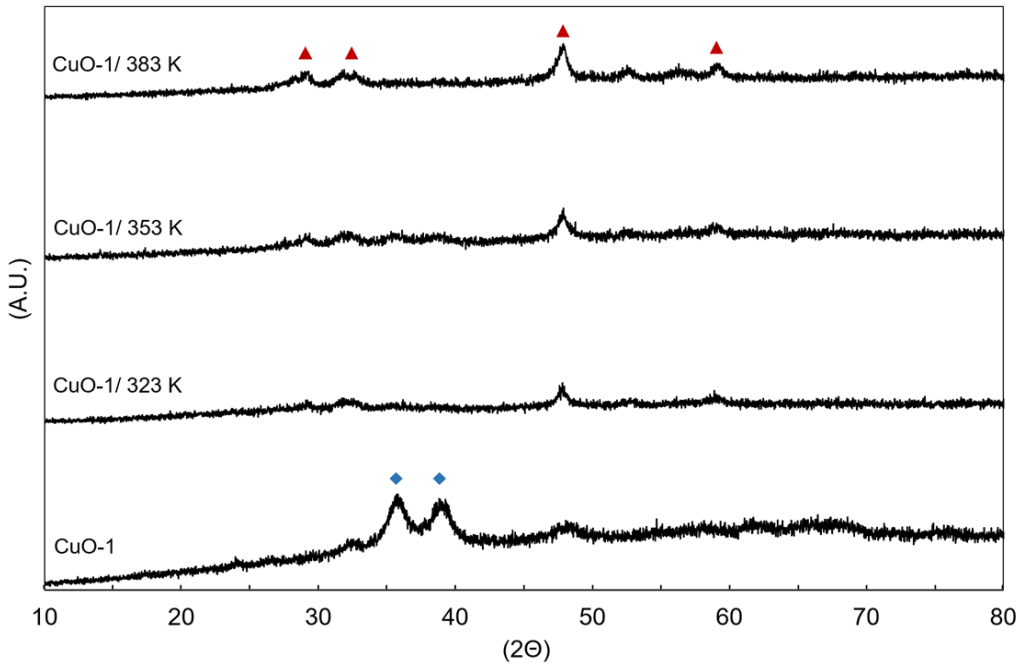

Figure 6-11: Diffraction patterns of fresh CuO-1 sorbent and spent samples for runs at 323, 353, and 383 K (using 1000 ppm-vol H_2S/N_2 and 90 cm^3(STP) min^{-1}). The XRD of spent samples are collected at 298 K and 1 atm after sulfidation at elevated temperatures. Blue diamonds correspond to characteristic CuO peaks and red triangles correspond to characteristic CuS peaks.

Since different $Cu_{2-x}S$ structures have different electronic and coordination environments of the S and Cu atoms, XANES provides insight into the type of species that is formed. Figure 6-12 shows the S K-edge XANES of the spent CuO-1 sample at 323 K, 353 K and 383 K, and CuO-2 and CuO-3 spent at 298 K. Three main observations can be made from this figure: (1) The white line amplitude (peak a) decreases with a decrease in crystallite size, (2) the white line is shifted to lower energy for spent samples at elevated temperatures (353 K and 383 K), and (3) a small pre-edge peak (peak b) is present only at elevated temperatures (353 K and 383 K). The first observation aligns with the discussion of the relationship between crystallite size and white line intensity in the fresh Cu K-edge XANES. The two other observations provide an evidence for the formation of different $Cu_{2-x}S$ species at elevated temperature.

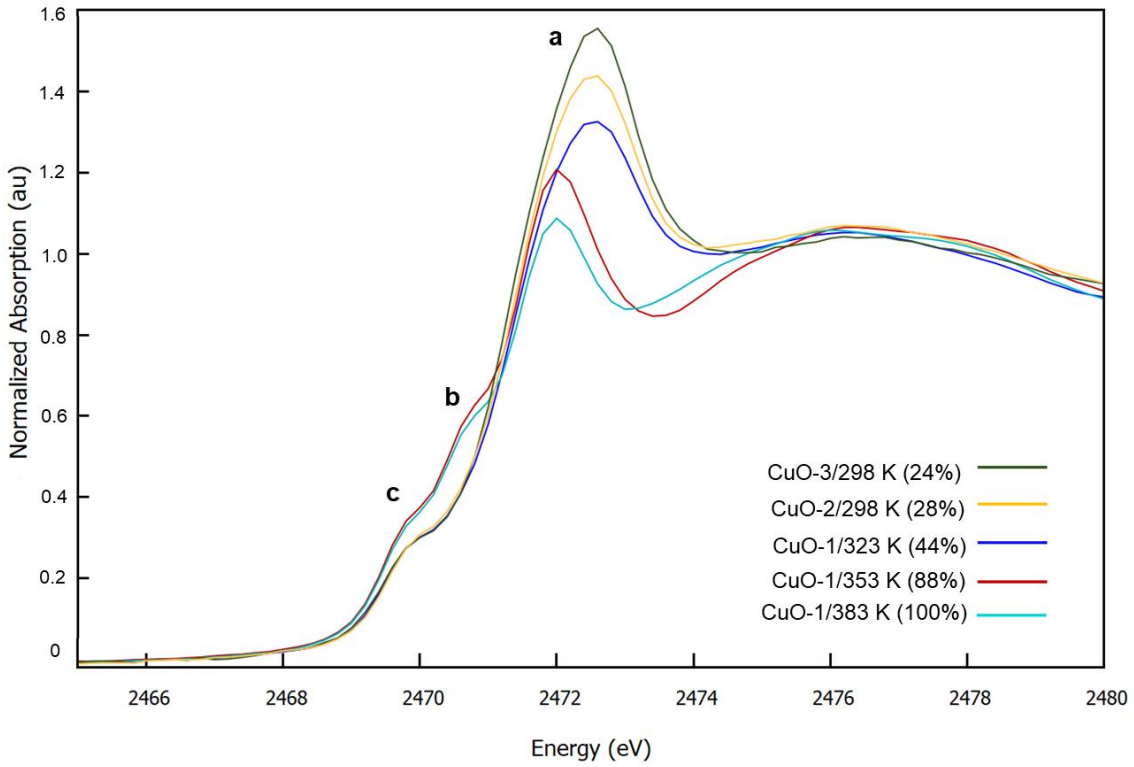

Figure 6-12: Normalized S K-edge XANES spectra for samples CuO-2 and CuO-3 after reaction at 298 K and CuO-1 after reaction at 323, 353, and 383 K (1000 ppm-vol H_2S/He, 298 K and 1 atm). The scans

were collected under flowing He. Experimental conversion of each sample is indicated in the figure legend.

In the S K-edge XANES of the reference covellite (CuS, Figure 6-13**)**, there are two characteristic pre-edge features, denoted as (b) and (c). These features have previously been assigned to a S^{2-} 1s → Cu^{2+} $3d^9$ transition (2469.9 eV) and a S_2^{2-} 1s → Cu^{2+} $3d^9$ transition (2470.7 eV).[253] It is apparent from the spectra shown in Figure 6-13 that in the spent CuO-1 samples at 383 K, both pre-edge peaks are present, but the second peak (b) is absent in the spectra collected on the spent sample at 323 K. (The conversion of CuO-1 at 383 K is 100%, Table 6-2). This difference is further highlighted by the second derivative plots of these spectra (inset of Figure 6-13). The white line (peak a) is assigned to a S_2^{2-} 1s → 3p transition,[253] confirming the presence of S_2^{2-} in all spent samples. Thus, rather than indicating the absence of disulfide ions, the absence of peak (b) in spent samples at low temperatures (298 and 353 K) indicates that the geometry of the S_2^{2-} in these samples differs from that of S_2^{2-} in bulk covellite (CuS). The pre-edge feature (peak b) is dipole forbidden and quadrupole allowed, and thus, it is present as a weak transition. When this feature is additionally forbidden by symmetry or spin inversion selection rules, it will be so weak that it will no longer be distinguishable from the background. Thus, the transition S_2^{2-} 1s → Cu^{2+} $3d^9$ must also be forbidden by symmetry selection rules for the CuO-1 samples after reaction at 298 and 353 K.

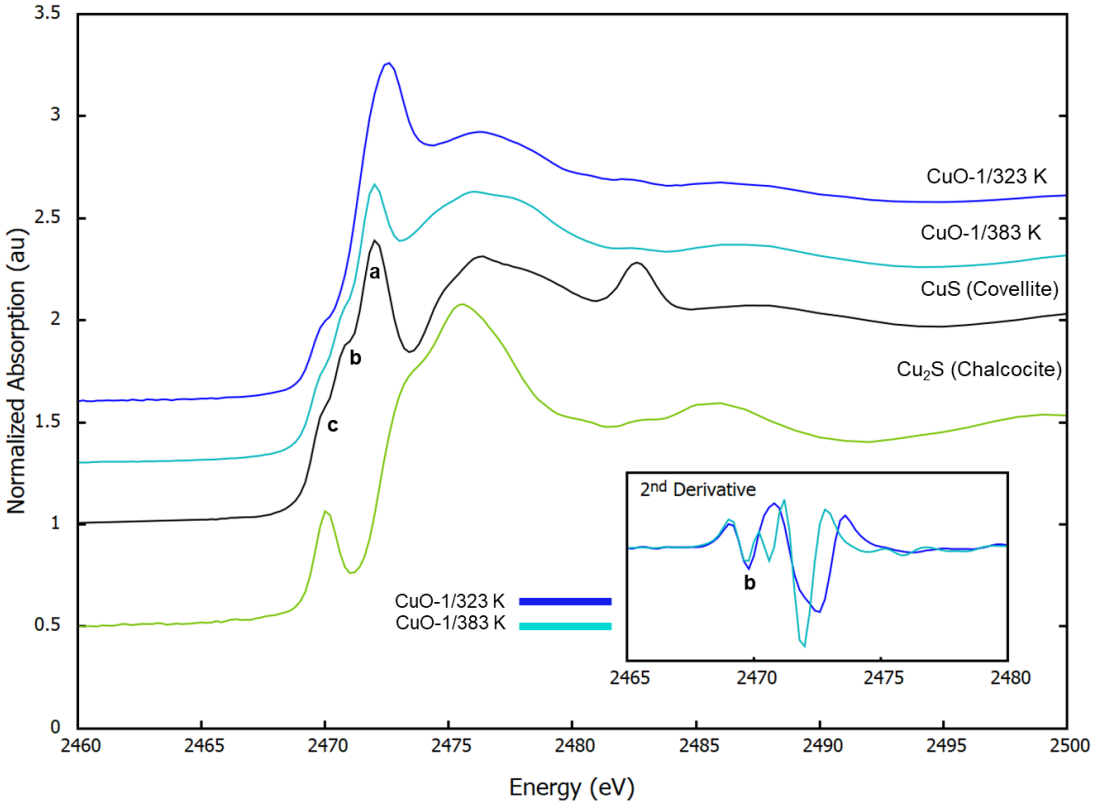

Figure 6-13: Normalized S K-edge XANES spectra for CuO-1 spent at 323 K and 383 K, and two copper sulfide references (CuS and Cu_2S). The spectra are offset for clarity. The inset shows the second derivative spectra of the spent samples highlighting the absence of peak b (S_2^{2-} 1s → Cu^{2+} $3d^9$) in the sulfided sample at 323 K.

To further explore whether the blue shift (shift to higher energy) of white line is characteristic only of spent samples at lower temperatures, in-situ S K-edge XANES spectra of CuO-1 sulfidation at elevated temperatures (353 K and 383 K) are inspected. Interestingly, the CuS species formed in the beginning of the sulfidation process at elevated temperatures matches those in spent samples at low temperatures (See Figure 6-14 for 353 K and Figure 6-15 for 383 K).[253] Figure 6-14 shows the move towards a dampened white line at lower energy, and the emergence of peak b as the reaction progresses at 353 K. Similar behavior is observed at 383 K (Figure 6-15) where the early spectrum, at low conversion, does not show the presence of peak b. This suggests that the formation of this distorted CuS is independent of temperature and

its presence is primarily dependent on the total conversion of CuO to CuS. Thus, because the sulfidation begins at interfaces (both the solid-gas interface and crystallite interfaces in the bulk), we suggest that it is at these interfaces that a geometrically distorted CuS structure is formed. As conversion proceeds, the intensity of peak b at 2470.7 eV (associated with the spectral features of bulk covellite) also increases, indicating the formation of bulk CuS away from the reaction interfaces.

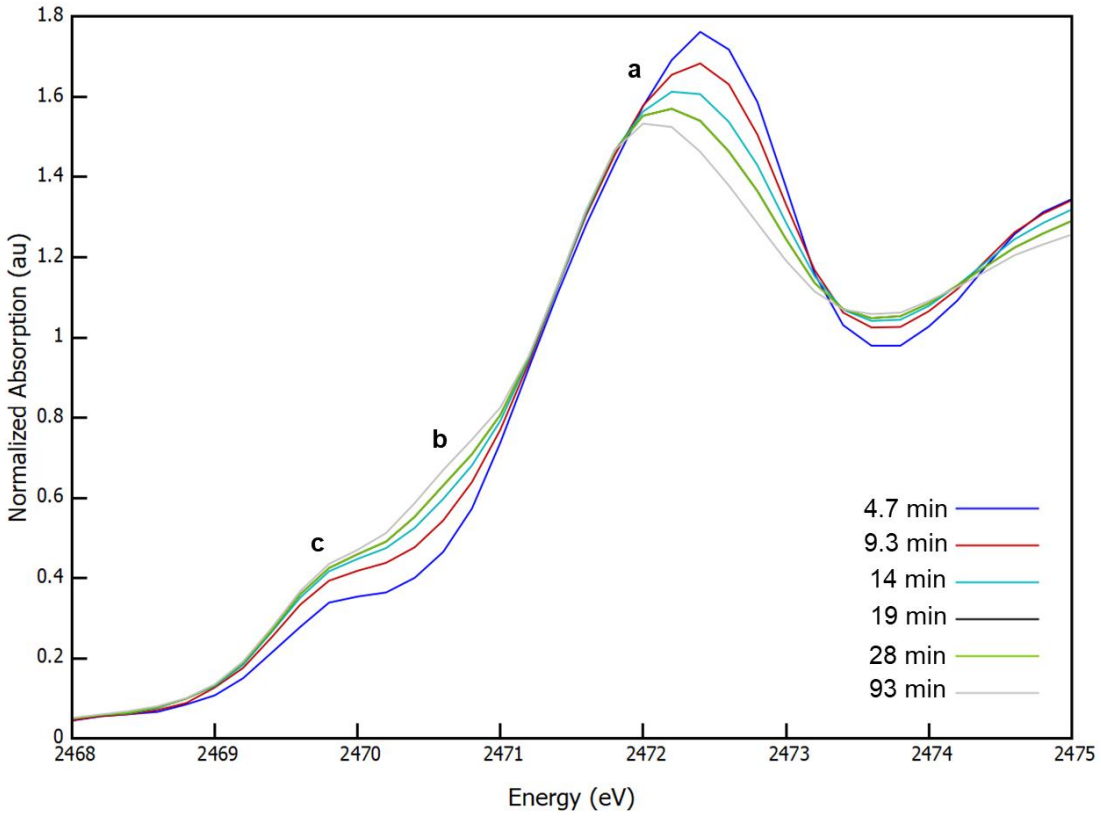

Figure 6-14: Normalized in-situ S K-edge XANES spectra for sample CuO-1 during sulfidation at 353 K, 1000 ppm-vol H_2S/He and 1 atm.

Concurrent with the growth of peak b, is the red shift (lower energy) of the white line observed at the latter stages of the sulfidation process at elevated temperatures. This peak is associated with a S_2^{2-} 1s → 3p transition[253] and it results from the hole character in the S_2^{2-} 3p orbitals due to the delocalization of these orbitals onto the electron deficient metal center. The

more electron-deficient metal centers are, the easier it will mix with the 3p orbitals of S_2^{2-}. Thus, small shifts in the energy of this peak can indicate the oxidation state of the metal center itself.[253] In other words, the environment of S_2^{2-} in spent samples at low temperatures is more electropositive than that of S_2^{2-} in bulk covellite. This further supports our theory of distorted CuS structure at the interface of CuO. The higher energy contribution of this peak, in the interfacial region, is because of the Cu^{2+} centers that are bonded to both O^{2-} and S_2^{2-} ligands. These centers are more electron deficient than Cu^{+}/Cu^{2+} centers in bulk covellite which are only bound to S^{2-} and S_2^{2-}. It is these same S_2-Cu-O centers which are responsible for the strained geometry that causes the disappearance of the 2470.7 eV peak.

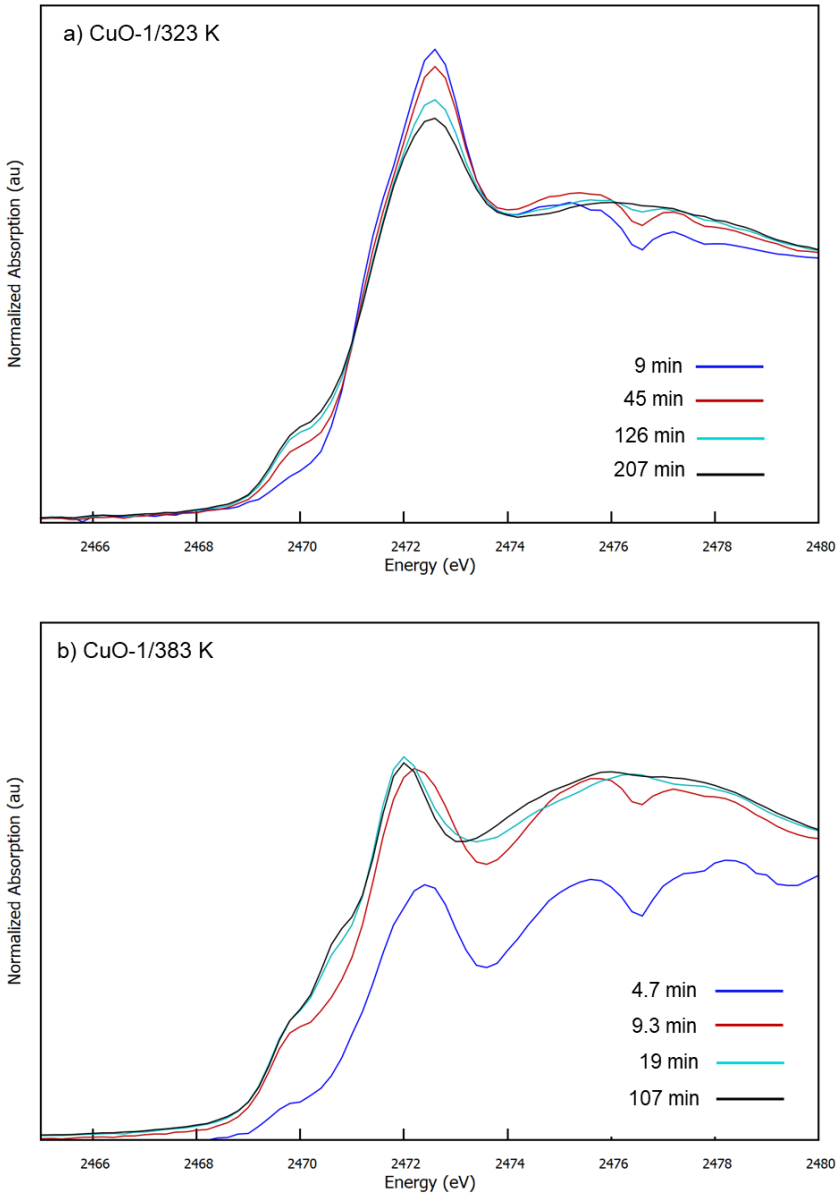

Figure 6-15: Selected normalized bulk in situ S K-edge XAS spectra of CuO-1 sulfidation with 1000 ppm H_2S/He at a) 323 K and b) 383 K. The spectra highlight the change in the formed CuS species as conversion increased.

6.3.4 Impact of CuS structure on reaction mechanism

Computational simulations using Density Functional Theory (DFT) on CuO surfaces show that sulfur exhibits a tendency towards forming covalent bonds with itself. DFT studies carried out by our group on CuO (111) and ($\bar{1}$11) surfaces, which are the most stable

thermodynamic surface (surface free energies of 0.75 and 0.89 J/m^2 respectively)[141] and are experimentally found in CuO materials,[249] show that, upon dissociative adsorption of H_2S molecules on CuO surfaces, sulfur atoms progressively replace oxygen atoms. As the reaction progresses and more H_2S is adsorbed (thus releasing H_2O), the sulfur coverage on the oxide surface increases, at which point close sulfur atoms start interacting among them via covalent bonding, which results in sulfur dimers appearing on the surface. Pathways on the CuO ($\bar{1}11$) surface show that elementary step structures that feature disulfide bond formation are more favorable than equivalent counterparts without these bonds. This is exemplified in two pathways, the first on a bare CuO ($\bar{1}11$) surface where multiple H_2S molecules participate in the reaction and the second on a partially sulfide CuO ($\bar{1}11$) surface where only one H_2S molecule is involved.

In the first case, disulfide bond formation stabilizes the structure of a step that requires migration of the hydroxyl. This is an energetically costly process since the hydroxyl is displaced from its equilibrium position on the lattice. However, with favorable sulfur-sulfur interaction, what will require a +43 kJ/mol increase in energy is reduced by 44% to only +24 kJ/mol. A snapshot of this improvement is shown in Figure 6-16, with the elementary step progression plotted against the reaction free energy. Only the part of the reaction involving hydroxyl migration is shown, with the case featuring disulfide formation in blue, and the case that does not in black. The blue curve lies below the black, highlighting disulfide bond formation as a favorable interaction that lowers the free energy of the system.

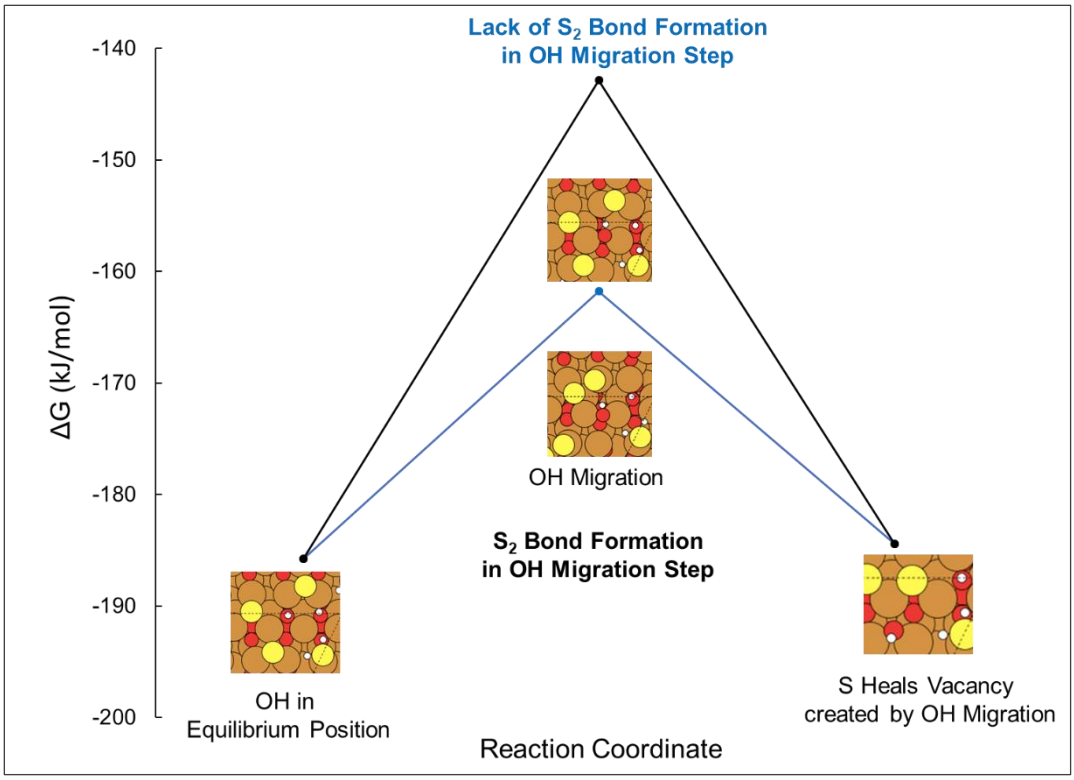

Figure 6-16: Part of the reaction pathway on a bare CuO ($\bar{1}11$) surface where multiple H_2S molecules participate in reaction, showing disulfide bond formation lowering the reaction free energy, rendering disulfide bond formation as an improvement on reaction favorability.

In the second case on the partially sulfide CuO ($\bar{1}11$) surface that simulates the surface in later stages of the reaction, disulfide bond formation lowers the energy of the structure for the elementary step involving the formation of a second hydroxyl and the subsequent hydroxyl migration step. The stabilizing effect is less pronounced for the second hydroxyl formation step, only by 2 kJ/mol, since it is already a greatly exothermic step. However, for the typically endothermic hydroxyl migration step, the presence of disulfide bonds makes the otherwise endothermic step exothermic, as seen in Figure 6-17, where the curve in blue (with disulfide formation) slopes downwards from steps B to C instead of upwards as shown in black (without disulfide formation). This corresponds to a change from +5 kJ/mol from steps to -4 kJ/mol from steps B to C. Observation of disulfide bond formation in energy minimization calculations for

proposed elementary steps of reaction suggests that disulfide bond formation is favorable during the reactive sorption of H_2S on CuO. These results further support our claim of the dominant presence of the disulfide ions on the surface of CuO crystallites which contributes significantly to the XANES signal at lower conversions.

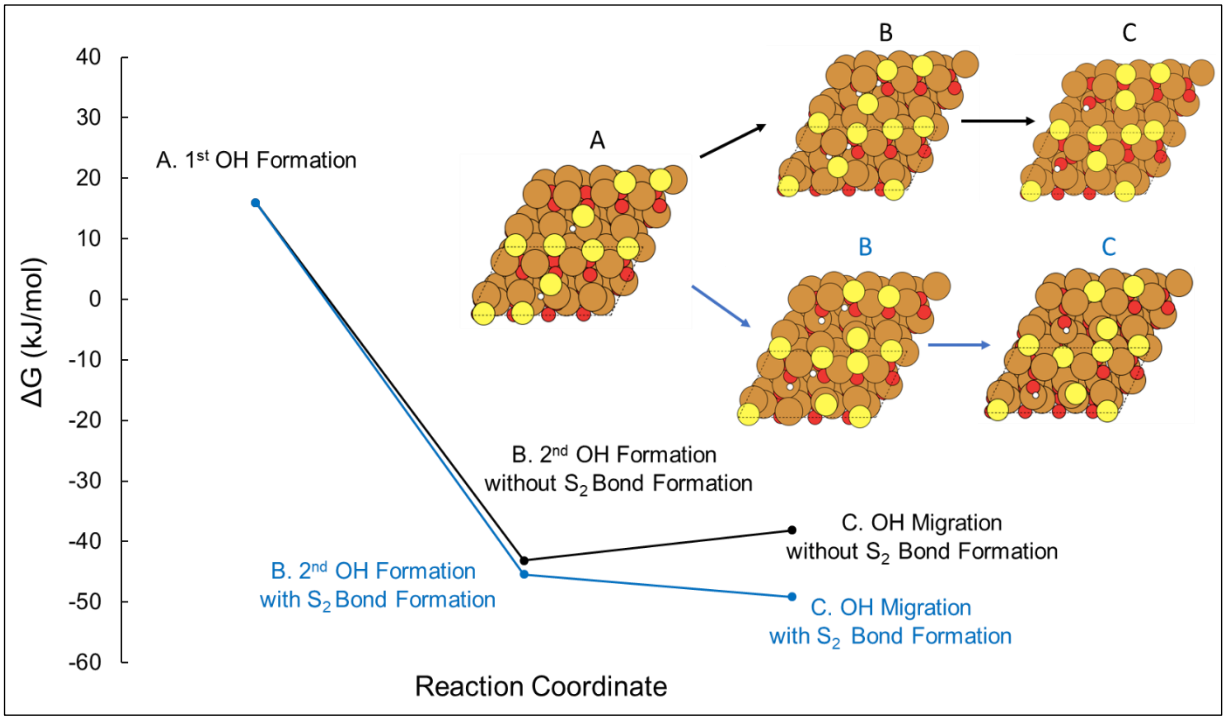

Figure 6-17: of the reaction pathway on a partially sulfided CuO ($\bar{1}11$) surface where one H_2S molecules participate in reaction, showing presence of disulfide bond formation making equivalent elementary step exothermic instead of endothermic (from step B to C).

Finally, XANES spectra taken at the Cu K-edge of the spent samples (Figure 6-18A) show that as temperature of sulfidation increases from 323 K to 383 K, the features of the CuO starting material, most notably the intense white line at 8998 eV, fade while the features of the covellite form of CuS grow in. Using tenorite (CuO) and covellite (CuS) standards as the basis set, linear combination analysis was performed to determine the degree of sulfidation in these materials. The results are shown in Table 6-2, showing a clear increase in total conversion of CuO to CuS as a function of temperature, with 100% conversion at 383 K. In all spectra, there

is a peak around 8978-8979 eV (highlighted by first derivative plot in Figure 6-18B). This peak is only present in compounds containing Cu^{2+} and is absent in the Cu_2S standard (yellow trace), as it results from a Cu^{2+} 1s → $3d^9$ transition.[253] Because this peak is forbidden by dipole selection rules, it is much weaker in systems with centrosymmetric ligands (as is the case of CuO) due to decreased p/d orbital hybridization. However, the presence of this peak in spent samples agrees with previous studies of CuS in the covellite structure.[10] Further evidence that Cu^{2+} is present in spent samples can be readily seen when comparing the first derivative of the XANES region (Figure 6-18B) for these materials. The sample sulfided at 323 K shows a weak pre-edge feature at 8979 eV, both because the material only contains 40% CuS, and because much of the CuS that forms is in a strained geometry. However, the strong single peak at 8980 eV from the Cu_2S standard is completely absent in the 323 K spent sample, indicating the lack of the formation of a Cu^{+}-S^{-2} species in this reaction.

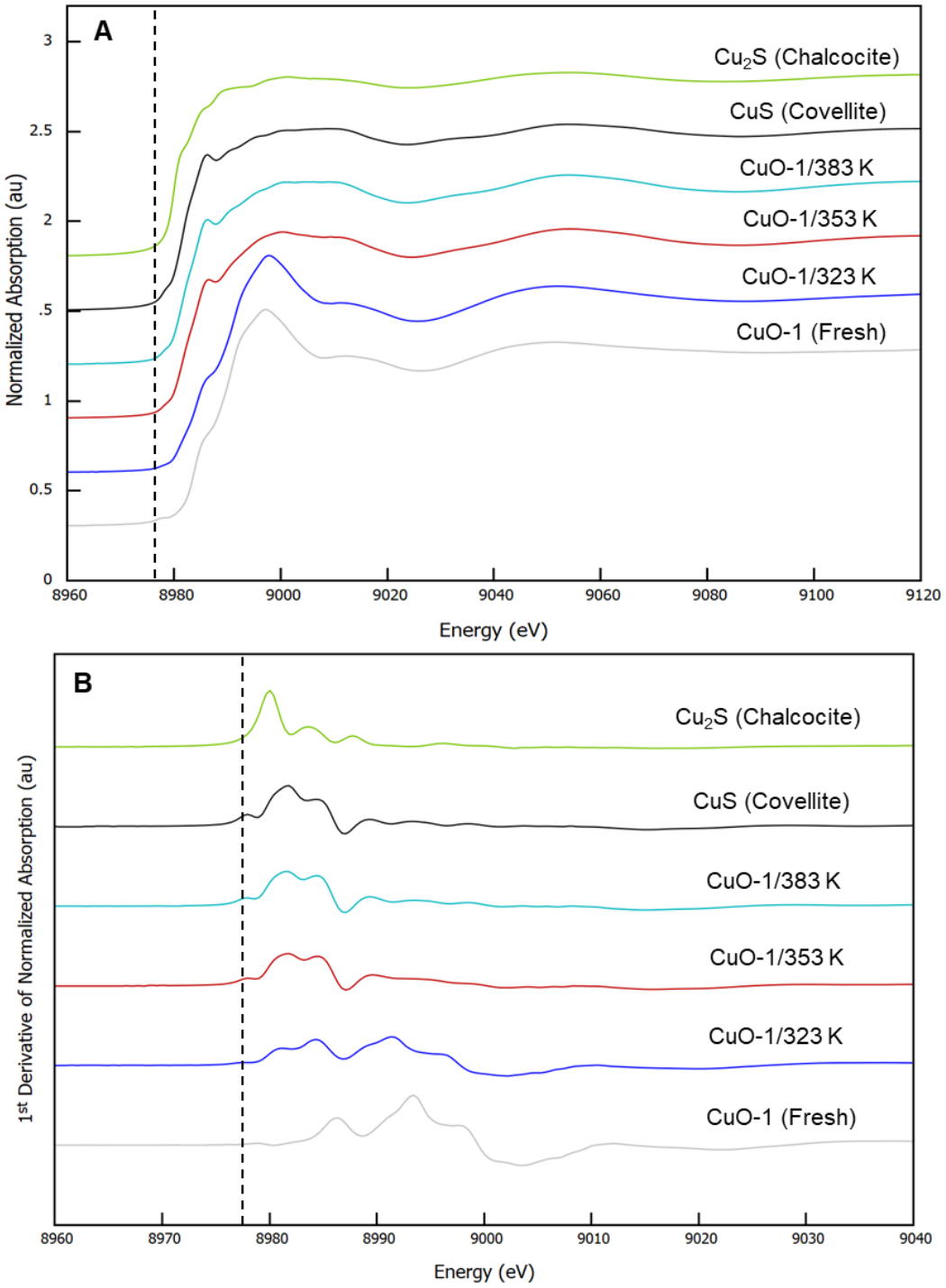

Figure 6-18: A) Normalized Cu K-edge XANES spectra for fresh CuO-1 sample, spent CuO-1 samples at 323, 353, and 383 K (1000 ppm-vol H_2S/He), and two copper sulfide references (CuS and Cu_2S). B) First derivative spectra of A) highlighting the pre-edge feature associated with Cu^{2+} 1s → $3d^9$ transition. Spectra offset for clarity.

Furthermore, the structure of the spent CuO species were analyzed by fitting of the EXAFS region of the Cu K-edge (Table E-2). By fixing the Cu-O contributions to the spectra and fitting the Cu-S scattering paths, it can be seen that covellite is a good fit for the spent material at higher conversions (353 and 383 K). At lower conversion, the Cu-S bond distance is appreciably longer (2.30 ± 0.02 Å at 323 K versus 2.26 ± 0.01 Å in covellite reference and sample spent at 383 K). In complement to the results at the S K-edge, this indicates that while the Cu is in a similar oxidation state to that in covellite at lower conversions, a strained geometry is generated by the initial sulfidation of the material. Finally, the coordination numbers of the Cu-S paths, derived from EXAFS models in the spent samples, were consistent with the change in conversion as temperature increased: 1.5 ± 0.5, 3.3 ± 0.1 and 3.4 ± 0.4 at 323 K, 353 K, and 383 K, respectively. These compare with 3.67 coordination in the averaged CuS model.

6.4 Conclusion

In conclusion, this study sheds light on the sulfidation mechanism of CuO sorbents during the uptake of H_2S. In particular, data are presented highlighting a unique structure at the interfacial CuO-CuS area which, consequently, unravels mechanistic details of the sulfidation process. S K-edge XANES showed evidence of S_2^{2-}, characteristic of CuS, for all spent samples, with a geometrically strained and more electropositive S_2^{2-} form at lower conversions (Spent samples at 298 K and 323 K and early *in-situ* sulfidation spectra of 353 K and 383 K). These differences are because the initially formed disulfide groups are bonded to Cu^{2+} which are bonded to O^{2-} in bulk CuO, as compared to S_2^{2-} in bulk covellite which are connected to Cu^{+}/Cu^{2+} that are bound to S^{2-} and S_2^{2}. The DFT simulations of CuO sulfidation paths (non-sulfided and partially sulfided (111) and ($\bar{1}$11) surfaces), suggest that the formation of disulfide ion is, indeed, thermodynamically favorable in the initial sulfidation stages which aligns with

our findings from S K-edge XANES. Finally, the Cu K-edge EXAFS fits of the sulfided samples show longer Cu-S scattering paths at lower conversions which, again, supports the strained interfacial geometry theory.

Chapter 7 | Lanthanum Induced Weakening of Lattice Copper-Oxygen Bonds Improves Hydrogen Sulfide Capacities of Copper Oxide Adsorbents

7.1 Introduction

The sorbents studied for reactive sorption of hydrogen sulfide (H_2S) consist mostly of the oxides, hydroxides, and carbonates of iron, zinc, and copper at 473-1073K.[265–267] Elevated process temperatures are used to mitigate the kinetic limitations encountered at low temperature which result in low utilization factors.[266,268] Among all studied sorbents, copper oxides (CuO and Cu_2O) are considered the most favorable sorbents for sulfur removal.[269] A comprehensive thermodynamic study of the copper-sulfur-oxygen system[270] show high equilibrium constants (e.g. $K_s = 6.3 \times 10^{17}$ for CuO sulfidation at 900K) which result in a decrease in H_2S concentration from several thousand ppm to the sub-ppm level. Nevertheless, CuO has low resistance to reduction to metallic copper (Cu) at high temperatures, which agglomerates and leads to structural degradation and poor kinetics.[133] Thus, CuO is often mixed with other metals or supported on inert matrices. The mixing of metals stabilizes Cu^{2+} and Cu^{1+} against reduction to Cu, which results in new compounds of superior sulfur removal capacities.[129] An example of this is the mixing and supporting of CuO and ZnO on SBA-15 zeolites using wetness impregnation which achieves an 87% oxide conversion at 423K.[271]

However, unlike high-temperature desulfurization studies there is limited work done on the removal of H_2S by metal oxides at low temperature.[272–274] Xue et al. investigated a series of pure metal oxides and mixed metal oxides (CuO, ZnO, NiO, CaO, SnO, Mn_3O_4, Zn-Mn-O, Zn-Co.O, Zn-Al-O, and Zn-Ti-Zr, which were prepared from various hydrous oxides and hydroxycarbonates precursors) and found that several of these oxides had high H_2S removal

capacity (10.0-28.0 g H_2S g^{-1} sorbent) at room temperature.[274] This suggests that the mixing and doping of oxides is promising not only at elevated temperatures where it mitigates reduction to elemental metals, but also at low temperatures.

A fundamental understanding of the CuO-H_2S reactions, and the structural and chemical changes incurred by introducing foreign atoms is necessary for optimal deployment of these technologies. To probe these processes at the molecular scale, advanced characterization techniques must be utilized in addition to bulk kinetic studies which, together, allow for relating structural and chemical parameters to sorbents performance. In our previous work, the effects of crystallite size and micro-porosity on the performance of chemically similar CuO sorbents was thoroughly investigated. CuO demonstrated an increase in removal capacity with crystallite size decrease with a maximum conversion of 44% for 2.8 nm crystallite size at room temperature.[28,249] The spatial and temporal evolution of reaction front within few millimeters-sized CuO sorbent was probed through simultaneous X-ray absorption spectroscopy (XAS) and transmission X-ray microscopy (TXM) which suggested the presence of pore diffusion resistance at the micro scale.[28]

In this work, we study the effects of lanthanum (La) additives on CuO sorbents' structural properties and sulfur removal performance through a combination of fixed bed kinetic studies and advanced synchrotron-based characterization techniques. La was selected because of its relatively large cationic radius (R_{La}/R_{Cu} = 1.5) compared to the more commonly studied additives such as Zinc, Nickel and Cobalt (R_x/R_{Cu} = 1.0). This difference in cationic radii is expected to introduce disruptions to the CuO lattice,[275,276] which would cause the formation of more vacancies that facilitate the diffusion of oxygen and sulfur atoms through solid phases.[277] To explore the structural and chemical changes upon lanthanum addition, we collected XAS

for fresh and spent reference commercial CuO-based sorbent and two lab-synthesized La-CuO sorbents (2:1 Cu to La ratio) prepared by different synthesis methods (sol-gel and co-precipitation with ammonium). XAS scans were collected at S K-, Cu K-, and La L_3-edges to provide complimentary evidence of the chemical and structural differences between the samples. In-situ XANES at S K-edge for the three samples at 1000 ppm H_2S/He, 1 atm, and 323K, provided kinetic information that are consistent with fixed-bed reactor results. Additionally, X-ray diffraction (XRD), N_2-physiosorption measurements (BET), scanning electron microscopy (SEM), transmission electron microscopy (TEM), and energy-dispersive X-ray spectroscopy (EDS) were used to form a comprehensive chemical and structural analysis of the samples.

7.2 Experimental Methods

7.2.1 Materials

The first La-CuO sample, denoted as CuO-La-1, was prepared using an acid-catalyzed sol-gel process.[210] 1.0 cm^3 of glacial acetic acid (VWR, ACS grade) was added to 300 cm^3 of 0.133 M copper (II) nitrate (Sigma Aldrich, 99%) and 0.067 M lanthanum (III) nitrate hexahydrate (Sigma Aldrich, 99%) under vigorous stirring and heating. At boiling point, 0.8 g of sodium hydroxide was added to the solution with continuous stirring, creating a precipitate. The supernatant was then poured off and the precipitate was washed with deionized water and ethanol (Sigma-Aldrich, 100%). The washed precipitate was then dried in air for 24 hours at 333 K.

The second La-CuO, CuO-La-2, sample was synthesized via an aqueous ammonia co-precipitation method.[278] 1 cm^3 of ammonium hydroxide (Fisher Scientific, ACS Plus) was

added dropwise to 300 cm^3 of aqueous 0.133 M copper (II) nitrate and 0.067 M lanthanum (III) nitrate hexahydrate solution until a precipitate formed. The precipitate was then allowed to settle, and the effluent was decanted. The sample was then washed and centrifuged twice, dried in a drying oven (353 K) overnight, and thermally treated at 873 K for 2 hours, afterwards.

Finally, a commercially produced CuO-based material (HiFUEL W230; lot number L04Y006; 63.5 wt% CuO, 25 wt% ZnO, and 10 wt% Al_2O_3) was purchased from Alfa Aesar. This sample is denoted as CuO-1 and was used as a reference for comparison with other lanthanum containing samples. Section 1.1 in the SI provides synthesis details for other pure CuO and La-doped samples.

7.2.2 Fixed bed sulfidation tests

The fixed-bed sorption breakthrough experiments analyzed in this study were carried out in the apparatus outlined in Figure 3-2. A tubular stainless-steel reactor with 0.25-inch outer diameter was packed with 100-180 mg of sorbents of 75-125 μm agglomerate size. The packed beds were 1.4-1.9 cm in height and were fixed between two plugs of quartz wool. The temperature of the reactor was set to 323 K and was regulated using a resistively heated jacket with a PID temperature controller (TEMPCO EPC-100). The inlet of the reactor consisted of 1000 ppm-vol H_2S in N_2 and was produced by diluting 1.0% H_2S/N_2 (Praxair) in UHP N_2. The total inlet flowrate of 90 sccm was controlled using MKS GE50A and GM50A flow controllers. An online gas chromatography (Agilent 7890B) with a sulfur chemiluminescence detector (SCD; Agilent 755) was used to measure the concentration of sulfur in inlet and outlet streams. The interior of the reactor and all the gas transfer lines were treated by an inert coating (SilcoNert 2000) which ensures that sulfur wouldn't adsorb onto the walls.

7.2.3 Non-synchrotron characterization techniques

The synthesized La-CuO sorbents and the commercial CuO sorbent, as described in the previous section, were characterized using a variety of techniques. Powder X-ray diffraction patterns were obtained on an X-ray diffractometer (JEOL JDX-3530 and Philips X-Pert) using Cu Kα radiation of 1.5410 Å to identify the CuO and La_2O_3 phases. The average crystallite sizes were found using Scherrer's formula. Nitrogen adsorption-desorption isotherms were measured at 77 K with a Micrometrics ASAP 2020 Plus system. Before measurements, the samples were degassed at 1×10^{-3} Torr and 573 K. The Brunauer-Emmett-Teller (BET) surface areas were calculated from the isotherms by using the BET equation. The pore size distribution was derived from the adsorption branches of the isotherms using the Barrett-Joyner-Halenda (BJH) model.

Scanning electron microscopy (NOVA 230 Nano SEM) was used to determine the morphology of the sorbents. The diameter of the sorbents was calculated from the SEM images using ImageJ software. Two transmission electron microscopy (TEM) systems were used to obtain scans for the samples that were dispersed on holey carbon grids. The first is a FEI Tecnai G(2) F30 S-Twin operated at 300kV; and the second is a JEOL 2010F 200kV equipped with an Oxford AZTEC 80 mm^2 SDD energy dispersive spectroscopy (EDS) detector with an ultrathin window. Basic STEM imaging was performed on the Tecnai F30, while selected area EDS was performed on the JEOL 2010F. In this technique, the microscope was operated in TEM mode, and the beam was condensed at higher spot sizes in order to limit the field of excitation to key areas of interest. This technique was used in place of STEM-EDS mapping due to the beam sensitivity of copper oxide materials. For this study, areas of interest were smaller clusters of crystallites – typically on the order of 50-100 nm. Because some samples showed variability

even at this size regime, more high-resolution EDS mapping was considered unnecessary. EDS spectra were collected at 8-10 spots in order to obtain an average value for each sample.

7.2.4 Synchrotron-based characterization

X-ray absorption spectra were recorded at Stanford Synchrotron Radiation Lightsource (SSRL, California, USA) at wiggler beamline 4-3 using a Si(111) double-crystal monochromator. The storage ring was operated at 3 GeV with a ring current of 494-500 mA in fill-in mode. The beam cross-section was 1 mm x 3 mm. X-ray absorption near-edge structure (XANES) spectra were recorded at the S K-edge (2472 eV) and La L_3-edge (5483 eV) in fluorescence mode using a 7-element silicon-drift detector (Canberra) and full extended X-ray absorption fine structure (EXAFS) at the Cu K-edge (8979 eV) in transmission mode. Obtaining XANES at multiple edges allows for unravelling the differences in the average chemical environments of each of the three elements, and subsequently, understanding the differences in sulfur removal performance between the sorbents. Collecting the EXAFS at the Cu K-edge allows for quantifying the structural and coordination changes which were incurred by introducing lanthanum to CuO sorbents. Finally, in-situ XAS experiments at S K-edge were used to deduce bulk kinetic and diffusion parameters to complement the fixed-bed experiments.

The sample was a wafer consisting of 36 mg of CuO-based sample mixed with 14 mg of boron nitride (BN) (Sigma Aldrich) for the S K-edge, and 2.4 mg of sample diluted with 47.6 mg BN for the Cu K-edge and La L_3-edge. The wafer was placed at 45° to the incident beam on a heated stage inside a 100 cm^3 cell, as described previously and as shown in Figure 6-2.[257]

For in-situ XAS sulfidation experiments at S K-edge, 1000 ppm H_2S in helium (Airgas) and helium (99.95%, Airgas) gases were used. Initially, the temperature of the cell is ramped

up to 50 °C at a ramp rate of 5 $K \cdot min^{-1}$ under a 20 sccm flow of helium. Once temperature stabilized, helium flow was stopped and 1000 ppm H_2S/He was introduced at 20 sccm and XAS scans were collected every 9 minutes. The samples were exposed to 1000 ppm H_2S/He flow for 4-6 hours until saturation was achieved. The cell was then purged by helium at 20 sccm and allowed to cool to room temperature before XAS scans of spent samples were obtained.

XAS data were analysed using ATHENA and ARTEMIS from the Demeter package of software.[241] The EXAFS data was extracted from 3.0-13.0 $Å^{-1}$ in k-space, and the Fourier transformed data were analysed in the range of 1.0-3.2 Å. Intensity and phase of scattering paths were calculated using FEFF6 based on crystallographic data from the Tenorite CuO structure (ICSD 16025).[242] EXAFS fitting was performed based on k, k^2, and k^3 weighting. S_0^2 was determined to be 0.73 for these samples based on fitting a reference copper foil with tabulated coordination numbers (*fcc*-Cu metal: ICSD 53247).[242]

7.3 Results and Discussion

7.3.1 Effects of nominal La content and synthesis method on sorbents removal capacity

This work started by exploring the effects of the synthesis method and the amount of La salt precursor on the La-CuO sorbents' sulfidation performance. Pure CuO and La-CuO sorbents were synthesized and tested for H_2S removal using fixed bed experiments at 323 K, 1 atm and an inlet H_2S concentration of approximately 1000 ppm-vol. The removal capacities, q_s, are defined as g H_2S per 100 g of CuO phase in the sorbent, where 42 wt.% corresponds to the stoichiometric conversion of CuO to CuS. Sulfidation tests for pure lanthanum oxide (La_2O_3) at the same conditions were performed and yielded no pickup (<0.5 wt.%). Thus, CuO was considered to be the only reactive phase in this work. Table 7-1 summarizes the synthesis

conditions, nominal La/Cu salts ratio in the synthesis precursors, crystallite size, removal capacities, and conversion of CuO phase for all the tested samples.

Table 7-1: Summary of sulfidation tests results for fixed beds of CuO-based samples at 1000 ppm-vol H_2S/N, 323 K and 1.0 atm.

Sample ID	La/Cu Salt Ratio	Synthesis Method	Synthesis/ Processing Conditions	Thermal Treatment	Crystallite Size (nm)	q_s (wt%)	% Conversion
CuO-1	Commercial	-	-	-	2.8	24.9 ± 0.3	59.2
CuO-2	100% Cu	Sol-gel	Synthesized at 373K for 45 minutes	Dried at 333K for 24 hours	3.3	21.9 ± 0.2	52.2
CuO-3	100% Cu			Dried at 333K for 24 hours then treated at 473K for 8 hours	8.0	20.4 ± 0.3	48.7
CuO-La-3	1:99	Sol-gel	Synthesized at 373K for 45 minutes	Dried at 333K for 24 hours	6.8	7.3 ± 0.1	17.4
CuO-La-4	1:9				8.0	13.0 ± 0.1	30.9
CuO-La-1	1:2				10.5	26.9 ± 0.4	63.9
CuO-La-2	1:2	Aq. ammonia	Centrifuging	Treated at 873K for 2 hours	4.3	35.8 ± 1.0	85.2
CuO-La-5	1:2	Co-precipitation	Synthesized at 373K for 45 minutes	Dried at 333K for 24 hours	2.1	25.0 ± 0.5	59.5

The results in Table 7-1 show that introducing La to the synthesis of CuO sorbents resulted in an enhancement in the sorbent removal capacity at for most samples. Two of the samples, CuO-La-1 and CuO-La-2 with 33% La content, achieved removal capacities of 26.9 wt.% and 35.8 wt.%, respectively. These results represent a 31% and 63% improvement in removal capacity compared to pure CuO samples of comparable crystallite sizes (CuO-2 and CuO-3 in Table 7-1). Comparing samples of similar crystallite size is important as previous work have demonstrated that crystallite size is the most influential factor in determining sorbents performance.[275] Table 7-1 also shows that the La-CuO samples with La content of 1% and 10% in the precursor salt didn't achieve an improvement in sulfur removal performance.

This might be the result of the precipitation of La as a separate La_2O_3 phase instead of mixing with the CuO phase for smaller amounts of La salt in synthesis precursor.[279]

The results in Table 7-1 also show that the sample prepared via precipitation with aqueous ammonia, CuO-La-2, achieved the highest removal capacity compared to the other two samples, CuO-La-1 and CuO-La-5, which are prepared via sol-gel and co-precipitation methods, respectively, with the same amount of La in the salt precursor (33%). Namely, CuO-La-2, with crystallite size of 4.3 nm achieved a removal capacity that is 43% higher than CuO-La-5 (2.1 nm) and 33% higher than CuO-La-1 (10.5 nm). In our previous work for pure samples, the synthesis method didn't affect the performance of the sorbents as long as they had similar crystallite size. The influence of the synthesis method in case of mixed samples is, then, a result of the level of inclusion of La within CuO lattice instead of precipitating as a separate phase. The addition of ammonia to the precipitation method controls the pH of the solution allowing slower precipitation of both phases, CuO and La_2O_3, and thus a higher chance of mixing Cu-La-O.[278] Different characterization methods in the following sections support this claim.

To further explore the effects of introducing La to CuO sorbents, the two best performing La-CuO samples, CuO-La-1 and CuO-La-2, were thoroughly characterized to identify the chemical and structural drivers for this improvement. Data from our previous characterization-kinetics studies on a CuO-based commercial sorbent (CuO-1)[28,208] are used to compare against the results for the La-CuO sorbents and to demonstrate the effects of La addition on the molecular features of CuO.

7.3.2 Physio-Chemical properties of La-CuO sorbents identified via non-synchrotron-based techniques

XRD was used to identify the crystalline phases and average CuO crystal sizes of CuO-1, CuO-LaO-1, and La-Cu-2. The XRD patterns **(**Figure 7-1**)** of the fresh adsorbents show diffraction peaks that are characteristic of the planes of a single-phase monoclinic CuO.[280] The average crystal sizes of the sorbents using Scherrer's formula based on the $2\theta=39^{\circ}$ peak were 10.5 nm for CuO-La-1, 4.3 nm for CuO-La-2, and 2.8 for CuO-1. These crystallites fall within the size range for measurable H_2S capacity (<24 nm) as identified in our previous work.[275] Peaks at $2\theta=29^{\circ}$ and 42° in the pattern for CuO-La-1 identify La_2O_3 and indicate that some of the La precipitated as a separate La_2O_3 phase during the sol-gel synthesis. These peaks were absent from the CuO-La-2 sample pattern, however, indicating that any La_2O_3 crystallites (if present) are too small to diffract X-rays. Moreover, Figure 7-1 shows the XRD patterns of the spent samples where peaks corresponding to both CuO and CuS were identified. The spent patterns are more difficult to interpret since CuS and La_2O_3 have overlapping peaks. A reduction in the intensity and size of the CuO peaks (and thus, crystallinity) was observed for all spent samples due to the conversion of CuO to CuS which is associated with a volume expansion (60%) that causes a disintegration of the crystals.

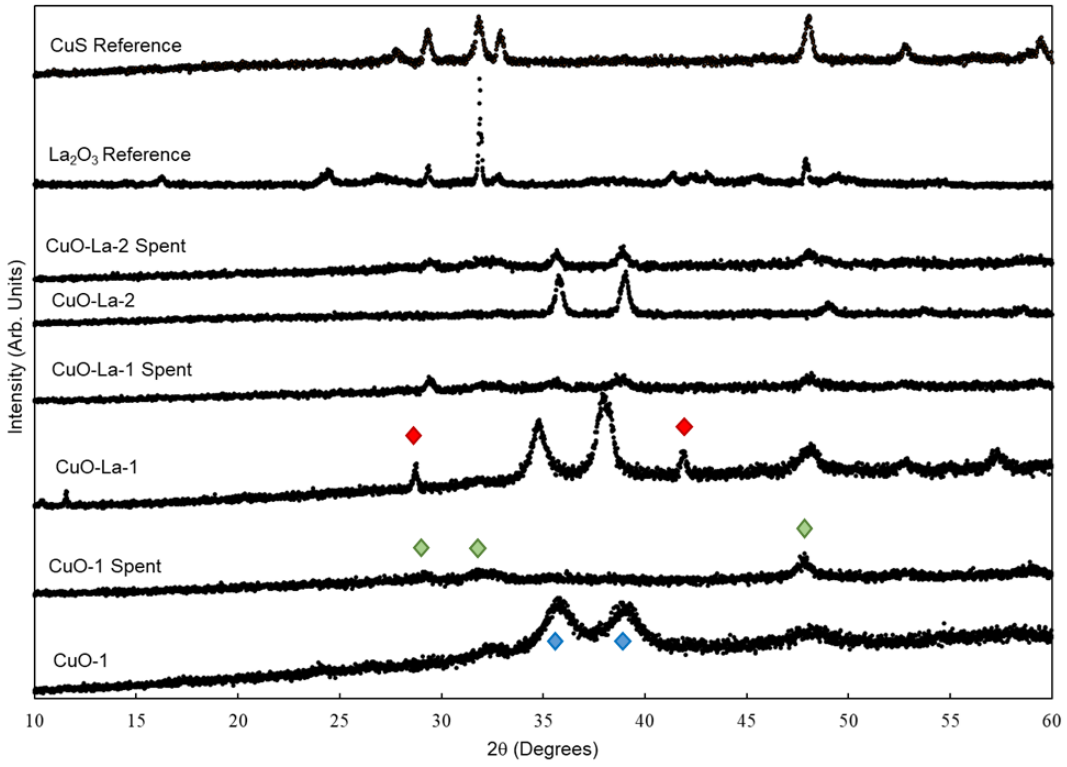

Figure 7-1: X-ray diffraction patterns of a commercial CuO sorbent (CuO-1), and two lanthanum-doped sorbents prepared via sol-gel (CuO-La-1) and ammonia co-precipitation (CuO-La-2), before and after reaction with 1000 ppm H_2S/N_2 at 323 K and 1 atm. CuS and La_2O_3 diffraction patterns are included as references. Blue markers indicate characteristic CuO peaks, green markers indicate characteristic CuS peaks, and red markers indicate La_2O_3 peaks.

N_2-physisorption measurements were performed for the samples (CuO-1, CuO-La-1, and CuO-La-2). Table 7-2 summarizes the structural parameters calculated from the experiments. Both La-CuO sorbents had surface areas that were lower than the commercial sorbent (23.44 $m^2\ g^{-1}$ for CuO-La-1 and 10.84 $m^2\ g^{-1}$ for CuO-La-2 compared to 63 $m^2\ g^{-1}$ for CuO-1). On the other hand, CuO-1 and CuO-La-1 exhibited comparable porosities (0.14 and 0.17 cm^3g^{-1} respectively) while CuO-La-2 had a considerably lower porosity of 0.019 cm^3g^{-1}. Thus, BET results confirm that surface area and porosity were not the determining factor for the sorbents' performance, as the sample with poorest porosity, CuO-La-2, achieved the highest removal capacity and conversion (85%). This is consistent with our findings in a previous study

that concludes that favored textural properties (i.e., small agglomerates in SEM, and larger surface areas and pore volumes) do not necessarily equate to improved performance when a metal additive is present.[281]

Table 7-2: Physiochemical properties of the La-doped CuO sorbents relative to the commercial CuO-based sorbent. [a] Based on XRD. [b] Based on BET. [c] Based on BJH method.

Sample ID	Synthesis Method	La molar % (Bulk)	La wt. % (TEM-EDS)	Crystallite Size (nm)[a]	S_{BET} (m^2g^{-1})[b]	V_{pore} (cm^3g^{-1})[c]
CuO-1	Commercial	0	-	2.8	63.00	0.14
CuO-La-1	Sol-gel	33	1.0 ± 1.4	10.5	23.44	0.17
CuO-La-2	Co-precipitation	33	3.3 ± 0.3	4.3	10.84	0.019

STEM and TEM images of the sol-gel, CuO-La-1, and ammonia co-precipitation, CuO-La-2, samples are shown in Figure 7-2. In Figure 7-2d, the CuO-La-2 particles of 20-50 nm size show uniform intensity across the width of each particle. An intensity line profile (Figure 7-2f) along the yellow line in Figure 7-2d shows the plateau of intensity across a single particle in the CuO-La-2 sample. Because STEM contrast is based primarily on atomic number, this implies that samples made by the ammonia co-precipitation method show uniformity of La and Cu distribution. In contrast, the La and Cu distribution in CuO-La-1 is less uniform as evidenced by the uneven intensity of the sample at the same 10 nm length scale as the crystallite size (Figure 7-2a). This rapidly varying intensity can be seen in the intensity line profile (Figure 7-2c) and gives the sample a textured appearance in STEM images. Additionally, the selected area EDS results (Figure 7-3) show that in any given 100 nm area, La is 3.3 ± 0.3 wt. % for CuO-La-2 sample, while CuO-La-1 averages at 1.0 ± 1.4 wt. %. The relatively low variation in the EDS results of the CuO-La-2 sample is consistent with the even intensity of each particle

throughout the sample in the STEM images. On the other hand, the high variation in the CuO-La-1 sample implies phase segregation which is consistent with XRD results.

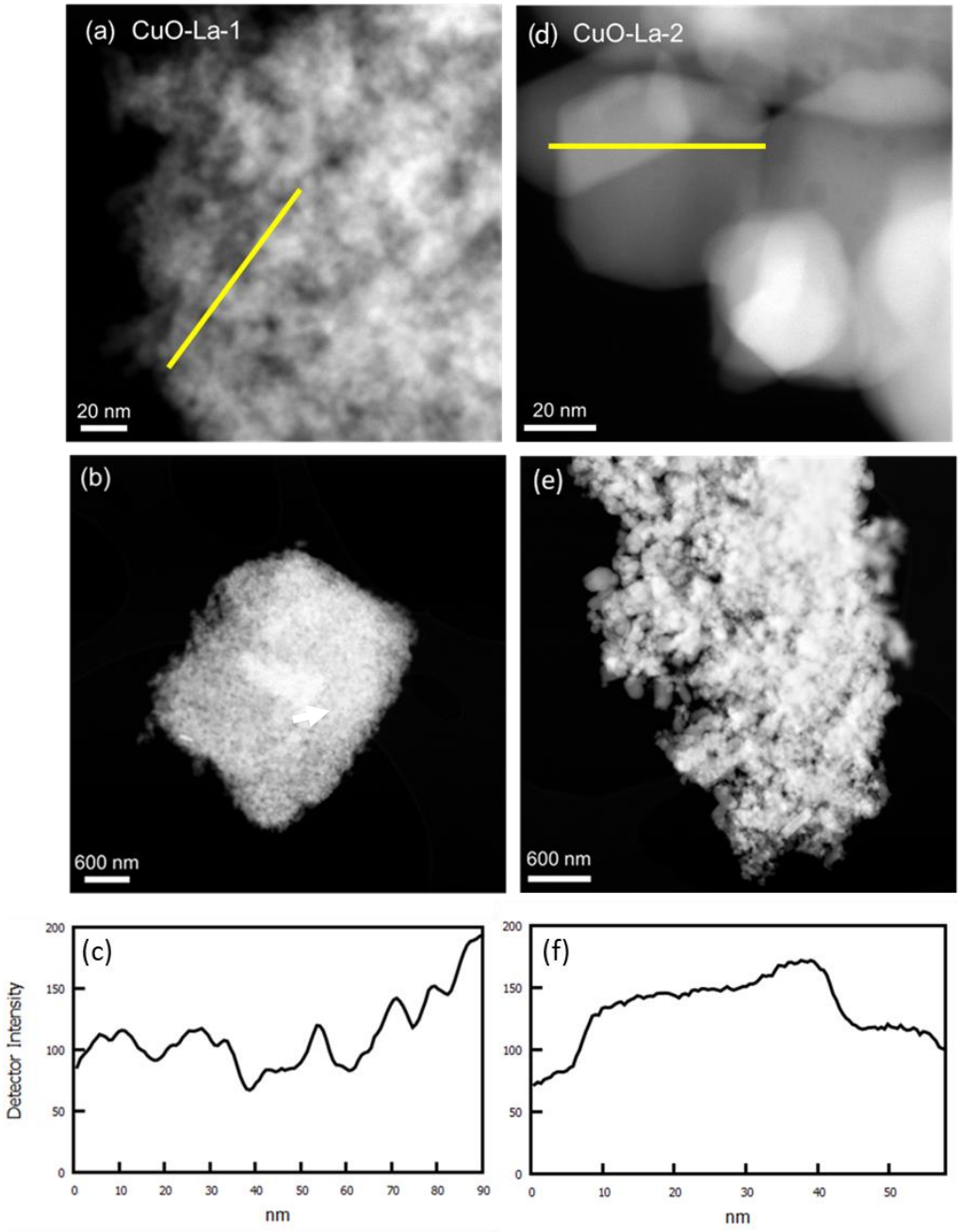

Figure 7-2: STEM images of CuO-La-1 (a-b) and CuO-La-2 (d-e). The detector intensity profiles for CuO-La-1 (c) and CuO-La-2 (f) are generated along the identified yellow lines in the STEM images. The smooth and additive intensity of CuO-La-2 indicates even distribution of the La species, in comparison with the blotchy appearance of Cu-O-La-1.

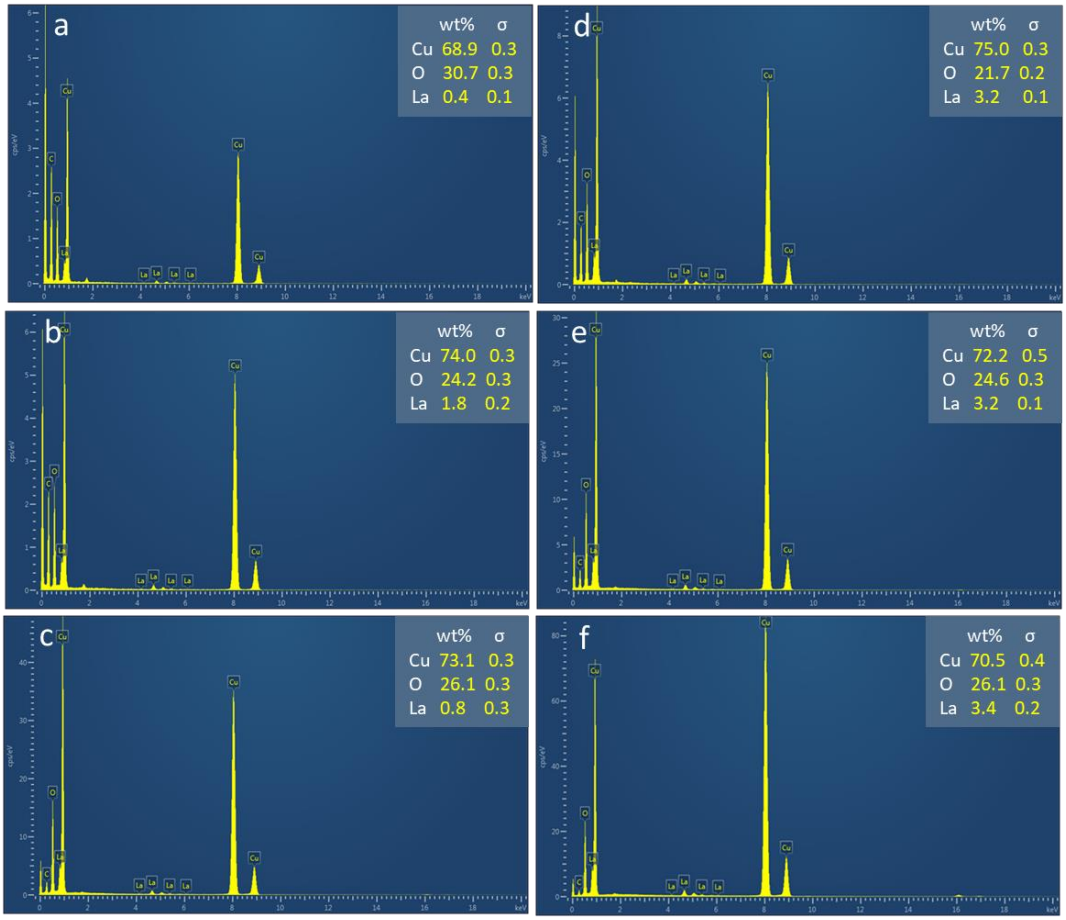

Figure 7-3: EDS spectra for selected 100 nm areas from STEM images of CuO-La-1 (a-c) and CuO-La-2 (d-f).

In summary, non-synchrotron-based characterization showed that CuO-La-2, compared to CuO-La-1, features smaller crystals and a more uniform distribution of La throughout the CuO phase. It also showed that this synthesis method resulted in more incorporation of La in the CuO phase, based on EDS, and smaller La_2O_3 crystals, based on XRD. These results suggest that the improvement in sulfur uptake by CuO-La-2, compared to CuO-La-1, is due to an increased Cu-O-La interfacial area which leads to a larger volume of disrupted CuO lattice that in turn facilitates the swapping of oxygen for sulfur ligands during the sulfidation reaction.

7.3.3 Multi-edge XAS study of changes in chemical environment

In order to investigate the structural and chemical changes induced by La addition to CuO sorbents, XAS experiments were performed at each of the Cu K, S K and La L_3-edges. For S and La-edges, XANES spectra were measured, while full EXAFS was measured for Cu K-edge. Figure 7-4 shows the Cu K-edge XANES region of the fresh samples: CuO-1, CuO-La-1, and CuO-La-2 which are qualitatively consistent with CuO XANES in previous studies.[208] The pre-edge feature at 8979 eV in all three samples arises from a Cu $1s^2$ to $3d^9$ dipole forbidden transition. This feature is indicative of Cu^{2+} species as there are no empty 3d orbitals in the Cu^+ species. The presence of Cu^{2+} species indicates, conclusively, that the spectra is indeed dominated by CuO. Nevertheless, the La-CuO samples display a 1.5 eV blue shift, and depression of white line peak, at 8997 eV, as compared to the CuO-1 spectra. This indicates that the copper in the La-CuO samples is more electron rich than that of the CuO-1[28] which is a result of oxygen pulling electron density away from La, with electronegativity of 1.1, towards Cu, with electronegativity of 1.9. This higher electron density on the Cu^{2+} atoms weakens the Cu-O bonds and results in easier replacement of O^{2-} by S^{2-}.

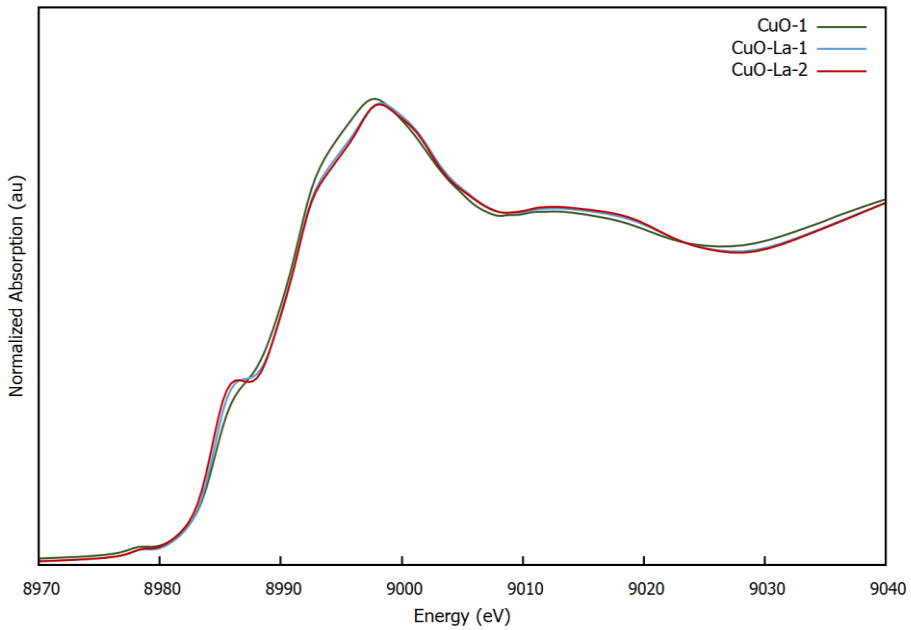

Figure 7-4: Normalized Cu K-edge XANES spectra for commercial CuO-based sample, CuO-1, and CuO samples with La additives, CuO-La-1 and CuO-La-2.

To further quantify the structural differences between La-CuO samples and the reference CuO-1 sample, the EXAFS regions of the Cu K-edge spectra of the fresh samples were modelled. The EXAFS best-fit model for all samples, Table F-1 and Figure F1-F3, included scattering paths matching hexagonal CuO structure, tenorite, in agreement with the XRD results. While the first shell Cu-O scattering path lengths for CuO-La-1 and CuO-La-2 match very well with those of CuO-1, the second shell Cu-O and third and fourth shell Cu-Cu scattering paths appear to be elongated by approximately 0.2 Å for La-doped samples. This can be explained by a distortion of the packing structure caused by the inclusion of lanthanum into the CuO lattice. The increase in 2nd and further coordination shell path lengths indicates a larger unit cell which should allow for easier sulfur diffusion through the lattice, thus making the La samples capable of removing more H_2S.

Finally, the coordination numbers of all samples appear to be lower than that of bulk CuO which consistent with the small crystallite sizes for all samples (<11 nm). Nevertheless, the La-doped samples appear to have lower coordination numbers than CuO-1, despite being of slightly higher crystallite size. This can be partially explained by the presence of Cu-La scattering paths that are unaccounted for in the fitting model.

XANES spectra were also measured at the Cu K-edge for spent samples at 1000 ppm-vol H_2S, 323 K, and 1 atm (Figure 7-5). For both La-CuO samples, linear combination analysis using tenorite (CuO) and covellite (CuS) standards as the basis set shows that approximately 50% of the oxygen had been replaced by sulfur during these in-situ experiments. For the CuO-La-1, this is the upper limit of sulfur uptake determined from fixed bed experiments. Again, these spectra show a blue-shifted and attenuated white line peak relative to that of spent CuO-1 sample, which is indicative of a more electron-rich Cu species. The absence of a strong peak at 8980 eV (characteristic of Cu_2S) in the spent samples, indicates that Cu^{+}-S^{-2} species are not formed in this reaction.[282]

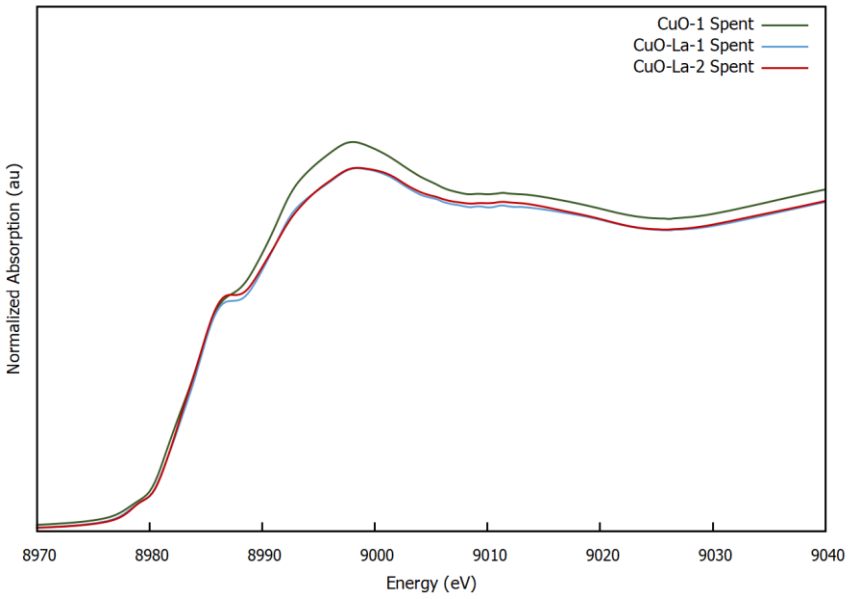

Figure 7-5: Normalized Cu K-edge XANES spectra for spent CuO-1, CuO-La-1 and CuO-La-2 sorbents at 323, 1 atm, and 1000 ppm-vol H_2S/He.

At the S K-edge, XANES spectra were collected for spent CuO-1, CuO-La-1, and CuO-La-2 under He flow, after an in-situ sulfidation at 1000 ppm-vol H_2S/He, 323 K, and 1 atm (Figure 7-6). Previous work on the XANES region of the sulfur K-edge has highlighted its ability to report on the oxidation state of sulfur in the sample, following the general trend that the more oxidized the sulfur species is, the higher in energy its white line peak will appear (peak a in Figure 7-6).[283,284] This indicates that, in comparison to CuO-1, the La-CuO samples possess sulfur species which are more electron rich.

Another important spectral feature that speciates the type of copper sulfide present are the pre-edge peaks at 2469.9 eV (c) and 2470.7 eV (b) in Figure 7-6. These features correspond to S^{2-} 1s → Cu^{2+} $3d^9$ and S_2^{2-} 1s → Cu^{2+} $3d^9$ transitions, respectively.[253] Figure 7-6 shows that the S K-edge spectra of both spent La-CuO samples and CuS reference contain both pre-edge features, while peak (b) is absent in the spent CuO-1 spectra. This difference is more apparent

in the second derivative plots of CuO-1 and CuO-La-2 spectra (inset of Figure 7-6). In a study that speciates the results of sulfidation of CuO at different temperatures (see chapter 5), the absence of peak b was associated with the formation of distorted CuS species at the interface of CuO/CuS which dominates the spectra at low conversions of CuO to CuS. Samples that achieve higher conversion exhibit higher intensity of peak b at 2470.7 eV in their K-edge XANES spectra which is consistent with the spectral features of bulk covellite. These observations are consistent with the extent of conversion of these samples CuO-1 (59%) CuO-La-1 (64%) and CuO-La-2 (85%). Finally, the presence of a peak at 2482-2483 eV in all samples (except CuO-La-2) indicates the presence of SO_4^{2-}, likely in the form of copper sulfate.[283] This is the result of some oxidation of the samples in air prior to running these scans and not a fundamental difference in reaction mechanism. The presence of the same peak in the CuS covellite reference confirms this assumption.

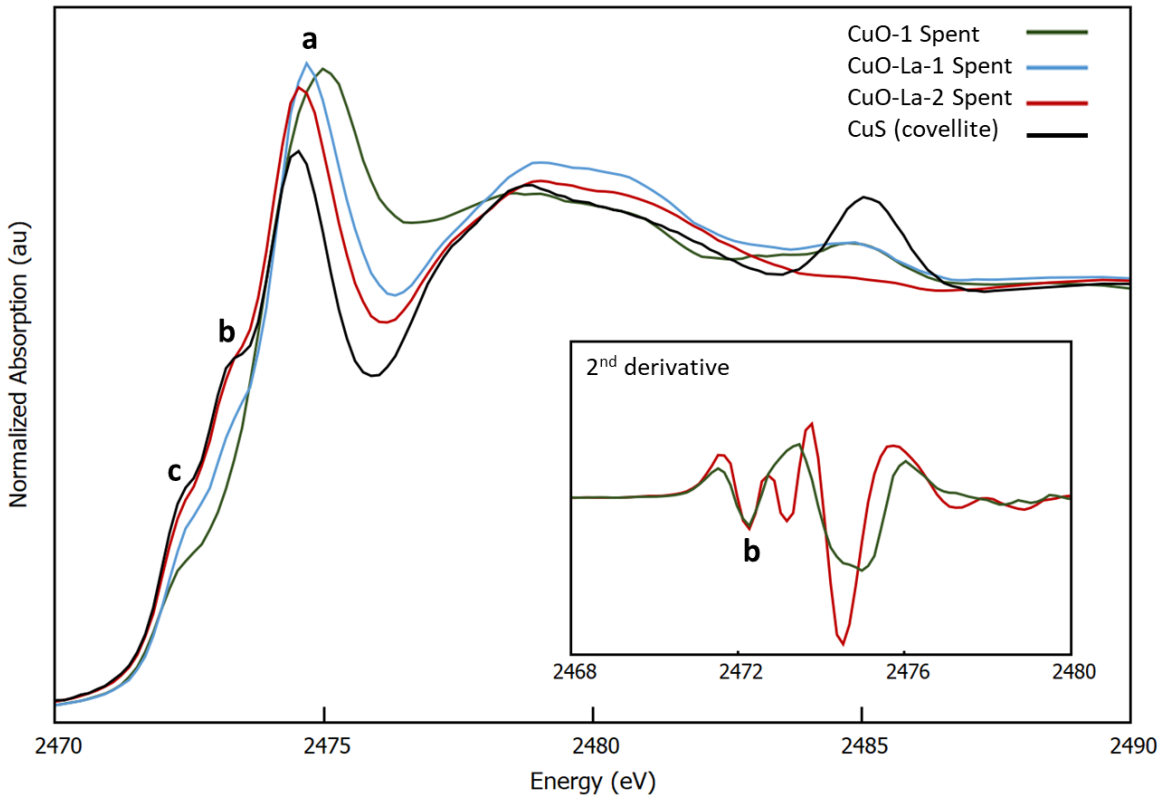

Figure 7-6: Normalized S K-edge XANES spectra for CuO-1, CuO-La-1, CuO-La-2 spent at 323 K, 1 atm, and 1000 ppm-vol H_2S/He and a covellite reference (CuS). The inset shows the second derivative spectra of the CuO-1 and CuO-La-2 spent samples highlighting the presence of peak b (S_2^{2-} 1s → Cu^{2+} $3d^9$) in the spent CuO-La-2 which indicates higher conversion and CuS-like products.

The similarity between CuO-La-1 and CuO-La-2 XANES at the Cu and S K-edges shows that the difference in performance between the two samples is not due to a difference in the form of sulfur products, but rather results from higher dispersion of La in CuO-La-2. On the other hand, the difference between the XANES of both La-CuO samples and CuO-1 indicates that the true source of the improvement of sulfur uptake upon lanthanum addition is electronic in nature.

Finally, XANES spectra taken at the La L_3-edge show that, in comparison to CuO-La-1 and La_2O_3 reference, CuO-La-2 sample shows a broadened white line feature (see Figure 7-7).

This broadening is characteristic of a decrease in La-O coordination.[285] This observation can be interpreted to be a result of the uniform dispersion of La in the CuO phase for CuO-La-2 sample, as La in this environment has a lower La-O coordination number than that of La_2O_3. This is consistent with the EDS results suggesting higher percentage of La in this sample and lower variations of La concentration from spot to spot. Nevertheless, after reaction, both La-CuO samples exhibit overlapping La L_3-edge spectra suggesting similar La environment in the spent samples. With the high conversion of Cu-La-2 sample (85%) the La-O coordination number increases since La doesn't react to form lanthanum sulfide but rather precipitates as La_2O_3 while the bulk of CuO converts to CuS.

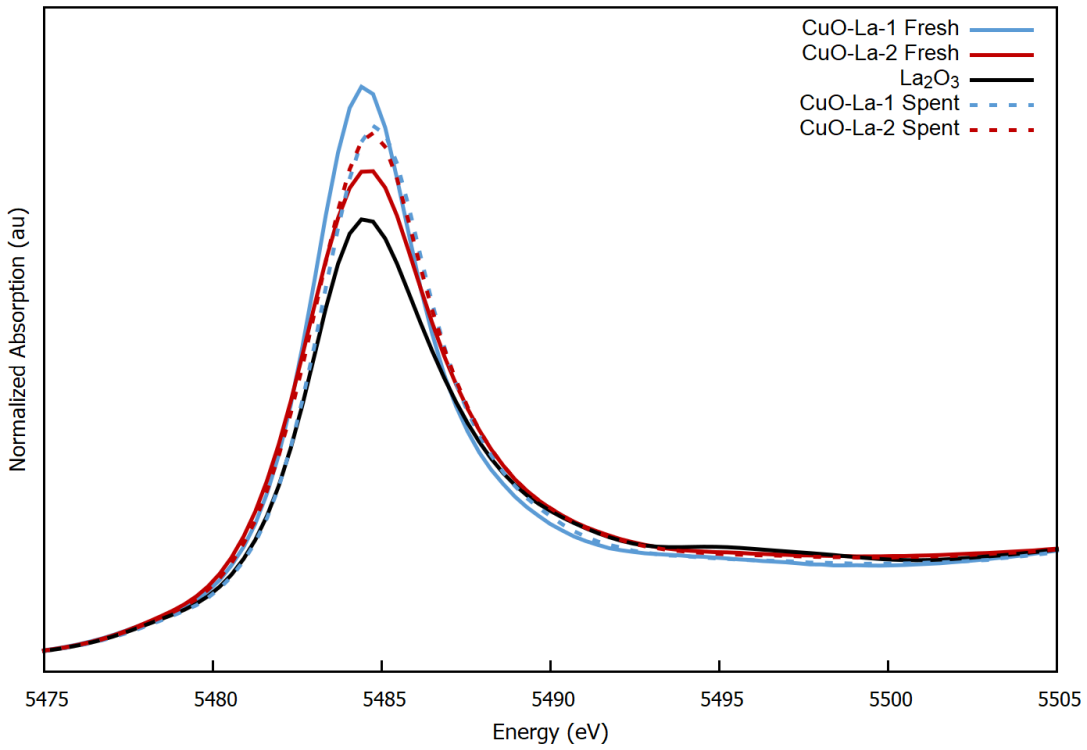

Figure 7-7: Normalized L_3-edge XANES spectra for CuO-La-1, CuO-La-2 both fresh and spent at 323 K, 1 atm, and 1000 ppm-vol H_2S/He and a lanthanum oxide reference (La_2O_3).

7.3.4 Bulk kinetics using in-situ XAS and fixed bed experiments

Fixed bed sorption experiments were run for all samples to determine removal capacity, q_s, at 1000 ppm-vol H_2S/N_2, 323 K, and 1 atm. The breakthrough curves of effluent H_2S concentration were then fit using Cooper linear driving force model (Equation 4)[182,208] to determine the sulfidation kinetics. Figure 7-8 shows the breakthrough curves for CuO-1, CuO-La-1, and CuO-La-2 experiments, normalized for inlet H_2S concentration, along with the model fits (black solid lines). Table 7-3 summarizes the model regressed rate parameter, k, the removal capacity, q_s, and the percentage of conversion for the CuO phase. The experiments were run under flow conditions that eliminate bulk and pore diffusion resistance contributions and, thus, k reflects the rate of uptake at the reaction surface.[208]

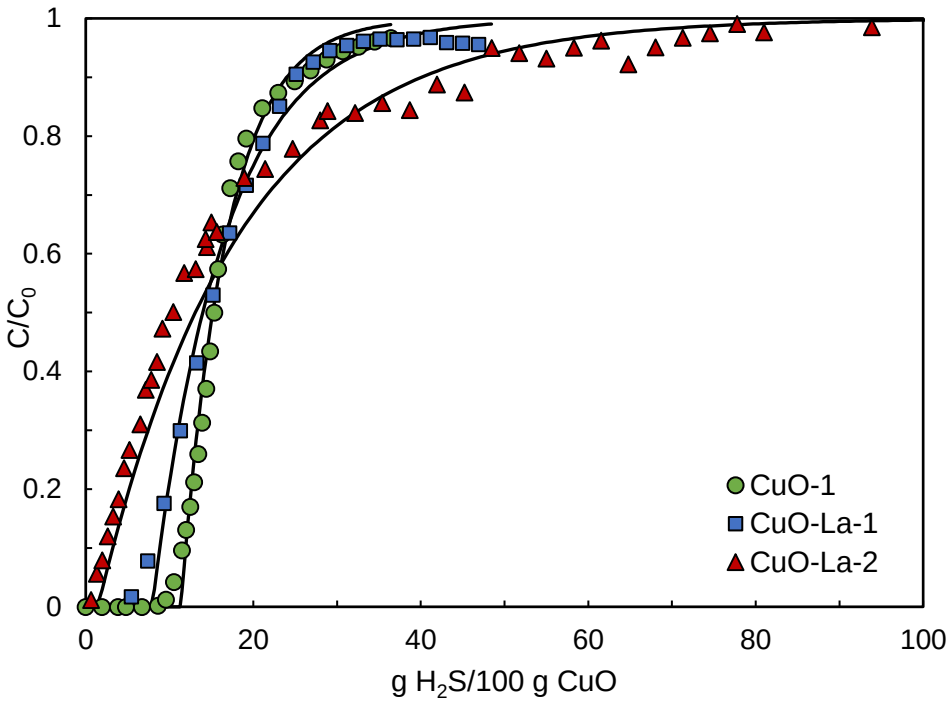

Figure 7-8: Breakthrough curves of normalized effluent H_2S concentration collected for fixed beds of the CuO-based sorbents at 1000 ppm-vol H_2S/N, 323 K and 1.0 atm. Solid black lines represent linear driving force model fit (Cooper model). Time is normalized by multiplying the time on stream with the mass flowrate of H_2S and dividing by mass of sorbent.

Table 7-3: Summary of rate parameters deduced from Cooper model fit, removal capacity, and conversion of CuO for fixed bed sorption tests at 1000 ppm-vol H_2S/N, 323 K and 1.0 atm.

Sample	k (s^{-1})	q_s (wt.%)	Conversion (%)
CuO-1	18 ±1.6	24.9	59.2
CuO-La-1	22 ±1.3	26.9	64.0
CuO-La-2	7.4 ±0.80	35.8	85.2

As reported in earlier section, fixed bed results show that La-doped samples achieved a conversion of 64 % and 85% for CuO-La-1 and CuO-La-2. Opposite to the trend in conversion, the rate parameter (k) values for CuO-1 (18 s^{-1}) and CuO-La-1 (22 s^{-1}) were more than double that of CuO-La-2 (7.4 s^{-1}). This indicates that lower rate parameters allow for more time for diffusion of H_2S to CuO surfaces resulting in higher conversion. On the other hand, fast accumulation of CuS layers results in a sooner inhibition for diffusion through products, and thus, lower conversion.[260]

In-situ XAS at S K-edge were also run to determine bulk sulfidation kinetics of CuO-1 and La-CuO sorbents. The S K-edge spectra show changes from H_2S like features, in the first few scans, to CuS like features as the reaction progresses (Figure 7-9). The edge steps for the scans were used to deduce the amount of sulfur in the sample at each point in time, where the maximum conversion from fixed bed experiments was assumed to correspond to the edge step for the spent sample from in-situ XAS experiments. The contribution of gaseous H_2S spectra, determined from the difference between spent sample spectra under H_2S and under He flow, was subtracted from all spectra prior to analysis.

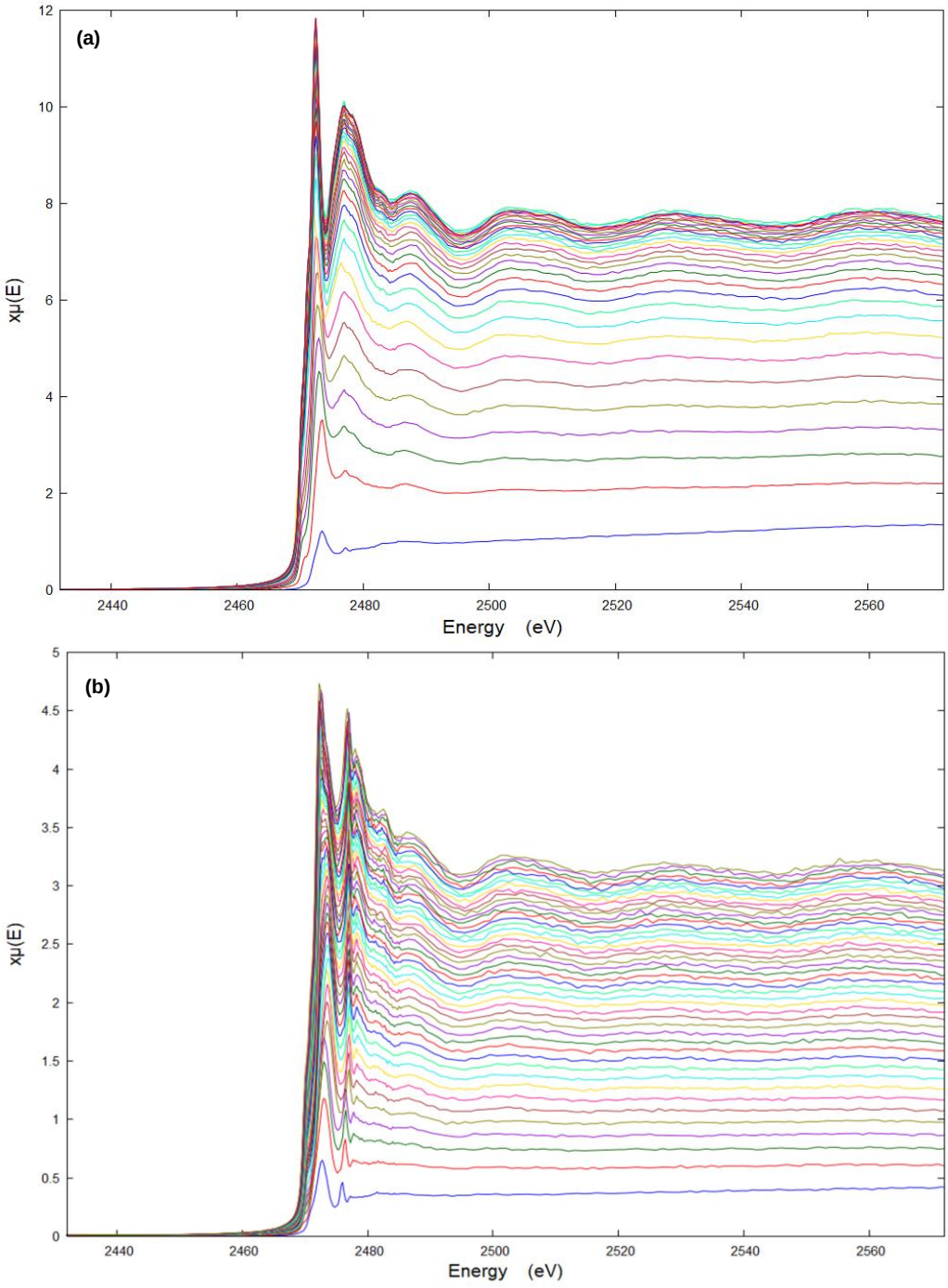

Figure 7-9: Bulk S K-edge XAS spectra of a) CuO-La-1 and b) CuO-La-2 as it was exposed to flowing 1000 ppm H_2S in helium at 323 K and 1 atm. XAS scans were taken every 9 minutes and the edge step increased consistently with time.

The conversion profiles for the three samples, as determined from sulfur content, are shown in Figure 7-10, while Table 7-4 summarizes the rate constants and effective diffusivities derived from random pore model (RPM) fits of the data (Equations 15-19).[174,176] The rate constant for CuO-1 (6.3 x 10^{-3} cm^4 mol^{-1} s^{-1}) was double that of CuO-La-1 (2.6 x 10^{-3} cm^4 mol^{-1} s^{-1}) and an order of magnitude larger than CuO-La-2 rate constant (7.1 x 10^{-4} cm^4 mol^{-1} s^{-1}). This trend can be observed in the the initial region of the conversion profiles, Figure 7-10, with the most rapid change in conversion for CuO-1, followed by CuO-La-1 and, then, CuO-La-2. This initial rapid change in conversion results in a shorter reaction-controlled regime, 20 minutes for CuO-1, compared to 55 minutes for CuO-La-1 and 125 minutes for CuO-La-2, followed by a slower diffusion controlled regime. These results are consistent with the fixed bed sorption results, and they confirm that higher rates result in early accumulation of CuS products in pores and surfaces which leads to restriction of further H_2S diffusion to reactive surface as demonstrated in earlier studies.[260] On the other hand, an opposite trend was observed for the effective diffusivity in the diffusion-controlled regime with the highest diffusivity value for CuO-La-2 (1.7 x 10^{-11} cm^2 s^{-1}). This suggests that, despite higher conversion which leads to higher product content, CuO-La-2 demonstrated the most facile access to reactive surfaces in its diffusion-controlled regime.

Table 7-4: Random pore model parameters from fits of the conversion profiles of S K-edge *in situ* sulfidation runs at 1000 ppm-vol H_2S/N_2, 323 K and 1.0 atm.

Sample	**k x 10^3 (cm^4 mol^{-1} s^{-1})**	**D x 10^{12} (cm^2 s^{-1})**
CuO-1	6.0 ±1.6	2.3 ±1.1
CuO-La-1	2.6 ±0.19	5.4 ±1.7
CuO-La-2	0.71 ±0.08	17 ±2.8

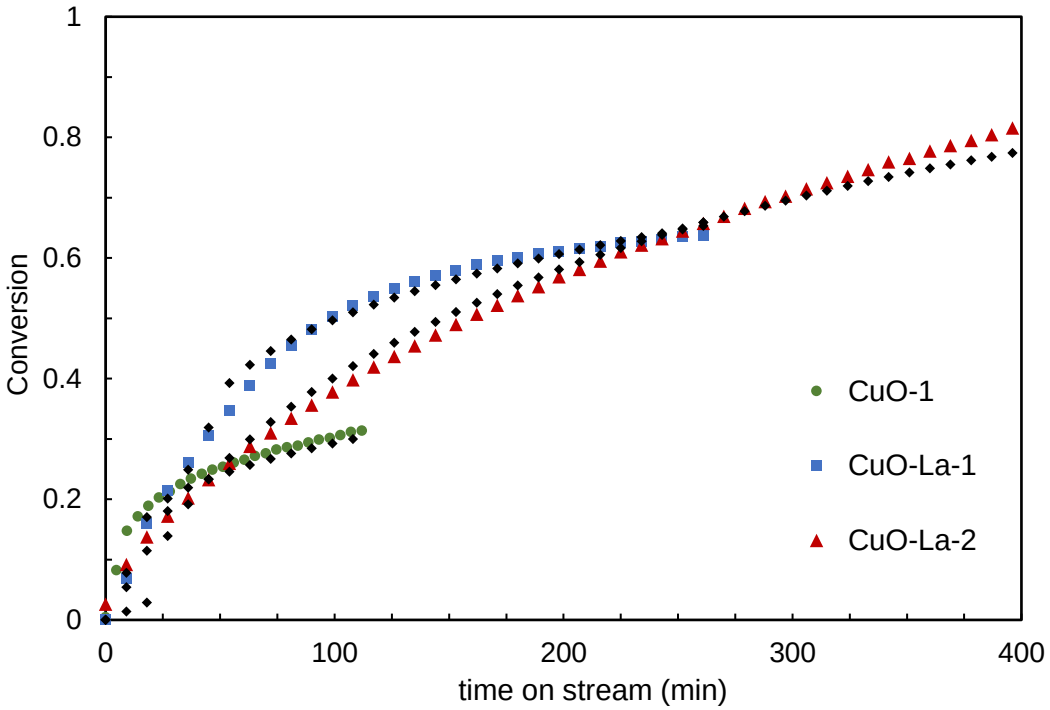

Figure 7-10: Conversion profiles of CuO in CuO-1 (green), CuO-La-1 (blue), and CuO-La-2 (red) to CuS as determined by in-situ S K-edge XAS experiments at 1000 ppm-vol H_2S/N, 323 K and 1.0 atm. Black dots represent RPM fits for the data.

7.4 Conclusion

In conclusion, a combination of conventional and synchrotron-based characterization methods allowed us to study the chemical and structural changes induced by the introduction of lanthanum to CuO sorbents, and the correlation between these changes and the enhanced performance of the sorbents. Lanthanum-doped sorbents, of similar bulk lanthanum content, prepared via different synthesis methods: sol-gel and co-precipitation with ammonium, yielded materials of different physiochemical properties and sulfur removal performance. Both samples achieved improved sulfur removal capacities despite having larger crystallite sizes and smaller surface area. This improved removal capacity was associated with slower rate parameters (both in fixed bed reactor, and gradient-less XAS wafer) compared to CuO-based reference sorbent. The slower rates allowed for expanding the reaction-controlled regime which resulted in

improved conversion. Cu K-edge EXAFS fits for the samples revealed that the introduction of lanthanum weakened the second shell Cu-O, evident by the elongation of this scattering path along with third and fourth shell Cu-Cu single scatterings. Cu K-edge XANES also revealed a more electron-rich environment for Cu in La-doped samples which makes the Cu-O bond more suspectable to breaking and, thus, more reactive towards sulfur. The La L_3-edge results revealed lower coordination of La-O in the co-precipitation sample, CuO-La-2, compared to the sol-gel sample, CuO-La-1, and bulk La_2O_3 reference, which is consistent with the higher content of La in CuO phase that was determined by STEM-EDS. In addition to higher La inclusion, uniform dispersion of La within CuO phase and smaller crystals allowed for higher Cu-La interaction and, thus, better performance improvement. These results show that lanthanum doping improves the sulfidation performance by both altering the average chemical environment of Cu making it more reactive towards S, and by disrupting the CuO lattice resulting in more vacancies and defects which enhance the diffusion of H_2S to reactive surfaces.

Chapter 8 | Conclusions

This dissertation work was motivated by the importance of developing a fundamental understanding of CuO-H_2S reactive sorption systems, in order to rationally design improved sorbents and optimize desulfurization process conditions.

The third chapter of this dissertation demonstrated the utility of simple linear driving force models in describing the reactive sorption process if the conditions are controlled so that bulk and pore diffusion resistances are negligible. Namely, the work from this section allowed for probing the effects of process conditions on these model-deduced rate values and establishing their relationship to rate constants from elementary mechanistic steps. The credibility of this relationship is further confirmed by comparing it to advanced synchrotron *in situ* tests which showed similar trends in both the pore model-deduced values from experiments on few micrometers-sized particles and linear driving force-deduced values from experiments for fixed beds of multiple grams of material. These findings are demonstrated thoroughly in Chapter 5 of this dissertation. Also, the effects of temperature on the rate parameters and capacity was tested against synchrotron *in situ* tests in Chapter 6 of this work. This work can be further expanded by testing a wider range of experimental conditions than what this dissertation covered. The practical impact of this work is that the results of these tests can guide the optimization of industrial desulfurization processes' conditions so that they achieve the highest possible conversion and rate values. Furthermore, the effect of trace amounts of common co-contaminants mixtures of sulfur compounds, H_2O, and O_2 (that are often present in natural gas streams) would be invaluable to solidify the practicality of these results.

Also, to further improve on this work, thermogravimetric techniques can be used to study the reactions of sulfur compounds with CuO. These thermogravimetric experiments are better suited to measure intrinsic reaction rates between gas phase contaminant molecules and solid phase sorbents because they are conducted under constant concentration conditions. In these thermogravimetric studies, time derivative of the fractional conversion can be expressed as the product of a time-independent reactivity function, which depends only on temperature and contaminant concentration, and a time-dependent geometric function. The geometric function depends on both the shape and size of the region where the rate-determining step (e.g., interfacial reaction, diffusion/growth at the product/reactant interface, or growth via diffusion) occurs and on the temperature and concentration of the contaminants. A series of experiments in which the temperature or concentration is suddenly changed at different extents of conversion can be used to establish the general form of the two functions, and microkinetic models can be proposed to derive specific equations for the two functions. These studies can provide a more detailed description of the process that separates the rate of reaction from diffusion through solid phases which fixed bed tests fail to achieve.

Aside from the effects of experimental conditions, the work in this dissertation shed light on the physicochemical properties that affect the H_2S performance of these materials. This aim is achieved in chapter 4 of this work. Several CuO-based nanomaterials were prepared and tested for their performance as low-temperature desulfurizing sorbents by performing fixed-bed sulfidation experiments at ambient temperature and pressure. These materials were prepared via various synthesis techniques, including sol-gel, precipitation, hydrothermal treatment in the presence of a polymer (PVP or PEO) or surfactant (P123), hydrolysis, and electrospinning. Despite differences between the various properties of the tested CuO sorbents as well as their

morphologies, a strong linear relationship was recognized between the sorbents' sulfur removal capacity and crystallite size, particularly when the crystallite size of CuO was below 26 nm. This data supports the hypothesis that decreasing CuO crystallite size leads to higher conversions possibly because of an increase in oxygen vacancies. A possible molecular reason for this is that decreasing crystallite size exposes more reactive surface facets in CuO that can facilitate H-S bond cleavage that is required to produce S atoms that can react with CuO moieties. Open facets can also facilitate the migration of S from surface to subsurface layers. An atomic scale explanation of the strong influence of crystallite size was also confirmed through model DFT computations, explaining how elementary reaction and molecular diffusion steps occur more rapidly and to a greater extent on smaller CuO crystallites. These computations provided further explanation to this effect which is that higher concentrations of 3-fold coordinated oxygen atoms are present in smaller crystals compared to 4-fold coordinated oxygen atoms in larger ones. These oxygen atoms are considerably more reactive towards sulfur moieties. The effect of residual carbon was also investigated, and it was found that carbon residues resulting from the use of a polymer (PVP or PEO) or a surfactant (P123) in the synthesis procedure remained on the surface of the sorbent after thermal treatment and detrimentally affected its H_2S uptake capacity. The practical impact of this work is that the industrial efforts should be focused on developing materials that have small crystallite sizes using synthesis methods that are carbon-free.

Subsequently, the mechanism of reaction propagation through CuO particles was explored in chapter 5 through XAS and TXM studies at Cu K-edge. Part of the study explored the effect of crystallite size on the reaction rates and capacities deduced from in situ XAS studies which showed consistent trends with the results obtained in chapter 4, as stated

previously. Specifically, the CuO-based sorbent with smaller (nearly amorphous) crystals achieved a considerably higher capacity than that of CuO materials with larger crystals. Interestingly, the study showed also that the rates of reaction followed an opposite trend than that of removal capacity which can be explained by the fact that higher initial reaction rates in lower performing materials caused fast coverage of reactive surfaces which inhibited further penetration of H_2S through product phase to react with fresh material. This explanation is also consistent with the fact that higher diffusivities were observed for higher performing materials which allowed for deeper penetration of reactive species. The high performing material was then subjected to in-situ operando TXM study that allowed for quantitative spatial-temporal monitoring of the structural and chemical changes within few micron-sized particles. The results of this study showed that the average kinetics within single particles mirror the reaction kinetics measured from fixed bed of sorbents. However, the operando TXM study detected that the growth of reaction fronts proceeds heterogeneously within the solid phase particles which suggests that pore diffusion persists even for particles less than 10 μm in size.

Moving on from the structural and chemical changes that are based on the Cu environment, chapter 6, provides a more detailed study of the sulfur environment which is necessary to speciate the formed $Cu_{2-x}S_x$ species. This was achieved by performing *in situ* XAS studies at both S K-edge and Cu K-edge. The complimentary results from both edges captured the changes in the formed CuS phase in real time and at different temperatures and extents of conversion. Unprecedently, the results from this study identified a unique structure at the interfacial CuO-CuS area which, consequently, unraveled mechanistic details of the sulfidation process. S K-edge XANES showed evidence of S_2^{2-}, characteristic of CuS, for all spent samples, with a geometrically strained and more electropositive S_2^{2-} form at lower conversions (Spent

samples at 298 K and 323 K and early *in situ* sulfidation spectra of 353 K and 383 K). These differences are explained by the fact that the initially formed disulfide groups are bonded to Cu^{2+} which are bonded to O^{2-} in bulk CuO, as compared to S_2^{2-} in bulk CuS which are connected to Cu^{+}/Cu^{2+} that are bound to S^{2-} and S_2^{2}. Furthermore, DFT simulations of CuO sulfidation paths (non-sulfided and partially sulfided (111) and ($\bar{1}$11) surfaces), suggest that the formation of disulfide ion is, indeed, thermodynamically favorable in the initial sulfidation stages. Finally, the Cu K-edge EXAFS fits of the sulfided samples show longer Cu-S scattering paths at lower conversions which, again, supports the strained interfacial geometry theory. The results of this study challenge the common belief that CuO-H_2S reactions result in one form of CuS. Indeed, this study shows, for the first time, the geometrical and electronic changes in the formed sulfide species as the reaction progresses.

Finally, the last chapter of this dissertation, branched out from pure CuO sorbents to explore the effects of introducing foreign atoms to CuO on the sulfur removal capacity. This section continued to employ a combination of conventional and synchrotron-based characterization methods which allowed for a study the of the chemical and structural changes induced by the introduction of lanthanum to CuO sorbents, and the correlation between these changes and the enhanced performance of the sorbents. Lanthanum-doped sorbents, of similar bulk lanthanum content, prepared via different synthesis methods: sol-gel and co-precipitation with ammonium, yielded materials of different physiochemical properties and sulfur removal performance. Both samples achieved improved sulfur removal capacities (85% and 61% conversion of La-doped CuO samples compared to 56% in the best performing CuO samples). This improved removal capacity was associated with slower rate parameters (both in fixed bed reactor, and gradient-less XAS wafer) compared to CuO-based reference sorbent. The slower

rates allowed for expanding the reaction-controlled regime which resulted in improved conversion which aligns with the results in chapter 5. Cu K-edge EXAFS fits for the samples revealed that the introduction of lanthanum weakened the second shell Cu-O, evident by the elongation of this scattering path along with an elongation of the third and fourth shell Cu-Cu single scattering paths. Cu K-edge XANES also revealed a more electron-rich environment for Cu in La-doped samples which makes the Cu-O bond more suspectable to breaking and, thus, more reactive towards sulfur. The La L_3-edge XANES results revealed lower coordination of La-O in the samples compared to bulk La_2O_3. This result suggests that La was indeed included within the CuO rather than present in a separate La_2O_3 phase. The results of this study show that lanthanum doping improves the sulfidation performance by both altering the average chemical environment of Cu making it more reactive towards S, and by disrupting the CuO lattice resulting in more vacancies and defects which enhances the diffusion of H_2S to reactive surfaces. This study can be expanded by performing DFT simulations for La-doped CuO samples to confirm the suggested reasoning of the cause of improved sulfur removal capacity. Moreover, other metal dopants of varying cationic sizes can be explored in future studies to confirm the hypothesis that metals of higher cationic size ratio cause more disruption of the CuO lattice.

For future work, the regeneration of spent CuO-based sorbents would be important for the commercialization of these sorbents. CuO in these reactive sorption processes is used for the removal of trace amounts of hydrogen sulfide and, thus, the reloading of beds is infrequent. Nevertheless, the regeneration of the spent beds after extended periods of use ensures the sustainable use of resources and minimizes the amount of waste that has to be landfilled. The oxidative regeneration methods (reaction with SO_2, O_2 and H_2O) that are commonly employed

for the regeneration of other metal oxides are extremely exothermic which risks sintering the sorbents and ruining their ability to absorb sulfur in the following cycles. Thus, careful control of temperature is important if this route is explored. Moreover, a common undesired side reaction for these oxidative processes is the formation of copper sulfate which is inert towards further desulfurization. Thus, studies focused on determining the ideal conditions that minimize both sorbents sintering and sulfate by-product formation are very important.

Appendix A | Supplementary Information for Chapter 2

Table A-1: Select results of sulfidation of pure and doped-copper and zinc oxide at various experimental conditions

Metal Oxide	Composition	Feed	Temperature (ºC)	Reactor Type	Synthesis Technique	Sulfur Removal Capacity (g of S/g of sorbent)
CuO-based	**(Me/Cu)**					
CuO[36]	0.00	1% H_2S in Helium	300	Fixed-bed	Complexation agent	0.23
CuO[10]	0.00	10 ppm H_2S in N_2	25	Tedlar Bag®	Co-precipitation	0.283
CuO[37]	0.00	1000 ppmv in N_2	21	Fixed bed	sol-gel	0.075
CuO[37]	0.00	1000 ppmv in N_2	21	Fixed bed	co-precipitation and hydrolysis	0.011
CuO[37]	0.00	1000 ppmv in N_2	21	Fixed bed	co-precipitation	0.003
Cu-Mo-O[36]	1.00	1% H_2S and 10% H_2 in He	300	Fixed-bed	Complexation agent	0.079
Cu-V-O[36]	1.00	1% H_2S and 10% H_2 in He	300	Fixed-bed	Complexation agent	0.059 moles of SO_2 formed /moles of H2S removed
Cu-Al-O ($CuAl_2O_4$)[48]	96.00	20% hydrogen, 25% H_2O, 1% H_2S, and 54% N_2	700	Packed bed/TGA	Complexation agent	$Wn=(m-m_0)/(m_0-m_f)$, normalized weight; 1.26
Cu-Al-O ($CuO-Al_2O_3$)[48]	2.02	15-20% hydrogen, 7-25% H_2O, 0.2-1% H_2S, and N_2	700	Packed bed/TGA	Complexation agent	$Wn=(m-m_0)/(m_0-m_f)$, normalized weight; 1.27
Cu-Fe-O ($CuFe_2O_4$)[129]	1.00	0.26% H_2S, 20% H_2, 6.85% H_2O, and 73% N_2	538	Fixed-bed	Complexation agent	Reported as normalized breakthrough time only
Cu-Fe-Al-O ($CuFe_2O_4$, $FeAl_2O_4$, CuO)[129]	2.00	0.26% H_2S, 20% H_2, 6.85% H_2O, and 73% N_2	650	Fixed-bed	Complexation agent	Reported as normalized breakthrough time only
Cu-Cr-O[286]	1.22	2 vol% H_2S, 10 vol% H_2, 20 wt% CO, 10 wt% CO_2, 10 wt% H_2O, and 48 wt% N_2	650	packed bed	Mixing, pelletizing	Reported as normalized breakthrough time only
ZnO-based	**(Me/Zn)**					
ZnO[38]	0.00	100 ppm H_2S balanced in He	250	Fixed-bed	Glycerine method	0.012
ZnO[38]	0.00	100 ppm H_2S balanced in He	250	Fixed-bed	Combustion method	0.017
ZnO[38]	0.00	100 ppm H_2S balanced in He	250	Fixed-bed	Aldrich (commercial)	0.0125
ZnO[84]	0.00	0.2 vol% H_2S in H_2/N_2 (1:1)	200	TGA	co-precipitation	0.0393
ZnO[10]	0.00	10 ppm H_2S in N_2	25	Tedlar Bag®	co-precipitation	0.032
Zn-Ca-O[100]	0.72	8 ppmv H_2S, 34.4% H_2, 20% H_2O, and balance being N_2	300	Fixed bed	Engelhard (commercial)	1.69

Metal Oxide	Composition	Feed	Temperature (ºC)	Reactor Type	Synthesis Technique	Sulfur Removal Capacity (g of S/g of sorbent)
Zn-Ca-O[100]	0.72	8 ppmv H_2S, 34.4% H_2, 20% H_2O, and balance being N_2	350	Fixed bed	Engelhard (commercial)	0.85
Zn-Ca-O[100]	0.72	8 ppmv H_2S, 34.4% H_2, 20% H_2O, and balance being N_2	375	Fixed bed	Engelhard (commercial)	0.6
Zn-Ca-O[100]	0.72	8 ppmv H_2S, 34.4% H_2, 20% H_2O, and balance being N_2	400	Fixed bed	Engelhard (commercial)	0.28
Zn-Fe-O ($ZnFe_2O_4$)[129]	2.00	1% H_2S, 15% H_2, 25% H_2O, and 59% N_2	600	Fixed bed	Complexation agent	Reported as normalized breakthrough time only
Zn-Bi-O[287]	0.33	2000 ppm in N_2	25	Stainless steel cell	Solvothermal	0.079
Zn-Fe-O[10]	0.33	10 ppm H_2S in N_2	25	Tedlar Bag®	co-precipitation	0.066
Zn-Ni-O[10]	0.33	10 ppm H_2S in N_2	25	Tedlar Bag®	co-precipitation	0.069
Zn-Co-O[10]	0.33	10 ppm H_2S in N_2	25	Tedlar Bag®	co-precipitation	0.134
Zn-Mn-O[10]	0.33	10 ppm H_2S in N_2	25	Tedlar Bag®	co-precipitation	0.152
Zn-Fe-Zr-O[10]	0.39	10 ppm H_2S in N_2	25	Tedlar Bag®	co-precipitation	0.075
Zn-Ti-Zr-O[10]	0.47	10 ppm H_2S in N_2	25	Tedlar Bag®	co-precipitation	0.145
Zn-Cu-Zr-O[10]	0.41	10 ppm H_2S in N_2	25	Tedlar Bag®	co-precipitation	0.135
Zn-Co-Al-O[10]	1.00	10 ppm H_2S in N_2	25	Tedlar Bag®	co-precipitation	0.107
Zn-Al-O[10]	0.33	10 ppm H_2S in N_2	25	Tedlar Bag®	co-precipitation	0.146
Zn-Ti-O[288]	0.50	1.5% H_2S, 11.7% H_2, 9.6% CO, 5.2% CO_2, N_2 balanced	650	Fixed bed	Physical mixing	0.18
Zn-Ti-Co-O[288]	1.53	1.5% H_2S, 11.7% H_2, 9.6% CO, 5.2% CO_2, N_2 balanced	650	Fixed bed	Physical mixing	0.22
Zn-Ti-O[288]	0.50	1.5% H_2S, 11.7% H_2, 9.6% CO, 5.2% CO_2, N_2 balanced	480	Fixed bed	Physical mixing	0.05
Zn-Ti-Co-O[288]	1.53	1.5% H_2S, 11.7% H_2, 9.6% CO, 5.2% CO_2, N_2 balanced	480	Fixed bed	Physical mixing	0.05
Zn-Cu-O[84]	0.03	0.2 vol% H_2S in H_2/N_2 (1:1)	200	TGA	co-precipitation	0.47 mol of S/mol of ZnO
Zn-Cu-O[84]	0.03	0.2 vol% H_2S in H_2/N_2 (1:1)	200	TGA	co-precipitation	0.61 mol of S/mol of ZnO
Zn-Al-Fe-O[289]	1.86	1.5 vol% H_2S, 11.7 vol% H_2, 9.6 vol% CO, 5.2 vol % CO_2, and N_2 balance	480	Fixed bed	Co-precipitation and physical mixing	0.18
Zn-Al-Co-O[289]	1.86	1.5 vol% H_2S, 11.7 vol% H_2, 9.6 vol% CO, 5.2 vol % CO_2, and N_2 balance	480	Fixed bed	Co-precipitation and physical mixing	0.175

Metal Oxide	Composition	Feed	Temperature (ºC)	Reactor Type	Synthesis Technique	Sulfur Removal Capacity (g of S/g of sorbent)
Zn-Al-Ni-O[289]	1.86	1.5 vol% H_2S, 11.7 vol% H_2, 9.6 vol% CO, 5.2 vol % CO_2, and N_2 balance	480	Fixed bed	Co-precipitation and physical mixing	0.2
Zn-Al-Ce-O[289]	1.80	1.5 vol% H_2S, 11.7 vol% H_2, 9.6 vol% CO, 5.2 vol % CO_2, and N_2 balance	480	Fixed bed	Co-precipitation and physical mixing	0.16

Table A-2: Possible reaction stoichiometries for sulfur compounds with different metal oxides

Metal Oxide	Composition	Feed	Temperature (ºC)	Reactor Type	Synthesis Technique	Sulfur Removal Capacity (g of S/g of sorbent)
Al_2O_3-based	(Me/Al)					
Al-Zn-O (ɣ-Al_2O_3)[49]	0.09	1% H_2S in N_2	600	Fluidized bed	Dry impregnation	Reported as normalized breakthrough time only
Al-Zn-O (α-Al_2O_3)[49]	0.09	1% H_2S in N_2	600	Fluidized bed	Dry impregnation	Reported as normalized breakthrough time only
Al-Ca-O (α-Al_2O_3)[49]	0.12	1% H_2S in N_2	600	Fluidized bed	Dry impregnation	Reported as normalized breakthrough time only
MgO-based	(Me/Mg)					
Mg-Zn-O[49]	0.03	1% H_2S in N_2	600	Fluidized bed	Dry impregnation	Reported as normalized breakthrough time only
Mg-Cu-O[49]	0.03	1% H_2S in N_2	600	Fluidized bed	Dry impregnation	Reported as normalized breakthrough time only
Mg-Ca-O[49]	0.05	1% H_2S in N_2	600	Fluidized bed	Dry impregnation	Reported as normalized breakthrough time only
Mg-Mn-O[49]	0.03	1% H_2S in N_2	600	Fluidized bed	Dry impregnation	Reported as normalized breakthrough time only
Mg-Zn-Cu-O[49]	0.05	1% H_2S in N_2	600	Fluidized bed	Dry impregnation	Reported as normalized breakthrough time only
La_2O_3-based	(Me/La)					

Metal Oxide	Composition	Feed	Temperature (ºC)	Reactor Type	Synthesis Technique	Sulfur Removal Capacity (g of S/g of sorbent)
La_2O_3[51]	0.00	250 ppm H_2S, 70% H_2, 5% H_2O, and He	800	Packed bed	Urea coprecipitation/ gelation method	0.06
La-Pr-O[51]	0.43	250 ppm H_2S, 70% H_2, 5% H_2O, and He	800	Packed bed	Urea coprecipitation/ gelation method	0.056
La-Ce-O[42]	0.43	0.1% H_2S, 50% H_2, 10% H_2O, He balance	650	packed bed	Urea co-precipitation/ gelation	0.032
SnO-based	(Me/Sn)					
SnO[10]	0.00	10 ppm H_2S in N_2	25	Tedlar Bag®	Co-precipitation	0.002
NiO-based	(Me/Ni)					
NiO[10]	0.00	10 ppm H_2S in N_2	25	Tedlar Bag®	Co-precipitation	0.002
Co_3O_4-based	(Me/Co)					
Co_3O_4[10]	0.00	10 ppm H_2S in N_2	25	Tedlar Bag®	Co-precipitation	0.006
Co-Si-O (3DOM structure)[290]	1.01	500 mg/m^3 H_2S, at 100 mL/min	30	Fixed bed	Colloidal crystal template method	0.075
Co-Si-O[290]	1.01	500 mg/m^3 H_2S, at 100 mL/min	30	Fixed bed	Colloidal crystal template method	0.012
Co-Si-O[290]	1.01	500 mg/m^3 H_2S, at 100 mL/min	30	Fixed bed	Colloidal crystal template method	0.028
Co-Si-O (3DOM structure)[290]	1.01	500 mg/m^3 H_2S, at 100 mL/min	30	Fixed bed	Colloidal crystal template method	0.189
CaO-based	(Me/Ca)					
CaO	0.00	10 ppm H_2S in N_2	25	Tedlar Bag®	co-precipitation	0.011
Mn_3O_4-based	(Me/Mn)					
Mn_3O_4[10]	0.00	10 ppm H_2S in N_2	25	Tedlar Bag®	co-precipitation	0.016
Ag_2O-based	(Me/Ag)					
AgO[10]	0.00	10 ppm H_2S in N_2	25	Tedlar Bag®	co-precipitation	0.031
CeO_2-based	(Me/Ce)					
CeO_2[42]	0.00	0.1% H_2S, 50% H_2, 10% H_2O, He balance	650	Packed bed	Urea co-precipitation / gelation	0.006
Ce-Cu-O[42]	0.11	0.1% H_2S, 50% H_2, 10% H_2O, He balance	650	Packed bed	Urea co-precipitation / gelation	0.0041
Ce-La-O[42]	0.43	0.1% H_2S, 50% H_2, 10% H_2O, He balance	650	Packed bed	Urea co-precipitation / gelation	0.0072

Metal Oxide	Composition	Feed	Temperature (ºC)	Reactor Type	Synthesis Technique	Sulfur Removal Capacity (g of S/g of sorbent)
Fe_2O_3-based	(Me/Fe)					
Fe-Al-O[291]	3.10	1% H_2S (10,000 ppmv), 10% H_2, and N_2	850	Fixed bed	Co-precipitation	0.2073
Fe-Al-Mn-O[291]	3.56	1% H_2S (10,000 ppmv), 10% H_2, and N_2	850	Fixed bed	Co-precipitation	0.1
Fe-Al-Mn-O[291]	4.13	1% H_2S (10,000 ppmv), 10% H_2, and N_2	850	Fixed bed	Co-precipitation	0.17
Fe-Al-Mn-O[291]	4.87	1% H_2S (10,000 ppmv), 10% H_2, and N_2	850	Fixed bed	Co-precipitation	0.2014
Fe-Al-Mn-O[291]	7.23	1% H_2S (10,000 ppmv), 10% H_2, and N_2	850	Fixed bed	Co-precipitation	0.2072

Table A-3: List of theoretical studies that investigate the adsorption of H_2S or other molecules on various metal oxides. The list is grouped by type of metal oxide studied, ordered as they appear in section 2.4, and specified with details on computational methods used. Subscripts in alphabetical order point out studies that do not involve H_2S and indicate what molecules were studied instead. **a**: S_2 adsorption on zincite $(10\bar{1}0)$ surface **b**: O_2, NO_2, H_2O, C_2H_5OH, and CH_3CHO adsorption on various CuO surfaces and nanowires **c**: H_2 adsorption on CuO(111) surface **d**: CO_2 adsorption on CuO (111), (111), and (011) **e**: H_2O adsorption on the CuO (111) surface **f**: H_2O adsorption on the CuO (111) surface **g**: SO_2 adsorption on CeO_2(111) and (110) **h**: SO_2 and SO_3 adsorption on MgO(001) **i**: S adsorption on MgO(001) **j**: Hg^0, HgCl, $HgCl_2$, HgO, and SO_2 adsoprtion on CaO(100) **k**: CO_2 and SO_2 sorption on the Li, Na, K, Rb, or Cs doped CaO(100)surface **l**: C_4H_4S adsorption on $Ti_xCe_{(1-x)}O_2$ mixed surface.

References	Authors	Metal Oxide	Method
		ZnO & Related Materials	
dhage2012	Dhage et al.	$Cu_xZnO_{(1-x)}$	DFT – B3LYP, LANL1MB with effective core potentials and 6-31G(d) basis set with Stuttgart effective core potential (SDD)
casarin1996 casarin1995	Casarin et al.	ZnO $(10\bar{1}0)$ and (0001)	LCAO-LDF molecular-cluster approach
rodriguez2000	Maiti & Rodriguez	ZnO (0001)	DFT – GGA, nonlocal ultrasoft pseudopotentials, Becke-88 for exchange37 and Perdew-91 for correlation
wang2013	Wang et al.	ZnO $(10\bar{1}0)$	DFT – GGA, PW91 functional, double-numeric quality basis set with polarization functions (DNP)
kazemi2017	Rad & Kazemi	ZnO nanocage	DFT – B3LYP, 6-311G (d,p) basis set DFT – ωb97XD, 6-311G (d,p) basis set
tong2018	Zheng et al.[a]	ZnO $(10\bar{1}0)$	DFT – GGA, norm-conserving and ultrasoft Vanderbilt pseudopotentials
hao2011	Sholl et al.	Zn_2TiO_4(010)	DFT – GGA, PW91 exchange-correlation functional, PAW potentials
		CuO & Related Materials	

References	Authors	Metal Oxide	Method
hu2010	Hu et al.[b]	CuO(111), ($\bar{1}$11), (110), (011), (101), (010), and (100)	DFT – GGA+U, PAW potentials
sun2015	Sun et al.	CuO(111)	DFT-D – GGA, PW91 functional, double numerical basis set with polarization functions (DNP)
zhang2017	Zhang et al.	CuO(111)	DFT-D – GGA, PW91 functional, DFT Semi-core Pseudopots (DSPP), double numerical basis set with polarization functions (DNP)
maimaiti2014	Elliott et al.[c]	CuO(111)	DFT – GGA+U, PBE & HSE06 functional, PAW potentials
mishra2015	de Leeuw et al.[d]	CuO(111), ($\bar{1}$11), and (011)	DFT – GGA+U, PBE functional, PAW potentials
yu2017	Feng et al.[e]	CuO(111)	DFT – GGA+U, PBE functional, PAW potentials
fronzi2017	Nolan & Fronzi[f]	CuO(111)	DFT – GGA+U, PBE functional, PAW potentials
stenlid2017	Stenlid et al.	Cu_2O(111) and (100)	DFT-D3 – GGA+U, PBE functional, periodic slab models
		CeO_2	
chen2007	Chen et al.	CeO_2(111)	DFT – GGA+U, PW91 functional, PAW potentials
yildiz2012	Yildiz & Marrocchelli	CeO_2(111)	DFT – GGA+U, PW91 functional, PAW potentials
mayernick2011	Janik et al.	CeO_2(111), CeO_2(111) doped with La or Tb	DFT – GGA+U, PW91 functional, PAW potentials
kullgren2014	Hermansonn et al.[g]	CeO_2 (111) and (110)	DFT – GGA+U, PBE functional, PAW potentials
		MgO & Related Materials	
bagheri2013	Bagheri & Moradi	MgO nanotube	DFT – B3LYP, 6-31G basis set
rodriguez2000	Maiti et al.	MgO(100) and NiMgO(100)	DFT – GGA, norm-conserving and ultrasoft Vanderbilt pseudopotentials
rodriguez2000b	Rodriguez et al.	MgO(100) and $Cr_xMg_{(1-x)}O$(100)	DFT – GGA, nonlocal ultrasoft pseudopotentials
schneider2001	Schneider et al.[h]	MgO(001)	DFT – GGA, PW91 functional, norm-conserving pseudopotentials, periodic supercell
xu2003	Zhang et al.[i]	MgO(001)	DFT – B3LYP, 6-311+G basis set
		CaO	
wilcox2008	Wilcox & Sasmaz[j]	CaO(100)	DFT – GGA, PW91 functional, ultrasoft Vanderbilt pseudopotentials
wang2017	Wang et al.[k]	CaO(100) doped with Li, Na, K, Rb, or Cs	DFT – GGA, PBE functional, ultrasoft Vanderbilt pseudopotentials
	Al_2O_3 & Cr_2O_3		
ionescu2002	Allouche et al.	γ-Al_2O_3 (100) and (110D)	DFT– GGA, PW91 functional, Kleinman-Bylander Pseudopotentials

References	Authors	Metal Oxide	Method
arrouvel2004	Raybaud et al.	γ-Al_2O_3 (110)	DFT– GGA, PW91 functional, PAW potentials
rodriguez1998	Rodriguez et al.	α-Al_2O_3 (0001) and α-Cr_2O_3 (0001)	ab initio SCF methods with cluster models, nonempirical effective core potentials (ECP's), double-ζ quality basis set augmented with polarization functions
nigussa2016	Nigussa et al.	Cr_2O_3 (0001)	DFT-D2 – GGA+U, PW91 functional, PAW potentials
rodriguez2000b	Rodriguez et al.	Cr_2O_3 (0001)	DFT – GGA, nonlocal ultrasoft pseudopotentials
		TiO_2	
abbasi2017	Abbasi & Sardroodi	TiO_2 nanoparticles (non-doped and N-doped)	DFT-D2 – GGA, PBE functional, numerical pseudo-atomic orbitals (PAOs)
janik2012	Janik et al.[l]	TiO_2 (Ce-doped)	DFT – GGA+U, PW91 functional, PAW potentials
		Fe_2O_3	
song2013	Song et al.	α-Fe_2O_3 (0001)	DFT – GGA+U, PBE functional, ultrasoft Vanderbilt pseudopotentials
lin2016	Lin et al.	α-Fe_2O_3 (0001)	DFT – GGA+U, PBE functional, ultrasoft Vanderbilt pseudopotentials
		NiO	
wang2012	Wang et al.	NiO (100)	DFT – GGA+U, PBE functional, PAW potentials

Appendix B | Supplementary Information for Chapter 3

Table B-1: Results summary for sulfidation of samples of CuO-based sorbent at various pellet size, contact time, temperature, pressure and feed concentration.

Run No.	d_p (μm)	T (K)	P (atm)	C_0 (ppm)	t_c (s)	L (cm)	Q (sccm)	q_s (wt.%)	$q_{B\&A}$ (wt.%)	Error (wt.%)	q_{cooper} (wt.%)	Error ± (wt.%)	$k \cdot 10^5$ (s^{-1})	Error$\cdot 10^5$ (s^{-1})	kK (s^{-1})	$1/kK \cdot 10^2$ (s)	$1/k_{rxn} \cdot 10^2$ (s)	$1/k_p \cdot 10^2$ (s)	$1/k_b \cdot 10^2$ (s)
1	125	294	1.0	960	0.31	3.2	113	12.2	12.6	1.3	13.7	0.5	5.0	0.2	6.4	15.6	15.3	0.3	0.0
2	125	294	1.0	1000	0.35	7.1	227	12.0	12.0	1.8	12.9	0.7	6.6	0.3	6.9	14.6	14.3	0.3	0.0
3	125	294	1.0	1380	0.58	7.1	135	12.4	13.5	1.3	13.8	1.3	9.4	0.0	7.7	12.9	12.7	0.3	0.0
4	125	294	1.0	2200	0.62	6.4	113	12.5	13.8	1.7	14.0	0.2	11.0	0.1	6.4	15.6	14.5	1.1	0.0
6	125	294	1.0	980	0.71	7.1	110	12.4	13.0	1.5	13.7	0.4	6.6	0.2	5.0	19.9	19.6	0.3	0.0
7	180	294	1.0	990	0.35	3.7	114	12.3	12.5	1.3	13.6	0.5	5.0	0.2	5.5	18.3	17.7	0.6	0.0
8	180	294	1.0	1000	0.66	6.8	113	13.2	14.2	1.5	14.7	0.5	7.7	0.3	9.5	10.5	10.0	0.6	0.0
9	212	423	1.1	1000	0.09	1.3	101	39.2	48.3	4.2	51.3	2.0	13.9	0.5	44.0	2.3	1.6	0.6	0.0
10	212	323	1.0	970	0.22	1.9	87	16.9	16.9	3.2	18.3	1.0	12.0	0.7	15.2	6.6	5.8	0.7	0.0
12	212	383	1.0	1016	0.05	1.0	172	31.9	34.7	5.6	38.4	2.3	15.2	0.9	46.5	2.1	1.5	0.7	0.0
13	212	338	1.0	1016	0.06	1.1	172	23.3	28.1	4.8	30.0	2.7	10.0	0.9	18.0	5.6	4.8	0.7	0.0
14	212	368	1.0	1016	0.11	1.0	78	29.1	31.1	4.5	32.9	1.8	16.1	0.9	39.8	2.5	1.8	0.7	0.0
15	212	363	1.1	980	0.15	1.3	72	30.3	36.7	3.0	38.5	1.9	13.4	0.7	27.8	3.6	2.9	0.7	0.0
17	212	294	1.0	1000	0.70	7.0	110	12.5	13.2	0.9	13.6	0.2	10.6	0.2	11.5	8.7	7.9	0.8	0.0
18	500	294	1.0	1000	0.39	3.8	110	11.2	11.5	1.0	12.1	0.5	11.8	0.5	11.4	8.7	4.5	4.2	0.0
19	500	294	1.0	980	0.72	6.5	100	10.8	10.7	2.1	11.7	0.7	9.0	0.6	9.8	10.2	6.0	4.2	0.0
20	500	294	1.0	960	0.75	4.0	58	10.1	9.6	0.8	9.7	0.3	10.6	0.3	9.7	10.3	6.1	4.2	0.0
21	500	294	1.4	960	0.94	6.5	107	11.2	12.4	0.7	12.7	0.3	10.7	0.3	8.7	11.5	7.1	4.3	0.0
22	500	294	2.0	950	1.22	6.7	120	11.8	12.8	0.3	13.1	0.9	12.0	0.8	7.3	13.7	9.2	4.4	0.1
24	500	294	1.6	920	2.16	4.2	180	11.2	12.2	0.2	12.4	0.9	13.7	1.0	5.1	19.7	15.3	4.3	0.1
25	600	294	1.0	1090	0.76	2.1	164	10.3	11.2	0.4	11.4	0.9	12.4	1.0	13.0	7.7	1.5	6.1	0.1
26	800	294	1.0	1050	0.43	1.3	174	10.1	12.3	0.4	12.8	0.8	11.0	0.7	11.4	8.8	-0.9	9.6	0.1
27	800	294	1.0	1050	0.76	2.2	174	9.5	11.6	0.3	11.9	0.7	11.2	0.7	10.1	9.9	0.2	9.6	0.1
28	800	294	1.0	1050	1.06	3.1	174	9.7	11.8	0.3	12.0	0.6	11.2	0.6	10.5	9.5	-0.1	9.6	0.1
29	1000	294	1.0	980	1.40	4.3	180	9.7	12.2	0.8	12.5	0.9	17.8	1.3	6.5	15.3	0.6	14.6	0.1

Appendix C | Supplementary Information for Chapter 4

Table C-1: Physiochemical properties and synthesis procedures of CuO sorbents prepared via sol-gel, precipitation and hydrolysis. [a] Based on XRD. [b] Based on BET. [c] Based on BJH method.

Sample ID	Synthesis Method	Precursors	Synthesis/Processing Conditions	Thermal Treatment	Crystallite Size (nm)[a]	S_{BET} (m^2g^{-1})[b]	V_{pore} (cm^3g^{-1})[c]
NP-1	Sol-gel	$Cu(Ac)_2{\cdot}3(H_2O)$, NaOH, CH_3COOH	Vacuum filtration	Dried at 313 K for 8 h	5	14.5	0.040
NP-2			Vacuum filtration	Dried at 313 K for 8 h, then treated at 623 K for 4 h	18	-	-
NP-3			Vacuum filtration	Dried at 313 K for 8 h, then treated at 823 K for 4 h	26	-	-
NP-4			Vacuum filtration	Dried at 313 K for 8 h, then treated at 1023 K for 4 h	53	-	-
NP-5			Centrifuging	Dried at 313 K for 8 h	9	-	-
NP-6			Centrifuging	Dried at 313 K for 8 h	11	-	-
NP-7	Precipitation	$Cu(NO_3)_2{\cdot}3(H_2O)$, NaOH	Vacuum filtration	Dried at 353 K for 14 h, then treated at 773 K for 4 h	18	58.8	0.181
NB-1	Precipitation	$Cu(NO_3)_2{\cdot}3(H_2O)$, NaOH	Aged for 72 h, vacuum filtration	Dried at 333 K for 12 h, then treated at 623 for 4 h	33	6.18	0.02
FP-1	Hydrolysis	$Cu(Ac)_2{\cdot}3(H2O)$	Synthesized at 373 for 45 minutes	Dried at 353 K for 12 h	10	-	-
FP-2	Precipitation	$Cu(NO_3)_2{\cdot}3(H_2O)$,	Synthesized at 353 for 8 h	Dried at 353 K for 12 h	13	-	-
FP-3	Precipitation	$Cu(NO_3)_2{\cdot}3(H_2O)$	Synthesized at 376 for 24 h	dried at 353 K for 12 h	19	59.1	0.079

Table C-2: Physiochemical properties and synthesis procedures of CuO sorbents prepared via hydrothermal treatment, and electrospinning. [a] Based on XRD. [b] Based on BET. [c] Based on BJH method. *weight ratio of polymer used to salt precursor.

Sample ID	Synthesis Method	Precursors (Polymer: Salt)*	Synthesis / Processing Conditions	Thermal Treatment	Crystallite Size (nm)[a]	S_{BET} (m^2g^{-1})[b]	V_{pore} (cm^3g^{-1})[c]
NPC-1	Hydrothermal	CuO (NP-7), P123 (1:1)	Hydrothermal at 383 K for 24 h	Dried at 353 K for 12 h, then treated at 823 K for 4 h Dried at 353 K	21	-	-
NPC-2		CuO (NP-7), PVP (MW=1,300,000) (1:1)			24	17.4	0.05
NPC-3		CuO (NP-7), PVP (MW=1,300,000) (1:9)			18	-	-
NPC-4		CuO (NP-7), PVP (MW=1,300,000) (2:7)			22	-	-
NPC-5		CuO (NP-7), PVP (MW=1,300,000) (2:3)			22	-	-
NF-1	Electrospinning	PEO (MW=300,000), EtOH, $Cu(NO_3)_2{\cdot}3(H_2O)$ (2.7:1)	14 inches, 30 kV, 1.0 cm^3/h	Treated at 823 K for 4 h at a ramping rate of 1 K/min	14	-	-
NF-2		PVP (1,300,000), EtOH, $Cu(NO_3)_2{\cdot}3(H_2O)$ (10:1)	15 inches, 35 kV, 5.0 cm^3/h	Treated at 898 K for 10 h at a ramping rate of 0.4 K/min	24	-	-
NF-3		PVP (40,000), EtOH, $Cu(NO_3)_2{\cdot}3(H_2O)$ (2.5:1)	18 inches, 30 kV, 1.0 cm^3/h	Treated at 823 K for 4 h at a ramping rate of 1 K/min	25	-	-
NF-4		PVP (1,300,000), EtOH, $Cu(NO_3)_2{\cdot}3(H_2O)$ (1:1)	6 inches, 20 kV, 1.0 cm^3/h	Treated at 773 K for 2 h at a ramping rate of 2 K/min	40	-	-
NF-5		PVP (1,300,000), MeOH, $Cu(NO_3)_2{\cdot}3(H_2O)$ (1:1)	18 inches, 30 kV, 1.0 cm^3/h	Treated at 823 K for 4 h at a ramping rate of 2 K/min	74	-	-
NF-6		PVP (1,300,000), EtOH, $Cu(NO_3)_2{\cdot}3(H_2O)$ (1:1)	22 inches, 30 kV, 1.0 cm^3/h	Treated at 823 K for 4 h at a ramping rate of 2 K/min	66	2.79	0.002

Appendix D | Supplementary Information for Chapter 5

Table D-1: Summary of the EXAFS fit parameters[a] characterizing the initial CuO samples. The EXAFS data was collected at room temperature in flowing helium.

Sample	Absorber-Backscatter Scattering Path	*N*	$10^3 \times \sigma^2$ (Å^2)	*R* (Å)	ΔE_0 (eV)	*k*-range (Å^{-1})	*R*-range (Å)
CuO-1	Cu-O	2.7 ± 0.3	1.8 ± 1.7	1.96 ± 0.01	1.7 ± 1.7	3.0-11.0	1.1-3.2
	Cu-O	1.3 ± 0.2	1.8 ± 1.7	2.82 ± 0.08			
	Cu-Cu	2.7 ± 0.3	6.7 ± 6.2	2.96 ± 0.03			
	Cu-Cu	2.7 ± 0.3	6.7 ± 6.2	3.16 ± 0.05			
	Cu-Cu	1.3 ± 0.2	6.7 ± 6.2	3.38 ± 0.08			
CuO-2	Cu-O	3.4 ± 4.3	2.2 ± 14.6	1.96 ± 0.10	7.1 ± 13.0	3.0-11.0	0.9-3.2
	Cu-O	1.7 ± 2.2	2.3 ± 14.6	2.78 ± 0.57			
	Cu-Cu	3.4 ± 4.3	4.2 ± 17.8	2.90 ± 0.21			
	Cu-Cu	3.4 ± 4.3	4.2 ± 17.8	3.08 ± 0.23			
	Cu-Cu	1.7 ± 2.2	4.2 ± 17.8	3.17 ± 0.28			

[a] Notation: S_0^2, amplitude reduction factor, *N*, coordination number, σ^2, disorder term (Debye-Waller factor), *R*, distance between absorber and backscatter, ΔE_0, energy correction term.

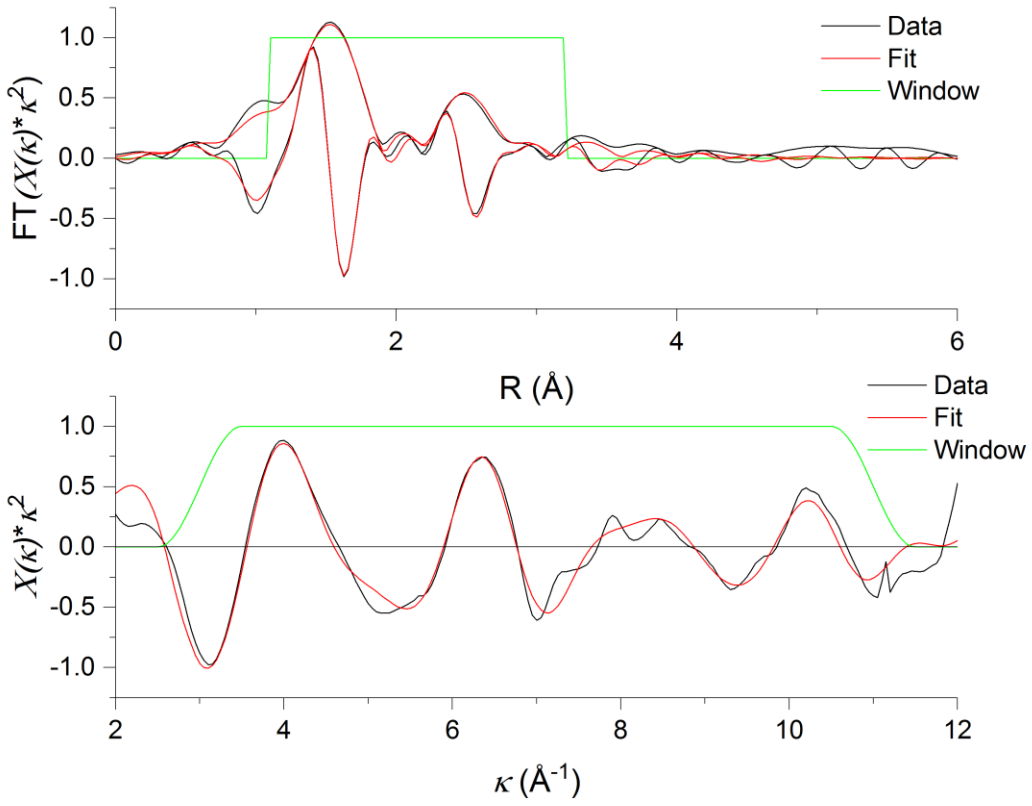

Figure D-1: EXAFS data and best-fit model characterizing the initial state of the commercial CuO sample, CuO-1. Spectra were collected at room temperature in flowing helium. **Top**: k^2-weighted magnitude and imaginary part of the Fourier transform of the data (black line) and fit (red line). **Bottom**: k^2-weighted EXAFS function of the data (black line) and fit (red line). The green line in both plots represents the window used to determine the number if independent parameters.

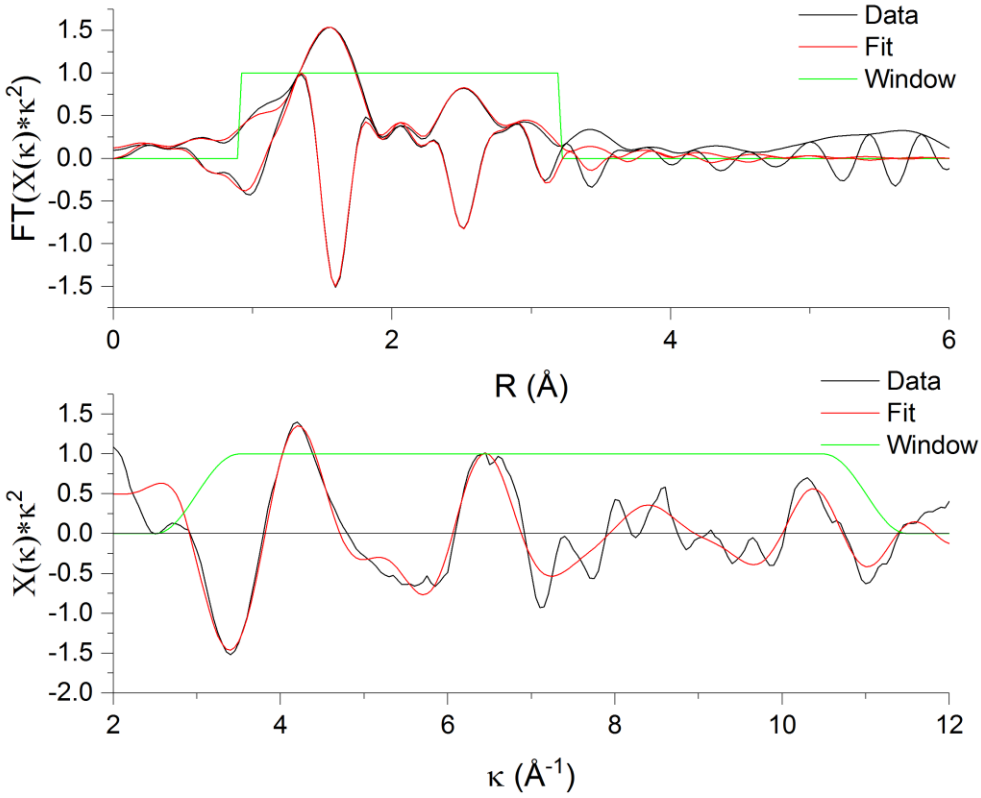

Figure D-2: EXAFS data and best-fit model characterizing the initial state of the CuO nanoparticle sample, CuO-2. Spectra were collected at room temperature in flowing helium. **Top**: k^2-weighted magnitude and imaginary part of the Fourier transform of the data (black line) and fit (red line). **Bottom**: k^2-weighted EXAFS function of the data (black line) and fit (red line). The green line in both plots represents the window used to determine the number if independent parameters.

Appendix E | Supplementary Information for Chapter 6

Table E-1: Summary of the Cu K-edge EXAFS fits demonstrating the effect of crystallite size on EXAFS fitting parameters for different CuO sorbents. The EXAFS data were collected at room temperature in flowing helium.

Sample	Absorber-Backscatter Scattering Path	N	$10^3 \times \sigma^2$ ($Å^2$)	R (Å)	ΔE_0 (eV)	k-range ($Å^{-1}$)	R-range (Å)
CuO-2 (7 nm)	Cu-O	2.5 ± 1.0	1.8 ± 5.4	1.95 ± 0.04	0.3 ± 6.1	3.0-11.3	1.0-3.2
	Cu-O	1.2 ± 0.5	1.8 ± 5.4	2.75 ± 0.08			
	Cu-Cu	2.5 ± 1.0	4.6 ± 8.0	2.95 ± 0.05			
	Cu-Cu	2.5 ± 1.0	4.6 ± 8.0	3.14 ± 0.07			
	Cu-Cu	1.2 ± 0.5	4.6 ± 8.0	3.36 ± 0.09			
CuO-3 (11 nm)	Cu-O	3.2 ± 0.4	3.0 ± 1.7	1.95 ± 0.01	-1.2 ± 1.9	3.0-11.3	1.0-3.2
	Cu-O	1.6 ± 0.2	3.0 ± 1.7	2.75 ± 0.08			
	Cu-Cu	3.2 ± 0.4	4.4 ± 3.0	2.90 ± 0.03			
	Cu-Cu	3.2 ± 0.4	4.4 ± 3.0	3.06 ± 0.03			
	Cu-Cu	1.6 ± 0.2	4.4 ± 3.0	3.18 ± 0.04			
CuO-4 (23 nm)	Cu-O	4.0 ± 0.6	3.6 ± 1.7	1.95 ± 0.01	-0.4 ± 1.5	3.0-11.3	1.0-3.2
	Cu-O	2.0 ± 0.3	3.6 ± 1.7	2.72 ± 0.06			
	Cu-Cu	4.0 ± 0.6	4.3 ± 1.8	2.89 ± 0.02			
	Cu-Cu	4.0 ± 0.6	4.3 ± 1.8	3.04 ± 0.02			
	Cu-Cu	2.0 ± 0.3	4.3 ± 1.8	3.16 ± 0.03			
CuO-5 (40 nm)	Cu-O	5.4 ± 0.5	3.6 ± 1.4	1.95 ± 0.01	-0.5 ± 1.4	3.0-11.3	1.0-3.2
	Cu-O	2.7 ± 0.2	3.6 ± 1.4	2.70 ± 0.05			
	Cu-Cu	5.4 ± 0.5	4.0 ± 1.4	2.89 ± 0.02			
	Cu-Cu	5.4 ± 0.5	4.0 ± 1.4	3.04 ± 0.02			
	Cu-Cu	2.7 ± 0.2	4.0 ± 1.4	3.15 ± 0.02			
Bulk CuO	Cu-O	4	3.0 ± 1.0	1.95 ± 0.01	7.9 ± 1.0	3-11.3	1.0-3.2
	Cu-O	2	3.0 ± 1.0	2.77 ± 0.05			
	Cu-Cu	4	5.0 ± 2.0	2.91 ± 0.01			
	Cu-Cu	4	5.0 ± 2.0	3.10 ± 0.01			
	Cu-Cu	2	3.0 ± 1.0	3.16 ± 0.01			

Table E-2: Summary of the Cu K-edge EXAFS fits characterizing the effect of temperature on CuO sulfidation products. The EXAFS data were collected for spent samples at room temperature in flowing helium, after sulfidation with 1000 ppm-vol H_2S/He. [a]Represents the coordination number of Cu-S without size and conversion effects.

Sample	Scattering Path	*N*	$10^3 \times \sigma^2$ (Å^2)	*R* (Å)	ΔE_0 (eV)	*Cu*-S[a] CN	*k*-range (Å^{-1})	*R*-range (Å)
Fresh CuO-1	Cu-O	3.0 ± 0.4	3.0 ± 2.1	1.95 ± 0.02	6.7 ± 1.9	0	3.0-11.3	1.0-3.22
	Cu-O	1.5 ± 0.2	3.0 ± 2.1	2.75 ± 0.08				
	Cu-Cu	3.0 ± 0.4	5.3 ± 3.5	2.95 ± 0.05				
	Cu-Cu	3.0 ± 0.4	5.3 ± 3.5	3.14 ± 0.07				
	Cu-Cu	1.5 ± 0.2	5.3 ± 3.5	3.36 ± 0.09				
Spent at 323 K	Cu-O	2.3	3.0	1.95	8.0 ± 0.8	3.4 ± 1.2	3.0-11.3	1.0-2.4
	Cu-S	1.5 ± 0.5	9.0 ± 5.6	2.30 ± 0.02				
Spent at 353 K	Cu-O	0.3	3.0	1.95	5.0 ± 0.8	3.8 ± 0.3	3.0-11.3	1.0-2.4
	Cu-S	3.3 ± 0.1	10.3 ± 1.2	2.27 ± 0.01				
Spent at 383 K	Cu-S	3.4 ± 0.4	9.4 ± 1.6	2.26 ± 0.01	4.3 ± 1.1	3.7	3.0-11.3	1.0-3.3
	Cu-Cu	3.7 ± 0.4	20.5 ± 5.4	3.34 ± 0.04				
CuS reference	Cu-S	2.4 ± 0.3	8.2 ± 1.6	2.26 ± 0.01	4.4 ± 1.2	3.7	3.0-11.3	1.0-3.4
	Cu-Cu	2.6 ± 0.3	20.1 ± 6.1	3.34 ± 0.04				

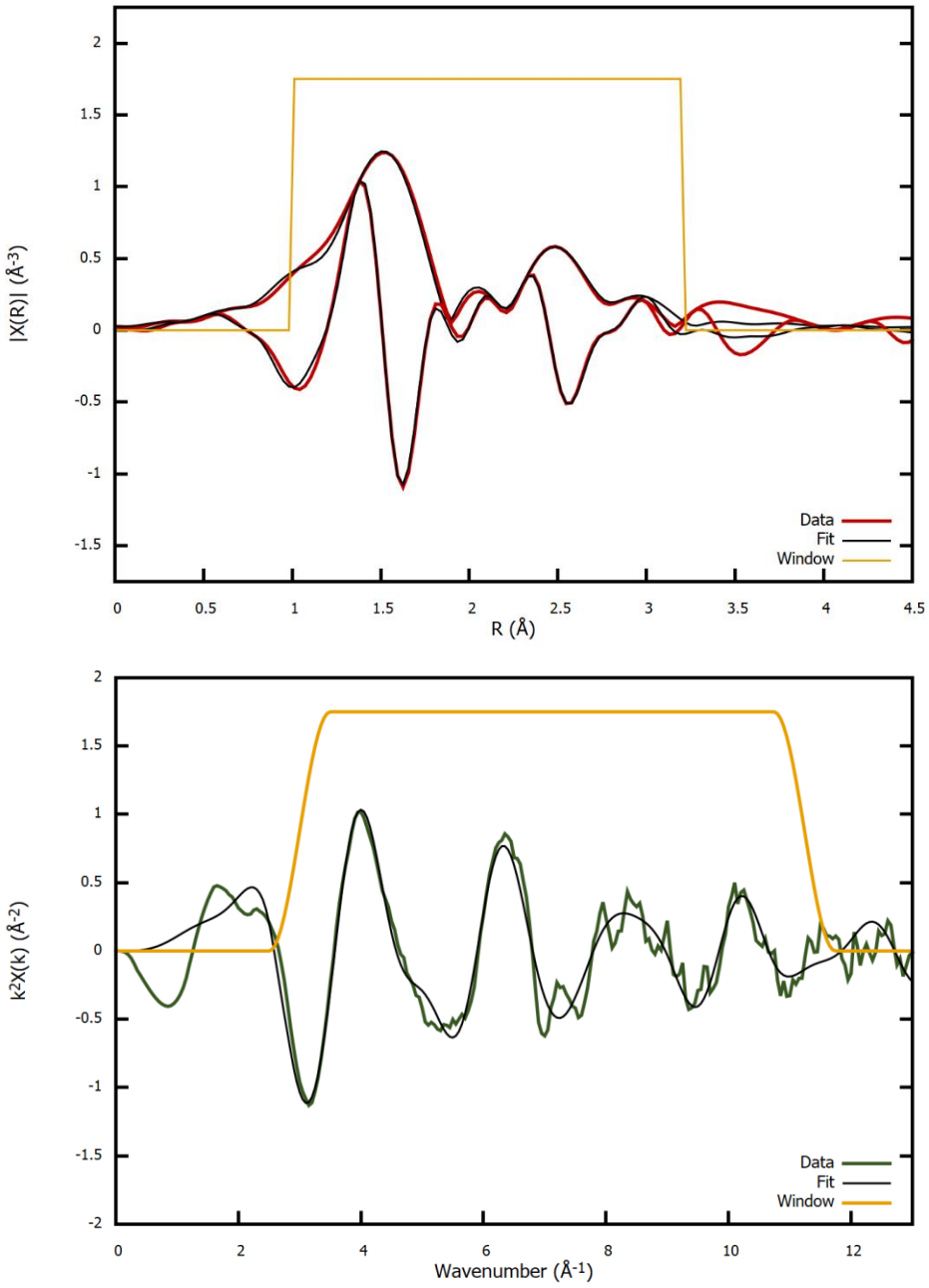

Figure E-1: EXAFS data and best-fit model characterizing the lab-synthesized CuO-2 sorbent (7 nm crystallite size). Spectra were collected at room temperature in flowing helium. **Top:** magnitude and imaginary part of the Fourier transform of the data (red lines) and fit (black line). **Bottom:** k^2-weighted EXAFS function of the data (green line) and fit (black line). The yellow line in both plots represents the window used to determine the number if independent parameters.

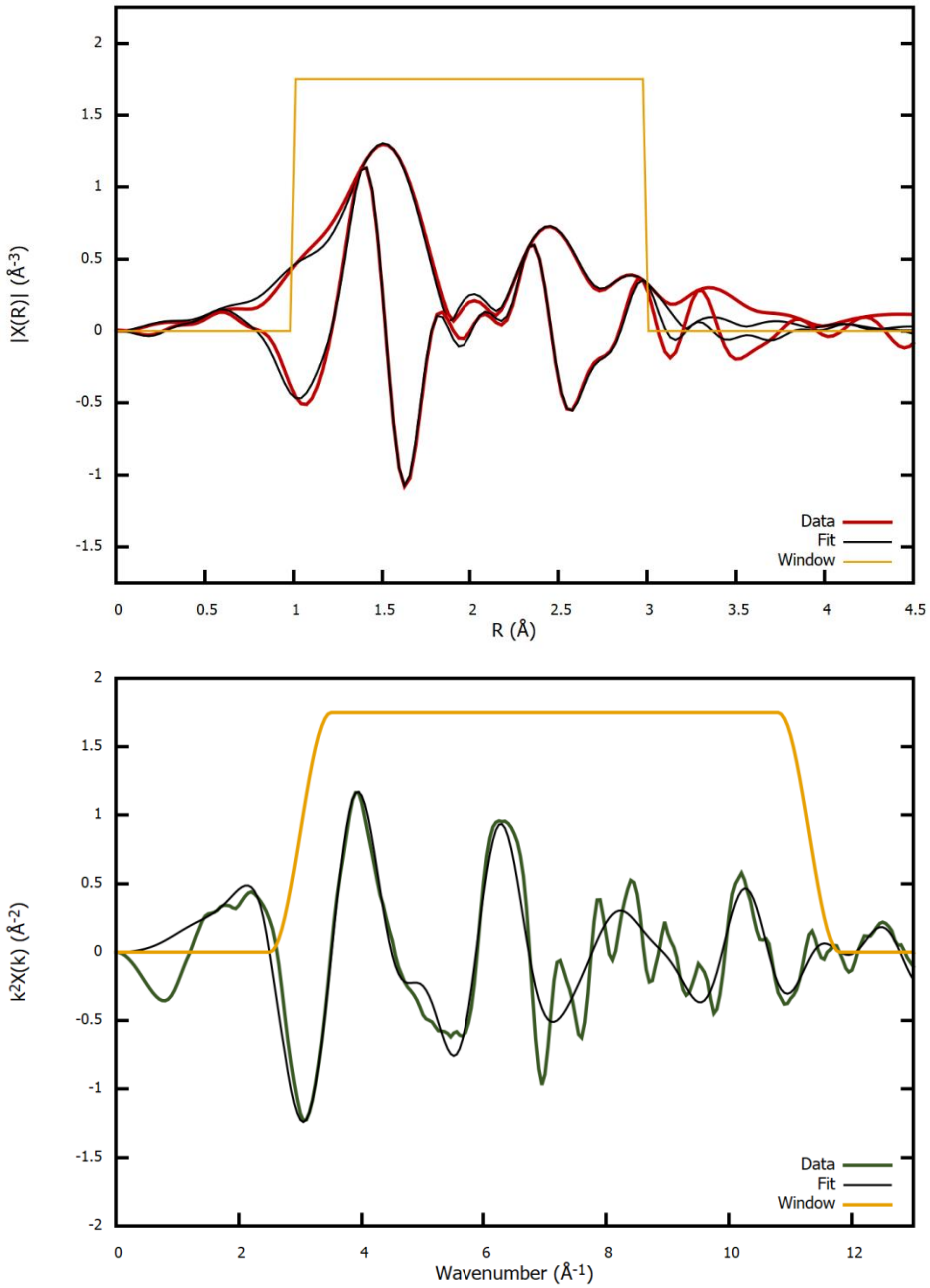

Figure E-2: EXAFS data and best-fit model characterizing the lab-synthesized CuO-3 sorbent (11 nm crystallite size). Spectra were collected at room temperature in flowing helium. **Top:** magnitude and imaginary part of the Fourier transform of the data (red lines) and fit (black line). **Bottom:** k^2-weighted EXAFS function of the data (green line) and fit (black line). The yellow line in both plots represents the window used to determine the number if independent parameters.

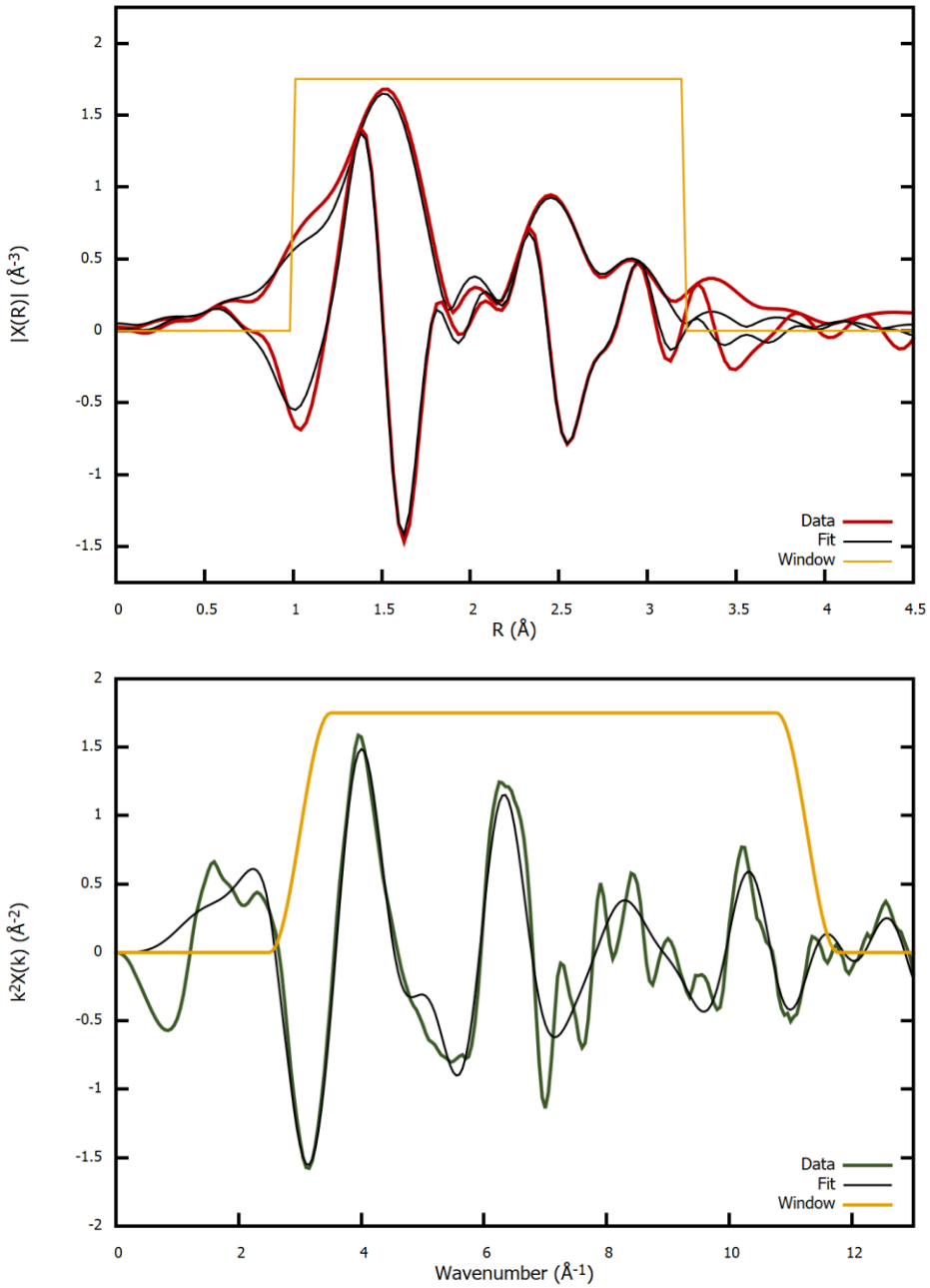

Figure E-3. EXAFS data and best-fit model characterizing the lab-synthesized CuO-4 sorbent (23 nm crystallite size). Spectra were collected at room temperature in flowing helium. **Top:** magnitude and imaginary part of the Fourier transform of the data (red lines) and fit (black line). **Bottom:** k^2-weighted EXAFS function of the data (green line) and fit (black line). The yellow line in both plots represents the window used to determine the number if independent parameters.

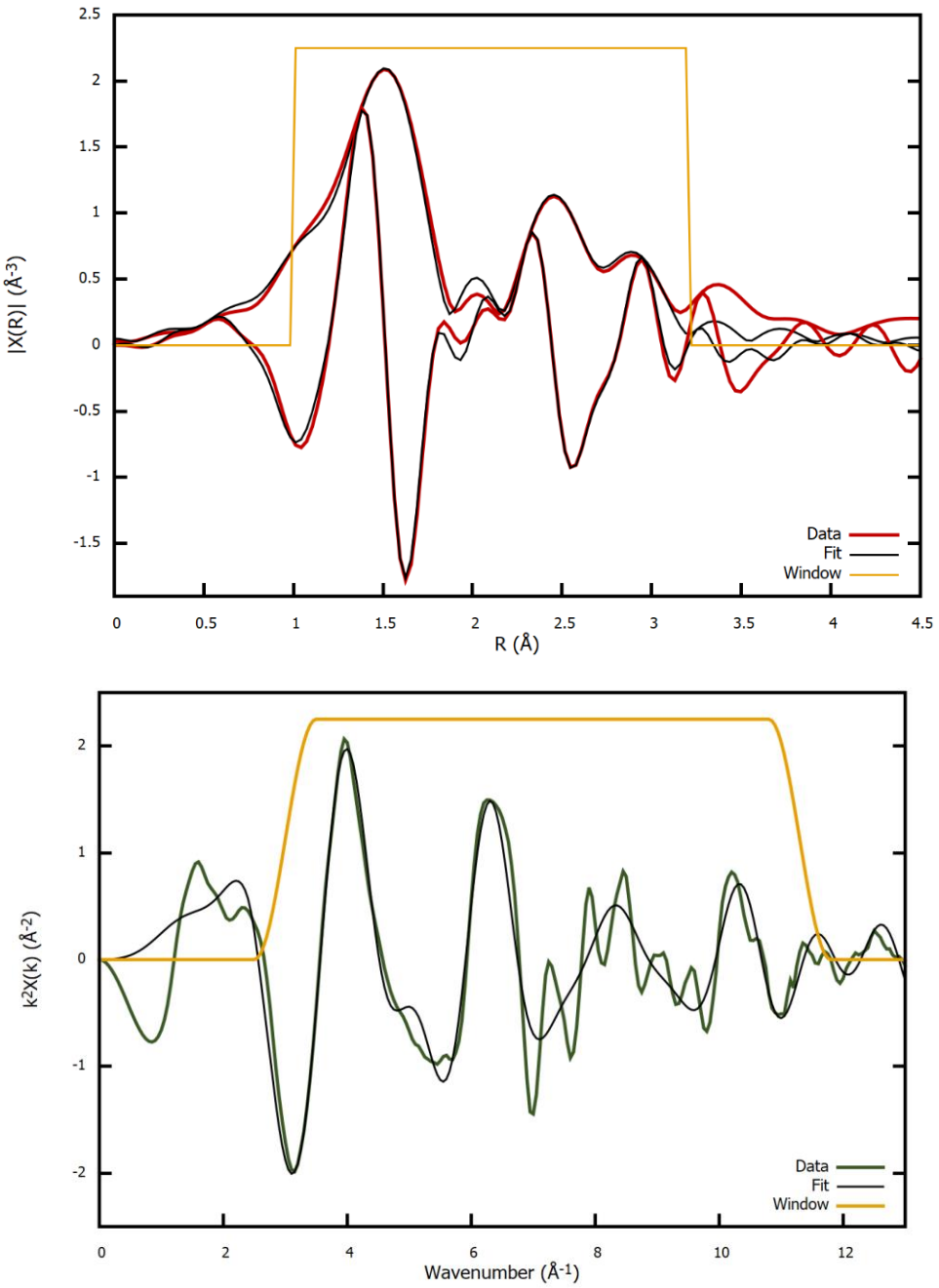

Figure E-4: EXAFS data and best-fit model characterizing the lab-synthesized CuO-5 sorbent (40 nm crystallite size). Spectra were collected at room temperature in flowing helium. **Top:** magnitude and imaginary part of the Fourier transform of the data (red lines) and fit (black line). **Bottom:** k^2-weighted EXAFS function of the data (green line) and fit (black line). The yellow line in both plots represents the window used to determine the number if independent parameters.

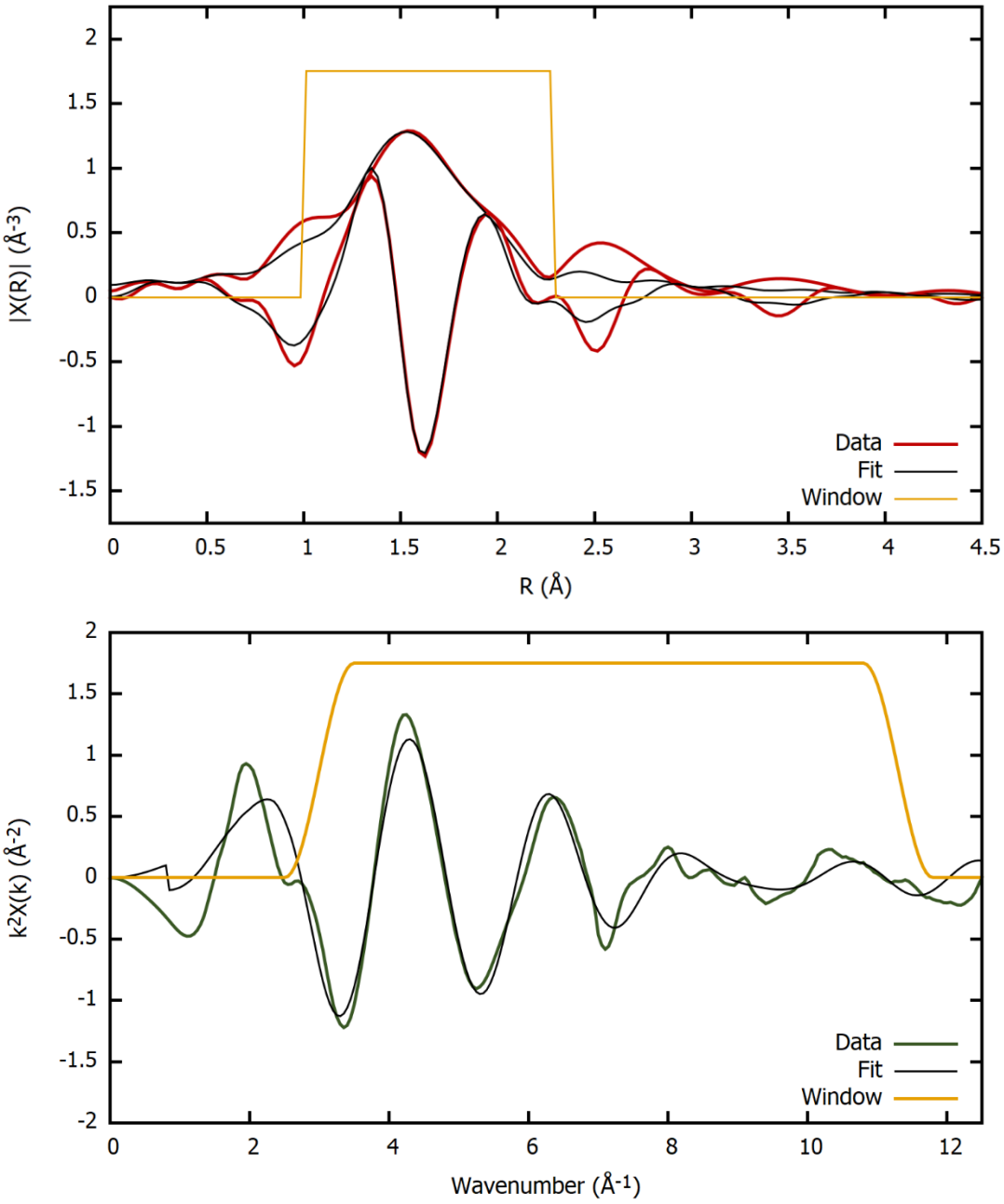

Figure E-5: EXAFS data and best-fit model characterizing spent CuO sample, CuO-1 at 323 K with 1000 ppm-vol H2S/He. Spectra were collected at room temperature in flowing helium. **Top:** magnitude and imaginary part of the Fourier transform of the data (red line) and fit (black line). **Bottom:** k^2-weighted EXAFS function of the data (green line) and fit (black line). The yellow line in both plots represents the window used to determine the number if independent parameters.

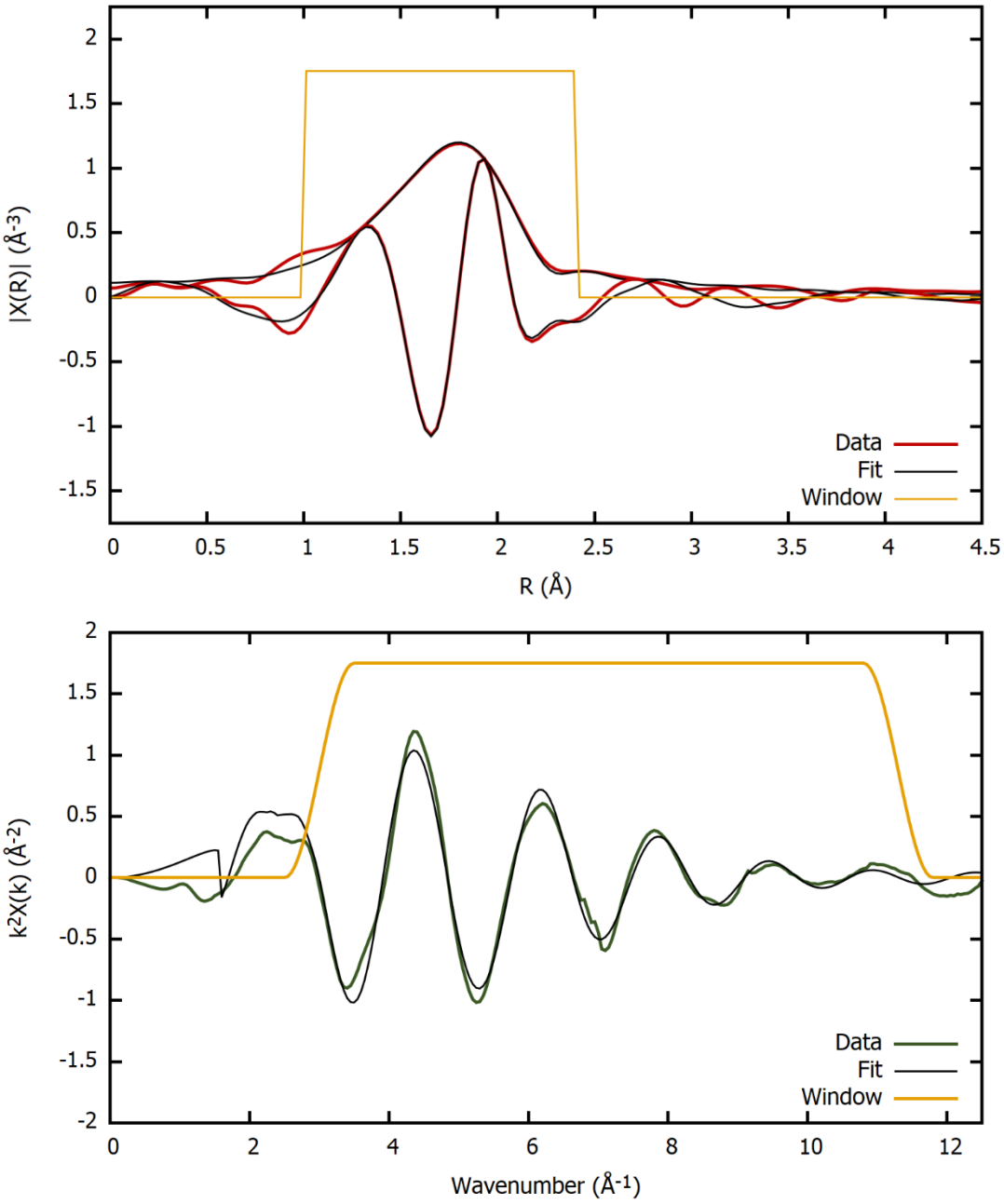

Figure E-6: EXAFS data and best-fit model characterizing spent CuO sample, CuO-1 at 353 K with 1000 ppm-vol H_2S/He. Spectra were collected at room temperature in flowing helium. **Top:** magnitude and imaginary part of the Fourier transform of the data (red line) and fit (black line). **Bottom:** k^2-weighted EXAFS function of the data (green line) and fit (black line). The yellow line in both plots represents the window used to determine the number if independent parameters.

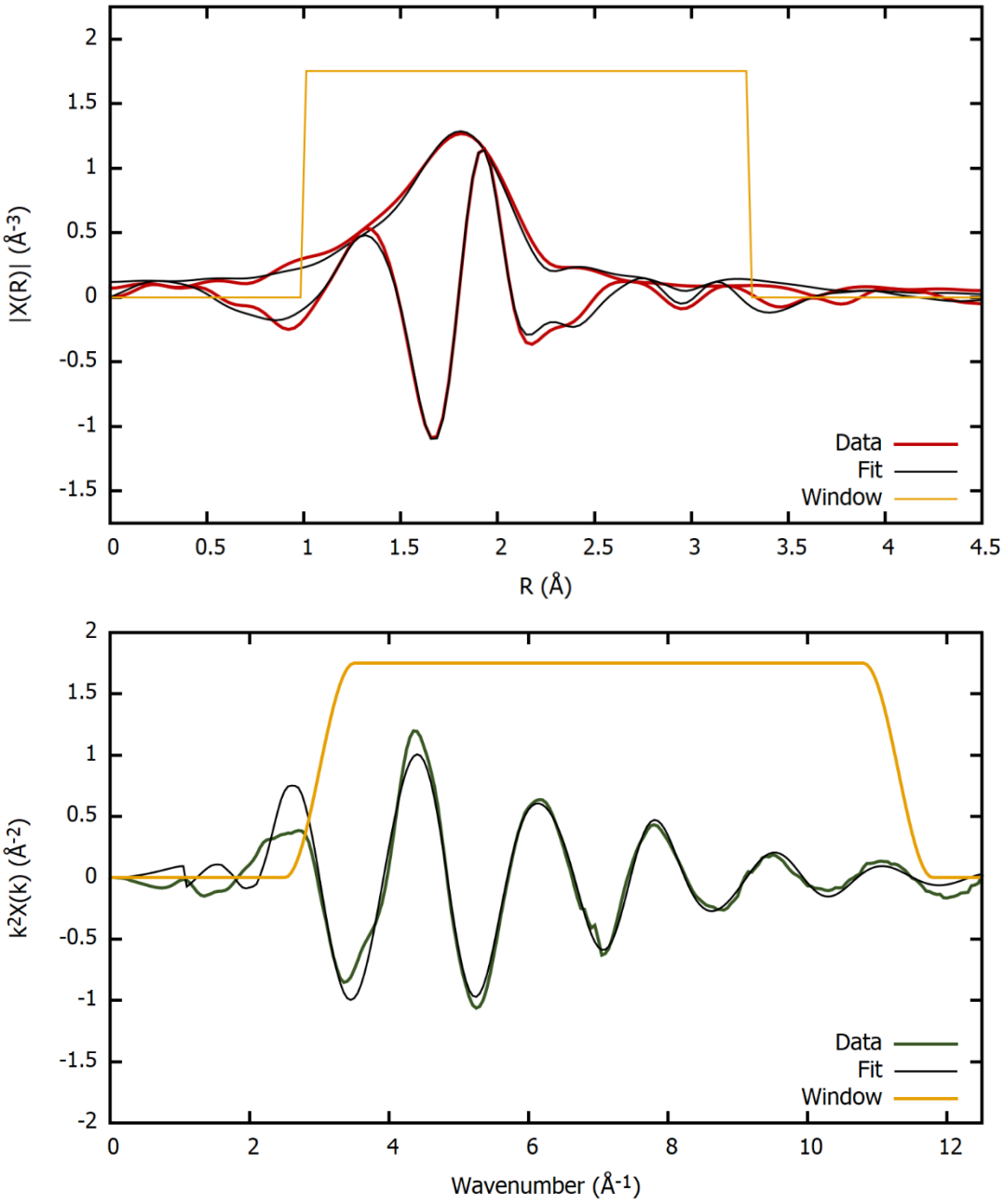

Figure E-7: EXAFS data and best-fit model characterizing spent CuO sample, CuO-1 at 383 K with 1000 ppm-vol H_2S/He. Spectra were collected at room temperature in flowing helium. **Top:** magnitude and imaginary part of the Fourier transform of the data (red line) and fit (black line). **Bottom:** k^2-weighted EXAFS function of the data (green line) and fit (black line). The yellow line in both plots represents the window used to determine the number if independent parameters.

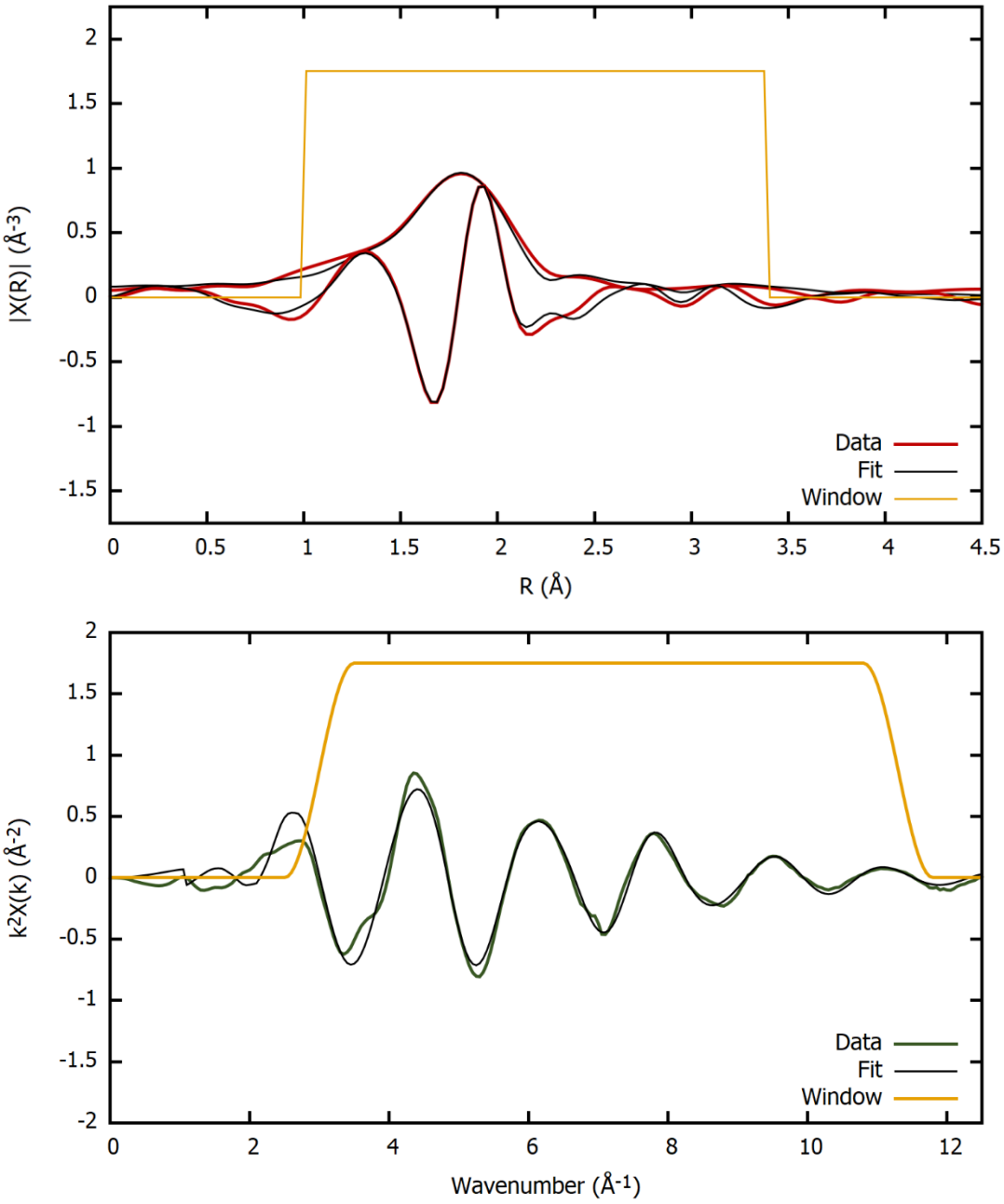

Figure E-8: EXAFS data and best-fit model characterizing CuS reference sample at room temperature in flowing helium. **Top:** magnitude and imaginary part of the Fourier transform of the data (red line) and fit (black line). **Bottom:** k^2-weighted EXAFS function of the data (green line) and fit (black line). The yellow line in both plots represents the window used to determine the number if independent parameters.

Appendix F | Supplementary Information for Chapter 7

Table F-1: Summary of the EXAFS fit parameters[a] characterizing the fresh CuO-La samples. The EXAFS data were collected at room temperature in flowing helium.

Sample	Absorber-Backscatter Scattering Path	*CN*	$10^3 \times \sigma^2$ ($Å^2$)	*R* (Å)	ΔE_0 (eV)	*k*-range ($Å^{-1}$)	*R*-range (Å)
CuO-La-1	Cu-O	3.3 ± 0.3	2.7 ± 1.7	1.95 ± 0.01	7.65 ± 1.0	3.0-12.0	1.0-3.2
	Cu-O	1.7 ± 0.2	2.7 ± 1.7	2.79 ± 0.08			
	Cu-Cu	3.3 ± 0.3	6.6 ± 6.2	2.94 ± 0.03			
	Cu-Cu	3.3 ± 0.3	6.6 ± 6.2	3.12 ± 0.05			
CuO-La-2	Cu-O	3.5 ± 0.1	3.2 ± 0.6	1.95 ± 0.01	7.80 ± 0.47	2.8-13.3	1.0-3.2
	Cu-O	1.7 ± 0.1	3.2 ± 0.6	2.77 ± 0.02			
	Cu-Cu	3.5 ± 0.1	5.0 ± 0.6	2.92 ± 0.01			
	Cu-Cu	3.5 ± 0.1	5.0 ± 0.6	3.11 ± 0.01			
CuO-1	Cu-O	3.6 ± 0.5	4.8 ± 2.1	1.93 ± 0.01	7.35 ± 1.36	3.0-11.0	1.0-3.2
	Cu-O	1.8 ± 0.2	4.8 ± 2.1	2.56 ± 0.04			
	Cu-Cu	3.6 ± 0.5	11.9 ± 6.1	2.85 ± 0.04			
	Cu-Cu	3.6 ± 0.5	11.9 ± 6.1	2.95 ± 0.05			

[a] Notation: S_0^2, amplitude reduction factor, *CN*, coordination number, σ^2, disorder term (Debye-Waller factor), *R*, distance between absorber and backscatter, ΔE_0, energy correction term.

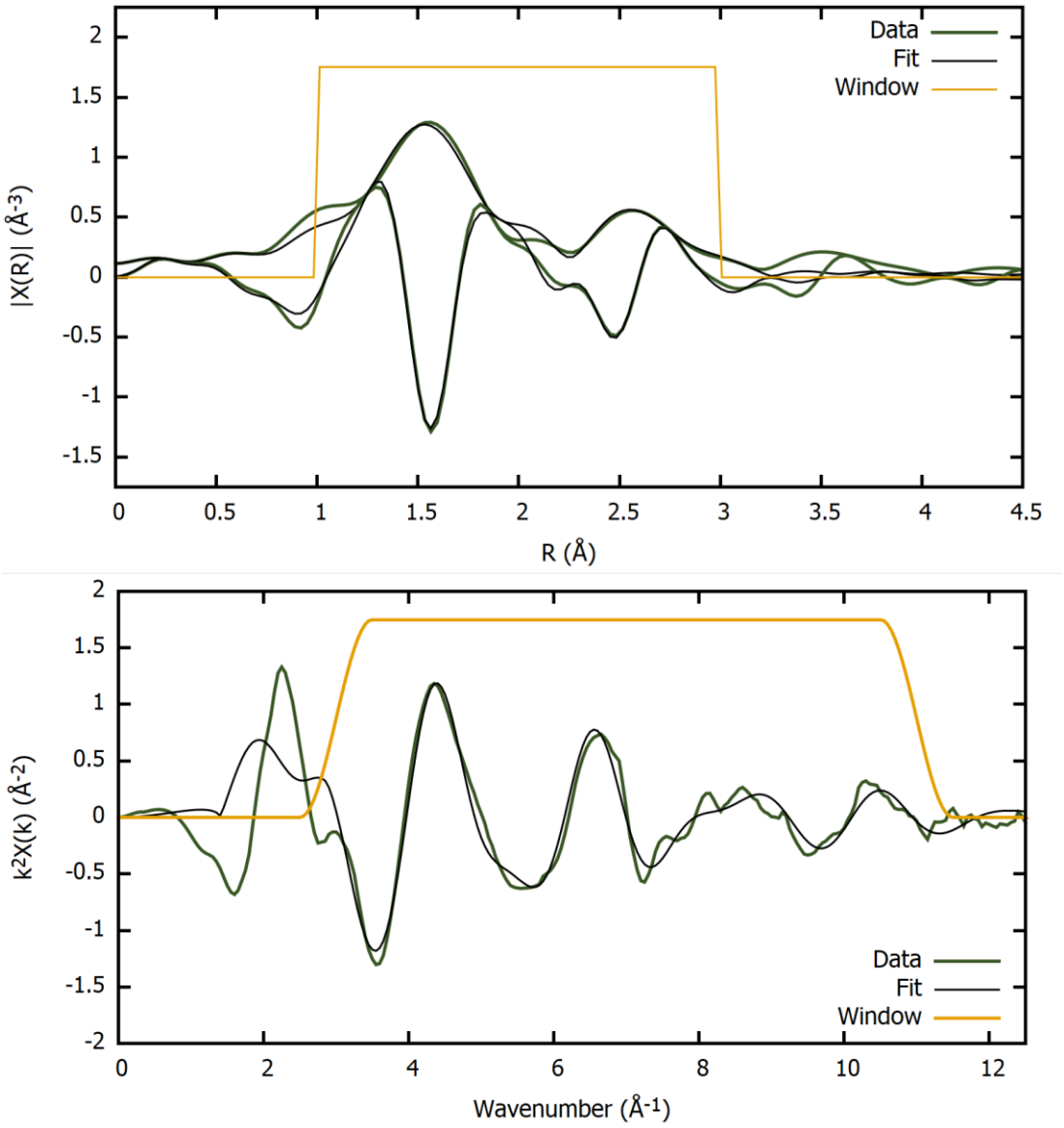

Figure F-1: EXAFS data and best-fit model characterizing the initial state of commercial CuO sample, CuO-1. Spectra were collected at room temperature in flowing helium. **Top:** magnitude and imaginary part of the Fourier transform of the data (green line) and fit (black line). **Bottom:** k^2-weighted EXAFS function of the data (green line) and fit (black line). The yellow line in both plots represents the window used to determine the number if independent parameters.

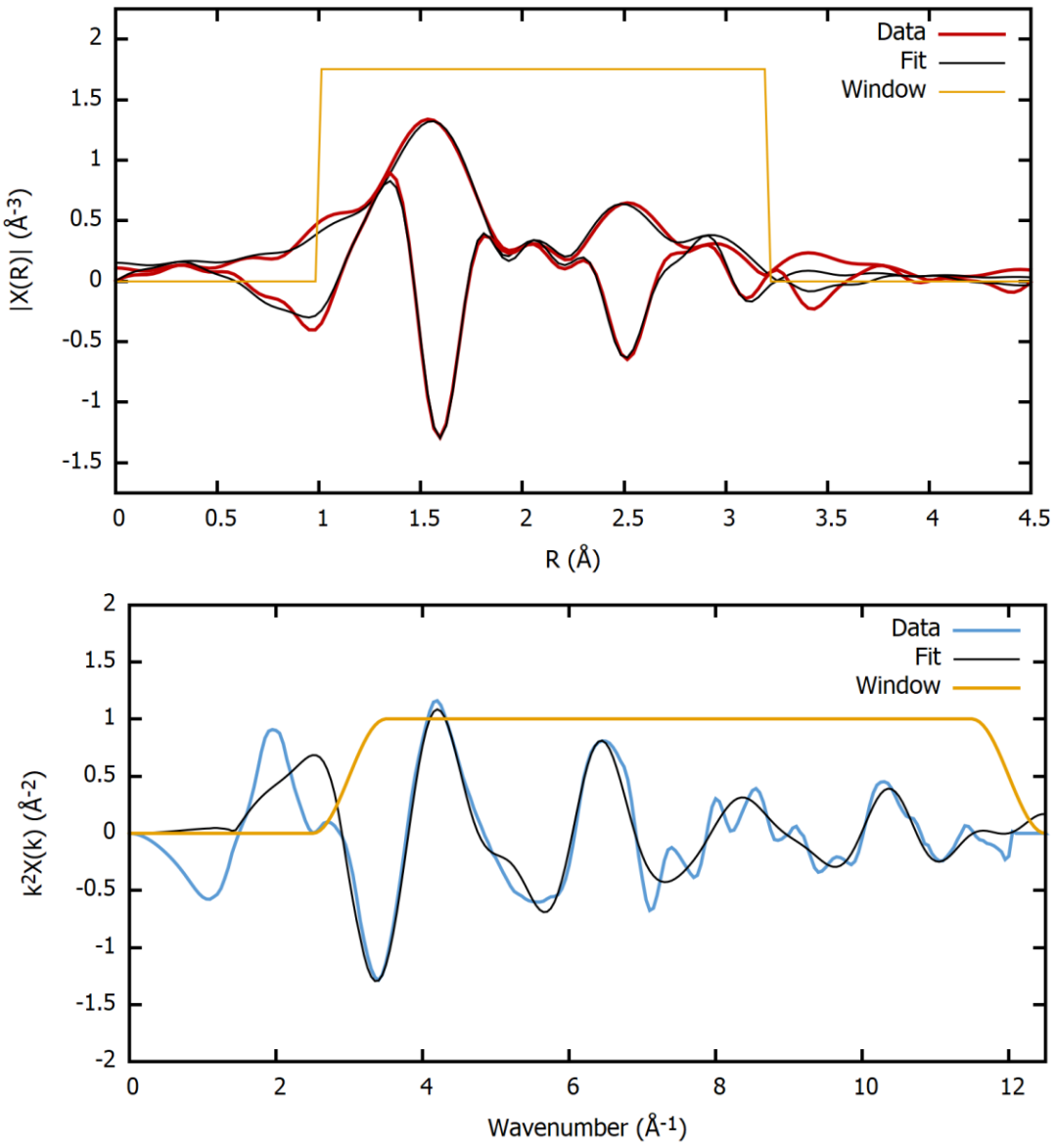

Figure F-2: EXAFS data and best-fit model characterizing the initial state of the sol-gel lanthanum-doped CuO sample, CuO-La-1. Spectra were collected at room temperature in flowing helium. **Top:** magnitude and imaginary part of the Fourier transform of the data (red line) and fit (black line). **Bottom:** k^2-weighted EXAFS function of the data (blue line) and fit (black line). The yellow line in both plots represents the window used to determine the number if independent parameters.

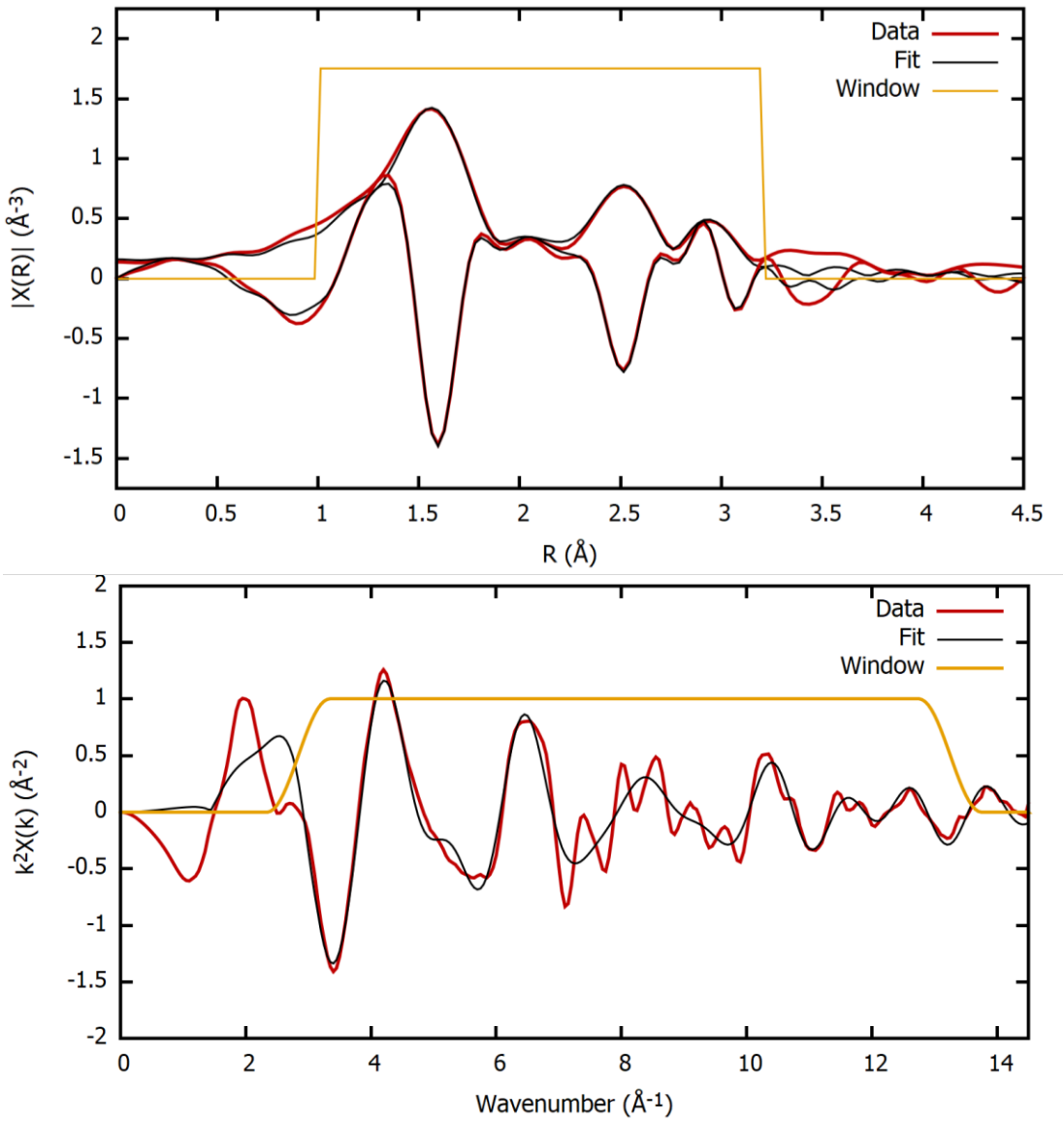

Figure F-3: EXAFS data and best-fit model characterizing the initial state of the ammonium co-precipitation lanthanum-doped CuO sample, CuO-La-2. Spectra were collected at room temperature in flowing helium. **Top:** magnitude and imaginary part of the Fourier transform of the data (red line) and fit (black line). **Bottom:** k^2-weighted EXAFS function of the data (red line) and fit (black line). The yellow line in both plots represents the window used to determine the number if independent parameters.

Bibliography

(1) Eckersley, N. Advanced Mercury Removal Technologies. *Energy Process. Can.* **2013**, *45* (6), 16–19.

(2) Hayes, M.; Åkerlindh, K. Combating the Threat of Mercury. *PTQ gas* **2012**, 55–55.

(3) Kidnay, A. J.; Parrish, W. *Fundamentals of Natural Gas Processing*; CRC Press: Boca Raton, 2006.

(4) Wilhelm, S. M.; National Risk Management Research Laboratory (U.S.). *Mercury in Petroleum and Natural Gas--Estimation of Emissions from Production, Processing, and Combustion*; U.S. Environmental Protection Agency, National Risk Management Research Laboratory: Research Triangle Park, NC, 2001.

(5) Song, C.; Ma, X. New Design Approaches to Ultra-Clean Diesel Fuels by Deep Desulfurization and Deep Dearomatization. *APCATB Appl. Catal. B Environ.* **2003**, *41* (1), 207–238.

(6) Wilhelm SM. Estimate of Mercury Emissions to the Atmosphere from Petroleum. *Environ. Sci. Technol.* **2001**, *35* (24), 4704–4710.

(7) Ruthven, D. M. *Principles of Adsorption and Adsorption Processes*; Wiley: New York, 1984.

(8) Samokhvalov, A.; Tatarchuk, B. Review of Experimental Characterization of Active Sites and Determination of Molecular Mechanisms of Adsorption, Desorption and Regeneration of the Deep and Ultradeep Desulfurization Sorbents for Liquid Fuels. *Catal. Rev.* **2010**, *52* (3), 381–410.

(9) Samokhvalov A; Tatarchuk BJ. Characterization of Active Sites, Determination of Mechanisms of H_2S, COS and CS_2 Sorption and Regeneration of ZnO Low-Temperature Sorbents: Past, Current and Perspectives. *Phys. Chem. Chem. Phys. PCCP* **2011**, *13* (8), 3197–3209.

(10) Xue, M.; Chitrakar, R.; Sakane, K.; Ooi, K. Screening of Adsorbents for Removal of H_2S at Room Temperature. *Green Chem.* **2003**, *5* (5), 529–534. https://doi.org/10.1039/B303167P.

(11) Westmoreland, P. R.; Gibson, J. B.; Harrison, D. P. Comparative Kinetics of High-Temperature Reaction between Hydrogen Sulfide and Selected Metal Oxides. *Environ. Sci. Technol.* **1977**, *11* (5), 488–491. https://doi.org/10.1021/es60128a007.

(12) Westmoreland, P. R.; Harrison, D. P. Evaluation of Candidate Solids for High-Temperature Desulfurization of Low-Btu Gases. *Environ. Sci. Technol.* **1976**, *10* (7), 659–661. https://doi.org/10.1021/es60118a010.

(13) Ramachandran, P. A.; Doraiswamy, L. K. Modeling of Noncatalytic Gas-solid Reactions. *AIChE J.* **1982**, *28* (6), 881–900. https://doi.org/10.1002/aic.690280602.

(14) Gibson, J. B.; Harrison, D. P. The Reaction between Hydrogen Sulfide and Spherical Pellets of Zinc Oxide. *Ind. Eng. Chem. Process Des. Dev.* **1980**, *19* (2), 231–237. https://doi.org/10.1021/i260074a005.

(15) Parandin, M. S.; Rashidi, H. Deep Desulfurization of Natural Gas by a Commercial ZnO Adsorbent: A Mathematical Study for Fixed-Bed Reactors. *J. Nat. Gas Sci. Eng.* **2018**, *59* (January), 116–123. https://doi.org/10.1016/j.jngse.2018.08.030.

(16) Azzam, S.; Simonetti, D. A. Linear Driving Force Approximations as Predictive Models for Reactive Sorption. *Energy Technol.* **2019**, *1900718*, 1–9. https://doi.org/10.1002/ente.201900718.

(17) Huang, J.; Zhao, J.; Wei, X.; Wang, Y.; Bu, X. Kinetic Studies on the Sulfidation and Regeneration of Zinc Titanate Desulfurization Sorbent. *Powder Technol.* **2008**, *180* (1–2), 196–202. https://doi.org/10.1016/j.powtec.2007.07.033.

(18) Ramachandran, P. A.; Smith, J. M. A Single-pore Model for Gas-solid Noncatalytic Reactions. *AIChE J.* **1977**, *23* (3), 353–361. https://doi.org/10.1002/aic.690230320.

(19) Bhatia, S. K.; D., PerlmutterD. A Rondom Pore Model for Fluid-Solid Reactions: I. Isothermal , Kinetic Control. *AIChE J.* **1980**, *26* (3), 379–386.

(20) Bhatia, S. K.; D., Perlmutter D. A Random Pore Model for Fluid-Solid Reactions: II. Diffusion and Transport Effects. *AIChE J.* **1981**, *27* (2), 247–254.

(21) Sotirchos, S. V.; Zarkanitis, S. A Distributed Pore Size and Length Model for Porous Media Reacting with Diminishing Porosity. *Chem. Eng. Sci.* **1993**, *48* (8), 1487–1502. https://doi.org/10.1016/0009-2509(93)80054-T.

(22) Monazam, E. R.; Shadle, L. J.; Berry, D. A. Modeling and Analysis of S-Sorption with ZnO in a Transport Reactor. *Chem. Eng. Sci.* **2008**, *63* (10), 2614–2623. https://doi.org/10.1016/j.ces.2008.01.035.

(23) Hartman, M.; Coughlin, R. W. Reaction of Sulfur Dioxide with Limestone and the Grain Model. *AIChE J.* **1976**, *22* (3), 490–498. https://doi.org/10.1002/aic.690220312.

(24) Bhatia, S. K.; Perlmutter, D. D. The Effect of Pore Structure on Fluid-Solid Reactions: Application to the Lime Reaction. *AIChE J.* **1981**, *27* (2), 226–234. https://doi.org/10.1002/aic.690270209.

(25) Borgwardt, R. H. Kinetics of the Reaction of SO_2 with Calcined Limestone. *Environ. Sci. Technol.* **1970**, *4* (1), 59–63. https://doi.org/10.1021/es60036a001.

(26) Sohn, H. Y.; Szekely, J. A Structural Model for Gas-Solid Reactions with a Moving Boundary—III. *Chem. Eng. Sci.* **1972**, *27* (4), 763–778. https://doi.org/10.1016/0009-2509(72)85011-5.

(27) Ramachandran, P. A.; Doraiswamy, L. K. Modeling of Noncatalytic Gas-Solid Reactions. *AIChE J.* **1982**, *28* (6), 881–900. https://doi.org/10.1002/aic.690280602.

(28) Hoffman, A. S.; Azzam, S.; Zhang, K.; Xu, Y.; Liu, Y.; Bare, S. R.; Simonetti, D. A. Direct Observation of the Kinetics of Gas–Solid Reactions Using *in Situ* Kinetic and Spectroscopic Techniques. *React. Chem. Eng.* **2018**, *3* (5), 668–675. https://doi.org/10.1039/C8RE00020D.

(29) Bohart, G. S.; Adams, E. Q. Some Aspects of the Behavior of Charcoal with Respect to Chlorine. *J. Am. Chem. Soc.* **1920**, *42* (3), 523–544. https://doi.org/10.1021/ja01448a018.

(30) Cooper, R. S. Slow Particle Diffusion in Ion Exchange Columns. *Ind. Eng. Chem. Fundam.* **1965**, *4* (3), 308–313. https://doi.org/10.1021/i160015a012.

(31) Yoshida, H.; Kataoka, T.; Ruthven, D. M. Analytical Solution of the Breakthrough Curve for Rectangular Isotherm Systems. *Chem. Eng. Sci.* **1984**, *39* (10), 1489–1497. https://doi.org/10.1016/0009-2509(84)80007-X.

(32) Knox, J. C.; Ebner, A. D.; Levan, M. D.; Coker, R. F.; Ritter, J. A. Limitations of Breakthrough Curve Analysis in Fixed-Bed Adsorption. *Ind. Eng. Chem. Res.* **2016**, *55* (16), 4734–4748. https://doi.org/10.1021/acs.iecr.6b00516.

(33) Cheah, S.; Carpenter, D. L.; Magrini-Bair, K. A. Review of Mid- to High-Temperature Sulfur Sorbents for Desulfurization of Biomass- and Coal-Derived Syngas. *Energy Fuels* **2009**, *23* (11), 5291–5307. https://doi.org/10.1021/ef900714q.

(34) Shah, M. S.; Tsapatsis, M.; Siepmann, J. I. Hydrogen Sulfide Capture: From Absorption in Polar Liquids to Oxide, Zeolite, and Metal–Organic Framework Adsorbents and Membranes. *Chem. Rev.* **2017**, *117* (14), 9755–9803. https://doi.org/10.1021/acs.chemrev.7b00095.

(35) Vamvuka, D.; Arvanitidis, C.; Zachariadis, D. Flue Gas Desulfurization at High Temperatures: A Review. *Environ. Eng. Sci.* **2004**, *21* (4), 525–548. https://doi.org/10.1089/1092875041358557.

(36) Yasyerli, S.; Dogu, G.; Ar, I.; Dogu, T. Activities of Copper Oxide and Cu−V and Cu−Mo Mixed Oxides for H2S Removal in the Presence and Absence of Hydrogen and Predictions of a Deactivation Model. *Ind. Eng. Chem. Res.* **2001**, *40* (23), 5206–5214. https://doi.org/10.1021/ie0010621.

(37) Azzam, S. A.; Alshafei, F. H.; López-Ausens, T.; Ghosh, R.; Biswas, A. N.; Sautet, P.; Prikhodko, S.; Simonetti, D. A. Effects of Morphology and Surface Properties of Copper Oxide on the Removal of Hydrogen Sulfide from Gaseous Streams. *Ind. Eng. Chem. Res.* **2019**, *58* (40), 18836–18847. https://doi.org/10.1021/acs.iecr.9b03975.

(38) Rosso, I.; Galletti, C.; Bizzi, M.; Saracco, G.; Specchia, V. Zinc Oxide Sorbents for the Removal of Hydrogen Sulfide from Syngas. *Ind. Eng. Chem. Res.* **2003**, *42* (8), 1688–1697. https://doi.org/10.1021/ie0208467.

(39) Lew, S.; Jothimurugesan, K.; Flytzani-Stephanopoulos, M. High-Temperature Hydrogen Sulfide Removal from Fuel Gases by Regenerable Zinc Oxide-Titanium Dioxide

Sorbents. *Ind. Eng. Chem. Res.* **1989**, *28* (5), 535–541. https://doi.org/10.1021/ie00089a006.

(40) Chung, J. B.; Chung, J. S. Desulfurization of H2S Using Cobalt-Containing Sorbents at Low Temperatures. *Chem. Eng. Sci.* **2005**, *60* (6), 1515–1523. https://doi.org/10.1016/j.ces.2004.11.002.

(41) Flytzani-Stephanopoulos, M.; Sakbodin, M.; Wang, Z. Regenerative Adsorption and Removal of H_2S from Hot Fuel Gas Streams by Rare Earth Oxides. *Science* **2006**, *312* (5779), 1508. https://doi.org/10.1126/science.1125684.

(42) Wang, Z.; Flytzani-Stephanopoulos, M. Cerium Oxide-Based Sorbents for Regenerative Hot Reformate Gas Desulfurization. *Energy Fuels* **2005**, *19* (5), 2089–2097. https://doi.org/10.1021/ef049664a.

(43) Guo, B.; Li, S.; Tian, Y. Performance of Cerium Oxides from Different Preparation Methods for Desulfurizing Hot Coal Gas. *ACS Omega* **2019**, *4* (5), 9301–9305. https://doi.org/10.1021/acsomega.9b00247.

(44) Wang, J.; Wang, L.; Fan, H.; Wang, H.; Hu, Y.; Wang, Z. Highly Porous Copper Oxide Sorbent for H2S Capture at Ambient Temperature. *Fuel* **2017**, *209*, 329–338. https://doi.org/10.1016/j.fuel.2017.08.003.

(45) Wang, X.; Sun, T.; Yang, J.; Zhao, L.; Jia, J. Low-Temperature H2S Removal from Gas Streams with SBA-15 Supported ZnO Nanoparticles. *Chem. Eng. J.* **2008**, *142* (1), 48–55. https://doi.org/10.1016/j.cej.2007.11.013.

(46) Dhage, P.; Samokhvalov, A.; Repala, D.; Duin, E. C.; Bowman, M.; Tatarchuk, B. J. Copper-Promoted ZnO/SiO_2 Regenerable Sorbents for the Room Temperature Removal of H2S from Reformate Gas Streams. *Ind. Eng. Chem. Res.* **2010**, *49* (18), 8388–8396. https://doi.org/10.1021/ie100209a.

(47) Li, F.; Yang, G. H.; Lei, T.; Yang, S. Y.; Wang, Y. H.; Wang, Y.; Jia, L. P. Preparation of Nano-Copper Oxide and Removal of Hydrogen Sulfide under Room Temperature. *Appl. Mech. Mater.* **2014**, *448–453*, 583–588. https://doi.org/10.4028/www.scientific.net/AMM.448-453.583.

(48) Patrick, V.; Gavalas, G. R.; Flytzani-Stephanopoulos, M.; Jothimurugesan, K. High-Temperature Sulfidation-Regeneration of Copper(II) Oxide-Alumina Sorbents. *Ind. Eng. Chem. Res.* **1989**, *28* (7), 931–940. https://doi.org/10.1021/ie00091a008.

(49) Christoforou, S. C.; Efthimiadis, E. A.; Vasalos, I. A. Sulfidation of Mixed Metal Oxides in a Fluidized-Bed Reactor. *Ind. Eng. Chem. Res.* **1995**, *34* (1), 83–93. https://doi.org/10.1021/ie00040a006.

(50) Slimane, R. B.; Abbasian, J. Regenerable Mixed Metal Oxide Sorbents for Coal Gas Desulfurization at Moderate Temperatures. *Adv. Environ. Res.* **2000**, *4* (2), 147–162. https://doi.org/10.1016/S1093-0191(00)00017-4.

(51) Valsamakis, I.; Si, R.; Flytzani-Stephanopoulos, M. Stability of Lanthanum Oxide-Based H2S Sorbents in Realistic Fuel Processor/Fuel Cell Operation. *J. Power Sources* **2010**, *195* (9), 2815–2822. https://doi.org/10.1016/j.jpowsour.2009.11.047.

(52) Huang, G.; He, E.; Wang, Z.; Fan, H.; Shangguan, J.; Croiset, E.; Chen, Z. Synthesis and Characterization of γ-Fe2O3 for H2S Removal at Low Temperature. *Ind. Eng. Chem. Res.* **2015**, *54* (34), 8469–8478. https://doi.org/10.1021/acs.iecr.5b01398.

(53) Förster, H.; Schuldt, M. Infrared Spectroscopic Study of the Adsorption of Hydrogen Sulfide on Zeolites NaA and NaCaA. *J. Colloid Interface Sci.* **1975**, *52* (2), 380–385. https://doi.org/10.1016/0021-9797(75)90213-1.

(54) Karge, H. G.; Raskó, J. Hydrogen Sulfide Adsorption on Faujasite-Type Zeolites with Systematically Varied Si-Al Ratios. *J. Colloid Interface Sci.* **1978**, *64* (3), 522–532. https://doi.org/10.1016/0021-9797(78)90394-6.

(55) Karge, H. G.; Ziółek, M.; Łaniecki, M. U.v./Vis and i.r. Spectroscopic Study of Hydrogen Sulphide Adsorption on Faujasite-Type Zeolites. *Zeolites* **1987**, *7* (3), 197–202. https://doi.org/10.1016/0144-2449(87)90050-9.

(56) Howard, J.; Kadir, Z. A. The Adsorption of H2S on Some Transition Metal Exchanged Zeolites: An Infrared Study. *Spectrochim. Acta Part Mol. Spectrosc.* **1985**, *41* (6), 825–831. https://doi.org/10.1016/0584-8539(85)80028-3.

(57) Garcia, C. L.; Lercher, J. A. Adsorption of Hydrogen Sulfide on ZSM 5 Zeolites. *J. Phys. Chem.* **1992**, *96* (5), 2230–2235. https://doi.org/10.1021/j100184a038.

(58) Crespo, D.; Qi, G.; Wang, Y.; Yang, F. H.; Yang, R. T. Superior Sorbent for Natural Gas Desulfurization. *Ind. Eng. Chem. Res.* **2008**, *47* (4), 1238–1244. https://doi.org/10.1021/ie071145i.

(59) Hutson, N. D.; Reisner, B. A.; Yang, R. T.; Toby, B. H. Silver Ion-Exchanged Zeolites Y, X, and Low-Silica X: Observations of Thermally Induced Cation/Cluster Migration and the Resulting Effects on the Equilibrium Adsorption of Nitrogen. *Chem. Mater.* **2000**, *12* (10), 3020–3031. https://doi.org/10.1021/cm000294n.

(60) Kumar, P.; Sung, C.-Y.; Muraza, O.; Cococcioni, M.; Al Hashimi, S.; McCormick, A.; Tsapatsis, M. H2S Adsorption by Ag and Cu Ion Exchanged Faujasites. *Spec. Issue - Corma60* **2011**, *146* (1), 127–133. https://doi.org/10.1016/j.micromeso.2011.05.014.

(61) Liu, T.; First, E. L.; Faruque Hasan, M. M.; Floudas, C. A. A Multi-Scale Approach for the Discovery of Zeolites for Hydrogen Sulfide Removal. *12th Int. Symp. Process Syst. Eng. 25th Eur. Symp. Comput. Aided Process Eng. PSE-2015ESCAPE-25 31 May - 4 June 2015 Cph. Den.* **2016**, *91*, 206–218. https://doi.org/10.1016/j.compchemeng.2016.03.015.

(62) Maghsoudi, H.; Soltanieh, M.; Bozorgzadeh, H.; Mohamadalizadeh, A. Adsorption Isotherms and Ideal Selectivities of Hydrogen Sulfide and Carbon Dioxide over Methane for the Si-CHA Zeolite: Comparison of Carbon Dioxide and Methane Adsorption with

the All-Silica DD3R Zeolite. *Adsorption* **2013**, *19* (5), 1045–1053. https://doi.org/10.1007/s10450-013-9528-1.

(63) Hamon, L.; Serre, C.; Devic, T.; Loiseau, T.; Millange, F.; Férey, G.; Weireld, G. D. Comparative Study of Hydrogen Sulfide Adsorption in the MIL-53(Al, Cr, Fe), MIL-47(V), MIL-100(Cr), and MIL-101(Cr) Metal−Organic Frameworks at Room Temperature. *J. Am. Chem. Soc.* **2009**, *131* (25), 8775–8777. https://doi.org/10.1021/ja901587t.

(64) Vellingiri, K.; Deep, A.; Kim, K.-H. Metal–Organic Frameworks as a Potential Platform for Selective Treatment of Gaseous Sulfur Compounds. *ACS Appl. Mater. Interfaces* **2016**, *8* (44), 29835–29857. https://doi.org/10.1021/acsami.6b10482.

(65) DeCoste, J. B.; Peterson, G. W. Metal–Organic Frameworks for Air Purification of Toxic Chemicals. *Chem. Rev.* **2014**, *114* (11), 5695–5727. https://doi.org/10.1021/cr4006473.

(66) Peralta, D.; Chaplais, G.; Simon-Masseron, A.; Barthelet, K.; Pirngruber, G. D. Metal–Organic Framework Materials for Desulfurization by Adsorption. *Energy Fuels* **2012**, *26* (8), 4953–4960. https://doi.org/10.1021/ef300762z.

(67) Vaesen, S.; Guillerm, V.; Yang, Q.; Wiersum, A. D.; Marszalek, B.; Gil, B.; Vimont, A.; Daturi, M.; Devic, T.; Llewellyn, P. L.; Serre, C.; Maurin, G.; De Weireld, G. A Robust Amino-Functionalized Titanium(Iv) Based MOF for Improved Separation of Acid Gases. *Chem. Commun.* **2013**, *49* (86), 10082–10084. https://doi.org/10.1039/C3CC45828H.

(68) Yang, Q.; Vaesen, S.; Vishnuvarthan, M.; Ragon, F.; Serre, C.; Vimont, A.; Daturi, M.; De Weireld, G.; Maurin, G. Probing the Adsorption Performance of the Hybrid Porous MIL-68(Al): A Synergic Combination of Experimental and Modelling Tools. *J. Mater. Chem.* **2012**, *22* (20), 10210–10220. https://doi.org/10.1039/C2JM15609A.

(69) Petit, C.; Mendoza, B.; Bandosz, T. J. Hydrogen Sulfide Adsorption on MOFs and MOF/Graphite Oxide Composites. *Chem. Phys. Chem* **2010**, *11* (17), 3678–3684. https://doi.org/10.1002/cphc.201000689.

(70) Allan, P. K.; Wheatley, P. S.; Aldous, D.; Mohideen, M. I.; Tang, C.; Hriljac, J. A.; Megson, I. L.; Chapman, K. W.; De Weireld, G.; Vaesen, S.; Morris, R. E. Metal–Organic Frameworks for the Storage and Delivery of Biologically Active Hydrogen Sulfide. *Dalton Trans.* **2012**, *41* (14), 4060–4066. https://doi.org/10.1039/C2DT12069K.

(71) Adib, F.; Bagreev, A.; Bandosz, T. J. Effect of Surface Characteristics of Wood-Based Activated Carbons on Adsorption of Hydrogen Sulfide. *J. Colloid Interface Sci.* **1999**, *214* (2), 407–415. https://doi.org/10.1006/jcis.1999.6200.

(72) Bagreev, A.; Adib, F.; Bandosz, T. J. Initial Heats of H_2S Adsorption on Activated Carbons: Effect of Surface Features. *J. Colloid Interface Sci.* **1999**, *219* (2), 327–332. https://doi.org/10.1006/jcis.1999.6485.

(73) Bandosz, T. J. Effect of Pore Structure and Surface Chemistry of Virgin Activated Carbons on Removal of Hydrogen Sulfide. *Carbon* **1999**, *37* (3), 483–491. https://doi.org/10.1016/S0008-6223(98)00217-6.

(74) Adib, F.; Bagreev, A.; Bandosz, T. J. Adsorption/Oxidation of Hydrogen Sulfide on Nitrogen-Containing Activated Carbons. *Langmuir* **2000**, *16* (4), 1980–1986. https://doi.org/10.1021/la990926o.

(75) Adib, F.; Bagreev, A.; Bandosz, T. J. Analysis of the Relationship between H2S Removal Capacity and Surface Properties of Unimpregnated Activated Carbons. *Environ. Sci. Technol.* **2000**, *34* (4), 686–692. https://doi.org/10.1021/es990341g.

(76) Bandosz, T. J. On the Adsorption/Oxidation of Hydrogen Sulfide on Activated Carbons at Ambient Temperatures. *J. Colloid Interface Sci.* **2002**, *246* (1), 1–20. https://doi.org/10.1006/jcis.2001.7952.

(77) Hussain, M.; Abbas, N.; Fino, D.; Russo, N. Novel Mesoporous Silica Supported ZnO Adsorbents for the Desulphurization of Biogas at Low Temperatures. *Chem. Eng. J.* **2012**, *188*, 222–232. https://doi.org/10.1016/j.cej.2012.02.034.

(78) Elyassi, B.; Wahedi, Y. A.; Rajabbeigi, N.; Kumar, P.; Jeong, J. S.; Zhang, X.; Kumar, P.; Balasubramanian, V. V.; Katsiotis, M. S.; Andre Mkhoyan, K.; Boukos, N.; Hashimi, S. A.; Tsapatsis, M. A High-Performance Adsorbent for Hydrogen Sulfide Removal. *Microporous Mesoporous Mater.* **2014**, *190*, 152–155. https://doi.org/10.1016/j.micromeso.2014.02.007.

(79) Bhandari, D. A.; Bessho, N.; Koros, W. J. Hollow Fiber Sorbents for Desulfurization of Natural Gas. *Ind. Eng. Chem. Res.* **2010**, *49* (23), 12038–12050. https://doi.org/10.1021/ie100157w.

(80) Seredych, M.; Bandosz, T. J. Reactive Adsorption of Hydrogen Sulfide on Graphite Oxide/Zr(OH)4 Composites. *Chem. Eng. J.* **2011**, *166* (3), 1032–1038. https://doi.org/10.1016/j.cej.2010.11.096.

(81) Seredych, M.; Mabayoje, O.; Bandosz, T. J. Visible-Light-Enhanced Interactions of Hydrogen Sulfide with Composites of Zinc (Oxy)Hydroxide with Graphite Oxide and Graphene. *Langmuir* **2012**, *28* (2), 1337–1346. https://doi.org/10.1021/la204277c.

(82) Ozekmekci, M.; Salkic, G.; Fellah, M. F. Use of Zeolites for the Removal of H_2S: A Mini-Review. *Fuel Process. Technol.* **2015**, *139*, 49–60. https://doi.org/10.1016/j.fuproc.2015.08.015.

(83) Gibson, J. B.; Harrison, D. P. The Reaction between Hydrogen Sulfide and Spherical Pellets of Zinc Oxide. *Ind. Eng. Chem. Process Des. Dev.* **1980**, *19* (2), 231–237. https://doi.org/10.1021/i260074a005.

(84) Skrzypski, J.; Bezverkhyy, I.; Heintz, O.; Bellat, J.-P. Low Temperature H_2S Removal with Metal-Doped Nanostructure ZnO Sorbents: Study of the Origin of Enhanced Reactivity in Cu-Containing Materials. *Ind. Eng. Chem. Res.* **2011**, *50* (9), 5714–5722. https://doi.org/10.1021/ie200240e.

(85) Li, L.; Sun, T. H.; Shu, C. H.; Zhang, H. B. Low Temperature H_2S Removal with 3-D Structural Mesoporous Molecular Sieves Supported ZnO from Gas Stream. *J. Hazard. Mater.* **2016**, *311*, 142–150. https://doi.org/10.1016/j.jhazmat.2016.01.033.

(86) Yang, Y.; Shi, Y.; Cai, N. Steam Regenerative Removal of Hydrogen Sulfide from Hot Syngas by a Novel Tin Oxide and Yttrium Oxide Sorbent. *Energy* **2017**, *122*, 214–220. https://doi.org/10.1016/j.energy.2017.01.081.

(87) Li, L.; Zhou, P.; Zhang, H.; Meng, X.; Li, J.; Sun, T. Mid-Temperature Deep Removal of Hydrogen Sulfide on Rare Earth (RE=Ce, La, Sm, Gd) Doped ZnO Supported on KIT-6: Effect of RE Dopants and Interaction between Active Phase and Support Matrix. *Appl. Surf. Sci.* **2017**, *407*, 197–208. https://doi.org/10.1016/j.apsusc.2017.01.128.

(88) Wu, J.; Liu, D.; Zhou, W.; Liu, Q.; Huang, Y. Status of Coal Gas H2S Removal. In *High-Temperature H2S Removal from IGCC Coarse Gas*; Wu, J., Liu, D., Zhou, W., Liu, Q., Huang, Y., Eds.; Springer Singapore: Singapore, 2018; pp 21–54. https://doi.org/10.1007/978-981-10-6817-1_2.

(89) Yang, C.; Wang, J.; Fan, H.-L.; Shangguan, J.; Mi, J.; Huo, C. Contributions of Tailored Oxygen Vacancies in ZnO/Al_2O_3 Composites to the Enhanced Ability for H_2S Removal at Room Temperature. *Fuel* **2018**, *215*, 695–703. https://doi.org/10.1016/j.fuel.2017.11.037.

(90) Bezverkhyy, I.; Skrzypski, J.; Safonova, O.; Bellat, J.-P. Sulfidation Mechanism of Pure and Cu-Doped ZnO Nanoparticles at Moderate Temperature: TEM and In Situ XRD Studies. *J. Phys. Chem. C* **2012**, *116* (27), 14423–14430. https://doi.org/10.1021/jp303181d.

(91) Baird, T.; C. Campbell, K.; J. Holliman, P.; W. Hoyle, R.; Huxam, M.; Stirling, D.; Peter Williams, B.; Morris, M. Cobalt-Zinc Oxide Absorbents for Low Temperature Gas Desulfurisation. *J. Mater. Chem.* **1999**, *9* (2), 599–605. https://doi.org/10.1039/A806909C.

(92) Carnes, C. L.; Klabunde, K. J. Unique Chemical Reactivities of Nanocrystalline Metal Oxides toward Hydrogen Sulfide. *Chem. Mater.* **2002**, *14* (4), 1806–1811. https://doi.org/10.1021/cm011588r.

(93) Habibi, R.; Rashidi, A. M.; Daryan, J. T.; zadeh, A. M. ali. Study of the Rod-Like and Spherical Nano-ZnO Morphology on H_2S Removal from Natural Gas. *Appl. Surf. Sci.* **2010**, *257* (2), 434–439. https://doi.org/10.1016/j.apsusc.2010.07.007.

(94) Garces, H. F.; Galindo, H. M.; Garces, L. J.; Hunt, J.; Morey, A.; Suib, S. L. Low Temperature H2S Dry-Desulfurization with Zinc Oxide. *Microporous Mesoporous Mater.* **2010**, *127* (3), 190–197. https://doi.org/10.1016/j.micromeso.2009.07.022.

(95) Garces, H. F.; Espinal, A. E.; Suib, S. L. Tunable Shape Microwave Synthesis of Zinc Oxide Nanospheres and Their Desulfurization Performance Compared with Nanorods and Platelet-Like Morphologies for the Removal of Hydrogen Sulfide. *J. Phys. Chem. C* **2012**, *116* (15), 8465–8474. https://doi.org/10.1021/jp210755t.

(96) Baird, T.; Denny, P. J.; Hoyle, R.; McMonagle, F.; Stirling, D.; Tweedy, J. Modified Zinc Oxide Absorbents for Low-Temperature Gas Desulfurisation. *J. Chem. Soc. Faraday Trans.* **1992**, *88* (22), 3375–3382. https://doi.org/10.1039/FT9928803375.

(97) Jiang, D.; Su, L.; Ma, L.; Yao, N.; Xu, X.; Tang, H.; Li, X. Cu–Zn–Al Mixed Metal Oxides Derived from Hydroxycarbonate Precursors for H2S Removal at Low Temperature. *Appl. Surf. Sci.* **2010**, *256* (10), 3216–3223. https://doi.org/10.1016/j.apsusc.2009.12.008.

(98) Twigg, M. V. *Catalyst Handbook*; Routledge, 2018.

(99) Davidson, J. M.; Lawrie, C. H.; Sohail, K. Kinetics of the Absorption of Hydrogen Sulfide by High Purity and Doped High Surface Area Zinc Oxide. *Ind. Eng. Chem. Res.* **1995**, *34* (9), 2981–2989.

(100) Novochinskii, I. I.; Song, C.; Ma, X.; Liu, X.; Shore, L.; Lampert, J.; Farrauto, R. J. Low-Temperature H2S Removal from Steam-Containing Gas Mixtures with ZnO for Fuel Cell Application. 1. ZnO Particles and Extrudates. *Energy Fuels* **2004**, *18* (2), 576–583.

(101) Tu, K. N.; Gösele, U. Hollow Nanostructures Based on the Kirkendall Effect: Design and Stability Considerations. *Appl. Phys. Lett.* **2005**, *86* (9), 093111.

(102) Kroger, F. A. The Chemistry of Imperfect Crystals. *Amst. Neth.* **1974**, *2*.

(103) Skrzypski, J.; Bezverkhyy, I.; Heintz, O.; Bellat, J.-P. Low Temperature H2S Removal with Metal-Doped Nanostructure ZnO Sorbents: Study of the Origin of Enhanced Reactivity in Cu-Containing Materials. *Ind. Eng. Chem. Res.* **2011**, *50* (9), 5714–5722.

(104) Hernández-Maldonado, A. J.; Yang, F. H.; Qi, G.; Yang, R. T. Desulfurization of Transportation Fuels by π-Complexation Sorbents: Cu (I)-, Ni (II)-, and Zn (II)-Zeolites. *Appl. Catal. B Environ.* **2005**, *56* (1–2), 111–126.

(105) Kohn, W.; Sham, L. J. Self-Consistent Equations Including Exchange and Correlation Effects. *Phys. Rev.* **1965**, *140* (4A), A1133–A1138. https://doi.org/10.1103/PhysRev.140.A1133.

(106) Keller, J. On the Formulation of the Hohenberg–Kohn–Sham Theory. *Int. J. Quantum Chem.* **1986**, *30* (S20), 767–768.

(107) Grönbeck, H. First Principles Studies of Metal-Oxide Surfaces. *Top. Catal.* **2004**, *28* (1–4), 59–69.

(108) Jia, M.-Y.; Xu, B.; Ding, X.-L.; He, S.-G.; Ge, M.-F. Experimental and Theoretical Study of the Reactions between Manganese Oxide Cluster Anions and Hydrogen Sulfide. *J. Phys. Chem. C* **2012**, *116* (45), 24184–24192.

(109) Dhage, P.; Samokhvalov, A.; McKee, M. L.; Duin, E. C.; Tatarchuk, B. J. Reactive Adsorption of Hydrogen Sulfide by Promoted Sorbents Cu-ZnO/SiO_2: Active Sites by Experiment and Simulation. *Surf. Interface Anal.* **2013**, *45* (5), 865–872.

(110) Polychronopoulou, K.; Galisteo, F. C.; Granados, M. L.; Fierro, J. L. G.; Bakas, T.; Efstathiou, A. M. Novel Fe–Mn–Zn–Ti–O Mixed-Metal Oxides for the Low-Temperature Removal of H2S from Gas Streams in the Presence of H2, CO2, and H2O. *J. Catal.* **2005**, *236* (2), 205–220.

(111) Casarin, M.; Maccato, C.; Tondello, E.; Vittadini, A. A Theoretical Investigation of Brønsted Acids Chemisorption on ZnO (0001). *Surf. Sci.* **1995**, *343* (1–2), 115–132.

(112) Jackson, K.; Pederson, M. R. Accurate Forces in a Local-Orbital Approach to the Local-Density Approximation. *Phys. Rev. B* **1990**, *42* (6), 3276.

(113) Rodriguez, J. A.; Maiti, A. Adsorption and Decomposition of H2S on MgO (100), NiMgO (100), and ZnO (0001) Surfaces: A First-Principles Density Functional Study. *J. Phys. Chem. B* **2000**, *104* (15), 3630–3638.

(114) Becke, A. D. Density-functional Thermochemistry. II. The Effect of the Perdew–Wang Generalized-gradient Correlation Correction. *J. Chem. Phys.* **1992**, *97* (12), 9173–9177.

(115) Martin, R. M.; Martin, R. M. *Electronic Structure: Basic Theory and Practical Methods*; Cambridge university press, 2004.

(116) Casarin, M.; Maccato, C.; Vittadini, A. An LCAO-LDF Study of the Chemisorption of H_2O and H_2S on ZnO (0001) and ZnO ($10\bar{1}0$). *Surf. Sci.* **1997**, *377*, 587–591.

(117) Pandiyan, R. Growth by Radio Frequency Sputtering and Characterisation of Rare Earth Doped Wide Bandgap Oxides, University of Trento, 2013.

(118) Ling, L.; Zhang, R.; Han, P.; Wang, B. DFT Study on the Sulfurization Mechanism during the Desulfurization of H2S on the ZnO Desulfurizer. *Fuel Process. Technol.* **2013**, *106*, 222–230.

(119) Burke, K.; Perdew, J. P.; Wang, Y. Derivation of a Generalized Gradient Approximation: The PW91 Density Functional. In *Electronic density functional theory*; Springer, 1998; pp 81–111.

(120) Perdew, J. P.; Burke, K.; Ernzerhof, M. Generalized Gradient Approximation Made Simple. *Phys. Rev. Lett.* **1996**, *77* (18), 3865.

(121) Vanderbilt, D. Soft Self-Consistent Pseudopotentials in a Generalized Eigenvalue Formalism. *Phys. Rev. B* **1990**, *41* (11), 7892–7895. https://doi.org/10.1103/PhysRevB.41.7892.

(122) Anisimov, V. I.; Zaanen, J.; Andersen, O. K. Band Theory and Mott Insulators: Hubbard U Instead of Stoner I. *Phys. Rev. B* **1991**, *44* (3), 943–954. https://doi.org/10.1103/PhysRevB.44.943.

(123) Liechtenstein, A. I.; Anisimov, V. I.; Zaanen, J. Density-Functional Theory and Strong Interactions: Orbital Ordering in Mott-Hubbard Insulators. *Phys. Rev. B* **1995**, *52* (8), R5467.

(124) Cramer, C. J. *Essentials of Computational Chemistry: Theories and Models*; John Wiley & Sons, 2013.

(125) Koch, W.; Holthausen, M. C. *A Chemist's Guide to Density Functional Theory*; John Wiley & Sons, 2015.

(126) Kazemi, M.; Rad, A. S. Sulfur Mustard Gas Adsorption on ZnO Fullerene-like Nanocage: Quantum Chemical Calculations. *Superlattices Microstruct.* **2017**, *106*, 122–128.

(127) Tong, X.; Lv, J.; Zheng, Y.; Huang, L. DFT Study on the Interaction between S_2 and Zincite ($10\bar{1}$ 0) Surface. *J. Taiwan Inst. Chem. Eng.* **2018**, *88*, 18–24.

(128) Hao, S.; Rankin, R. B.; Johnson, J. K.; Sholl, D. S. Surface Reactions of AsH3, H2Se, and H2S on the Zn2TiO4(010) Surface. *Surf. Sci.* **2011**, *605* (7), 818–823. https://doi.org/10.1016/j.susc.2011.01.025.

(129) Tamhankar, S. S.; Bagajewicz, M.; Gavalas, G. R.; Sharma, P. K.; Flytzani-Stephanopoulos, M. Mixed-Oxide Sorbents for High-Temperature Removal of Hydrogen Sulfide. *Ind. Eng. Chem. Process Des. Dev.* **1986**, *25* (2), 429–437. https://doi.org/10.1021/i200033a014.

(130) Laperdrix, E.; Costentin, G.; Saur, O.; Lavalley, J. C.; Nedez, C.; Savin-Poncet, S.; Nougayrede, J. Selective Oxidation of H2S over CuO/Al2O3: Identification and Role of the Sulfurated Species Formed on the Catalyst during the Reaction. *J. Catal.* **2000**, *189* (1), 63–69.

(131) Park, S.; Park, S.; Jung, J.; Hong, T.; Lee, S.; Kim, H. W.; Lee, C. H_2S Gas Sensing Properties of CuO-Functionalized WO3 Nanowires. *Ceram. Int.* **2014**, *40* (7), 11051–11056.

(132) Westmoreland, P. R.; Harrison, D. P. Evaluation of Candidate Solids for High-Temperature Desulfurization of Low-Btu Gases. *Environ. Sci. Technol.* **1976**, *10* (7), 659–661.

(133) Kyotani, T.; Kawashima, H.; Tomita, A. High-Temperature Desulfurization with Copper-Containing Sorbents. *Environ. Sci. Technol.* **1989**, *23* (2), 218–223. https://doi.org/10.1021/es00179a014.

(134) Hu, J.; Li, D.; Lu, J. G.; Wu, R. Effects on Electronic Properties of Molecule Adsorption on CuO Surfaces and Nanowires. *J. Phys. Chem. C* **2010**, *114* (40), 17120–17126.

(135) Sun, S.; Zhang, D.; Li, C.; Wang, Y. DFT Study on the Adsorption and Dissociation of H 2 S on CuO (111) Surface. *RSC Adv.* **2015**, *5* (28), 21806–21811.

(136) Zhang, J.; Liu, M.; Zhang, R.; Wang, B.; Huang, Z. Insight into the Properties of Stoichiometric, Reduced and Sulfurized CuO Surfaces: Structure Sensitivity for H2S Adsorption and Dissociation. *Mol. Catal.* **2017**, *438*, 130–142.

(137) Wöll, C. The Chemistry and Physics of Zinc Oxide Surfaces. *Prog. Surf. Sci.* **2007**, *82* (2–3), 55–120.

(138) Cohen, A. J.; Mori-Sánchez, P.; Yang, W. Challenges for Density Functional Theory. *Chem. Rev.* **2011**, *112* (1), 289–320.

(139) Dudarev, S. L.; Botton, G. A.; Savrasov, S. Y.; Humphreys, C. J.; Sutton, A. P. Electron-Energy-Loss Spectra and the Structural Stability of Nickel Oxide: An LSDA+ U Study. *Phys. Rev. B* **1998**, *57* (3), 1505.

(140) Maimaiti, Y.; Nolan, M.; Elliott, S. D. Reduction Mechanisms of the CuO (111) Surface through Surface Oxygen Vacancy Formation and Hydrogen Adsorption. *Phys. Chem. Chem. Phys.* **2014**, *16* (7), 3036–3046.

(141) Mishra, A. K.; Roldan, A.; de Leeuw, N. H. CuO Surfaces and CO2 Activation: A Dispersion-Corrected DFT+U Study. *J. Phys. Chem. C* **2016**, *120* (4), 2198–2214. https://doi.org/10.1021/acs.jpcc.5b10431.

(142) Fronzi, M.; Nolan, M. First-Principles Analysis of the Stability of Water on Oxidised and Reduced CuO (111) Surfaces. *RSC Adv.* **2017**, *7* (89), 56721–56731.

(143) Neveux, L.; Chiche, D.; Bazer-Bachi, D.; Favergeon, L.; Pijolat, M. New Insight on the ZnO Sulfidation Reaction: Evidences for an Outward Growth Process of the ZnS Phase. *Chem. Eng. J.* **2012**, *181–182*, 508–515. https://doi.org/10.1016/j.cej.2011.09.019.

(144) Schulz, K. H.; Cox, D. F. Photoemission and Low-Energy-Electron-Diffraction Study of Clean and Oxygen-Dosed Cu_2O (111) and (100) Surfaces. *Phys. Rev. B* **1991**, *43* (2), 1610.

(145) Zhang, R.; Liu, H.; Li, J.; Ling, L.; Wang, B. A Mechanistic Study of H_2S Adsorption and Dissociation on Cu_2O (1 1 1) Surfaces: Thermochemistry, Reaction Barrier. *Appl. Surf. Sci.* **2012**, *258* (24), 9932–9943.

(146) Becke, A. D. A Multicenter Numerical Integration Scheme for Polyatomic Molecules. *J. Chem. Phys.* **1988**, *88* (4), 2547–2553.

(147) Lin, J.; May, J. A.; Didziulis, S. V.; Solomon, E. I. Variable-Energy Photoelectron Spectroscopic Studies of Hydrogen Sulfide Chemisorption on Cuprous Oxide and Zinc Oxide Single-Crystal Surfaces: HS-Bonding to Copper (I) and Zinc (II) Sites Related to Catalytic Poisoning. *J. Am. Chem. Soc.* **1992**, *114* (12), 4718–4727.

(148) Stenlid, J. H.; Johansson, A. J.; Leygraf, C.; Brinck, T. Computational Analysis of the Early Stage of Cuprous Oxide Sulphidation: A Top-down Process. *Corros. Eng. Sci. Technol.* **2017**, *52* (sup1), 50–53.

(149) Chen, H.-T.; Choi, Y.; Liu, M.; Lin, M. C. A First-Principles Analysis for Sulfur Tolerance of CeO_2 in Solid Oxide Fuel Cells. *J. Phys. Chem. C* **2007**, *111* (29), 11117–11122.

(150) Marrocchelli, D.; Yildiz, B. First-Principles Assessment of H_2S and H_2O Reaction Mechanisms and the Subsequent Hydrogen Absorption on the CeO_2 (111) Surface. *J. Phys. Chem. C* **2012**, *116* (3), 2411–2424. https://doi.org/10.1021/jp205573v.

(151) Mayernick, A. D.; Li, R.; Dooley, K. M.; Janik, M. J. Energetics and Mechanism for H_2S Adsorption by Ceria-Lanthanide Mixed Oxides: Implications for the Desulfurization of Biomass Gasifier Effluents. *J. Phys. Chem. C* **2011**, *115* (49), 24178–24188.

(152) Kullgren, J.; Lu, Z.; Yang, Z.; Hermansson, K. Sulfidation and Sulfur Recovery from SO2 over Ceria. *J. Phys. Chem. C* **2014**, *118* (31), 17499–17504.

(153) Bagheri, Z.; Moradi, M. DFT Study on the Adsorption and Dissociation of Hydrogen Sulfide on MgO Nanotube. *Struct. Chem.* **2014**, *25* (2), 495–501.

(154) Rodriguez, J. A.; Jirsak, T.; Pérez, M.; Chaturvedi, S.; Kuhn, M.; González, L.; Maiti, A. Studies on the Behavior of Mixed-Metal Oxides and Desulfurization: Reaction of H_2S and SO_2 with Cr_2O_3 (0001), MgO (100), and $Cr_xMg_{1-x}O$ (100). *J. Am. Chem. Soc.* **2000**, *122* (49), 12362–12370.

(155) Schneider, W. F.; Li, J.; Hass, K. C. Combined Computational and Experimental Investigation of SO x Adsorption on MgO. *J. Phys. Chem. B* **2001**, *105* (29), 6972–6979.

(156) Xu, Y.-J.; Li, J.-Q.; Zhang, Y.-F. S Adsorption at Regular and Defect Sites of the MgO (001) Surface: Cluster Model Study at DFT Level. *Surf. Rev. Lett.* **2003**, *10* (04), 691–695.

(157) Sasmaz, E.; Wilcox, J. Mercury Species and SO_2 Adsorption on CaO (100). *J. Phys. Chem. C* **2008**, *112* (42), 16484–16490. https://doi.org/10.1021/jp801250h.

(158) Wang, W.; Fan, L.; Wang, G.; Li, Y. CO_2 and SO_2 Sorption on the Alkali Metals Doped CaO(100)Surface: A DFT-D Study. *Appl. Surf. Sci.* **2017**, *425*, 972–977. https://doi.org/10.1016/j.apsusc.2017.07.158.

(159) Ionescu, A.; Allouche, A.; Aycard, J.-P.; Rajzmann, M.; Hutschka, F. Study of γ-Alumina Surface Reactivity: Adsorption of Water and Hydrogen Sulfide on Octahedral Aluminum Sites. *J. Phys. Chem. B* **2002**, *106* (36), 9359–9366.

(160) Peri, J. B. A Model for the Surface of γ-Alumina1. *J. Phys. Chem.* **1965**, *69* (1), 220–230.

(161) Knözinger, H.; Ratnasamy, P. Catalytic Aluminas: Surface Models and Characterization of Surface Sites. *Catal. Rev.* **1978**, *17* (1), 31–70. https://doi.org/10.1080/03602457808080878.

(162) Tsyganenko, A. A.; Mardilovich, P. P. Structure of Alumina Surfaces. *J. Chem. Soc. Faraday Trans.* **1996**, *92* (23), 4843–4852.

(163) Arrouvel, C.; Toulhoat, H.; Breysse, M.; Raybaud, P. Effects of PH_2O, PH_2S, PH_2 on the Surface Properties of Anatase–TiO2 and γ-Al2O3: A DFT Study. *J. Catal.* **2004**, *226* (2), 260–272.

(164) Rodriguez, J. A.; Chaturvedi, S.; Kuhn, M.; Hrbek, J. Reaction of H_2S and S_2 with Metal/Oxide Surfaces: Band-Gap Size and Chemical Reactivity. *J. Phys. Chem. B* **1998**, *102* (28), 5511–5519.

(165) Nigussa, K. N.; Borck, Ø.; Støvneng, J. A. Adsorption of H_2S on α-Cr_2O_3 (0001) Surfaces: A Density Functional Theory Investigation. *Corros. Sci.* **2016**, *111*, 1–12.

(166) Abbasi, A.; Sardroodi, J. J. Adsorption and Dissociation of H_2S on Nitrogen-Doped TiO_2 Anatase Nanoparticles: Insights from DFT Computations. *Surf. Interfaces* **2017**, *8*, 15–27.

(167) Guo, J.; Janik, M. J.; Song, C. Density Functional Theory Study on the Role of Ceria Addition in $Ti_xCe_{1-x}O_2$ Adsorbents for Thiophene Adsorption. *J. Phys. Chem. C* **2012**, *116* (5), 3457–3466.

(168) Song, J.; Niu, X.; Ling, L.; Wang, B. A Density Functional Theory Study on the Interaction Mechanism between H_2S and the α-Fe_2O_3 (0001) Surface. *Fuel Process. Technol.* **2013**, *115*, 26–33.

(169) Lin, C.; Qin, W.; Dong, C. H_2S Adsorption and Decomposition on the Gradually Reduced α-Fe_2O_3 (001) Surface: A DFT Study. *Appl. Surf. Sci.* **2016**, *387*, 720–731.

(170) Wang, B.; Nisar, J.; Ahuja, R. Molecular Simulation for Gas Adsorption at NiO (100) Surface. *ACS Appl. Mater. Interfaces* **2012**, *4* (10), 5691–5697.

(171) Favergeon, L.; Morandini, J.; Pijolat, M.; Soustelle, M. A General Approach for Kinetic Modeling of Solid-Gas Reactions at Reactor Scale: Application to Kaolinite Dehydroxylation. *Oil Gas Sci. Technol. – Rev. D'IFP Energ. Nouv.* **2013**, *68* (6), 1039–1048. https://doi.org/10.2516/ogst/2012018.

(172) Sadegh-Vaziri, R.; Babler, M. U. Numerical Investigation of the Outward Growth of ZnS in the Removal of H_2S in a Packed Bed of ZnO. *Chem. Eng. Sci.* **2017**, *158*, 328–339. https://doi.org/10.1016/j.ces.2016.10.038.

(173) Chrostowski, J. W.; Georgakis, C. Pore Plugging Model for Gas-Solid Reactions. In *Chemical Reaction Engineering*; Weekman, V. W., Luss, D., Eds.; American Chemical Society: Washington, D. C., 1978; Vol. 65, pp 225–237. https://doi.org/10.1021/bk-1978-0065.ch019.

(174) Bhatia, S. K.; Perlmutter, D. D. A random pore model for fluid-solid reactions: I. Isothermal, kinetic control. *AIChE J.* **1980**, *26* (3), 379–386. https://doi.org/10.1002/aic.690260308.

(175) Berg, K. L.; Olsen, S. E. Kinetics of Manganese Ore Reduction by Carbon Monoxide. *Metall. Mater. Trans. B* **2000**, *31* (3), 477–490. https://doi.org/10.1007/s11663-000-0154-4.

(176) Bhatia, S. K.; Vartak, B. J. Reaction of Microporous Solids: The Discrete Random Pore Model. *Carbon* **1996**, *34* (11), 1383–1391. https://doi.org/10.1016/S0008-6223(96)00080-2.

(177) Wen, C. Y. Noncatalytic Heterogenous Solid-Fluid Reaction Models. *Ind. Eng. Chem.* **1968**, *60* (9), 34–54. https://doi.org/10.1021/ie50705a007.

(178) Dziembaj, R.; Malczyk, J.; Baranski, A. Oxygen Corrosion of Calcined Cokes: II. Nonlinear Nucleation Model of This Oxygen Corrosion. *Carbon* **1991**, *29* (3), 329–334. https://doi.org/10.1016/0008-6223(91)90201-S.

(179) Evangelos A, E.; Stratis V, S. A Partially Overlapping Grain Model for Gas—Solid Reactions. *Chem. Eng. Sci.* **1993**, *48* (7), 1201–1212. https://doi.org/10.1016/0009-2509(93)81002-D.

(180) Garza-Garza, O.; Duduković, M. P. A Variable Size Grain Model for Gas-Solid Reactions with Structural Changes. *Chem. Eng. J.* **1982**, *24* (1), 35–45. https://doi.org/10.1016/0300-9467(82)80048-8.

(181) V. Sotirchos, S. On a Class of Random Pore and Grain Models for Gas-Solid Reactions. *Chem. Eng. Sci.* **1987**, *42* (5), 1262–1265. https://doi.org/10.1016/0009-2509(87)80084-2.

(182) Cooper, R. S. Slow Particle Diffusion in Ion Exchange Columns. *Ind. Eng. Chem. Fundam.* **1965**, *4* (3), 308–313. https://doi.org/10.1021/i160015a012.

(183) Bohart, G. S.; Adams, E. Q. Some Aspects of The Behavior of Charcoal with Respect to Chlorine. **1920**, *42* (3), 523–544.

(184) Bohart, G. S.; Adams, E. Q. Some Aspects of the Behavior of Charcoal with Respect to Chlorine. *J. Am. Chem. Soc.* **1920**, *42* (3), 523–544. https://doi.org/10.1021/ja01448a018.

(185) Belfiore, L. A. *Transport Phenomena for Chemical Reactor Design*; John Wiley & Sons, 2003.

(186) Lee, H. H. *Heterogeneous Reactor Design*; Butterworth, 1985.

(187) Cooney, D. O. *Adsorption Design for Wastewater Treatment*, 1 edition.; CRC Press: Boca Raton, Fla., 1998.

(188) McCarthy, D. J. On the Applicability of the Nucleation Model for Oxidation of Carbons. *Carbon* **1993**, *31* (1), 63–69. https://doi.org/10.1016/0008-6223(93)90156-5.

(189) Poling, B. E.; Prausnitz, J. M.; O'Connell, J. P. *The Properties of Gases and Liquids 5E*; McGraw Hill Professional, 2000.

(190) Szekely, J.; Evans, J. W.; Sohn, H. *Gas-Solid Reactions*; Elsevier, 1976. https://doi.org/10.1016/B978-0-12-680850-6.X5001-X.

(191) Rosso, I.; Galletti, C.; Bizzi, M.; Saracco, G.; Specchia, V. Zinc Oxide Sorbents for the Removal of Hydrogen Sulfide from Syngas. *Ind. Eng. Chem. Res.* **2003**, *42* (8), 1688–1697. https://doi.org/10.1021/ie0208467.

(192) Balichard, K.; Nyikeine, C.; Bezverkhyy, I. Nanocrystalline $ZnCO_3$—A Novel Sorbent for Low-Temperature Removal of H_2S. *J. Hazard. Mater.* **2014**, *264*, 79–83. https://doi.org/10.1016/j.jhazmat.2013.10.068.

(193) Kang, S.-H.; Bae, J. W.; Kim, S.-M.; Jun, K.-W. Effect of Phosphorus Modification on $Cu-ZnO-Al_2O_3$ for the Removal of H_2S. *Energy Fuels*. **2008,** *22* (4), 2580-2584 https://doi.org/10.1021/ef800054h.

(194) Montes, D.; Tocuyo, E.; González, E.; Rodríguez, D.; Solano, R.; Atencio, R.; Ramos, M. A.; Moronta, A. Reactive H2S Chemisorption on Mesoporous Silica Molecular Sieve-Supported CuO or ZnO. *Microporous Mesoporous Mater.* **2013**, *168*, 111–120. https://doi.org/10.1016/j.micromeso.2012.09.018.

(195) Elyassi, B.; Wahedi, Y. Al; Rajabbeigi, N.; Kumar, P.; Jeong, J. S.; Zhang, X.; Kumar, P.; Balasubramanian, V. V; Katsiotis, M. S.; Andre Mkhoyan, K.; Boukos, N.; Hashimi, S. Al; Tsapatsis, M. A High-Performance Adsorbent for Hydrogen Sulfide Removal. *Microporous Mesoporous Mater.* **2014**, *190*, 152–155. https://doi.org/10.1016/j.micromeso.2014.02.007.

(196) Pineda, M.; Palacios, J. M.; Alonso, L.; García, E.; Moliner, R. Performance of Zinc Oxide Based Sorbents for Hot Coal Gas Desulfurization in Multicycle Tests in a Fixed-Bed Reactor. *Fuel* **2000**, *79* (8), 885–895. https://doi.org/10.1016/S0016-2361(99)00218-5.

(197) Bagajewicz, M. J.; Tamhankar, S. S.; Stephanopoulos, M. F.; Gavalas, G. R. Hydrogen Sulfide Removal by Supported Vanadium Oxide. *Environ. Sci. Technol.* **1988**, *22* (4), 467–470. https://doi.org/10.1021/es00169a017.

(198) Chauk, S. S.; Agnihotri, R.; Jadhav, R. A.; Misro, S. K.; Fan, L.-S. Kinetics of High-Pressure Removal of Hydrogen Sulfide Using Calcium Oxide Powder. *AIChE J.* **2000**, *46* (6), 1157–1167. https://doi.org/10.1002/aic.690460608.

(199) Karvan, O.; Atakül, H. Investigation of CuO/Mesoporous SBA-15 Sorbents for Hot Gas Desulfurization. *Fuel Process. Technol.* **2008**, *89* (9), 908–915. https://doi.org/10.1016/j.fuproc.2008.03.004.

(200) Jiang, D.; Su, L.; Ma, L.; Yao, N.; Xu, X.; Tang, H.; Li, X. Cu–Zn–Al Mixed Metal Oxides Derived from Hydroxycarbonate Precursors for H2S Removal at Low Temperature. *Appl. Surf. Sci.* **2010**, *256* (10), 3216–3223. https://doi.org/10.1016/j.apsusc.2009.12.008.

(201) Sánchez, J. M.; Ruiz, E.; Otero, J. Selective Removal of Hydrogen Sulfide from Gaseous Streams Using a Zinc-Based Sorbent. *Ind. Eng. Chem. Res.* **2005**, *44* (2), 241–249. https://doi.org/10.1021/ie0497902.

(202) Barin, I.; Kubaschewski, O.; Knacke, O. Thermochemical Properties of Inorganic Substances: Supplement. Springer-Verlag: Berlin ; New York 1977, pp lxxxviii, 861 p.

(203) Karvan, O.; Sirkecioğlu, A.; Atakül, H. Investigation of Nano-CuO/Mesoporous SiO2 Materials as Hot Gas Desulphurization Sorbents. *Fuel Process. Technol.* **2009**, *90* (12), 1452–1458. https://doi.org/10.1016/j.fuproc.2009.06.027.

(204) Balsamo, M.; Cimino, S.; de Falco, G.; Erto, A.; Lisi, L. ZnO-CuO Supported on Activated Carbon for H2S Removal at Room Temperature. *Chem. Eng. J.* **2016**, *304*, 399–407. https://doi.org/10.1016/j.cej.2016.06.085.

(205) Ko, T.-H.; Chu, H.; Chaung, L.-K. The Sorption of Hydrogen Sulfide from Hot Syngas by Metal Oxides over Supports. *Chemosphere* **2005**, *58* (4), 467–474. https://doi.org/10.1016/j.chemosphere.2004.09.029.

(206) Yasyerli, S.; Dogu, G.; Ar, I.; Dogu, T. Activities of Copper Oxide and Cu−V and Cu−Mo Mixed Oxides for H2S Removal in the Presence and Absence of Hydrogen and Predictions of a Deactivation Model. *Ind. Eng. Chem. Res.* **2001**, *40* (23), 5206–5214. https://doi.org/10.1021/ie0010621.

(207) Li, Z.; Flytzani-Stephanopoulos, M. Cu−Cr−O and Cu−Ce−O Regenerable Oxide Sorbents for Hot Gas Desulfurization. *Ind. Eng. Chem. Res.* **1997**, *36* (1), 187–196. https://doi.org/10.1021/ie960245d.

(208) Azzam, S.; Simonetti, D. A. Linear Driving Force Approximations as Predictive Models for Reactive Sorption. *Energy Technol.* **2019**, 1900718. https://doi.org/10.1002/ente.201900718.

(209) Carnes, C. L.; Klabunde, K. J. Unique Chemical Reactivities of Nanocrystalline Metal Oxides toward Hydrogen Sulfide. *Chem. Mater.* **2002**, *14* (4), 1806–1811. https://doi.org/10.1021/cm011588r.

(210) Kayani, Z. N.; Umer, M.; Riaz, S.; Naseem, S. Characterization of Copper Oxide Nanoparticles Fabricated by the Sol–Gel Method. *J. Electron. Mater.* **2015**, *44* (10), 3704–3709. https://doi.org/10.1007/s11664-015-3867-5.

(211) Zhu, J.; Bi, H.; Wang, Y.; Wang, X.; Yang, X.; Lu, L. Synthesis of Flower-like CuO Nanostructures via a Simple Hydrolysis Route. *Mater. Lett.* **2007**, *61* (30), 5236–5238. https://doi.org/10.1016/j.matlet.2007.04.037.

(212) Huang, J.; Tang, F.; Gu, C.; Shi, C.; Zhai, M. Flower-like CuO Hierarchical Nanostructures: Synthesis, Characterization, and Property. *Front. Optoelectron.* **2012**, *5* (4), 429–434. https://doi.org/10.1007/s12200-012-0293-7.

(213) Liu, C.; Zhang, L.; Deng, J.; Mu, Q.; Dai, H.; He, H. Surfactant-Aided Hydrothermal Synthesis and Carbon Dioxide Adsorption Behavior of Three-Dimensionally Mesoporous Calcium Oxide Single-Crystallites with Tri-, Tetra-, and Hexagonal Morphologies. *J. Phys. Chem. C* **2008**, *112* (49), 19248–19256. https://doi.org/10.1021/jp8064568.

(214) Yu, J. C.; Xu, A.; Zhang, L.; Song, R.; Wu, L. Synthesis and Characterization of Porous Magnesium Hydroxide and Oxide Nanoplates. *J. Phys. Chem. B* **2004**, *108* (1), 64–70. https://doi.org/10.1021/jp035340w.

(215) Biesinger, M. C.; Lau, L. W. M.; Gerson, A. R.; Smart, R. St. C. Resolving Surface Chemical States in XPS Analysis of First Row Transition Metals, Oxides and Hydroxides: Sc, Ti, V, Cu and Zn. *Appl. Surf. Sci.* **2010**, *257* (3), 887–898. https://doi.org/10.1016/j.apsusc.2010.07.086.

(216) Kresse, G.; Furthmüller, J. Efficient Iterative Schemes for Ab Initio Total-Energy Calculations Using a Plane-Wave Basis Set. *Phys. Rev. B* **1996**, *54* (16), 11169.

(217) Kresse, G.; Furthmüller, J. Efficiency of Ab-Initio Total Energy Calculations for Metals and Semiconductors Using a Plane-Wave Basis Set. *Comput. Mater. Sci.* **1996**, *6* (1), 15–50.

(218) Kresse, G.; Hafner, J. Ab Initio Molecular-Dynamics Simulation of the Liquid-Metal–Amorphous-Semiconductor Transition in Germanium. *Phys. Rev. B* **1994**, *49* (20), 14251.

(219) Kresse, G.; Hafner, J. Ab Initio Molecular Dynamics for Liquid Metals. *Phys. Rev. B* **1993**, *47* (1), 558.

(220) Wang, L.; Maxisch, T.; Ceder, G. Oxidation Energies of Transition Metal Oxides within the GGA+ U Framework. *Phys. Rev. B* **2006**, *73* (19), 195107.

(221) Zhang, Q.; Zhang, K.; Xu, D.; Yang, G.; Huang, H.; Nie, F.; Liu, C.; Yang, S. CuO Nanostructures: Synthesis, Characterization, Growth Mechanisms, Fundamental Properties, and Applications. *Prog. Mater. Sci.* **2014**, *60*, 208–337. https://doi.org/10.1016/j.pmatsci.2013.09.003.

(222) Nolan, M.; Elliott, S. D. The P-Type Conduction Mechanism in Cu 2 O: A First Principles Study. *Phys. Chem. Chem. Phys.* **2006**, *8* (45), 5350–5358.

(223) Su, D.; Xie, X.; Dou, S.; Wang, G. CuO Single Crystal with Exposed {001} Facets - A Highly Efficient Material for Gas Sensing and Li-Ion Battery Applications. *Sci. Rep.* **2014**, *4* (1), 5753. https://doi.org/10.1038/srep05753.

(224) Mohan, V. M.; Raja, V.; Sharma, A. K.; Narasimha Rao, V. V. R. Ion Transport and Battery Discharge Characteristics of Polymer Electrolyte Based on PEO Complexed with NaFeF4 Salt. *Ionics* **2006**, *12* (3), 219. https://doi.org/10.1007/s11581-006-0035-1.

(225) Aguirre, J. M.; GutiÃ\copyrightrrez, A.; Giraldo, O. Simple Route for the Synthesis of Copper Hydroxy Salts. *J. Braz. Chem. Soc.* **2011**, *22*, 546–551.

(226) Zhang, Q.; Zhang, K.; Xu, D.; Yang, G.; Huang, H.; Nie, F.; Liu, C.; Yang, S. CuO Nanostructures: Synthesis, Characterization, Growth Mechanisms, Fundamental Properties, and Applications. *Prog. Mater. Sci.* **2014**, *60*, 208–337. https://doi.org/10.1016/j.pmatsci.2013.09.003.

(227) Borodko, Y.; Lee, H. S.; Joo, S. H.; Zhang, Y.; Somorjai, G. Spectroscopic Study of the Thermal Degradation of PVP-Capped Rh and Pt Nanoparticles in H_2 and O_2 Environments. *J. Phys. Chem. C* **2010**, *114* (2), 1117–1126. https://doi.org/10.1021/jp909008z.

(228) Kozak, D. S.; Sergiienko, R. A.; Shibata, E.; Iizuka, A.; Nakamura, T. Non-Electrolytic Synthesis of Copper Oxide/Carbon Nanocomposite by Surface Plasma in Super-Dehydrated Ethanol. *Sci. Rep.* **2016**, *6*, 21178.

(229) Biljana, Š.; E., B. C.; Alison, C.; G., C. R. Copper Oxide – Graphite Composite Electrodes: Application to Nitrite Sensing. *Electroanalysis 19* (1), 79–84. https://doi.org/10.1002/elan.200603708.

(230) Sick, G.; Schwerdtfeger, K. Hot Desulfurization of Coal Gas with Copper. *Metall. Trans. B* **1987**, *18* (3), 603–609.

(231) Samokhvalov, A.; Tatarchuk, B. J. Characterization of Active Sites, Determination of Mechanisms of H_2S, COS and CS_2 Sorption and Regeneration of ZnO Low-Temperature Sorbents: Past, Current and Perspectives. *Phys. Chem. Chem. Phys.* **2011**, *13* (8), 3197–3209. https://doi.org/10.1039/C0CP01227K.

(232) Gibson, J. B.; Harrison, D. P. The Reaction between Hydrogen Sulfide and Spherical Pellets of Zinc Oxide. *Ind. Eng. Chem. Process Des. Dev.* **1980**, *19* (2), 231–237. https://doi.org/10.1021/i260074a005.

(233) Lew, S.; Sarofim, A. F.; Flytzani-Stephanopoulos, M. Sulfidation of Zinc Titanate and Zinc Oxide Solids. *Ind. Eng. Chem. Res.* **1992**, *31* (8), 1890–1899. https://doi.org/10.1021/ie00008a009.

(234) Ruiz-Martínez, J.; Beale, A. M.; Deka, U.; O'Brien, M. G.; Quinn, P. D.; Mosselmans, J. F. W.; Weckhuysen, B. M. Correlating Metal Poisoning with Zeolite Deactivation in an Individual Catalyst Particle by Chemical and Phase-Sensitive X-Ray Microscopy. *Angew. Chem. Int. Ed.* **2013**, *52* (23), 5983–5987. https://doi.org/10.1002/anie.201210030.

(235) Flytzani-Stephanopoulos, M.; Sakbodin, M.; Wang, Z. Regenerative Adsorption and Removal of H_2S from Hot Fuel Gas Streams by Rare Earth Oxides. *Science* **2006**, *312* (5779), 1508–1510. https://doi.org/10.1126/science.1125684.

(236) Neveux, L.; Chiche, D.; Pérez-Pellitero, J.; Favergeon, L.; Gay, A.-S.; Pijolat, M. New Insight into the ZnO Sulfidation Reaction: Mechanism and Kinetics Modeling of the ZnS Outward Growth. *Phys. Chem. Chem. Phys.* **2013**, *15* (5), 1532–1545. https://doi.org/10.1039/C2CP42988H.

(237) Liu, Y.; Meirer, F.; Williams, P. A.; Wang, J.; Andrews, J. C.; Pianetta, P. TXM-Wizard: A Program for Advanced Data Collection and Evaluation in Full-Field Transmission X-Ray Microscopy. *J. Synchrotron Radiat.* **2012**, *19* (Pt 2), 281–287. https://doi.org/10.1107/S0909049511049144.

(238) Meirer, F.; Cabana, J.; Liu, Y.; Mehta, A.; Andrews, J. C.; Pianetta, P. Three-Dimensional Imaging of Chemical Phase Transformations at the Nanoscale with Full-Field Transmission X-Ray Microscopy. *J. Synchrotron Radiat.* **2011**, *18* (Pt 5), 773—781. https://doi.org/10.1107/S0909049511019364.

(239) Gonzalez-Jimenez, I. D.; Cats, K.; Davidian, T.; Ruitenbeek, M.; Meirer, F.; Liu, Y.; Nelson, J.; Andrews, J. C.; Pianetta, P.; de Groot, F. M. F.; Weckhuysen, B. M. Hard X-Ray Nanotomography of Catalytic Solids at Work. *Angew. Chem. Int. Ed.* **2012**, *51* (48), 11986–11990. https://doi.org/10.1002/anie.201204930.

(240) Lin, F.; Liu, Y.; Yu, X.; Cheng, L.; Singer, A.; Shpyrko, O. G.; Xin, H. L.; Tamura, N.; Tian, C.; Weng, T.-C.; Yang, X.-Q.; Meng, Y. S.; Nordlund, D.; Yang, W.; Doeff, M. M. Synchrotron X-Ray Analytical Techniques for Studying Materials Electrochemistry in Rechargeable Batteries. *Chem. Rev.* **2017**, *117* (21), 13123–13186. https://doi.org/10.1021/acs.chemrev.7b00007.

(241) Ravel, B.; Newville, M. ATHENA, ARTEMIS, HEPHAESTUS: Data Analysis for X-Ray Absorption Spectroscopy Using IFEFFIT. *J. Synchrotron Radiat.* **2005**, *12* (4), 537–541. https://doi.org/10.1107/S0909049505012719.

(242) Inorganic Crystal Structure Database – ICSD | FIZ Karlsruhe https://www.fiz-karlsruhe.de/de/produkte-und-dienstleistungen/inorganic-crystal-structure-database-icsd (accessed Aug 31, 2019).

(243) Weng, T.-C.; Waldo, G. S.; Penner-Hahn, J. E. A Method for Normalization of X-Ray Absorption Spectra. *J. Synchrotron Radiat.* **2005**, *12* (Pt 4), 506–510. https://doi.org/10.1107/S0909049504034193.

(244) Kuzmin, A.; Chaboy, J. EXAFS and XANES Analysis of Oxides at the Nanoscale. *IUCrJ* **2014**, *1* (Pt 6), 571–589. https://doi.org/10.1107/S2052252514021101.

(245) Velu, S.; Suzuki, K.; Gopinath, C. S.; Yoshida, H.; Hattori, T. XPS, XANES and EXAFS Investigations of CuO/ZnO/Al_2O_3/ZrO_2 Mixed Oxide Catalysts. *Phys Chem Chem Phys* **2002**, *4* (10), 1990–1999. https://doi.org/10.1039/B109766K.

(246) Liu, H.; Zeng, F.; Gao, S.; Wang, G.; Song, C.; Pan, F. Contributions of Magnetic Properties in Epitaxial Copper-Doped ZnO. *Phys Chem Chem Phys* **2013**, *15* (31), 13153–13161. https://doi.org/10.1039/C3CP51894A.

(247) Dunne, S. R. Industrial Gas Phase Adsorptive Separations. In *Zeolites in Industrial Separation and Catalysis*; John Wiley & Sons, Ltd, 2010; pp 273–305. https://doi.org/10.1002/9783527629565.ch9.

(248) Ruthven, D. M. *Principles of Adsorption and Adsorption Processes*; John Wiley & Sons: New York, 1984.

(249) Azzam, S. A.; Alshafei, F. H.; López-Ausens, T.; Ghosh, R.; Biswas, A. N.; Sautet, P.; Prikhodko, S.; Simonetti, D. A. Effects of Morphology and Surface Properties of Copper Oxide on the Removal of Hydrogen Sulfide from Gaseous Streams. *Ind. Eng. Chem. Res.* **2019**, *58* (40), 18836–18847. https://doi.org/10.1021/acs.iecr.9b03975.

(250) Pattrick, R. A. D.; Mosselmans, J. F. W.; Charnock, J. M.; England, K. E. R.; Helz, G. R.; Garner, C. D.; Vaughan, D. J. The Structure of Amorphous Copper Sulfide Precipitates: An X-Ray Absorption Study. *Geochim. Cosmochim. Acta* **1997**, *61* (10), 2023–2036. https://doi.org/10.1016/S0016-7037(97)00061-6.

(251) Fjellvåg, H.; Grønvold, F.; Stølen, S.; Andresen, A.; Müller-Käfer, R. Low-Temperature Structural Distortion in CuS. *Z. Krist. - Z Krist.* **1988**, *184*, 111–121. https://doi.org/10.1524/zkri.1988.184.1-2.111.

(252) Li, D.; Bancroft, G. M.; Kasrai, M.; Fleet, M. E.; Feng, X. H.; Yang, B. X.; Tan, K. H. S K- and L-Edge XANES and Electronic Structure of Some Copper Sulfide Minerals. *Phys. Chem. Miner.* **1994**, *21* (5), 317–324. https://doi.org/10.1007/BF00202096.

(253) Kumar, P.; Nagarajan, R.; Sarangi, R. Quantitative X-Ray Absorption and Emission Spectroscopies: Electronic Structure Elucidation of Cu_2S and CuS. *J. Mater. Chem. C* **2013**, *1* (13), 2448. https://doi.org/10.1039/c3tc00639e.

(254) Mercury - The Cambridge Crystallographic Data Centre (CCDC) https://www.ccdc.cam.ac.uk/solutions/csd-system/components/mercury/ (accessed Oct 17, 2019).

(255) Bare, S.; Ressler, T. Chapter 6 Characterization of Catalysts in Reactive Atmospheres by X-Ray Absorption Spectroscopy. *Adv. Catal. - ADVAN CATAL* **2009**, *52*, 339–465. https://doi.org/10.1016/S0360-0564(08)00006-0.

(256) Koningsberger, D. C.; Prins, R. (eds.). *X-Ray Absorption: Principles, Applications, Techniques of EXAFS, SEXAFS, and XANES*; John Wiley and Sons,New York, NY: United States, 1988.

(257) Bolin, T. B.; Wu, T.; Schweitzer, N.; Lobo-Lapidus, R.; Kropf, A. J.; Wang, H.; Hu, Y.; Miller, J. T.; Heald, S. M. In Situ Intermediate-Energy X-Ray Catalysis Research at the Advanced Photon Source Beamline 9-BM. *Catal. Today* **2013**, *205*, 141–147. https://doi.org/10.1016/j.cattod.2012.09.034.

(258) Sharma, A.; Varshney, M.; Park, J.; Ha, T.-K.; Chae, K.-H.; Shin, H.-J. XANES, EXAFS and Photocatalytic Investigations on Copper Oxide Nanoparticles and Nanocomposites. *RSC Adv.* **2015**, *5* (28), 21762–21771.

(259) Marinkovic, N. S.; Sasaki, K.; Adzic, R. R. Determination of Single- and Multi-Component Nanoparticle Sizes by X-Ray Absorption Spectroscopy. *J. Electrochem. Soc.* **2018**, *165* (15), J3222–J3230. https://doi.org/10.1149/2.0281815jes.

(260) Hoffman, A. S.; Azzam, S.; Zhang, K.; Xu, Y.; Liu, Y.; Bare, S. R.; Simonetti, D. A. Direct Observation of the Kinetics of Gas–Solid Reactions Using in Situ Kinetic and Spectroscopic Techniques. *React. Chem. Eng.* **2018**, *3* (5), 668–675. https://doi.org/10.1039/C8RE00020D.

(261) EVANS, H. T. Djurleite ($Cu_{1.94}S$) and Low Chalcocite (Cu_2S): New Crystal Structure Studies. *Science* **1979**, *203* (4378), 356–358.

(262) Koto, K.; Morimoto, N. The Crystal Structure of Anilite. *Acta Crystallogr. B* **1970**, *26* (7), 915–924. https://doi.org/10.1107/S0567740870003370.

(263) R. J. Goble, R. I.; George Robinson. Geerite, Cu (Sub 1.60) S, a New Copper Sulfide from Dekalb Township, New York. *Can. Mineral.* **1980**, *18* (4), 519–523.

(264) Mumme, W. G.; Gable, R. W.; Petricek, V. The Crystal Structure of Roxbyite, Cu58S32. *Can. Mineral.* **2012**, *50* (2), 423–430. https://doi.org/10.3749/canmin.50.2.423.

(265) Rosso, I.; Galletti, C.; Bizzi, M.; Saracco, G.; Specchia, V. Zinc Oxide Sorbents for the Removal of Hydrogen Sulfide from Syngas. *Ind. Eng. Chem. Res.* **2003**, *42* (8), 1688–1697. https://doi.org/10.1021/ie0208467.

(266) Garces, H. F.; Galindo, H. M.; Garces, L. J.; Hunt, J.; Morey, A.; Suib, S. L. Low Temperature H2S Dry-Desulfurization with Zinc Oxide. *Microporous Mesoporous Mater.* **2010**, *127* (3), 190–197. https://doi.org/10.1016/j.micromeso.2009.07.022.

(267) Balichard, K.; Nyikeine, C.; Bezverkhyy, I. Nanocrystalline ZnCO3-A Novel Sorbent for Low-Temperature Removal of H_2S. *J. Hazard. Mater.* **2014**, *264*, 79–83. https://doi.org/10.1016/j.jhazmat.2013.10.068.

(268) Girard, V.; Baudot, A.; Chiche, D.; Bazer-Bachi, D.; Bounie, C.; Geantet, C. Rational Selection of Single Oxide Sorbents for Syngas Desulfurization Regenerable at Reduced Temperature: Thermochemical Calculations and Experimental Study. *Fuel* **2014**, *128*, 220–230. https://doi.org/10.1016/j.fuel.2014.02.058.

(269) Jalan, V. Studies involving high temperature desulfurization/regeneration reactions of metal oxides for fuel cell development. Final report https://digital.library.unt.edu/ark:/67531/metadc1061781/ (accessed Aug 18, 2019). https://doi.org/10.2172/5143010.

(270) Rosenqvist, T. Phase Equilibria in the Pyrometallurgy of Sulfide Ores. *Metall. Trans. B* **1978**, *9* (3), 337–351. https://doi.org/10.1007/BF02654407.

(271) Elyassi, B.; Wahedi, Y. A.; Rajabbeigi, N.; Kumar, P.; Jeong, J. S.; Zhang, X.; Kumar, P.; Balasubramanian, V. V.; Katsiotis, M. S.; Andre Mkhoyan, K.; Boukos, N.; Hashimi, S. A.; Tsapatsis, M. A High-Performance Adsorbent for Hydrogen Sulfide Removal. *Microporous Mesoporous Mater.* **2014**, *190*, 152–155. https://doi.org/10.1016/j.micromeso.2014.02.007.

(272) Huang, G.; He, E.; Wang, Z.; Fan, H.; Shangguan, J.; Croiset, E.; Chen, Z. Synthesis and Characterization of γ-Fe2O3 for H2S Removal at Low Temperature. *Ind. Eng. Chem. Res.* **2015**, *54* (34), 8469–8478. https://doi.org/10.1021/acs.iecr.5b01398.

(273) Baird, T.; Campbell, K. C.; Holliman, P. J.; Hoyle, R.; Stirling, D.; Williams, B. P. Mixed Co-Zn-Al Oxides as Absorbents for Low-Temperature Gas Desulfurisation. *J. Chem. Soc. Faraday Trans.* **1995**, *91* (18), 3219–3230. https://doi.org/10.1039/FT9959103219.

(274) Xue, M.; Chitrakar, R.; Sakane, K.; Ooi, K. Screening of Adsorbents for Removal of H2S at Room Temperature. *Green Chem.* **2003**, *5* (5), 529–534. https://doi.org/10.1039/B303167P.

(275) Azzam, S. A.; Alshafei, F. H.; López-Ausens, T.; Ghosh, R.; Biswas, A. N.; Sautet, P.; Prikhodko, S.; Simonetti, D. A. Effects of Morphology and Surface Properties of Copper Oxide on the Removal of Hydrogen Sulfide from Gaseous Streams. *Ind. Eng. Chem. Res.* **2019**, *58* (40), 18836–18847. https://doi.org/10.1021/acs.iecr.9b03975.

(276) Grant, D. J. W.; York, P. A Disruption Index for Quantifying the Solid State Disorder Induced by Additives or Impurities. II. Evaluation from Heat of Solution. *Int. J. Pharm.* **1986**, *28* (2–3), 103–112. https://doi.org/10.1016/0378-5173(86)90233-4.

(277) Sun, X.-Y.; Zhang, X.; Sun, X.; Qian, N.-X.; Wang, M.; Ma, Y.-Q. Improved Adsorption and Degradation Performance by S-Doping of (001)-TiO $_2$. *Beilstein J. Nanotechnol.* **2019**, *10*, 2116–2127. https://doi.org/10.3762/bjnano.10.206.

(278) Singhal, S.; Kaur, J.; Namgyal, T.; Sharma, R. Cu-Doped ZnO Nanoparticles: Synthesis, Structural and Electrical Properties. *Phys. B Condens. Matter* **2012**, *407* (8), 1223–1226. https://doi.org/10.1016/j.physb.2012.01.103.

(279) Jansons, A. W.; Koskela, K. M.; Crockett, B. M.; Hutchison, J. E. Transition Metal-Doped Metal Oxide Nanocrystals: Efficient Substitutional Doping through a Continuous Growth Process. *Chem. Mater.* **2017**, *29* (19), 8167–8176. https://doi.org/10.1021/acs.chemmater.7b02176.

(280) AAsbrink, S.; Norrby, L.-J. A Refinement of the Crystal Structure of Copper(II) Oxide with a Discussion of Some Exceptional e.s.d.'s. *Acta Crystallogr. Sect. B* **1970**, *26* (1), 8–15. https://doi.org/10.1107/S0567740870001838.

(281) Azzam, S.; Alshafei, F. H.; Lopez-Ausens, T.; Ghosh, R.; Biswas, A. N.; Sautet, P.; Prikhodko, S. V.; Simonetti, D. A. Effects of Morphology and Surface Properties of Copper Oxide on the Removal of Hydrogen Sulfide from Gaseous Streams. *Ind. Eng. Chem. Res.* **2019**. https://doi.org/10.1021/acs.iecr.9b03975.

(282) Lamberti, C. The Use of Synchrotron Radiation Techniques in the Characterization of Strained Semiconductor Heterostructures and Thin Films. *Surf. Sci. Rep.* **2004**, *53* (1–5), 1–197. https://doi.org/10.1016/j.surfrep.2003.12.001.

(283) Pickering, I. J.; Prince, R. C.; Divers, T.; George, G. N. Sulfur K-Edge X-Ray Absorption Spectroscopy for Determining the Chemical Speciation of Sulfur in Biological Systems. *FEBS Lett.* **1998**, *441* (1), 11–14. https://doi.org/10.1016/S0014-5793(98)01402-1.

(284) Fleet, M. E.; Liu, X.; Harmer, S. L.; King, P. L. Sulfur K-Edge XANES Spectroscopy: Chemical State and Content Of Sulfur In Silicate Glasses. *Can. Mineral.* **2005**, *43* (5), 1605–1618. https://doi.org/10.2113/gscanmin.43.5.1605.

(285) Asakura, H.; Shishido, T.; Teramura, K.; Tanaka, T. Local Structure and La L $_1$ and L $_3$ -Edge XANES Spectra of Lanthanum Complex Oxides. *Inorg. Chem.* **2014**, *53* (12), 6048–6053. https://doi.org/10.1021/ic500381z.

(286) Abbasian, J.; Slimane, R. B. A Regenerable Copper-Based Sorbent for H2S Removal from Coal Gases. *Ind. Eng. Chem. Res.* **1998**, *37* (7), 2775–2782. https://doi.org/10.1021/ie980047h.

(287) Sandra, F.; Schade, E.; Leistner, M.; Grothe, J.; Kaskel, S. Solvothermal Synthesis of a Bismuth/Zinc Mixed Oxide Material for H2S Removal at Room Temperature: Synthesis, Performance, Characterization and Regeneration Ability. *Mater. Chem. Phys.* **2017**, *199*, 329–339. https://doi.org/10.1016/j.matchemphys.2017.06.063.

(288) Jun, H. K.; Lee, T. J.; Ryu, S. O.; Kim, J. C. A Study of Zn−Ti-Based H_2S Removal Sorbents Promoted with Cobalt Oxides. *Ind. Eng. Chem. Res.* **2001**, *40* (16), 3547–3556. https://doi.org/10.1021/ie0011167.

(289) Jung, S. Y.; Lee, S. J.; Lee, T. J.; Ryu, C. K.; Kim, J. C. H2S Removal and Regeneration Properties of Zn–Al-Based Sorbents Promoted with Various Promoters. *Catal. Today* **2006**, *111* (3), 217–222. https://doi.org/10.1016/j.cattod.2005.10.029.

(290) Wang, J.; Yang, C.; Zhao, Y.-R.; Fan, H.-L.; Wang, Z.-D.; Shangguan, J.; Mi, J. Synthesis of Porous Cobalt Oxide and Its Performance for H2S Removal at Room Temperature. *Ind. Eng. Chem. Res.* **2017**, *56* (44), 12621–12629. https://doi.org/10.1021/acs.iecr.7b02934.

(291) Zeng, B.; Yue, H.; Liu, C.; Huang, T.; Li, J.; Zhao, B.; Zhang, M.; Liang, B. Desulfurization Behavior of Fe–Mn-Based Regenerable Sorbents for High-Temperature H_2S Removal. *Energy Fuels* **2015**, *29* (3), 1860–1867. https://doi.org/10.1021/ef502092v.